

UNIVERSITY OF BUCHAREST  
FACULTY OF PHYSICS

A Systematic Description of the Wobbling Motion  
in Odd-Mass Nuclei Within a Semi-Classical  
Formalism

**Scientific Coordinator:**  
Prof. Dr. Em. A. A. Raduta

**PhD Student:**  
Robert Poenaru

A thesis submitted for the degree of  
*Doctor of Philosophy*

March 2023

## *Acknowledgements*

### **A Systematic Description of the Wobbling Motion in Odd-Mass Nuclei Within a Semi-Classical Formalism**

*It has been quite a journey...* These five years showed me that many results can be achieved through hard work and dedication, but also much more can lie ahead of us in terms of new projects, new discoveries, and innovative theories.

Firstly, I would like to express my gratitude to Prof. Apolodor Aristotel Raduta, my coordinator and also mentor. His patience, work ethic, and constant support gave me the necessary motivation to keep going and improve in every aspect specific to academic research. Big thanks to my family for the tremendous emotional help and life advices offered when needed. Moreover, I would like to thank my highschool teacher Gabriela Pojoreanu, for igniting in me a love for Physics and fostering my curiosity about the laws of Nature.

I am forever grateful to my medical team - Dr. Demian, Dr. Mester, Dr. Radu and Dr. Zarma - whose unwavering support and expertise have been instrumental in my recovery and well-being. Completing my studies and this thesis would not have been possible without their attentive care. I want to extend heartfelt thanks to Aurica for her invaluable guidance in helping me and my family understand the importance of time in matters of health. And to my cousin Alex, who has been a constant source of support and encouragement - thank you for always being there.

Finally, I would like to believe that by reading this thesis our work and achieved results will be appreciated.

# Contents

<b>Acknowledgements</b>	<b>ii</b>
<b>1 Introduction</b>	<b>1</b>
1.1 Aim . . . . .	2
1.2 Motivation . . . . .	3
1.3 Thesis Structure . . . . .	4
<b>2 Theoretical Aspects of Nuclear Deformation</b>	<b>7</b>
2.1 Shape of Nuclei . . . . .	8
2.1.1 Multipole deformations . . . . .	8
2.1.2 Quadrupole Deformation . . . . .	10
2.1.3 Axial quadrupole deformations . . . . .	12
2.1.4 Non-Axial quadrupole deformations . . . . .	13
2.1.5 Lund Convention . . . . .	15
2.2 Nuclear Models . . . . .	16
2.2.1 Deformed Shell Model . . . . .	16
2.2.2 Deformed Shell Model - Nilsson Model . . . . .	17
2.2.3 Single-particle states in deformed nuclei . . . . .	20
2.2.4 Collective Model . . . . .	26
2.2.5 Bohr Hamiltonian . . . . .	26
2.2.6 Nuclear Vibration . . . . .	28
2.2.7 Nuclear Rotation . . . . .	31
2.2.8 Superimposed Rotations and Vibrations . . . . .	35
2.2.9 Collective Quantities . . . . .	37
2.2.9.1 R - Energy Ratio . . . . .	37
2.2.9.2 Rotational Frequencies . . . . .	38
2.2.9.3 Moments of Inertia . . . . .	39
2.2.9.4 Electric Quadrupole Moment . . . . .	42
2.3 Triaxial Nuclei and Their Signatures . . . . .	45
2.3.1 Non-axial nuclei . . . . .	47
2.3.2 Triaxial Rotor Model . . . . .	48
2.3.3 Triaxial Particle + Rotor Model . . . . .	49
2.3.4 Stable Triaxial Deformation . . . . .	54
2.3.5 Fingerprints of Triaxiality . . . . .	56

2.3.6	Chiral motion . . . . .	57
2.3.7	Wobbling Motion . . . . .	58
<b>3</b>	<b>Wobbling Motion in Nuclei</b>	<b>63</b>
3.1	Wobbling Motion in Even-Even Nuclei . . . . .	63
3.1.1	Triaxial rotor energy vs. wobbling energy . . . . .	70
3.1.2	Testing the Harmonic Approximation . . . . .	71
3.1.2.1	Energy Spectrum . . . . .	71
3.1.2.2	Transition Probabilities . . . . .	73
3.1.2.3	General Discussion . . . . .	75
3.2	Wobbling Motion in Odd-Mass Nuclei . . . . .	76
3.3	Wobbling Nuclei - A Complete Catalog . . . . .	86
3.3.1	Wobbling around A=100 . . . . .	87
3.3.2	Wobbling around A=130 . . . . .	88
3.3.3	Wobbling around A=160 . . . . .	90
3.3.4	Wobbling around A=180 . . . . .	92
3.3.5	Wobbling Motion - Experimental Chart . . . . .	95
3.4	Concluding Remarks . . . . .	95
<b>4</b>	<b>New Theoretical Formalism</b>	<b>99</b>
4.1	Previous Work - Foundation . . . . .	99
4.2	Re-interpretation of the Wobbling Motion . . . . .	102
4.2.1	Variational Principle . . . . .	103
4.2.2	Classical Equations of Motion . . . . .	105
4.2.3	Classical Energy Function (CEF) . . . . .	107
4.2.3.1	Canonical Factors - Qualitative Analysis . . . . .	107
4.2.3.2	Critical Region . . . . .	108
4.2.4	Wobbling Frequencies . . . . .	110
4.2.5	An Alternative Approach . . . . .	116
4.3	A New Band Structure in Lu Isotopes . . . . .	124
4.3.1	Variational States . . . . .	125
4.3.2	Fitting Parameters . . . . .	128
4.4	Numerical Results in Lu Isotopes . . . . .	130
4.4.1	Numerical Parameters . . . . .	133
4.4.2	Energies . . . . .	135
4.4.3	Alignment . . . . .	138
4.4.4	Reference Energy . . . . .	141
4.4.5	Dynamic MOI . . . . .	144
4.4.6	Electromagnetic Transitions . . . . .	146
4.4.6.1	E2 Transitions . . . . .	147
4.4.6.2	M1 Transitions . . . . .	154
4.5	Concluding Remarks . . . . .	161
<b>5</b>	<b>Novel Description of the Wobbling Bands</b>	<b>165</b>
5.1	Parity Partner Bands . . . . .	166

5.1.1	Parity of the wave-function . . . . .	169
5.1.2	Redefined Energy Spectrum . . . . .	170
5.2	Numerical Results . . . . .	171
5.2.1	Energy spectrum . . . . .	172
5.2.2	Interpretation of the parameter set . . . . .	176
5.3	Classical Energy Function (CEF) . . . . .	178
5.3.1	CEF - Stability Regions . . . . .	179
5.3.2	Classical 3D Trajectories . . . . .	184
5.4	Concluding Remarks . . . . .	189
<b>6</b>	<b>Study of the Wobbling Motion via a Boson Description</b>	<b>193</b>
6.1	Angular Momentum - Boson Representation . . . . .	194
6.2	Theoretical Framework . . . . .	197
6.2.1	Potential Energy for the PRM Hamiltonian . . . . .	197
6.2.2	Another boson expansion for the angular momentum . . . . .	202
6.2.3	Harmonic Approximation of the Energy . . . . .	202
6.3	Classical Description of the Hamiltonian . . . . .	205
6.4	Electromagnetic Transitions . . . . .	217
6.5	Numerical Results . . . . .	219
6.5.1	Excitation Energies . . . . .	220
6.5.2	On the Chiral Character of the Wobbling Motion . . . . .	226
6.5.3	Electromagnetic Transitions . . . . .	230
6.5.4	Concluding Remarks . . . . .	231
<b>7</b>	<b>General Conclusions</b>	<b>235</b>
<b>A</b>	<b>Shell Model</b>	<b>241</b>
A.1	Shell model . . . . .	241
A.2	Nilsson Orbitals . . . . .	249
<b>B</b>	<b>Two-State Mixing</b>	<b>257</b>
<b>C</b>	<b>Rotational Bands in Nuclei</b>	<b>263</b>
C.1	Deformation Aligned Bands . . . . .	264
C.2	Rotation Aligned Bands . . . . .	265
<b>D</b>	<b>Personal Contributions</b>	<b>269</b>
D.1	Published Papers . . . . .	269
D.1.1	ISI Indexed Papers Published In-Scope . . . . .	270
D.1.2	ISI Indexed Papers Published Out-of-Scope . . . . .	270
D.1.3	Non-ISI Papers Published Out-of-Scope . . . . .	270
D.2	Conferences . . . . .	270
D.2.1	International . . . . .	270
D.2.2	National . . . . .	270
<b>List of Figures</b>		<b>271</b>

**List of Tables****287**

# Chapter 1

## Introduction

Ground-state nuclei possessing spherical or axial symmetry are predominant across the chart of nuclides. Near closed shells, the deformation is sufficient that models based on spherical symmetries can be used to describe nuclear properties (e.g., energies, quadrupole moments, and so on). Besides the spherical and axially-symmetric shapes, the existence of triaxial nuclear deformation was theoretically predicted a long time ago [1]. The rigid triaxiality of nuclei is defined by the asymmetry parameter  $\gamma$ , giving rise to a unique behavior concerning the system dynamics. Lately, triaxial nuclei drew a lot of attention within the nuclear physics community, since the description of nuclear properties represents a real challenge from an experimental and also theoretical standpoint. Great progress towards experimental setups being able to perform measurements of high-spin has only been possible after the 2000s. It is worth mentioning that some experiments regarding alpha- $\alpha$  particle reactions induced in heavy nuclei in the early 1960s (e.g., [2]) helped to produce a decent amount of data for the rotational in the high-spin region ( $\geq 20\hbar$ ).

The physics of *high-spin* states has been studied since the early 1950s, with the breakthrough on the theoretical side made by Bohr and Mottelson [1]. The nuclear rotation was described in terms of the rotational degrees of freedom associated with other nuclear degrees of freedom such as particle-vibration, quadrupole-quadrupole, parity, and so on. The spherical shell-model only describes nuclei near the closed shells. On the other hand, for nuclei that are far from closed shells, a deformed potential must be utilized. In the case of even-even nuclei, unique band

structures resulting from vibrations and rotations of the nuclear surface appear in the energy range  $0 - 2$  MeV.

Even though triaxiality has an elusive character, two phenomena, i.e., wobbling motion and chiral bands are uniquely attributed to triaxial shapes. Consequently, these two were intensively searched by using advanced techniques. In this work, the focus is given exclusively on the first effect, although it is worth specifying that the current team provides a unified description of both phenomena in their most recent work [3], which stands out as the first-ever theoretical treatment describing wobbling and chirality on an equal footing.

Quantized wobbling modes were first discovered experimentally in  $^{163}\text{Lu}$ , where the presence of the odd-proton  $i_{13/2}$  grants the apparition of multiple rotational bands to appear around the yrast line. This experiment consisted of populating high-spin states with a  $^{29}\text{Si}$  beam interacting with a thin target of  $^{139}\text{La}$ . Later on, other odd- $A$  nuclei were discovered as exhibiting wobbling excitations, and all the experimental findings will be mentioned in the following chapters. The nuclei having a triaxial shape can rotate about any of the principal axes, causing rich collective spectra to emerge. The family of rotational bands is described in terms of vibrational excitations. As a classical analog, nuclear wobbling motion corresponds to the spinning motion of an asymmetric top. The experimental fingerprints for wobbling motion indicate that the energy spectrum behaves as  $\sim I(I + 1)$  concerning the angular momentum, there is a clear dominance of electric transitions over the magnetic ones, and the nuclei have large quadrupole moments. All these quantities will be exploited in detail in the coming chapters.

## 1.1 Aim

The objective of this research is two-fold. On one side, the theoretical description of wobbling motion is treated in detail, starting from the required nuclear models specific to deformed nuclei, and reaching a set of key properties of the phenomenon. Differences between wobbling that occurs in odd- but also even-mass nuclei are depicted since each situation manifests in remarkable ways. Once the general formalism behind this effect is presented, an inventory of all the currently identified nuclei will be made, providing clear explanations for the band structure and also the relevant parameters describing deformation. The complete overview of all

existing wobbling nuclei is encapsulated in a unified informative chart, which is one of the unique features of the research, and a first within the literature.

The second objective of this present work is to describe the wobbling mechanism by means of a novel semi-classical approach. Indeed, the important quantities related to collective excitations are properly reproduced by the, i.e., excitation energies, quadrupole moments, transition probabilities, and many more. This model starts from an initial quantal Hamiltonian that is dequantized through a variational method. A set of classical equations of motion that describe triaxial nuclei are obtained, and a classical energy function is granted by the approach. This function is a remarkable feature of the developed framework, as this fully analytical expression (containing only classical variables that were obtained via the dequantization) will provide an insight into multiple analyses: energy spectrum, stability of the wobbling motion, critical regions, phase transitions and even possible changes in the wobbling regime.

Another remarkable feature of the current model is the geometrical interpretation of the rotational motion specific to triaxial nuclei, which is described in both a two- and three-dimensional space. Also unique to this research is the introduction of two concepts that are related to the band structures of odd-mass nuclei. These are the Signature Partner Bands and Parity Partner Bands and they can be considered hallmarks of the theory. Finally, it should be noted that this work consistently employs graphical representations such as workflow diagrams, schematics, and charts to facilitate a clearer understanding of the underlying mechanisms where possible.

## 1.2 Motivation

Over the years, many theoretical interpretations were suggested for the description of the wobbling motion and its main features. The Triaxial Rotor Model [1, 4] and the Particle Rotor Model [5] are quantal models that are solved exactly in the laboratory frame. Other investigations are based on mean-field theories, such as the Random Phase Approximation [6], the Angular Momentum Projection [7], and also the Collective Hamiltonian [8] were adopted.

This research aimed at a semi-classical description of the wobbling phenomenon due to its advantage in keeping close contact with the ‘classical picture’ of the

system dynamics. Certainly, working with a set of classical equations of motion is much easier than having to deal with quantum mechanical objects that do not have a clear one-to-one correspondence with classical mechanics. It will be shown that the rotational motion of a triaxial nucleus can be approximated quite well with that of a rigid rotator, meaning that the energy spectrum could be accurately described through quantities that have concise physical meaning (i.e., moments of inertia, angular momentum, angular frequency). Moreover, the analytical spectrum that is achieved by solving the equations for an odd-mass nucleus is indeed remarkable, since it will be described by separated degrees of freedom associated with an even-even core and a valence nucleon that interacts with the core. The variational method proves to be an efficient tool in accurately depicting the energy spectra and transition probabilities of several odd- $A$  nuclei within the  $A = 160$  mass region.

The lack of studies of geometrical treatments for the wobbling motion encouraged the team to pursue such an analysis. A two-dimensional evaluation shows if regions of stability exist, meaning that one can identify the energies at which the total angular momentum exhibits stable precessional motion. Taking the formalism a step further, the wobbling motion is explored within the space generated by the three components of the total angular momentum. The two constants of motion, i.e., the total energy and the total spin are graphically represented in the same picture, and their intersection signifies the allowed trajectories that the angular momentum precesses around. Each trajectory corresponds to a particular set of spin and energies, meaning that the entire spectrum of a wobbling nucleus can be interpreted. Using the classical view of the angular momentum and the total energy for a triaxial ellipsoid represents the onset of a fully unified description of nuclear deformation. Moreover, this phenomenological and semi-classical model gives results that are on par with fully microscopic or quantal descriptions (much more complex), making it a successful tool in describing collective phenomena.

### 1.3 Thesis Structure

This thesis is structured in the following way. [Chapter 2](#) begins with the study of the nuclear surface using the expansion of the radius  $R$  in terms of collective coordinates and spherical harmonics. The multipole modes are presented and a focus on the quadrupole  $\lambda = 2$  excitation mode is considered. This is the main

vibrational mode causing triaxial deformation of the nucleonic matter. Within the approximation of the nuclear surface, the deformation parameters  $\beta_2$  and  $\gamma$  are introduced, which give a direct insight into the degree of elongation and asymmetry between the ellipsoid axes. Furthermore, the theoretical models necessary to describe the deformed nuclei are sketched in Section 2.2 within the same chapter. Starting with the Spherical Shell-Model, a step-by-step procedure is considered and more complete models such as the Deformed Shell, Nilsson, or even the Collective model are constructed. The last section of the chapter (Section 2.3) presents two fingerprints of triaxiality, i.e., chiral motion and wobbling motion. Concerning the chiral bands, some experimental data are presented, and nucleonic configurations that lead to the apparition of chiral motion are geometrically represented.

Wobbling motion, which is the ‘core’ topic of this research is treated in **Chapter 3**, where its physical meaning is given. The difference between wobbling in odd- and even-mass nuclei is provided, and the two wobbling regimes that emerge in the odd- $A$  nuclei are portrayed. A quantal approximation made by Frauendorf in Ref. [9] shows that based on the alignment of the valence nucleon and the even-even core, two possible wobbling modes occur: transverse and longitudinal. The modes are properly outlined giving geometrical interpretations and showing key differences between the involved quantities. Using an approximation for an initial Hamiltonian of a rigid triaxial rotor, a proper analytical expression is obtained for the even- $A$  nuclei. The energy spectrum is defined as the sum between a quadratic term in angular momentum and a harmonic-like term. With this formula, the experimental wobbling bands in  $^{130}\text{Ba}$  are successfully reproduced, together with the transition probabilities of the collective states. Also in Chapter 3, all known experimental findings concerning wobbling excitations are specified, finishing with a chart that contains relevant parameters for each nucleus in particular.

In **Chapter 4**, the theoretical formalism for describing odd-mass nuclei is employed. This semi-classical model starts from a Time-Dependent Variational Equation applied on a Particle-Rotor Hamiltonian. From this, a classical energy function is attained, and it is used two describe the excited spectra of triaxial nuclei. The energy spectrum is parametrized in terms of the moments of inertia, the triaxiality  $\gamma$ , and the interaction strength between the core and the odd-particle. These five free parameters are determined by fitting the excitation energies of  $^{161,163,165,167}\text{Lu}$  to the experimental data. Other quantities such as transition probabilities, alignments, and dynamical moments of inertia are calculated for each

isotope with the obtained parameter set. A key feature of the approach depicted in Chapter 4 is the renormalization of the wobbling band structure in terms of Signature Partner Bands. The method is contrasted with a prior description that utilized an alternative mechanism for generating wobbling excitations.

A novel method for studying wobbling motion in odd-mass nuclei is discussed in Chapter 5, starting from the considerations made in the previous chapter. Herein, through the concept of Parity Partner Bands, it is shown that the wave-function describing the triaxial nuclei admits states of both positive and negative parity, which makes it possible to use an even simpler analytical spectrum of  $^{163}\text{Lu}$ . Another fitting method is used for the entire spectrum, including a rotational band that previously was treated separately. Consequently, a set of results that are very close to the real values is obtained. For a classical description, these results are quite impressive, as they are the first within the literature that achieve deviations under 100 keV across the entire spectrum of  $^{163}\text{Lu}$ . Identification of phase transitions, where the nucleus could change its rotational mode, but also regions where rotational motion is unstable, are obtained through graphical representations within a space generated by dequantized variables that describe the rotational degrees of freedom for the particle + rotor system.

Chapter 6 presents a specialized description of wobbling motion in odd-mass nuclei, based on a recent case study conducted by the team on  $^{135}\text{Pr}$ . Utilizing a boson representation for the angular momentum components and the Hamiltonian yielded accurate results for both the energy spectrum and transition probabilities. The numerical implementation of this approach involved fitting experimental data and utilizing a set of well-established trigonometric functions - specifically, the Jacobi Elliptic Functions. These functions will offer a valuable understanding of the potential energy, wobbling frequency, and stability of odd-mass triaxial nuclei.

In Chapter 7, general concluding remarks are provided that summarize the key findings and contributions of this work to the topic of Nuclear Structure. These conclusions highlight the significance of the research and its implications for future studies in this field. It should be noted that several chapters contain dedicated conclusions providing further insights into their specific topics.

# Chapter 2

## Theoretical Aspects of Nuclear Deformation

In order to understand nuclei in terms of their shape and to get a grasp on how deformation plays a major role in affecting the dynamics of nuclear matter, it is necessary to introduce a few definitions and theoretical models. These will represent fundamental *tools* in the development of the formalism, which will be presented later on. It is rather intuitive that a key characteristic related to the size and shape of the nucleus is its radius. Therefore, the first section aims at giving insight into the nuclear radius and how it can be approximated, showing that different approximations lead to specific types of deformations. Moreover, a realistic description of nuclei would require a time-dependent behavior of their surface, i.e., via surface vibrations or surface oscillations. They will be covered as well throughout this chapter.

As an outline of this chapter, the parametrization of nuclear shapes and deformations are detailed in Section 2.1, while Section 2.2 covers the fundamental features of some nuclear models. Lastly, Section 2.3 will introduce the unique characteristics of nuclei lacking symmetry in regards to their equilibrium shape. A set of conclusions that emerge from all sections is inferred at the end of the chapter.

## 2.1 Shape of Nuclei

The nuclear surface can be described through an expansion of the spherical harmonics with some time-dependent parameters as *expansion coefficients*. The expression of the nuclear shape is given as [10]:

$$R(\theta, \varphi, t) = R_0 \left( 1 + \sum_{\lambda=0}^{\infty} \sum_{-\lambda}^{\lambda} \alpha_{\lambda\mu}(t) Y_{\lambda}^{\mu}(\theta, \varphi) \right), \quad (2.1)$$

where  $R$  denotes the nuclear radius. The radius is given as a function of spherical coordinates  $\theta, \varphi$  and time. The radius of the spherical nucleus when all the expansion coefficients vanish is denoted by  $R_0$ . It is worth mentioning that the expansion coefficients  $\alpha_{\lambda\mu}$  act as *collective coordinates*, since the time-dependent amplitudes describe the vibrations of the nuclear surface. This will be also re-iterated in Section 2.2.5 from this chapter.

### 2.1.1 Multipole deformations

In the expansion of the nuclear radius defined by Eq. 2.1, the different values for  $\lambda$  will determine different effects regarding the physical aspects of the nucleus. As such, the first values of  $\lambda$  will be examined in terms of their physical meaning.

**Monopole mode** This corresponds to the first value of  $\lambda = 0$ . This is the simplest mode of *deformation* of a nuclear surface. Within this approximation, the spherical harmonic  $Y_0^0$  is constant, which would imply that any non-vanishing values for  $\alpha_{00}$  will correspond to the change in radius of the nucleus. This kind of excitation is also called *breathing mode* of the nucleus [1, 10]. The energy required for this kind of excitation mode is very large, since it implies a compression of the nuclear matter, making this mode irrelevant in the low-lying excited spectra of atomic nuclei.

**Dipole mode** Corresponds to  $\lambda = 1$ . In reality, this type of mode does not manifest itself as a deformation of the nucleus, but rather as a shift of the nuclear center of mass.

**Quadrupole mode** Excited mode that correspond to  $\lambda = 2$  are the most important collective excitations. The loss of axial symmetry, triaxial deformations,

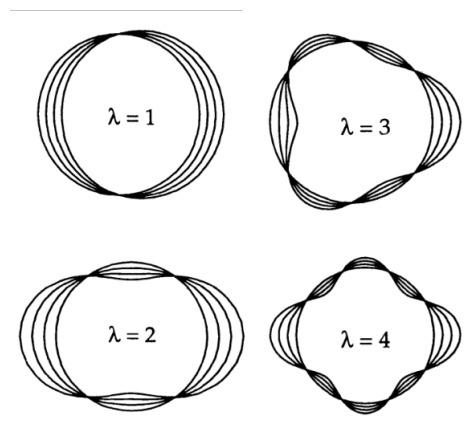


FIGURE 2.1: Graphical representation of the first few modes of excitations of the nuclear surface. The figure is taken from Ref. [10].

and other shape-specific features are direct consequences of quadrupole excitations.

**Octupole mode** It corresponds to  $\lambda = 3$ , representing the main asymmetric excitations of a nucleus with states of negative-parity. The specific shape of a nuclear system governed by octupole deformations is similar to that of a pear.

**Hexadecapole deformations** Excitations with  $\lambda = 4$  are considered the highest angular momenta which can provide relevant information for the nuclear phenomena. Currently, there is no clear evidence for pure excitations with hexadecapole nature, however, these excitations seem to have a major role in the admixture to quadrupole excitations for the ground-state shape of heavy nuclei [10].

The multipole deformations for the cases  $\lambda = 1, 2, 3$  and  $\lambda = 4$  are shown in Fig. 2.1. Excitations with higher angular momentum than these have no practical application within the study of atomic nuclei. Moreover, one can also see that there is an intrinsic limitation on the maximal value of  $\lambda$ , which dictates the individual bumps of the surface (see Fig. 2.1). These bumps are described by the spherical harmonics  $Y_\lambda^\mu$ , and they decrease in size with increasing values of  $\lambda$ , but with the physical limitation given by the size of the nucleon diameter.

### 2.1.2 Quadrupole Deformation

One of the most important excitation modes (vibrational degrees of freedom) is the quadrupole deformation, corresponding to  $\lambda = 2$ . In the case of pure quadrupole deformation, the nuclear surface will be given by the following expression:

$$R(\theta, \varphi) = R \left( 1 + \sum_{\mu=-2}^2 \alpha_{2\mu} Y_2^\mu(\theta, \varphi) \right). \quad (2.2)$$

From this expression, the term  $\alpha_{00}$  is of second order in  $\alpha_{2\mu}$  and it can be neglected further on. This term also reflects the conservation of volume [10, 11]. The real and independent degrees of freedom from the above expression are:  $\alpha_{20}$ , the real and imaginary parts of  $\alpha_{21}$ , and the real and imaginary parts of  $\alpha_{22}$ . More insight in regards to the quadrupole shape of the nucleus can be achieved if one expresses  $R$  in terms of Cartesian coordinates. The spherical harmonics will attain a new form, depending on the Cartesian components of the unit vector pointing in a direction defined by  $(\theta, \varphi)$ :

$$\xi = \sin \theta \cos \varphi, \quad \eta = \sin \theta \sin \varphi, \quad \zeta = \cos \theta, \quad (2.3)$$

with the condition  $\xi^2 + \eta^2 + \zeta^2 = 1$ . With the expressions of the spherical harmonics as functions of  $(\xi, \eta, \zeta)$ , the nuclear radius will change accordingly. A relationship between the Cartesian components and the spherical ones for the deformation can be also obtained if all coefficients  $\alpha_{2\mu}$  are written as functions of  $\alpha_{ij}$  (with  $i, j = \xi, \eta, \zeta$ ). Since the Cartesian deformations give the stretch/contraction of the nucleus in a given direction, a first interpretation of the physical meaning behind the parameters  $\alpha_{2\mu}$  can be established:

- $\alpha_{20}$ : describes the stretching of the  $z$  axis with respect to the  $y$  and  $x$  axes.
- $\alpha_{2-2}$  and  $\alpha_{22}$ : give the relative length of the  $x$  axis compared to the  $y$  axis. Moreover, it also gives the oblique deformation in the  $x - y$  plane.
- $\alpha_{2-1}$  and  $\alpha_{21}$ : describe an oblique deformation, but with respect to the  $z$  axis.

With the set of parameters defined above, the shape and orientation of the nucleus can have arbitrary values (the coefficients  $\alpha_{2\mu}$  are mixing the shape and orientation), making the parametrization somewhat problematic. In order to fix that, the

geometry can be changed if one considers the *principal axis system*. When using this reference frame, the number of parameters is still unchanged, however their physical significance becomes clearer. By denoting the new coordinate system with primed letters, the nuclear radius will be described as a function  $R = R(\xi', \eta', \zeta')$ , with the conditions that  $\alpha'_{ij} = 0$ ,  $i \neq j$ . The condition will further imply that the newly expressed parameters ( $\alpha'_{2\mu}$ ) have the following form:

$$\begin{aligned}\alpha'_{2\pm 1} &= 0 , \\ \alpha'_{2\pm 2} &\equiv a_2 , \\ \alpha'_{20} &\equiv a_0 ,\end{aligned}\tag{2.4}$$

where the conveniently denoted terms  $a_2$  and  $a_0$  depend on the Cartesian components  $\alpha_{\xi,\xi}$ ,  $\alpha_{\eta,\eta}$ ,  $\alpha_{\zeta,\zeta}$ . From this set of equations the physical significance of the five real and independent parameters is as follows:

- $a_0$  is indicating the stretch of  $z'$  axis w.r.t. the  $x'$  and  $y'$  axes.
- $a_2$  is indicating the asymmetry between the lengths of  $x'$  and  $y'$  axes, respectively.
- the three *Euler angles*  $\Theta = (\theta_1, \theta_2, \theta_3)$  that determine the orientation of the PA system  $(x', y', z')$  with respect to the laboratory-fixed frame  $(x, y, z)$ .

The advantage in working within this coordinate system is clearly emphasized: rotation and shape vibration degrees of freedom are completely separated. A change in the Euler angles will emerge as a pure rotation of the nucleus, while a change in shape will be affected exclusively by the  $a_0$  and  $a_2$  parameters. If  $a_2 = 0$ , then the nucleus has is symmetric around the  $z$ -axis (equal lengths along the  $x$  and  $y$  directions). Another way of describing the excitations of quadrupole type is to adopt the parameters introduced by Bohr in Ref. [12]. These two parameters can be viewed as a set of polar coordinates in the space generated by  $a_0$  and  $a_2$ , namely:

$$\begin{aligned}a_0 &= \beta_2 \cos \gamma , \\ a_2 &= \frac{1}{\sqrt{2}} \beta_2 \sin \gamma ,\end{aligned}\tag{2.5}$$

where the numeric factor  $1/\sqrt{2}$  was added such that the following relation holds true:

$$\sum_{\mu} |\alpha_{2\mu}|^2 = \sum_{\mu} |\alpha'_{2\mu}|^2 = a_0^2 + 2a_2^2 = \beta_2^2 . \quad (2.6)$$

It is worth mentioning that Eq. (2.6) is rotationally invariant, having the same value in the laboratory and the principal axes systems. Now that the shape of the nucleus (i.e., the nuclear surface radius  $R$ ) can be described consistently with the parameters defined in Eq. (2.5), one can calculate the stretching of the nuclear radius along any of the directions is given in terms of  $(\beta, \gamma)$  as follows:

$$\delta R_k = \sqrt{\frac{5}{4\pi}} \beta \cos\left(\gamma - \frac{2\pi k}{3}\right) . \quad (2.7)$$

### 2.1.3 Axial quadrupole deformations

Using this set of new coordinates, the expression of the nuclear radius for axially quadrupole-deformed nuclei is given as:

$$R(\theta, \varphi) = R_0 (1 + \beta_2 Y_2^0(\theta, \varphi)) , \quad (2.8)$$

where the parameter  $\beta_2$  is called the *quadrupole deformation parameter*, and its value dictates whether the nucleus is *oblate* (i.e., a flattened sphere), *prolate* (i.e., an elongated sphere, like a rugby ball), or *spherical*. The nuclear shapes that are characterized only by  $\beta_2$  (i.e.,  $\gamma = 0$ ) have shapes that correspond to spheroids. These shapes are axially symmetric, meaning that they only have one deformed axis. For the axially-symmetric quadrupole deformations, the parameter  $\beta_2$  can be related to the axes of the spheroid via Eq. (2.7).

Taking a look at Fig. 2.2, one can see the variations of the three axes with respect to  $\gamma$ . When  $\gamma = 0^\circ$ , the nucleus is elongated along the  $z'$  axis, but the  $x'$  and  $y'$  axes are identical (the prolate case). As  $\gamma$  increases, the  $x'$  axis grows, while the other two axes decrease in size, making a region with *triaxial shapes*. Symmetry is reached again at  $\gamma = 60^\circ$ , where  $x'$  and  $z'$  axes are equal but longer than  $y'$  axis, making the nucleus look like a flattened shape (the oblate case). This pattern is repeated every  $\gamma = 60^\circ$ , where alternating prolate/oblate shapes occur. It is possible to summarize the various nuclear shapes with a graphical

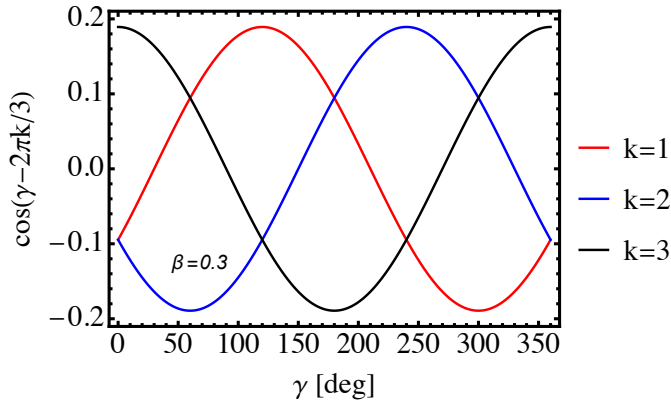


FIGURE 2.2: Graphical representation with the stretching of the nuclear axes  $\delta R_k$ ,  $k = 1, 2, 3$ , corresponding to the increase in axis lengths along the  $x$ ,  $y$ , and  $z$  directions. The representation used an arbitrary value  $\beta_2 = 0.3$ . Figure was reproduced according to the calculations done in Ref. [10].

representation within in the  $(\beta, \gamma)$  plane. In Fig. 2.3 one can see the oblate shapes at  $\gamma = 60^\circ, 180^\circ, 300^\circ$ , while prolate shapes appear at  $\gamma = 0^\circ, 120^\circ, 240^\circ$ .

### 2.1.4 Non-Axial quadrupole deformations

Besides the nuclei characterized by a *spheroidal* shape where two of the principal axes are equal, there are also *triaxial* (or non-axial) nuclei. The triaxial shapes are defined by the  $\gamma$  degree of freedom: a parameter which dictates the asymmetry between the three axes of the nucleus (e.g., it describes a stretching along an axis that is perpendicular to the symmetry axis). The nuclear radius for the axially-asymmetric quadrupole deformations is given by:

$$R(\theta, \varphi) = R_0 \left( 1 + \beta_2 \cos \gamma Y_2^0(\theta, \varphi) + \frac{1}{\sqrt{2}} \sin \gamma (Y_2^2(\theta, \varphi) + Y_2^{-2}(\theta, \varphi)) \right), \quad (2.9)$$

which is different from Eq. (2.8). The values  $\gamma = 0^\circ$  and  $\gamma = 60^\circ$  correspond to symmetric prolate and oblate shapes, respectively. Between these values, the triaxial region exist, with *maximal triaxiality* reached at  $\gamma = 30^\circ$ . The deformation parameters  $(\beta, \gamma)$  are also called the Hill-Wheeler set [13]. In Eq. (2.9), the

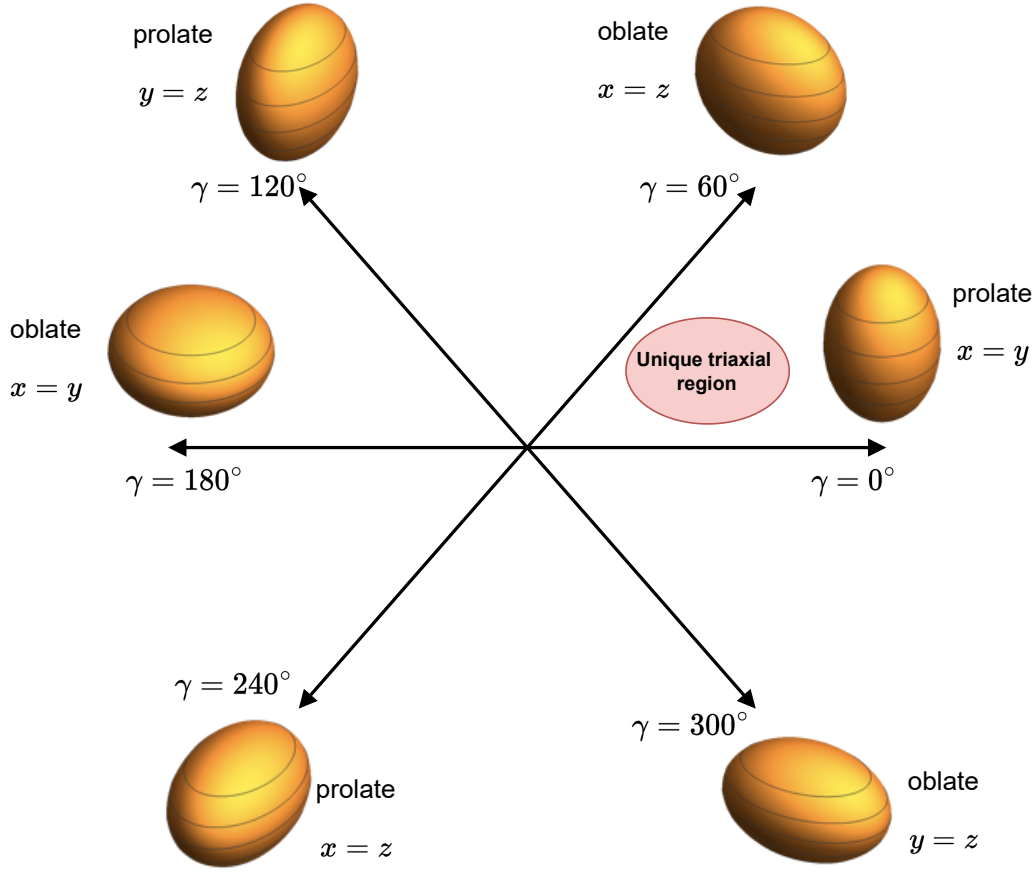


FIGURE 2.3: Beta-gamma plane divided into six regions. The part delimited from  $\gamma = 0^\circ$  to  $\gamma = 60^\circ$  can be considered as the representative one, while others can be reproduced from this interval.

spherical harmonics are expressed as follows:

$$\begin{aligned} Y_2^0(\theta, \varphi) &= \frac{1}{4} \sqrt{\frac{5}{\pi}} (3 \cos^2 \theta - 1) , \\ Y_2^2(\theta, \varphi) &= \frac{1}{4} e^{2i\varphi} \sqrt{\frac{15}{2\pi}} \sin^2 \theta , \\ Y_2^{-2}(\theta, \varphi) &= \frac{1}{4} e^{-2i\varphi} \sqrt{\frac{15}{2\pi}} \sin^2 \theta , \end{aligned} \quad (2.10)$$

and substituting these terms in  $R(\theta, \varphi)$ , the structure Eq. (2.9) will become [1, 14]:

$$R(\theta, \varphi) = R_0 \left[ 1 + \sqrt{\frac{5}{16\pi}} \beta \left( \cos \gamma (3 \cos^2 \theta - 1) + \sqrt{3} \sin \gamma \sin^2 \theta \cos 2\varphi \right) \right] . \quad (2.11)$$

Regarding the nuclear shapes that were described in Fig. 2.3, the redundancies of the  $(\beta, \gamma)$  variables are:

- for  $\beta_2 > 0$  the nucleus is *prolate* for  $\gamma = 0^\circ, 120^\circ, 240^\circ$
- for  $\beta_2 > 0$  the nucleus is *oblate* for  $\gamma = 60^\circ, 180^\circ, 300^\circ$
- for  $\gamma = 0^\circ, 180^\circ$ , the symmetry axis is the  $z$ -axis of the intrinsic frame
- for  $\gamma = 120^\circ, 300^\circ$ , the symmetry axis is the  $x$ -axis of the intrinsic frame
- for  $\gamma = 60^\circ, 240^\circ$ , the symmetry axis is the  $y$ -axis of the intrinsic frame.

### 2.1.5 Lund Convention

The so-called Lund convention [14] somewhat solves this repetitiveness, by selecting a rotational axis according to the set of rules described below:

- The quadrupole deformation parameter  $\beta_2$  is always positive:  $\beta_2 \geq 0$
- The rotation around the smallest axis ( $s$ -axis) implies the constraint on the triaxiality parameter  $0^\circ \leq \gamma \leq 60^\circ$
- The rotation around the longest axis ( $l$ -axis) implies the constraint on the triaxiality parameter  $-120^\circ \leq \gamma \leq -60^\circ$
- The rotation around the medium/intermediate axis ( $i$ -axis) implies the constraint on the triaxiality parameter  $-60^\circ \leq \gamma \leq 0^\circ$ .

Considering the Lund convention and Eq. (2.7), one can re-write the set of stretching values as follows:

$$\frac{R_x - R_0}{R_0} = \sqrt{\frac{5}{4\pi}} \beta_2 \cos\left(\gamma - \frac{2}{3}\pi\right), \quad (2.12)$$

$$\frac{R_y - R_0}{R_0} = \sqrt{\frac{5}{4\pi}} \beta_2 \cos\left(\gamma - \frac{4}{3}\pi\right), \quad (2.13)$$

$$\frac{R_z - R_0}{R_0} = \sqrt{\frac{5}{4\pi}} \beta_2 \cos\gamma. \quad (2.14)$$

For the axially symmetric deformation (i.e.,  $\gamma = 0$ ), the quadrupole parameter  $\beta_2$  can be derived as follows:

$$\beta_2 = \frac{4}{3} \sqrt{\frac{\pi}{5}} \frac{R_z - R_x}{R_0} , \quad (2.15)$$

where  $R_z - R_x$  is the difference between the major ( $R_z$ ) and minor ( $R_x$ ) axes of the ellipsoid. This equation for  $\beta_2$  shows how for oblate deformations,  $\beta_2 < 0$  (implying that  $R_z < R_x$ ), while for prolate deformations  $\beta_2 > 0$  (implying that  $R_z > R_x$ ). Within literature, usual values for  $\beta_2$  range from 0.2 - 0.3 (known as *normal deformation*) to 0.4 - 0.6 (known as strong or *superdeformation*). Very often, an alternative description of the nuclear deformation is used in terms of the parameter  $\epsilon_2$  that relates to  $\beta_2$  via the formula [15]:

$$\epsilon_2 \approx \frac{R_z - R_x}{R_0} = \frac{3}{4} \sqrt{\frac{5}{\pi}} \beta_2 = 0.946 \beta_2 . \quad (2.16)$$

## 2.2 Nuclear Models

In the following section, a discussion will be made about the nuclear models that are used in order to describe phenomena specific to rotating nuclei. Since the focus of this work emerges from a *class* of properties that usually applies to the high-spin region, it makes sense to consider all the theoretical notions that cover the underlying effects.

### 2.2.1 Deformed Shell Model

A formalism which describes the nuclear properties is the *Shell Model*. It is based on an approximation of the independent motion for a nucleon within an average potential. The potential is generated by the interaction of that nucleon with all the remaining nucleons from the compounding nucleus. It works really well for spherical nuclei and it is a successful tool in reproducing and predicting the properties of nuclear states. The theory also proves to be efficient for excited states having nucleonic configurations that are dominated by a single nucleon or a very small number of ‘extra’ nucleons. However, this version of the Shell Model works well only for magic nuclei, nuclei that have both even number of protons and neutrons, and nuclei whose shapes are not well deformed. In order

to give a realistic description of a larger class of nuclei (e.g., deformed, odd  $Z$ , odd  $N$ , and so on), the *Deformed Shell-Model* should be employed. This will be described in the following subsection, while a general overview of the concepts regarding the formerly mentioned model is made in Appendix A. Therein, the simple harmonic oscillator, and a modified version that is amended with additional terms are introduced. As it will be shown, these are used to obtain the Hamiltonian for the Deformed Shell Model.

### 2.2.2 Deformed Shell Model - Nilsson Model

The idea that some nuclei are deformed in their ground-state was enforced experimentally a long time ago, when measuring quantities such as density distributions or nuclear quadrupole moments [15]. The non-spherical shapes are given by the existence of nucleonic configurations, which lie away from the major shell closure. In Section 2.1 from this chapter, the description of the nuclear shapes was treated using the well-known formula of the nuclear radius (see Eq. (2.1)), resulting in the *spherical*, *axially-symmetric*, and *axially-asymmetric* nuclear shapes.

Developed by Nilsson in 1955 [16] for treating the *deformed nuclei*, it is a modified shell model with deformations taken into account by the use of the *anisotropic harmonic oscillator* (AHO) (see Appendix A for the simple and modified ones). Similarly as for the basic shell model, the goal is to obtain an expression for the single-particle energies of a nucleon. The basic Hamiltonian corresponding to this kind of system is shown below [17]:

$$H = H_0 + a_1 \vec{l} \cdot \vec{s} + a_2 l^2 , \quad (2.17)$$

where  $H_0$  is the AHO term. The general expression for this kind of oscillator is:

$$H_{\text{AHO}} \equiv H_0 = -\frac{\hbar^2}{2m} \nabla^2 + \frac{1}{2} m(\omega_x^2 x^2 + \omega_y^2 y^2 + \omega_z^2 z^2) . \quad (2.18)$$

In the expression of the single-particle Hamiltonian, the constants  $a_1$  and  $a_2$  are usually determined via adjustments to the experimental results. It can be seen that both the centrifugal-like term  $l^2$ , which simulates a flattening of the oscillator potential, and the  $\vec{l} \cdot \vec{s}$  term are also present here, as it was the case for the spherical

shell model. However, the explicit form of Eq. (2.17) is as follows:

$$H_{\text{Nil}} = -\frac{\hbar^2}{2m} \nabla^2 + \frac{1}{2} m(\omega_x^2 x^2 + \omega_y^2 y^2 + \omega_z^2 z^2) - 2\kappa\hbar\omega_0(\vec{l} \cdot \vec{s}) - 2\kappa\hbar\omega_0\mu(l^2 - \langle l^2 \rangle_N) . \quad (2.19)$$

The parameters  $\kappa$  and  $\mu$  act as strength parameters for the spin-orbit coupling term and the centrifugal term, respectively. The last term is a correction, which was introduced by Gustafson et al. [18]. The three *oscillator frequencies* are chosen to be inversely proportional to the semi-axis lengths of the deformed ellipsoid (denoted by  $a_x$ ,  $a_y$ , and  $a_z$ ) such that:

$$\omega_r = \omega_0 \frac{R_0}{a_r} , \quad r = x, y, z . \quad (2.20)$$

For the spherical case, the oscillator frequency  $\hbar\omega_0$  is set to  $41A^{-1/3}$  MeV (calculation for this value arise from the shell model with SHO [17]). For the axially-symmetric case, one can choose the  $z$ -axis as symmetry axis, implying that the oscillator frequencies along the  $x$  and  $y$  axes are equivalent (that is  $\omega_x = \omega_y \equiv \omega_\perp$ ). Following the calculations done in [17], one can express the two relevant oscillator frequencies in terms of a deformation parameter  $\epsilon_2$  (whose dependence on the quadrupole deformation parameter  $\beta_2$  has been shown in Eq. (2.16)) as such:

$$\omega_\perp^2 = \omega_0^2 \left(1 + \frac{2}{3}\epsilon_2\right) , \quad (2.21)$$

$$\omega_z^2 = \omega_0^2 \left(1 - \frac{4}{3}\epsilon_2\right) . \quad (2.22)$$

Moreover, a dependence on the deformation parameter itself is employed for the frequency  $\omega_0$  that appears in the expressions for  $\omega_\perp$  and  $\omega_z$ , respectively:

$$\omega_0 = \left(1 - \frac{4}{3}\epsilon_2^2 - \frac{16}{27}\epsilon_2^3\right)^{-1/6} , \quad (2.23)$$

where  $\bar{\omega}_0$  can be considered a constant written as  $\bar{\omega}_0 = (\omega_x \omega_y \omega_z)^{1/3} = \text{const}$ . This is coming from the harmonic oscillator at zero deformation and by considering the conservation of the nuclear volume. The energy eigenvalue  $\varepsilon_q$  for the nucleonic state  $\psi_q$  belonging to a deformed nucleus can be determined by solving the

Schrödinger equation associated to each nucleon in particular:

$$H_{\text{Nil}}\psi_q = \varepsilon_q\psi_q , \quad (2.24)$$

where the index  $q$  denotes a set with all the relevant quantum numbers. This set is also called the *asymptotic quantum numbers*, which are used to specify a *Nilsson orbital*. The well-known notation is as follows (still considering the  $z$ -axis as the symmetry axis):

$$\Omega^\pi [N n_z \Lambda] . \quad (2.25)$$

- $\Lambda$  is the projection of the particle's orbital a.m. along the symmetry axis (component of  $l$  along  $z$ )
- $N$  the principal quantum number of the major shell. It also determines the parity as  $\pi = (-1)^N$ , making the notation from Eq. (2.25) somewhat redundant
- $n_z$  is the number of oscillator quanta along the symmetry axis. More precisely, it gives the number of nodes for the wave-function along the direction of the  $z$ -axis
- $\Omega$  is the projection of the particle's total a.m. along the symmetry axis (i.e.,  $\mathbf{j}$ ). Moreover, the projection of the intrinsic spin of a nucleon onto the symmetry axis can have the values  $\Sigma = \pm \frac{1}{2}$ , so that  $\Omega = \Lambda + \Sigma = \pm \frac{1}{2}$ .

Fig. 2.4 shows the geometrical meaning of the asymptotic quantum numbers for the Nilsson model. Indeed, for a single nucleon orbiting a deformed core, the vector  $\mathbf{R}$  represents the angular momentum of a *rotating nucleus*, the vector  $\mathbf{I}$  represents the total a.m. of the entire nucleus,  $\mathbf{j}$  is the total a.m. of the single-particle (that is  $\mathbf{j} = \mathbf{l} + \mathbf{s}$ ). However, two more quantum numbers should be mentioned: the projection of the total a.m.  $\mathbf{I}$  onto the symmetry axis, denoted by  $K$ , and the projection of the same vector onto the laboratory axis, referred to as  $M$ .

Regarding the quantum numbers sketched in Fig. 2.4, there is an important aspect which needs to be specified about the projections  $K$  and  $\Omega$ , respectively. Indeed, it is clear that compared to the spherical case, where different orientations are irrelevant to the energy spectrum of nucleons, in the deformed case different directions in space lead to different energies. The orientation is in fact specified

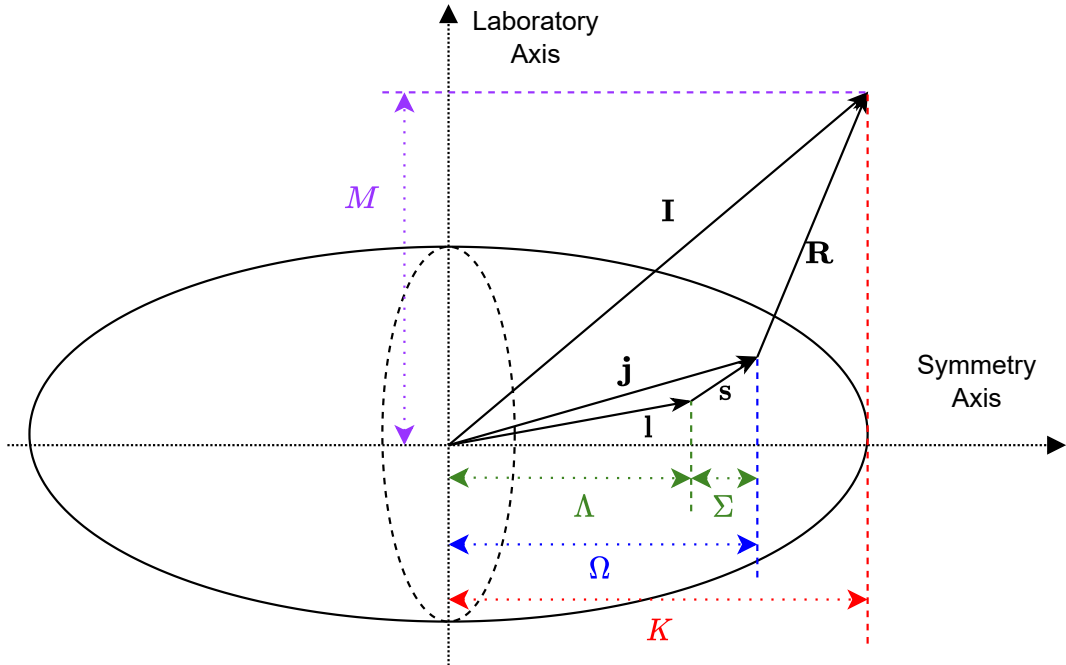


FIGURE 2.4: Geometrical interpretation of the Nilsson's asymptotic quantum numbers. This figure is inspired from Ref. [19]

by the *magnetic sub-state* of the nucleon, i.e., the projection of the total angular momentum on the symmetry axis. This projections is denoted by  $\Omega$  for the single-particle, however, because the rotational angular momentum  $\mathbf{R}$  in the axially deformed is perpendicular to the symmetry axis for low-lying states, then it will have no contribution to  $K$ , meaning that one can use  $\Omega$  and  $K$  interchangeably.

### 2.2.3 Single-particle states in deformed nuclei

It is instructive to go into detail about the quantum numbers defined in Eq. (2.25), since the orbits characterizing the nucleons point out the nature of deformations that take place. The quantum numbers  $N$ ,  $n_z$ , and  $\Lambda$  are good quantum numbers only when the nuclear deformation is large, meaning that  $\epsilon$  (or equivalently  $\beta$ ) tends to infinity. In fact, this is the main reason why they are called asymptotic quantum numbers. However, the numbers  $\Omega$  and  $\pi$  remain good quantum numbers even for low and moderate deformations for the nucleus. It should be noted that if  $N$  is even, then  $(\Lambda + n_z)$  is also even. Similarly, if  $N$  is odd, then the sum of the other two quantum numbers must also be odd [15].



FIGURE 2.5: A simple sketch showing the single-particle orbits for the  $j = 7/2$  nucleonic state, along the symmetry axis for a *prolate* deformation. The actual projections are  $\Omega_1 = \frac{1}{2}$ ,  $\Omega_2 = \frac{3}{2}$ ,  $\Omega_3 = \frac{5}{2}$ , and  $\Omega_4 = \frac{7}{2}$ . The figure was inspired from Ref. [20].

Since the eigenvalues of the Hamiltonian  $H_{\text{Nil}}$  ultimately depend on the deformation parameter  $\epsilon$ , each nucleon will have an orbit (energy) that is deformation dependent. At zero deformation all the energy levels for a single-particle state will have a  $2j + 1$  degeneracy. This translates to the fact that all  $2j + 1$  possible orientations of  $\vec{j}$  are equivalent. On the other side, when the potential is deformed, this will no longer hold, i.e., the energy levels in the deformed potential will depend on the spatial orientation of the orbit itself.

As an example, a nucleon from the  $f_{7/2}$  shell will be considered. This nucleon can have eight possible components in the range  $\Omega = [-\frac{7}{2}, \frac{7}{2}]$ . Because of the reflection symmetry, the positive components of  $\Omega$  will have the same energy as the negative ones, leading to a degeneracy of the levels. Additionally, the single-particle  $f_{7/2}$  state will split up into four new states when deformation emerges:  $\Omega = \frac{1}{2}, \frac{3}{2}, \frac{5}{2}, \frac{7}{2}$  (all of negative parity). In Figs. 2.5 - 2.6 the different orbits of the odd particle are given for both prolate and oblate deformations.

From Figs. 2.5 - 2.6, it can be seen that the first orbit (denoted by orbit 1) lies

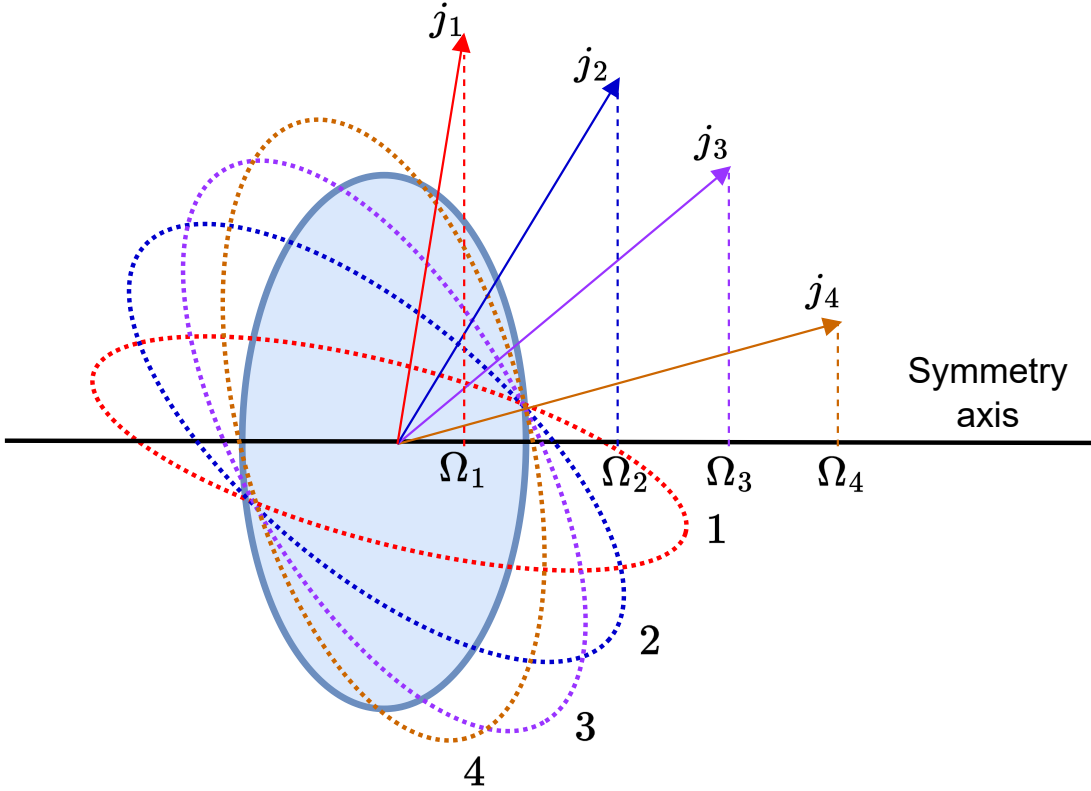


FIGURE 2.6: A simple sketch showing the single-particle orbits for the  $j = 7/2$  nucleonic state, along the symmetry axis for an *oblate* deformation. The actual projections are  $\Omega_1 = \frac{1}{2}$ ,  $\Omega_2 = \frac{3}{2}$ ,  $\Omega_3 = \frac{5}{2}$ , and  $\Omega_4 = \frac{7}{2}$ . The figure was inspired from Ref. [20].

closest to the core in the prolate case, while in the oblate case this is true for orbit 4. This will influence the interaction strength, meaning that for the prolate case, the orbit 1 will interact the strongest with the *core*, while in the oblate case, it is the orbit 4 having the strongest interaction with the bulk core. Moreover, the strength of interaction indicates the magnitude of the energies for each projection: the stronger the interaction between the orbit and the core, the more tightly bound and lower in energy these states are. For prolate deformations, the orbits with the smallest  $\Omega$  ‘prefer’ to lie lower in energy (interacting strongly with the core). For oblate deformations, the opposite is true: orbits with the maximal  $\Omega$  interact the strongest with the core and, therefore, lie lowest in energy.

Another way of looking at the coupling of the single-particle with the bulk core can be given in terms of overlaps of their corresponding wave-functions (eigenstates). Indeed, a nucleon lying in the lowest  $\Omega$  orbit will have a *maximum* wave-function overlap with a prolate core. On the other hand, nucleons lying in the highest  $\Omega$  orbits will have maximum overlap with the oblate core. The overlap gives

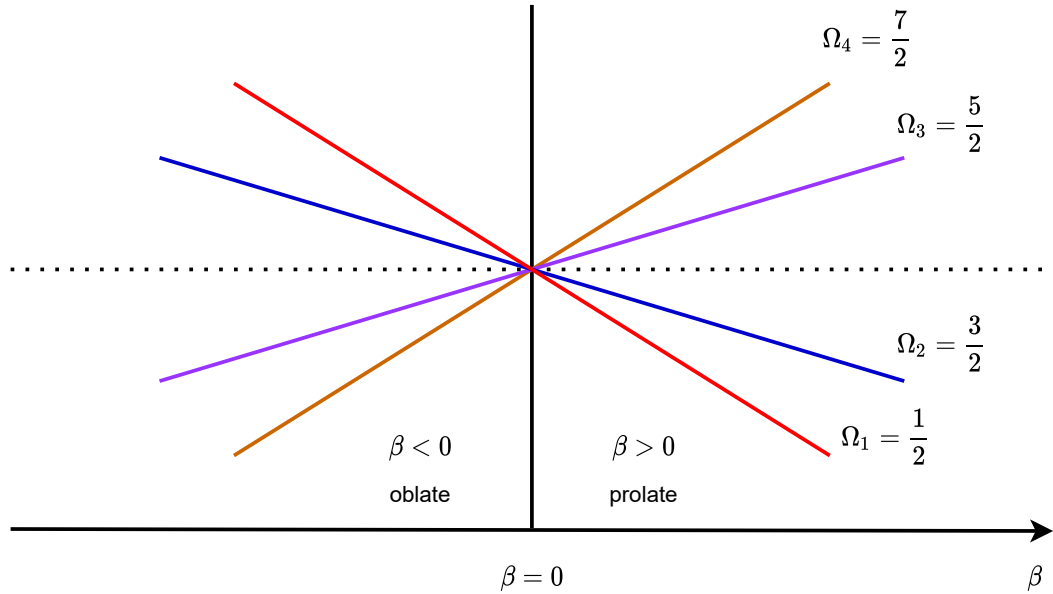


FIGURE 2.7: The effect of deformation for the particle state  $f_{7/2}$ . It can be seen that  $\Omega_1$  component lies lowest in energy for the oblate deformation and  $\Omega_4$  component lies the lowest in energy for an oblate deformation.

the overall binding energy between the two systems (i.e., core and particle), as explained in the previous paragraph. A discussion about the wave-function overlap and the nuclear density distribution [9, 21] will be made in the following chapters. The induced degeneracy due to deformation for a particle state  $l_j$  is shown in Fig. 2.7, for  $f_{7/2}$ .

Obviously, the sketch shown in Fig. 2.7 is just an instructive example and it does not represent an accurate description of the single-particle energies for deformed nuclei. In fact, if the potential is deformed, the quantum numbers  $l$  and  $j$  are not valid anymore (a.m. is no longer a constant of motion for non-spherical potentials). A proper description of the single-particle orbits is represented by the so-called *Nilsson diagrams*, where the energy for each state is represented as a function of the deformation parameter. Remember that the energies are in fact the eigenvalues of the Schrödinger equation associated with the initial Nilsson deformed Hamiltonian (see Eq. (2.24)). Diagrams that show such spectra are represented in Figs. 2.8 - 2.9. It can be seen that each state within a Nilsson diagram is represented as a solid line or a dashed line, depending on its parity (remember that the parity quantum number is given by  $(-1)^N$  or, equivalently, by  $(-1)^l$ ). The orbital labelling from the Figs. 2.8 - 2.9 is consistent with the one defined in the previous subsection. Another important aspect which can be seen in the Nilsson diagrams (for some orbits) is the ‘crossing’ between states with different quantum numbers. More

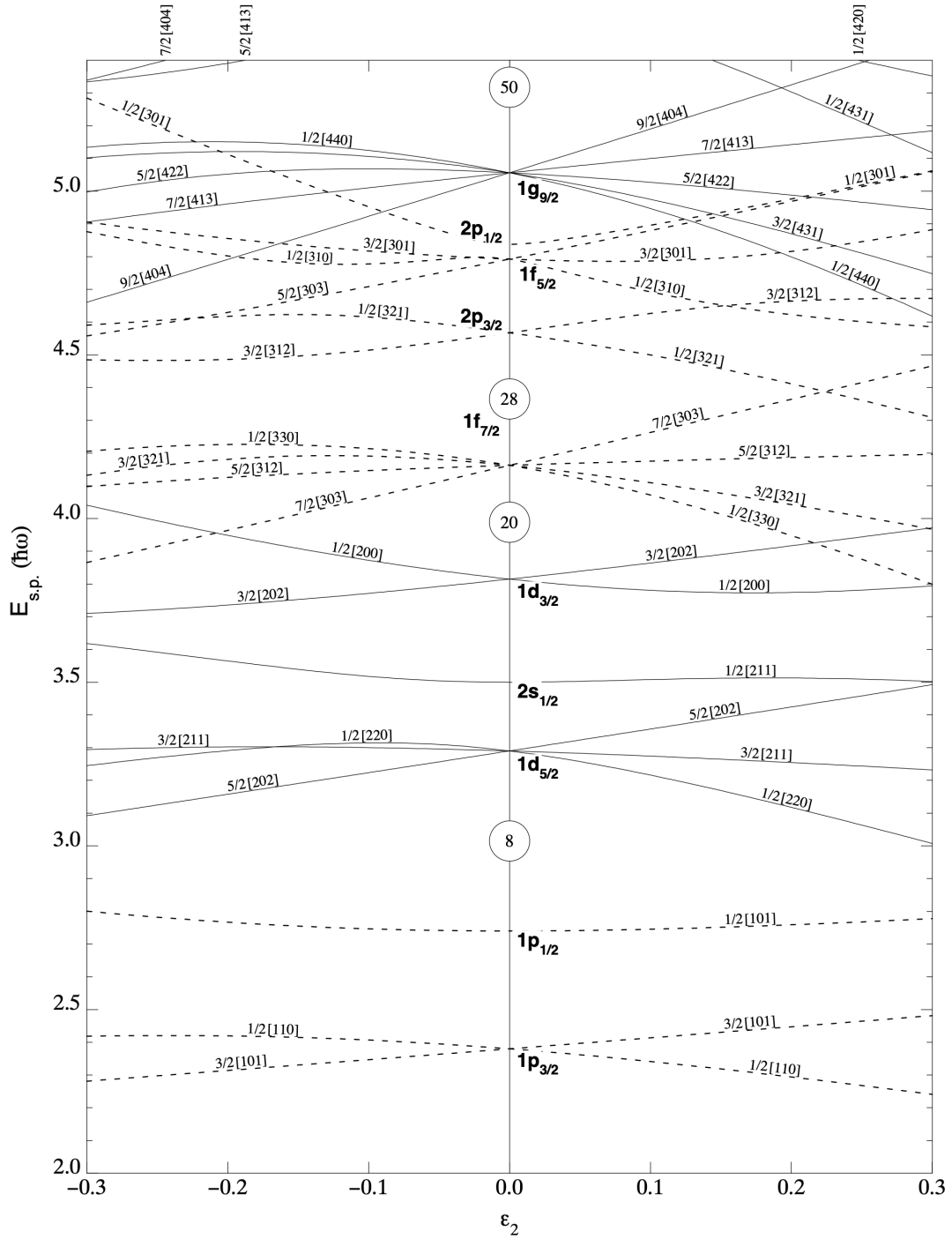


FIGURE 2.8: A Nilsson diagram for protons or neutrons, with  $Z$  or  $N \leq 50$ . Picture taken from Ref. [22].

insight into the geometrical interpretation of the Nilsson orbitals is provided in Section A.2 from Appendix A.

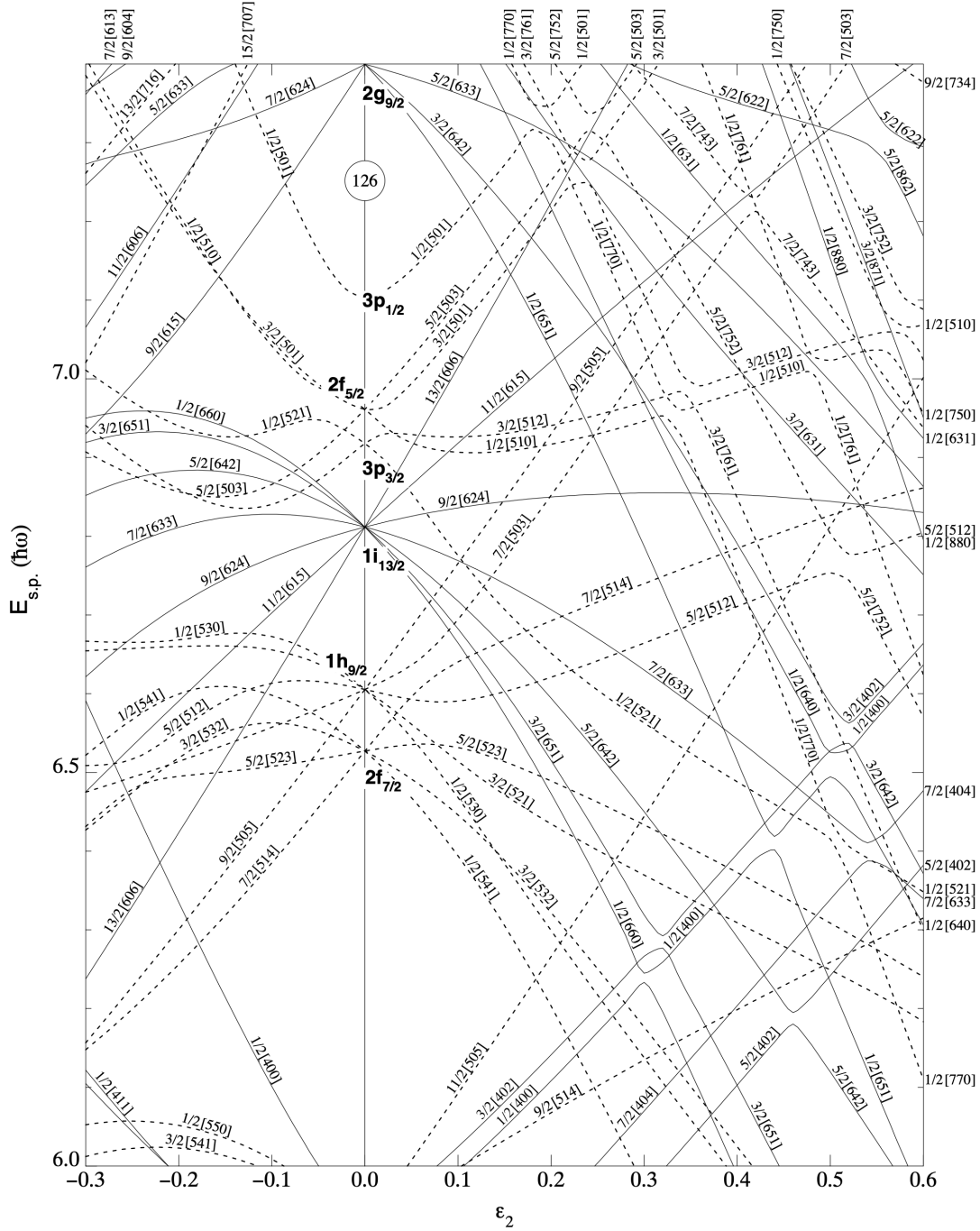


FIGURE 2.9: A Nilsson diagram for neutrons, with  $82 \leq N \leq 126$ . Picture taken from Ref. [22].

## 2.2.4 Collective Model

Although the previous single-particle model is able to successfully treat many nuclei, the single-nucleon motion in a deformed potential is not enough to describe phenomena such as nuclear fission or quantities like quadrupole moments of deformed nuclei [23]. Moreover, lifetime measurements through single-particle calculations fail to reproduce experimental data on some gamma-ray transitions of quadrupole nature [24].

The collective model is one of the most ‘complete’ tools in describing the nuclear phenomena across the chart of nuclides. It brought tremendous progress within the nuclear community by validating and predicting the nuclear behavior at different spin ranges. A major feature of this model is the introduction of the so-called *rotational bands*. Developed by Bohr and Mottelson [1, 25] more than 50 years ago, the Nuclear Collective Model is based on the Liquid-Drop-Model [26–28]. Moreover, the predictions for nuclear deformation made by Rainwater [29] played another fundamental role. The basic assumption is that the nuclear density distribution can be approximated as a droplet with shape-specific degrees of freedom. This droplet is also vibrating and rotating. According to the discussion from Section 2.1, the nuclear radius was described in terms of a set of *collective coordinates*, which dictate the shape evolution with time.

## 2.2.5 Bohr Hamiltonian

As a first step, the concept of a nuclear liquid drop is used to construct the Hamiltonian. The droplet exhibits shape and surface oscillations, which have a dynamical character. These shape oscillations are illustrated in Fig. 2.10, where a vibrating nucleus is represented, having a spherical *equilibrium* shape. Since the collective coordinates are time-dependent, at each moment in time, the nuclear radius  $R$  will be defined in the direction given by the radial coordinates  $\theta, \varphi$ . By using Eq. (2.1) that characterizes the *vibrations* of a nuclear surface, one can give the Hamiltonian of *collective* nature as [11, 17]:

$$H_{\text{coll}} \equiv T + V = \frac{1}{2} \sum_{\lambda\mu} \left[ B_\lambda \left| \frac{d\alpha_{\lambda\mu}}{dt} \right|^2 + C_\lambda |\alpha_{\lambda\mu}|^2 \right]. \quad (2.26)$$

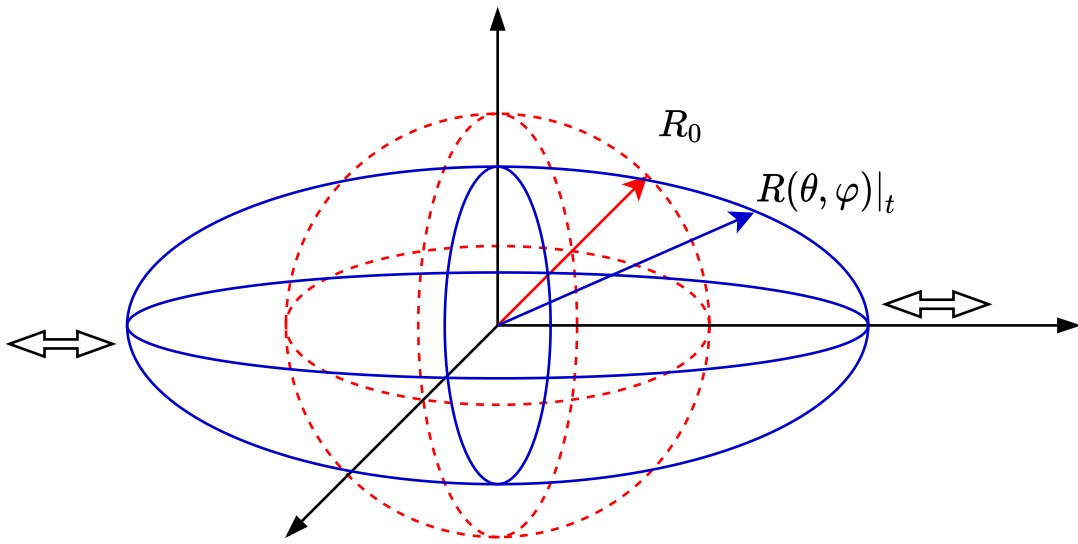


FIGURE 2.10: The vibration of a nucleus whose equilibrium shape is a spheroid, with nuclear radius  $R_0$  (*average nuclear radius*) and the nuclear radius  $R$  at a different moment in time. The equilibrium shape is represented by the red color, while the surface vibration is represented by the blue color. The oscillations are depicted through the double arrows.

The Hamiltonian is invariant under rotations and also invariant under time reversal [30]. The real numbers  $B_\lambda$  and  $C_\lambda$  represent the *inertial* and *stiffness* parameters. Choosing the body-fixed axis as a reference system will simplify the results, since the system's axes coincide with the principal axes of the ellipsoid itself. Assuming this coordinate system and an axial ellipsoid, the kinetic term from  $H_{\text{coll}}$  can be decomposed into a *rotational* and a *vibrational* part, i.e.,  $T = T_{\text{vib}} + T_{\text{rot}}$ . Their expressions are given in terms of the deformation parameters  $(\beta, \gamma)$ , the mass parameters  $B_2$  (for the quadrupole deformations) and the stiffness parameters  $C_2$ . Thus, the vibrational term is [31]:

$$T_{\text{vib}} = \frac{1}{2}B_2 \left( \dot{\beta}^2 + \beta^2 \dot{\gamma}^2 \right) , \quad (2.27)$$

and the rotational term is [31]:

$$T_{\text{rot}} = \frac{1}{2} \sum_i^3 \mathcal{I}_i \omega_i^2 , \quad (2.28)$$

where the three principal axes of the ellipsoid are indexed by  $i = 1, 2, 3$ . In the expression of  $T_{\text{rot}}$ , two crucial physical quantities arise, namely the angular velocities around each body-fixed axis and the functions  $\mathcal{I}_k$  that will eventually

play the role of *moments of inertia*.

There are two types of moments of inertia that describe the nuclear rotation: the rigid-like MOI and the irrotational (hydrodynamical) MOI, having the following expressions [11, 12]:

$$\mathcal{I}_k^{\text{rig}} = \frac{2}{5}mAR_0^2 \left( 1 - \sqrt{\frac{5}{4\pi}\beta \cos\left(\gamma - \frac{2\pi}{3}k\right)} \right), \quad (2.29)$$

$$\mathcal{I}_k^{\text{irr}} = \frac{3}{2\pi}mAR_0^2\beta^2 \sin^2\left(\gamma - \frac{2\pi}{3}k\right). \quad (2.30)$$

The dependence of the two types of MOI on the triaxiality parameter  $\gamma$  (and fixed  $\beta$ ) can be seen in Fig. 2.11. The differences between the rigid and irrotational MOI are as follow:

- The irrotational MOI vanish when the ellipsoid has axial symmetry
- $\mathcal{I}^{\text{irr}}$  is much more sensitive to the deformation  $\beta$ , while the rigid MOI have most of the contribution coming from a typical rigid sphere
- The *experimental* MOI of well-deformed nuclei show that the *real* MOI within a nucleus are neither irrotational, nor rigid-like, but in fact they follow:

$$\mathcal{I}^{\text{irr}} < \mathcal{I}^{\text{exp}} < \mathcal{I}^{\text{rig}}, \quad (2.31)$$

In the following two subsections, each type of degree of freedom will be described, giving the main characteristics of the energy spectra associated with the two motions.

### 2.2.6 Nuclear Vibration

The energy spectrum is composed of levels built from the oscillator frequencies. The absorption or emission of vibration-like energy quanta (i.e., phonons) when the nucleus transitions to a higher or a lower energy state will be in terms of dipole, quadrupole, octupole, etc. vibrating phonons. These excitations will generate the ground and excited states, resulting in a ‘collection’ of *vibrational bands*. Since



FIGURE 2.11: Comparison between the rigid-like and irrotational-like MOI defined in Eq. (2.30), which are typical for a rigid rotator or an irrotational motion of a fluid. The deformation parameter  $\beta$  is fixed  $\beta = 0.3$ .

the quadrupole effects are of interest within the current work, a spectrum specific to quadrupole vibrations  $\lambda = 2$  phonons can be seen in Fig. 2.12.

A quantity often used within the measurements of nuclear properties is the ratio between the second and the first excited states within a band. These ratios are usually denoted by  $E(4^+)/E(2^+)$  (the state  $4^+$  belongs to the triplet phonon state depicted in Fig. 2.12), and the theoretical value for the vibrational model gives a value of 2. However, some experimental results point out to a value close to 2.2 for nuclei below  $A = 150$ , and a constant value of 3.3 for  $150 < A < 190$  (refer to Fig. 2.19). It should be noted that for the latter case, the value of the ratio is specific to another kind of nucleonic motion: *rotation*, which will be discussed in the following section. Example of experimental *vibrational bands* for several even- $A$  nuclei are shown in Fig. 2.13.

There can also be vibrational bands in odd- $A$  nuclei. Indeed, if one considers the nucleus as a spherical even-even core plus an extra nucleon, the *final* nuclear states are formed by coupling an individual  $j$  orbit with the vibrational states of the core. An example is  $^{63}\text{Cu}$ , which has the ground state  $3/2^-$ . The g.s. for this nucleus is given by the last *uncoupled* nucleon that occupies a shell. In fact, for this particular nucleus, it is the  $2p_{3/2}$  proton that will give the final spin and parity of the nucleus. The vibrational spectrum is regarded as coupling the aforementioned proton with the  $^{62}\text{Ni}$  core. Indeed, by taking a  $2^+$  vibrational phonon from the even- $A$  nucleus, then the (odd-proton + phonon) system can generate a sequence of energy states with angular momenta  $I = 1/2, 3/2, 5/2, 7/2$  and negative parity states. The

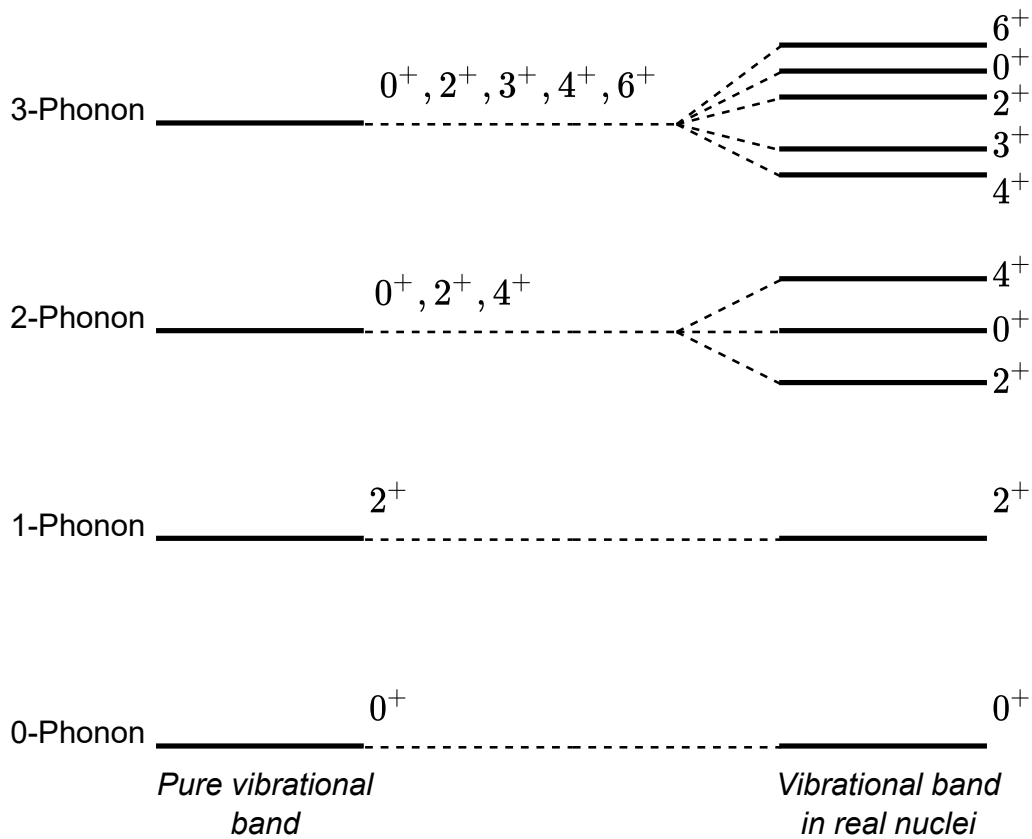


FIGURE 2.12: Illustration of vibrational bands built as excitations of multiple phonons on a ground state. The left side reflects an ideal harmonic vibrator, with the degenerate spin states indicated for each level. Right side shows non-degenerate vibrational levels that exist in nuclei. Keep in mind that each phonon level is built as multiple excitations of a *quadrupole phonon*.

energy levels depicted in Fig. 2.14 show the particle-core coupling effects on the vibrational structure in odd-mass nuclei.

Since the quadrupole vibrations carry an angular momentum of  $\lambda = 2$ , there can be two types of vibrations in a deformed nucleus: one corresponding to  $K = 0$  and one for  $K = 2$ . The  $K = 0$  vibrational motion is called  $\beta$ -vibration, and this induces small fluctuations in the quadrupole deformation parameter, but it preserves the axial symmetry of the nucleus (the vibration is aligned with the deformation axis). The  $K = 2$  vibration is called the  $\gamma$ -vibration, which is responsible for fluctuations in the triaxiality parameter  $\gamma$ . A qualitative description for such an oscillation can be explained in terms of an american football [20]:  $\gamma$ -vibrations consist of a simultaneous pushing and pulling of the ball on its sides, while the  $\beta$  vibrations correspond to continuous pushing and pulling on the ends of the football. An



FIGURE 2.13: Vibrational bands in even- $A$  nuclei. **Left:** The experimental energy levels for  $^{120}\text{Te}$ . The triplet states that correspond to  $\lambda = 2$  can be seen, together with the quintuplet formed by adding three phonons to the  $0^+$  ground state. Experimental data are taken from [32]. **Middle:** The experimental data for  $^{60}\text{Ni}$ . For simplicity, only the first two phonon states are represented. Experimental data were taken from Ref. [33]. **Right:** The experimental data for a vibrational-like structure in  $^{44}\text{Ca}$  [34]. Note the highest energy level coming from the vibrational motion corresponding to an *octupole* mode ( $\lambda = 3$ ).

illustration explaining the geometrical meaning of the  $\beta$  and  $\gamma$  vibrations in nuclei can be seen in Fig. 2.15.

## 2.2.7 Nuclear Rotation

The rotational-kinetic term from  $H_{\text{coll}}$  is called the *rotational energy*, and its expression is given by [37]:

$$\hat{T}_{\text{rot}} = \frac{\hat{I}_1^2}{2\mathcal{I}_1} + \frac{\hat{I}_2^2}{2\mathcal{I}_2} + \frac{\hat{I}_3^2}{2\mathcal{I}_3}. \quad (2.32)$$

The three operators that appear in Eq. (2.32) are the projections of the total angular momentum  $\mathbf{I}$  on the body-fixed axes (see Fig. 2.16 for reference). Note that throughout the text, the angular momentum will be interchangeably represented with an arrow or by bold letters.



FIGURE 2.14: The experimental data of the vibrational states in  $^{63}\text{Cu}$  [35]. The  $2^+$  phonon state in  $^{62}\text{Ni}$  is also shown. The experimental data for  $^{62}\text{Ni}$  are taken from Ref. [36]. The blue rectangle tries to emphasize that the quadruplet in  $^{63}\text{Cu}$  is formed by the coupling of the odd proton to the  $2^+$  vibrational state from the neighboring nucleus.

An important conclusion emerging from the work of Bohr and Mottelson [12] (also see discussion in Ref. [10]) is that no rotations about the symmetry axis are possible for spherical nuclei or axially deformed nuclei. Indeed, every nucleus which contains energy states that are generated by the rotational motion has these bands due to the rotation about an axis that is different from the symmetry axis, and its shape is either axially-symmetric or axially-asymmetric [38]. In its motion, a nucleus can generate angular momentum in two ways:

- *collectively*: via combined rotations and vibrations of the nuclear droplet (the rotation + vibration spectrum of a nucleus will be shown in the next section)
- *single-particle excitations*: unpaired nucleons can rearrange themselves in such a way that they account to the nuclear spin



FIGURE 2.15: The  $\beta$  and  $\gamma$  vibrations occurring in nuclei. The initial nucleus in this example is of prolate type. Each mode of vibration is visualized from the side-view and top-view, respectively. This figure was inspired from Ref. [31].

The coupling of the droplet's rotational a.m.  $\mathbf{R}$  with the single-particle angular momentum of a valence nucleon  $\mathbf{j}$  can be seen in Fig. 2.16. Based on the expression of  $T_{\text{rot}}$  from Eq. (2.28), its quantized form given in Eq. (2.32), and the coupling scheme depicted in Fig. 2.16, it is possible to construct a Hamiltonian that corresponds to rotating nucleus with no valence particle. More precisely, the  $\mathbf{j}$  term is neglected, such that only the pure collective motion of a nucleus is emphasized ( $\mathbf{I} = \mathbf{R}$ ). The energy spectrum for an even-even nucleus is thus expressed as [4]:

$$E_{\text{rot}}(I) = \frac{\hbar^2}{2\mathcal{I}_{\perp}} I(I+1) . \quad (2.33)$$

In the above expression,  $\mathcal{I}_{\perp}$  corresponds to an axis that is perpendicular to the symmetry axis (i.e., either 1-axis or the 2-axis) of the ellipsoid. In the case of axial symmetry both moments are equivalent, such that the general notation  $\mathcal{I}_{\perp}$  is made. As an observation, since there is no single-particle contribution, the quantized angular momentum  $I$  is equivalent to  $R$ . The spectrum defined by Eq. (2.33) leads to energy spacings  $\propto I(I+1)$ , which is also met in the molecular spectra. The ground-state will always be the state  $0^+$ , and due to the *mirror symmetry*



FIGURE 2.16: The coupling of the collective angular momentum with the angular momentum of a single-particle for an axially deformed nucleus that is rotating about an axis perpendicular to the deformation axis.

that is required for the wave-functions describing the even-even nuclei, every other excited state will be represented by an even value of the spin:  $2^+, 4^+, \dots$  [11]. The ratio  $E(4^+)/E(2^+)$  for these bands is 3.33. This is indeed the best signature for the rotational phenomena in nuclei, indicating a clear presence of deformation + rotational motion. In a previous work by the current team (Raduta et al. [39]), some spectra of even-even  $^{158}\text{Er}$  were studied, and agreement with the observed experimental data was impressive. The energy spectra obtained from Eq. (2.33) has a classical counterpart known within literature as the *symmetric top*. Fig 2.17 shows some examples of rotational bands in even- $A$  nuclei.

The spectra of a simple rigid rotator assumes that the projection  $K$  of the total angular momentum for the ground-state of even-even nuclei is  $K = 0$ . So the next step is to consider more general cases of nuclear rotation. There are two general cases of rotational bands that can occur, and both require the coupling scheme of a rotor with a valence nucleon, such that the angular momentum will be  $\mathbf{I} = \mathbf{R} + \mathbf{j}$  (so both situations will correspond to odd- $A$  nuclei). The two situations are called



FIGURE 2.17: Experimental data showing the rotational bands in even-even nuclei. Note the spacing between the states that increases with  $I$  via the rule from Eq. (2.33). Experimental data are taken from Refs. [40, 41].

*Deformation aligned bands* and *Rotation aligned bands* [42]. These are detailed in Appendix C.

## 2.2.8 Superimposed Rotations and Vibrations

Up until now, the collective rotations and vibrations were discussed separately. The small vibrations of the nuclear surface lead to band structures constructed via the quadrupole phonons carrying  $\lambda = 2$  units of angular momentum. The proper picture of a rotating deformed nucleus consists of a stable *equilibrium shape* that is determined by *i*) the *rapid internal motion of the nucleons* within the nuclear potential and *ii*) their entire distribution doing a *slow rotation* having a negligible effect on the nuclear structure or on the individual nucleonic orbits.

Besides the two (separated) degrees of freedom for the nuclear system (i.e., collective rotation and vibrations), they can also be superimposed on each other. Starting from the expression of the *Collective Bohr's Hamiltonian*, the spectrum can be described by the general Hamiltonian:

$$H_{\text{coll}} = T + V = T_{\text{vib}} + T_{\text{rot}} + V \quad (2.34)$$

A separation of the Hamiltonian terms in three main components will be made: one associated to the  $\beta$ -vibration, one for  $\gamma$ -vibrational mode, and the third term is the rotation of a rigid rotor characterized by a total spin  $I$  and well-defined MOI. Following the separation, the spectrum will be [11, 31]:

$$E_{n_\beta n_\gamma IK} = \hbar\omega_\beta \left( n_\beta + \frac{1}{2} \right) + \hbar\omega_\gamma \left( n'_\gamma + \frac{1}{2}|K| \right) + \frac{\hbar^2}{2\mathcal{I}} [I(I+1) - K^2] . \quad (2.35)$$

Note the two harmonic-like solutions that make the vibrational mode present in the energy formula. The two ‘frequencies’ are given in terms of the stiffness and inertia parameters.

$$\omega_\beta = \sqrt{\frac{C_0}{B_2}}, \quad \omega_\gamma = \sqrt{\frac{C_2}{B_2}}, \quad (2.36)$$

and the two quantum numbers are as follows [31]:

$$n_\beta = 0, 1, \dots , \quad (2.37)$$

$$n'_\gamma = 2n_\gamma + 1, \quad n_\gamma = 0, 1, \dots . \quad (2.38)$$

The allowed values for the quantum numbers are as [31]:

$$K = 0, 2, 4, \dots ,$$

$$I = \begin{cases} K, K+1, K+2, \dots & \text{for } K \neq 0 \\ 0, 2, 4, \dots & \text{for } K = 0 \end{cases} . \quad (2.39)$$

Consequently, the spectrum of a typical nucleus in which both vibration and rotation occur has a set of bands that are characterized by the quantum numbers  $K, n_\beta, n_\gamma$ . This collective spectrum is exemplified in Fig. 2.18, and the main bands are:

1. the ground-state band, having states with even  $I$ , where excitation energies are constructed from the rotor term
2. the  $\beta$  band, starting above the g.s. band with  $\hbar\omega_\beta$  and containing only even spins



FIGURE 2.18: The energy spectrum specific to the Collective Model with *Rotations + Vibration*. Each quantum number is also shown at the bottom of the bands. This figure is taken from Ref. [31].

3. the  $\gamma$  band, corresponding to  $K = 2$  (as explained in a previous section). It is distinguished from the  $\beta$  band because it starts with  $2^+$  as first state and it contains both odd and even spins.
4. the higher-level bands are the  $n_\gamma = 1$  and  $K = 4$  bands for  $\gamma$ -vibrational mode, and the  $\beta$  band with  $n_\beta = 2$ .

## 2.2.9 Collective Quantities

In this section, some important quantities that are strictly related to the collective nature of nuclei will be described. Indeed, one can understand nuclear deformation, energy spectra, and behavior of nuclei with respect to spin by studying quantities such as *rotational frequencies*, *moments of inertia*, *quadrupole moments*, and so on. The comparison with experimental data for these quantities can help validate the theoretical assertions that are initially made, which represents a crucial test of any model.

### 2.2.9.1 R - Energy Ratio

As discussed before, the energy ratio between the first excited  $4^+$  state to the first excited  $2^+$  state is a very good test of rotational or vibrational spectra of nuclei.



FIGURE 2.19: The experimental ratio  $R_{4+}/2+$  in even- $Z$  and even- $N$  nuclei. Each line is connecting sequences of isotopes. Note the two important values for  $R_{4+}/2+$ , namely 2 and 3.33 given for a perfect vibrator and a pure rotator, respectively. Text with magenta color marks the magic numbers for  $Z$  or  $N$ .

This plot was inspired from Ref. [15].

The evolution of this ratio across the mass number  $A$  and a classification between *vibrational* vs. *rotational* character is made in Fig. 2.19.

### 2.2.9.2 Rotational Frequencies

In the classical limit the angular frequency:

$$\omega = l_{\text{cls.}}/\mathcal{I} , \quad (2.40)$$

describes the kinetic energy of a rotating object. Indeed,  $\omega$  is frequency of rotation around a particular direction, and its quadratic behavior gives the energy:

$$E = \frac{1}{2}\mathcal{I}\omega^2 , \quad (2.41)$$

The above expression can also be given in terms of the angular momentum  $l_{\text{cls.}}$ , such that the final energy becomes  $E_{\text{cls.}} = l_{\text{cls.}}^2/(2\mathcal{I})$ . Quantum mechanically, it was shown that  $l^2$  is expressed as  $\hat{l}_{\text{quantum}}^2 = \hbar^2 l(l+1)$ . Bengtsson et al. [43] calculated the so-called *Routhians* (single-particle energies within the rotating frame of reference), and they found a *canonical* relation between the energies and rotational

frequencies:

$$\omega = \frac{dE(I)}{dI_x} , \quad (2.42)$$

where the term  $I_x$  is called the *aligned angular momentum*, and it usually denotes the experimental spin of every state minus a reference value [44]. The signature property discussed in Appendix C plays a pivotal role in determining  $I_x(I)$ , since the projection  $K$  of the angular momentum onto the deformation axis must be taken into account:

$$I_x(I) = \sqrt{\left(I + \frac{1}{2}\right)^2 - K^2} , \quad (2.43)$$

In the case of  $K = 0$  bands, the aligned angular momentum reaches a simplified form  $I_x^2 = (I + \frac{1}{2})^2$ . The value of  $K$  is typically the band-head's angular momentum [43, 45]. Alternatively, for a sequence of states where  $\Delta I = 2\hbar$ , the rotational frequency is usually calculated as:

$$\omega \equiv \hbar\omega_{\text{rot}}(I) = \frac{E_\gamma(I \rightarrow I - 2)}{2} . \quad (2.44)$$

The rotational frequency is used to represent many quantities that characterize collective motion and nuclear deformation. Representing the total or the aligned angular momenta as functions of  $\omega$  can show whether multiple bands have the same nature. Moreover, representing the MOI as function of  $\omega$  will also give an insight on the intrinsic structure of the nucleus. Another interesting feature that is present in high-spin spectra of nuclei is the so-called *backbending* phenomena. This phenomenon appears due to the Coriolis effect: nucleons can suffer a de-pairing that makes their a.m. to align with the rotational axis, causing a sharp increase in the MOI [11, 46]. These kind of effects are correlated to high deformation, increased rotation, and change in the nucleonic alignment.

### 2.2.9.3 Moments of Inertia

This is a crucial quantity that describes the degree of deformation and asymmetry of the nuclear shape (remember discussion from Section 2.1). It is possible to retrieve an *experimental* value for the MOI by inferring the energy spacing between

consecutive levels of a collective spectrum. A classification of types of MOI was done in Eq. (2.30), where the MOI dependence on the deformation parameters and even the mass parameter  $B_\lambda$  was shown. The most general expression for the MOI can be written as [47]:

$$\mathcal{I} = \frac{\hbar^2}{2} \left( \frac{dE}{dJ(J+1)} \right)^{-1}, \quad (2.45)$$

where the classical angular momentum  $J$  is related to its quantum equivalent via the correction  $J = I + 1/2$  (see Eq. (2.43)). Practically, the derivative can be expressed in terms of the aligned angular momentum  $I_x$ . Moreover, there are two types of MOI describing the characteristics of the rotational bands: the *kinematical* and *dynamical* moments of inertia. The kinematic MOI is given by [48]:

$$\mathcal{I}^{(1)} = \frac{\hbar I_x}{\omega} = \hbar^2 I_x \left( \frac{dE}{dI_x} \right)^{-1}, \quad (2.46)$$

while the dynamic moment of inertia is expressed as [48]:

$$\mathcal{I}^{(2)}(I) = \hbar \frac{dI_x}{d\omega} = \hbar^2 \left( \frac{d^2 E}{dI_x^2} \right)^{-1}, \quad (2.47)$$

or, equivalently, as:

$$\mathcal{I}^{(2)}(I) = \hbar^2 \frac{4}{\Delta E_\gamma(I)} = \hbar^2 \frac{4}{E_\gamma(I+2, I) - E_\gamma(I, I-2)}. \quad (2.48)$$

As mentioned, the sharp or abrupt irregularities of the MOI with respect to the increase in rotational frequency is known as backbending. The Figs. 2.20 - 2.21 show experimental MOI as function of the squared rotational frequency.

Indeed, by looking at the evolution of  $\mathcal{I}$  from Figs. 2.20 - 2.21, some sharp increases are noted. These are usually attributed to the centrifugal stretching in the rotational model [51]. Moreover, the constant increase in  $\mathcal{I}$  is considered to occur due to the slow and constant quenching of the pairing correlations between nucleons [52]. The abrupt changes are explained as rapid phase transitions of the nucleonic matter [53] exclusively due to the Coriolis Anti-Pairing effect. On the other hand, backbending can also be explained via the band-crossing of two intersecting bands having different moments of inertia. Certainly, the *non-crossing*



FIGURE 2.20: The moment of inertia as function of rotational frequencies for three even-even nuclei. **Left:** The MOI for  $^{162,164}\text{Hf}$  nuclei, with their corresponding rotational ground-state bands. **Right:** The MOI for the first two rotational bands in  $^{166}\text{Hf}$ . Experimental data for these two nuclei are taken from Ahmad et al. [47].

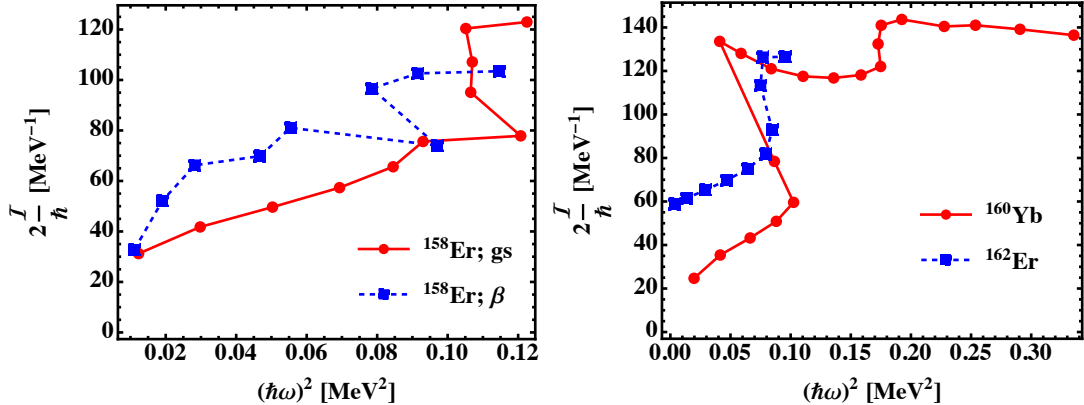


FIGURE 2.21: **Left:** The MOI for  $^{158}\text{Er}$  nucleus, with the ground-state band  $K^\pi = 0^+$  and the  $\beta$ -vibrational band with the same quantum numbers. Experimental data are taken from [40]. **Right:** The MOI for  $^{160}\text{Yb}$  compared with  $^{162}\text{Er}$ . Experimental data are taken from [49] ( $A = 158$ ) and [50] ( $A = 162$ ).

effect makes the bands approach each other as much as the interaction strength allows [11] (see Appendix B).

Usually, the graphical representations of the MOI (kinematic or dynamic) as functions of  $\omega$  (or, equivalently,  $I$ ) are useful when comparing multiple spectra in the same nucleus. Based on their behavior w.r.t. rotational frequency or spin, one can determine if the bands belong to the same intrinsic structure.

### 2.2.9.4 Electric Quadrupole Moment

An important indicator of nuclear deformation is the *electric quadrupole moment* [38], which measures the ‘departure’ of the nuclear shape away from spherical symmetry (through elongation and asymmetry). The most general expression of the intrinsic quadrupole moment for a rotating nucleus is given in terms of its *charge density distribution* [15]:

$$Q_0 = \int (3z^2 - r^2) \rho(r)_{\text{ch}} dv . \quad (2.49)$$

This shows how the nuclear charge distribution inside the nucleus plays a pivotal role in determining the nuclear deformation. A relationship between the deformation parameter  $\beta$  and the quadrupole moment itself can be approximated (in second order of  $\beta$ ) as [20]:

$$Q_0 = \frac{3}{\sqrt{5\pi}} R^2 Z \beta (1 + 0.16\beta) , \quad (2.50)$$

where  $R$  is given as  $R = R_0 A^{1/3}$  and  $R_0 = 1.2$  fm. For values of  $\beta$  that correspond to *strongly deformed* nuclei (i.e.,  $\beta \sim 0.3$ ), higher order terms are not necessary. According to the discussion concerning the nuclear shapes,  $\beta$  describes the eccentricity of the deformed ellipsoid (albeit prolate or oblate). The difference between a prolate and oblate ellipsoid is that for prolate (oblate) case there is an *extension* in one (two) direction and a *squeezing* in the other two (one). Depending on the value of  $\beta$ , the quadrupole moments for nuclei will be positive (indicating a prolate deformation) or negative (giving an oblate deformation). The experimental values of  $\beta_2$  for rare-earth nuclei are shown in Fig. 2.22. Note that for  $\beta_2$  the subscript ‘2’ will be used or dismissed freely throughout this work, but it will signify the same quantity.

In order to understand the behavior of  $\beta_2$  shown in Fig. 2.22, some shell-model considerations need to be taken into account. Firstly, when deformation kicks in, the individual  $j$  orbits within a major shell are nearly empty, resulting in positive values for the quadrupole moments of the nucleons from these orbits. With increasing deformation, large and positive values  $Q(\beta)$  are present. Furthermore, as the shells start to fill, contributions from individual  $j$  orbits to the total quadrupole moment will accumulate, making its value to decrease, vanish, and eventually becoming negative near the shell closure [15].



FIGURE 2.22: The quadrupole deformation parameter  $\beta_2$  as a function of the mass number  $A$  for a few isotopes in the rare-earth region. These values were determined from the experimental transition probabilities  $0^+ \rightarrow 2^+$ . The figure is reproduced from Ref. [15].

The *observed* quadrupole moment (also known as *spectroscopic* or *measured*) can be obtained via a transformation to the laboratory frame applied to  $Q_0$ , meaning that the spectroscopic quadrupole moment has the result [15]:

$$Q = \left[ \frac{3K^2 - I(I+1)}{(I+1)(2I+3)} \right] Q_0 , \quad (2.51)$$

where the quantum number  $K$  is the projection of  $I$  onto the symmetry (deformation) axis. The dependence of  $Q$  on both  $K$  and  $I$  emphasizes the fact that the observed shape of a rotating nucleus is not equivalent to the shape in the intrinsic frame of reference. Consider the case of a prolate nucleus rotating about an axis that is perpendicular to the symmetry axis. Then the *averaged* density distribution of the nuclear matter will look more like an oblate shape (see Fig. 2.23). As a result, when the intrinsic quadrupole moment is positive, the observed one will have a negative value, resulting in the  $I(I+1) > 3K^2$  condition from Eq. (2.51).

Another important quantity used as a ‘test’ for collectivity and deformation is the *reduced electric quadrupole transition probability*, or  $B(E2)$ . This transition probability can be given in terms of the quadrupole moment introduced in Eq.



FIGURE 2.23: The average flattened (oblate) density distribution generated by the rotation of a prolate nucleus. As the ‘initial’ prolate nucleus with its nuclear density (represented by the gray ellipse with dashed borders) being distributed along the deformed axis exhibits rotation, the rotated shape will generate an averaged oblate disk along the rotational axis (represented by the blue). This is why the observed quadrupole moment  $Q$  will have a negative sign if  $Q_0 > 0$ .

(2.49) through the following form [1]:

$$B(E2; I_i \rightarrow I_f) = \frac{5}{16\pi} e^2 Q_0^2 \langle I_i K 20 | I_f K \rangle^2 , \quad (2.52)$$

where the squared factor  $\langle I_i K 20 | I_f K \rangle^2$  is the Clebsch-Gordan coefficient, also written as  $\langle I_i K 20 | I_f K \rangle \equiv C_{K0K}^{I_i 2 I_f}$ . In the case of  $0^+ \rightarrow 2^+$  transition, the reduced probability will be given by [15]:

$$B(E2; 0^+ \rightarrow 2^+) = \frac{5}{16\pi} e^2 Q_0^2 . \quad (2.53)$$

The transition probability from Eq. (2.52) is a special case that can be applied to nuclei possessing *axial symmetry*. This is because the involved transitions are not affected by a change of the projection  $K$ . From the quadratic dependence of the intrinsic quadrupole moment on  $\beta$ , high values (e.g.  $\beta \approx 0.3$ ) will lead to  $B(E2)$  that are one or even two orders of magnitude higher than those specific to nearly spherical nuclei  $\beta_{\text{sph}} \approx 0.05$ . Usually, the valence nucleons are causing some core polarizations, which will affect the ‘final’ structure of the electric quadrupole moment. For example, in an odd- $Z$  and even- $N$  nucleus, the total quadrupole moment  $Q$  (also referred to as *single-particle quadrupole moment*  $Q_{\text{s.p.}}$ ) is given

by the following expression [17]:

$$Q = -\langle r^2 \rangle \frac{2j-1}{2j+2} \frac{e_{\text{eff}}}{e} \equiv Q_{\text{s.p.}}, \quad (2.54)$$

where  $e_{\text{eff}}$  represents the *effective charge* of the nucleus [54]. The mean squared radius corresponds to the radial function of the particle within that  $j$  orbital. An interesting characteristic emerging from Eq. (2.54) is that odd- $A$  nuclei having  $I = 1/2$  will give a vanishing quadrupole moment  $Q$ . Although this situation concerns the measured (i.e., the observed) moment, the odd- $A$  nucleus with  $I = 1/2$  does not necessarily imply that the system has no quadrupole moment. In fact, according to Eq. (2.51), the spectroscopic moment is expressed in terms of the intrinsic component  $Q_0$ , so it is possible to have a vanishing  $Q$  while  $Q_0$  is non-zero. The same circumstance is met for the case of even-even nuclei.

The experimental data from Fig. 2.24 show the magnitude of  $Q$  that would correspond to the value given by Eq. (2.54). One can see sharp increases with the nucleonic number for some nuclei (e.g.,  $^{167}\text{Er}$  or  $^{175}\text{Lu}$ ) and some very strong decreases to negative values (e.g.,  $^{123}\text{Sn}$ ). These alternations between positive (prolate) and negative (oblate)  $Q$  values are also located near the magic numbers. Moreover, when the odd-particle is a neutron, the nucleus still exhibits a non-zero quadrupole moment, meaning that to some extent, the last nucleon is not the sole player regarding the quantitative behavior of  $Q$ .

The experimental data for  $Q$  (the spectroscopic quadrupole moment in units of *barn* or b) for the lowest  $2^+$  states of even- $Z$  and even- $N$  nuclei are graphically represented in Fig. 2.25, where both positive and negative values can be observed. As already explained, a negative  $Q$  value ( $Q = -2$  b for nuclei with permanent deformation belonging to the mass range  $150 \leq A \leq 190$ ) will correspond to an intrinsic quadrupole moment  $Q_0 = 7$  b, which results in deformation parameter  $\beta \approx 0.29$ . Such values indicate substantial eccentricities of the nuclear matter.

## 2.3 Triaxial Nuclei and Their Signatures

It is important to understand why the nuclear community focuses their attention on highly deformed nuclei. Firstly, the engineering difficulty in building the proper infrastructure that allows physicist to create experiments for such studies is in itself



FIGURE 2.24: The measured quadrupole moments  $Q$  as per Eq. (2.54), given in units of  $ZR^2$ , as function of the odd proton ( $Z$ ) and neutron ( $N$ ) numbers, respectively (arrows signify the magic numbers). Experimental data are taken from Ref. [17].

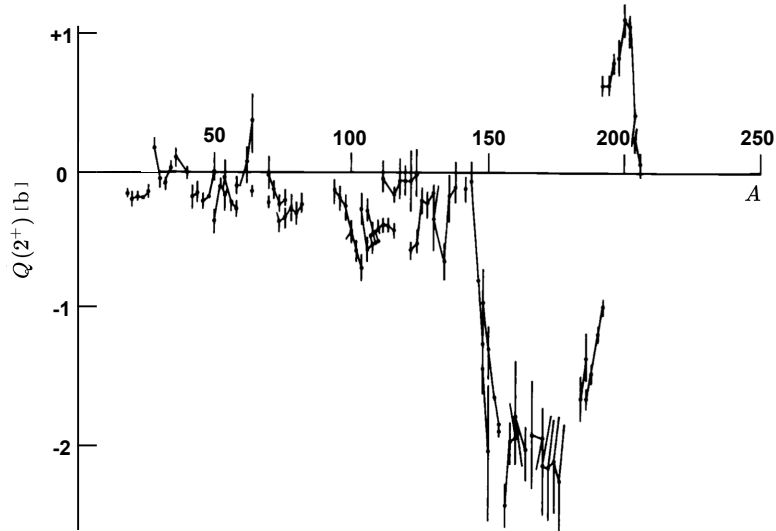


FIGURE 2.25: The measured quadrupole moment for the first excited  $2^+$  states in even-even nuclei. The expression of  $Q$  was defined in Eq. (2.51). The lines between data-points connect the isotope sequences. The figure was reproduced with the experimental data taken from [20].

an impressive and motivating challenge. Secondly, the entire detection mechanism requires complex software (most of it built by the same physicists) and a high-performance numerical analysis of the generated data. Moreover, having a clear picture of the unique characteristics for these nuclei helps to identify and construct a set of *fingerprints* that can be considered tests when searching and studying deformed nuclei. Based on them, one can decide whether the experimental findings indicate triaxiality or not.

### 2.3.1 Non-axial nuclei

In order to define a collective spectra with rotational character for a nucleus, deformation is required. A discussion regarding excitation energies focused on pure rotors or nuclei with axially symmetric shapes (i.e., prolate or oblate) is made in Appendix C. The relevant quantities that are involved in the rotational motion for a deformed nucleus are the moments of inertia (introduced in Section 2.2.9.3) corresponding to the principal axes of the deformed ellipsoid:  $\mathcal{I}_{1,2,3}$ .

Even though calculations are performed with the rigid-like MOI or the irrotational-like, their dependence on the deformation parameters  $\beta_2$  and  $\gamma$  is present (recall expressions given in Eq. (2.30)). Taking a closer look at their evolution with  $\gamma$ , one can see that indeed, similar MOI can only occur at certain values (see Fig. 2.11). When referring to their ground state, nuclei can be regarded as such:

- **Spherical:** all MOI are equal and no deformations are present
- **Axially-symmetric:** two identical MOI and  $\beta_2$  parameter plays a role in characterizing the nuclear shapes
- **Triaxial:** all three MOI are different, the quadrupole deformation  $\beta_2$  and also the triaxiality parameter  $\gamma$  are describing the nuclear shapes

Most of the isotopes are either spherical or symmetric in their ground state [55], but triaxial shapes might occur as ground state [56]. A rigid (fixed) value for  $\gamma$  is required such that triaxial stable nuclei can exist. Thus, one can distinguish between the  $\gamma$ -soft and  $\gamma$ -rigid nuclei. Even more interesting are the structures occurring at very large values of quadrupole deformation  $\beta_2$  and  $\gamma \approx 30^\circ$  (where maximal triaxiality occurs). It will be shown that these nuclei will lead to band

structures that are called *Triaxial Strongly Deformed* bands (TSD) [57, 58]. Tri-axial nuclei are a special class of nuclei, where a complete asymmetry between the moments of inertia exists (given by  $\gamma$ ) and the quadrupole deformation is large.

### 2.3.2 Triaxial Rotor Model

The general Hamiltonian for a *triaxial system* is given in terms of the components of the total angular momentum operator  $\hat{I}$  and the moments of inertia for the deformed ellipsoid, similarly as it was the case for the *rotational Hamiltonian* within the symmetric case:

$$\hat{H} = \frac{\hat{I}_1^2}{2\mathcal{I}_1} + \frac{\hat{I}_2^2}{2\mathcal{I}_2} + \frac{\hat{I}_3^2}{2\mathcal{I}_3}, \quad (2.55)$$

where the indices correspond to each of the principal axes of the rotational ellipsoid. More often, the notations  $A_{1,2,3} = \hbar^2 / (2\mathcal{I}_{1,2,3})$  are used in the Hamiltonian's expression, leading to  $A_1 \neq A_2 \neq A_3$  for the triaxial nuclei. Shi et al. [59] show a very straightforward way of obtaining the eigenvalues for the *triaxial rigid rotor*, following the quantum treatment made by Davydov and Filippov for the rigid rotor without symmetry axis [4]:

$$\begin{aligned} \hat{H} &= \hat{H}_{\text{diag}} + \hat{H}_{\text{non-diag}}, \\ \hat{H}_{\text{diag}} &= \left[ \frac{1}{2} (A_1 + A_2) (\hat{I}^2 - \hat{I}_3^2) + A_3 \hat{I}_3^2 \right], \\ \hat{H}_{\text{non-diag}} &= \frac{1}{4} (A_1 - A_2) (\hat{I}_+^2 + \hat{I}_-^2). \end{aligned} \quad (2.56)$$

Expressing the Hamiltonian in this way is useful because there is a clear difference between a diagonal term and one that mixes states with different  $K$  (i.e.,  $\Delta K = \pm 2$ ). It is important to emphasize that this kind of Hamiltonian is still invariant to rotations with  $\pi$  around the principal axes, meaning that the eigenvalue problem can be solved with the basis  $|IMK\rangle$ , were the wave-function is described as [59]:

$$|IMK\rangle = \sqrt{\frac{2I+1}{16\pi^2(1+\delta_{K0})}} [|IMK\rangle + (-)^I |IM-K\rangle], \quad (2.57)$$

where  $|IM \pm K\rangle$  are the Wigner  $\mathcal{D}$ -functions, which determine the *orientation* of the nucleus itself. The  $K$  quantum number is the projection of  $I$  onto the 3-axis of the body-fixed frame (intrinsic frame of reference), and  $M$  represents the

projection of  $I$  onto the  $z$ -axis of the laboratory frame. This wave-function is quite similar to the one defined in Eq. (C.9) from Appendix C. Indeed, by using these functions as a basis, the total Hamiltonian can be diagonalized in the following manner [59]:

$$\hat{H}_{IK} = \frac{1}{2}(A_1 + A_2) [I(I+1) - K^2] + A_3 K^2 , \quad (2.58)$$

with the notation  $H_{IK} \equiv \langle IK | \hat{H} | IK \rangle$ . The non-diagonal term will have the energy states given as [59]:

$$\hat{H}_{IK\pm 2} = \frac{1}{4}(A_1 - A_2)\sqrt{(I \mp K)(I \pm K + 1)(I \mp K - 1)(I \pm K + 2)} , \quad (2.59)$$

where  $\hat{H}_{IK\pm 2} \equiv \langle IK | \hat{H} | IK \pm 2 \rangle$ . Such calculations were performed by the team for  $^{158}\text{Er}$  (see Fig. 8 from [39]) and the results of the diagonalization procedure were in complete agreement with alternative descriptions for  $\hat{H}$ .

### 2.3.3 Triaxial Particle + Rotor Model

In this section, the Hamiltonian for a system composed of one single-particle and a triaxial core, which is usually applied to odd- $A$  nuclei, will be discussed. In fact, the main framework that will be described in the remaining chapters starts from the triaxial PRM [4]. Davydov et al. developed the triaxial PRM model for explaining the low-lying collective spectra of  $2^+$  states within transitional nuclei. The Hamiltonian of this system is composed of a term for the even-even core and another one for a single-particle *moving in a quadrupole deformed mean-field*:

$$\hat{H} = \hat{H}_{\text{rot}} + \hat{H}'_{\text{sp}} . \quad (2.60)$$

Here, an important observation must be made regarding the second term. Usually, the single-particle Hamiltonian  $\hat{H}'_{\text{sp}}$  is composed of an *intrinsic energy* coming from the  $j$ -shell in which the nucleon is orbiting, and an *effective energy* that characterizes the interaction between the particle and the core, which has a quadrupole nature. Consequently, the Hamiltonian  $\hat{H}'_{\text{sp}}$  should be written as:

$$\hat{H}'_{\text{sp}} = \hat{h}_0^j + \hat{H}_{\text{int}}^{\text{quad}} ,$$

where  $\hat{h}_0^j$  is the former term and  $\hat{H}_{\text{int}}^{\text{quad}}$  is the latter one. For example, Ring et al. [11] uses the SHO for describing  $\hat{h}_0^j$ . The interaction Hamiltonian is in fact a  $\gamma$ -deformed Nilsson potential, which was previously discussed (see Section 2.2.2), with its general expression:

$$\hat{H}_{\text{int}}^{\text{quad}} = \kappa\beta r^2 \left[ \cos \gamma Y_2^0 + \frac{\sin \gamma}{\sqrt{2}} (Y_2^2 + Y_2^{-2}) \right]. \quad (2.61)$$

Furthermore, this deformed potential gives the energy splittings for the nucleonic orbits (recall the Nilsson diagrams from Figs. 2.8 - 2.9), and it can be expressed in terms of the atomic mass  $A$  and the quadrupole deformation parameter  $\beta_2$  [60]:

$$\hat{H}_{\text{int}}^{\text{quad}} = \frac{206}{A^{1/3}} \beta_2 \left[ \cos \gamma Y_2^0 + \frac{\sin \gamma}{\sqrt{2}} (Y_2^2 + Y_2^{-2}) \right]. \quad (2.62)$$

However, the generalized expressions from Eqs. (2.61) - (2.62) can be re-written for a single-particle characterized by its total angular momentum  $\mathbf{j}$  in the following way:

$$\hat{H}_{\text{int}}^{\text{quad}} = \frac{V}{j(j+1)} \left[ \cos \gamma (3j_z^2 - \mathbf{j}^2) - \sqrt{3} \sin \gamma (j_x^2 - j_y^2) \right], \quad (2.63)$$

where the entire interaction strength between the particle and the core is embedded in the *single-particle potential strength*  $V$ . This parameter is very important in the present research, since the theoretical results regarding energy spectra are obtained through the numerical determination of  $V$ . Obviously, the three components of the single-particle angular momentum are represented by  $j_x$ ,  $j_y$ , and  $j_z$ .

Peng et al. [60] gave a description for odd-odd nuclei within  $A \approx 100$  and  $A \approx 130$  mass regions using a Hamiltonian in which two valence nucleons were coupled to the triaxial core. Indeed, their Hamiltonian was constructed in the following way:

$$\hat{H} = \hat{H}_{\text{intr}} + \hat{H}_{\text{coll}}, \quad (2.64)$$

where  $\hat{H}_{\text{coll}}$  is the typical rotor Hamiltonian (such as the one defined in Eq. (2.55)) and  $\hat{H}_{\text{intr}}$  represents the sum of a proton and neutron contribution:

$$\hat{H}_{\text{intr}} = h_p + h_n. \quad (2.65)$$

The term  $\hat{H}_{\text{intr}}$  can be viewed as an intrinsic part that describes the deformation of the core and the motion of the nucleons within the mean-field. A remarkable



FIGURE 2.26: The quadrupole potential  $\hat{H}_{\text{int}}^{\text{quad}}$  as defined in Eq. (2.62), represented as a function of the angular coordinates  $\theta$  and  $\varphi$ . Calculations were done with fixed parameters  $\beta_2$ ,  $\gamma$ , and for  $A = 163$ .

feature of this approach is that the problem can be extrapolated to a case with multiple protons and neutrons, invoking some sort of ‘scalability’ of their model. The single-particle energies for protons and neutrons from Eq. (2.65) have a similar form as the one stated in Eq. (2.63), namely it is given as:

$$h_{p(n)} = \pm \frac{1}{2} C_\beta \left[ \left( j_3^2 - \frac{j(j+1)}{3} \right) \cos \gamma + \frac{1}{2\sqrt{3}} (j_+^2 + j_-^2) \sin \gamma \right] , \quad (2.66)$$

with the alternating signs corresponding to the proton and neutron, respectively. Note the switch of axes labelling from  $(x, y, z)$  to  $(1, 2, 3)$ , and the introduction of ladder operators  $(j_+, j_-)$ . The *coupling parameter*  $C_\beta$  is a measure of energy (typically expressed in MeV) and its value depends linearly on  $\beta_2$ :

$$C_\beta = \frac{195}{j(j+1)} \frac{1}{A^{1/3}} \beta_2 . \quad (2.67)$$

It is worth giving quantitative results on the quadrupole potential and the single-particle Hamiltonian described above. As such, a simple numerical application will be employed, obtaining graphical representations with the behavior of these quantities with respect to the deformation parameters. Firstly, the potential  $\hat{H}_{\text{int}}^{\text{quad}}$  will be analyzed in the polar plane defined by the angles  $(\theta, \varphi)$ . For nuclei near the  $A \approx 160$  region, it is common to have values of  $\beta_2 \in [0.2, 0.4]$  and  $\gamma \approx 20^\circ$ . The quadrupole potential  $\hat{H}_{\text{int}}^{\text{quad}}$  is numerically evaluated, and the results can be seen in Figs. 2.26 - 2.27.



FIGURE 2.27: The quadrupole potential  $\hat{H}_{\text{int}}^{\text{quad}}$  as defined in Eq. (2.62). Calculations were done with fixed parameters  $\beta_2$ ,  $\gamma$ , and  $A = 163$ .

Concerning the numerical evaluation of  $h$  given in Eq. (2.66) (hereafter, the indices  $p, n$  are dismissed), one can take the diagonal components of  $h$  and apply the rules only for one proton. As a result, the *mixing terms*  $j_+$  and  $j_-$  from  $h$  will not contribute at all, since their average with the protonic states  $|jk\rangle$  will give zero. Only the  $(j_3^2 - j(j+1)/3)$  term will affect the diagonal components of  $h$ . For a proton state  $|jk\rangle$ , where  $k = -j, \dots, j$ , the diagonal element  $\langle jk| h |jk\rangle$  will be:

$$h_{jk} \equiv \langle jk| h |jk\rangle = \frac{1}{2} C_\beta \cos \gamma \langle jk| \left( j_3^2 - \frac{j(j+1)}{3} \right) |jk\rangle , \quad (2.68)$$

which can be simplified to:

$$h_{jk} = \frac{1}{2} C_\beta \cos \gamma \left( k^2 - \frac{j(j+1)}{3} \right) . \quad (2.69)$$

These matrix elements will be functions of deformation parameters and projection  $k$  of the particle's angular momentum onto the 3-axis. Since  $j_3$  is applied twice on  $|jk\rangle$  state, the final result will be  $k^2$ , so only the positive values can be considered for the numerical application  $k = 1/2, \dots, j$ . The qualitative evolution of  $h_{jk}$  as function of  $\beta_2$  and  $\gamma$  is studied for a nucleus with  $A = 167$  in which the odd-particle is either a proton in the  $h_{11/2}$ -shell or in the  $i_{13/2}$ -shell. The behavior of  $h_{jk}$  w.r.t. the quadrupole deformation parameter can be seen in Fig. 2.28, while Fig. 2.29 shows the behavior of  $h_{jk}$  w.r.t. the triaxiality parameter  $\gamma$ .

In reference to this evaluation, one can observe the fact that the single-particle

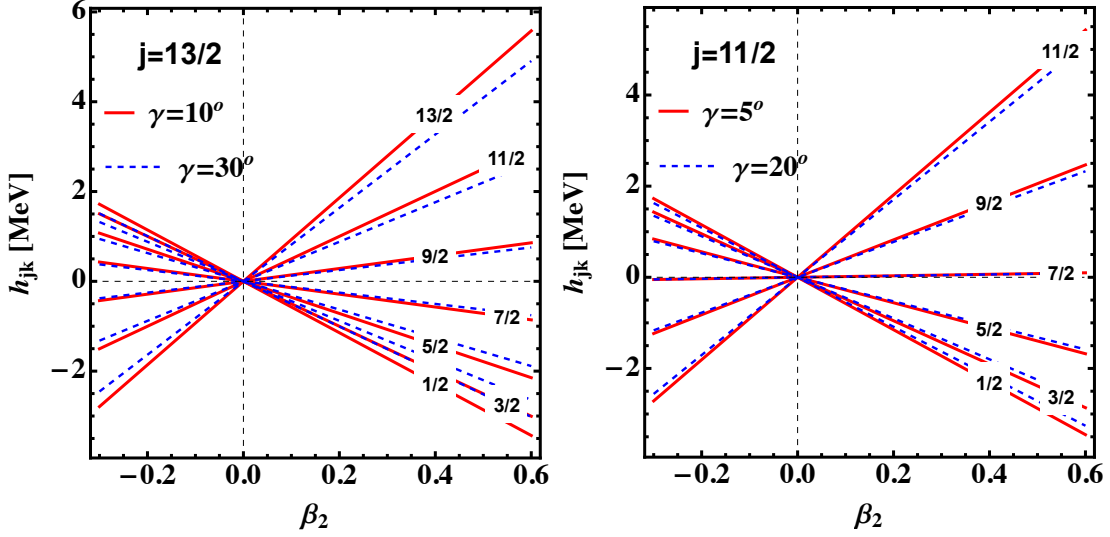


FIGURE 2.28: The evolution of the diagonal matrix elements  $h_{jk}$  defined in Eqs. (2.68) - (2.69) w.r.t. the quadrupole parameter  $\beta_2$ , for one proton on a deformed  $j$ -shell and a fixed triaxiality parameter  $\gamma$ . See text for details.

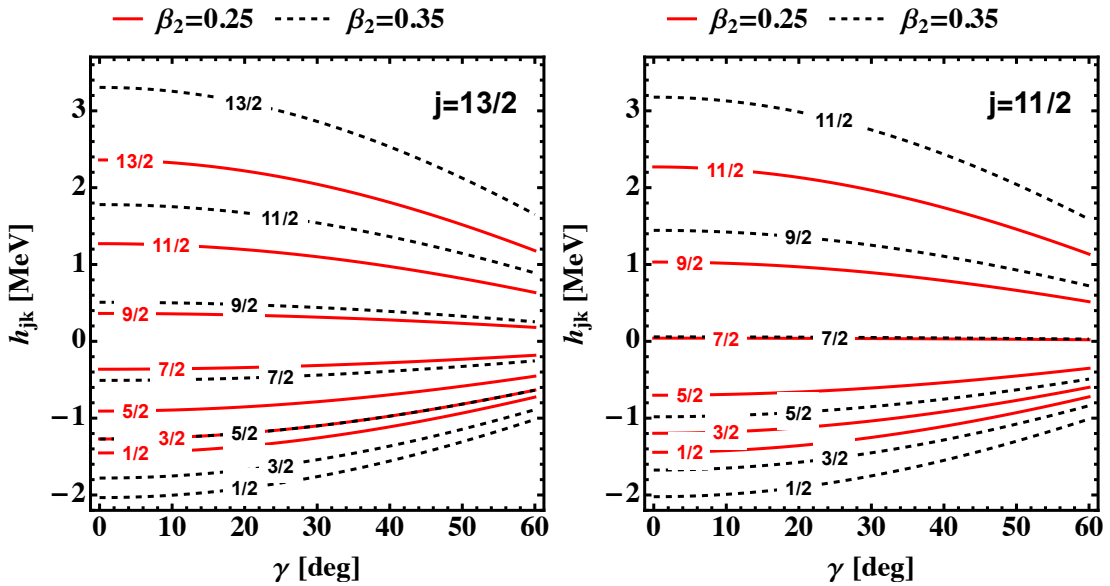


FIGURE 2.29: The evolution of the diagonal matrix elements  $h_{jk}$  defined in Eqs. (2.68) - (2.69) w.r.t. the triaxiality parameter  $\gamma$  for one proton on a deformed  $j$ -shell and a fixed deformation parameter  $\beta_2$ . See text for details.

energies are independent on the sign of  $\gamma$  since the cosine function is even. However, this is not the case when calculations are done for the non-diagonal elements, because states with different  $k$  will add contributions to  $h$  via the sine function. For the evolution of  $h_{jk}$  w.r.t.  $\gamma$ , the lines from Fig. 2.28 are almost similar, indicating that the diagonal components are not very sensitive to nuclear triaxiality. On the other hand, a difference in  $\beta_2$  between the components will result in large gaps. Going back to the general Hamiltonian given in Eq. (2.60) and putting together Eqs. (2.61) - (2.63), it can be brought to a ‘final’ form. The rotor part, the single-particle contributions, and the quadrupole deformation of the mean-field are clearly depicted [11]:

$$\hat{H} = \sum_{i=1}^3 \frac{R_i^2}{2\mathcal{I}_i} + h_0^j + \frac{V}{j(j+1)} \left[ \cos \gamma (3j_3^2 - j^2) - \sqrt{3} \sin \gamma (j_1^2 - j_2^2) \right]. \quad (2.70)$$

Regarding the dynamical character of  $\hat{H}$  defined in Eq. (2.70), the coupling of the high- $j$  particle with a rotor will create special physical effects, which can be classified in the following way [11]:

- rotational energy is always minimized by the rotation of the core around the axis with the largest MOI
- alignment of the odd particle will always prefer a maximal mass overlap with the core
- in terms of their angular momentum, the *Coriolis effect* will always tend to align the particle with the core

Concluding this section, the energy spectrum for an odd- $A$  nucleus can be described using the triaxial PRM. It is a starting ground for many theoretical descriptions that aim at confirming and predicting phenomena specific to highly deformed nuclei.

### 2.3.4 Stable Triaxial Deformation

The stability of a triaxial nucleus is related to the presence (existence) of minima within the *Potential Energy Surface* [11]. This energy surface characterizes the shape of the nucleus with respect to the deformation parameters  $\beta$  and  $\gamma$ .

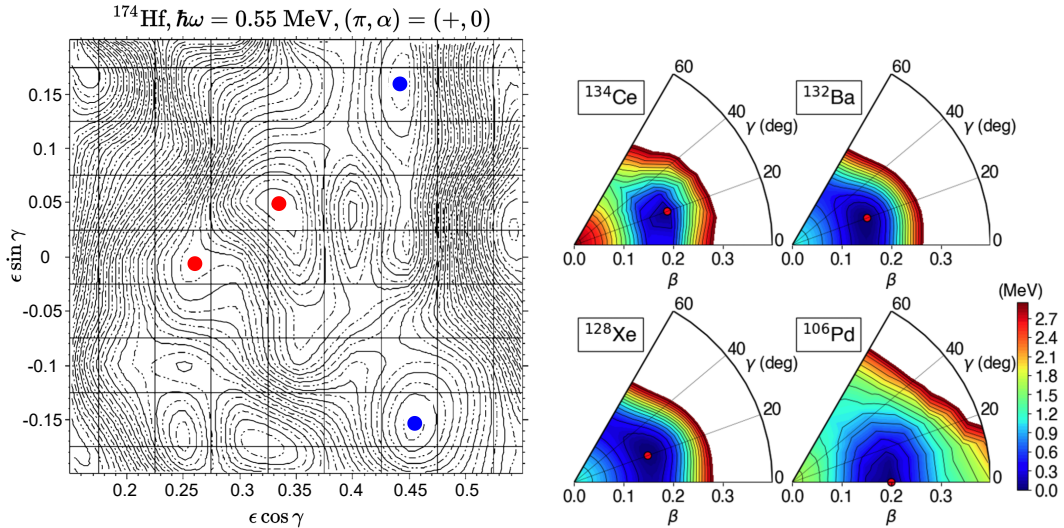


FIGURE 2.30: **Left:** Potential energy surface for  $^{174}\text{Hf}$ , evaluated at a constant rotational frequency. Positive parity and signature  $\alpha = 0$  were considered in the evaluation. Four minima that could be attributed to known configurations are identified which are marked with red colored dots (normal deformation) and blue dots (strong deformation). This figure was adapted from Ref. [63]. **Right:** PES for some even-even nuclei. Note the rather shallow triaxial minima for all nuclei, and the  $\gamma$ -soft nature of all the nuclei except for  $^{106}\text{Pd}$ , whose minimum is achieved at a null triaxiality parameter. This figure was taken from Ref. [64].

These solutions will consist of graphical representations in the  $(\beta, \gamma)$ -plane, where different values of the potential energy appear. Lower values represent a higher degree of stability. Typically one can find regions of stability across the plane with well-defined values for  $\beta$  and  $\gamma$  at which the nucleus is stable and deformed. On the other hand, if the energy variation is rather flat in the  $\gamma$  degree of freedom, but centered around a finite  $\beta$ , then this nucleus is called  $\gamma$ -*unstable*. These energy surfaces are a key indicator of stability with respect to the deformation parameters. Examples of energy surfaces for some nuclei are shown in Figs. 2.30 - 2.31. It is remarkable the fact that small quantum fluctuations will exist around the minima. The energies depicted in Figs. 2.30 - 2.31 are created using a so-called *Ultimate Cranker* code implementation, which has been developed in Refs. [61, 62]. This implementation is based on a Nilsson deformed potential with pairing interaction included, and it is able to give the values for  $(\beta, \gamma)$  at which a nucleus might achieve stability, practically identifying local and global minima within the potential energy surface.

Within the  $A \approx 160$  mass region there are several nuclei in which TSD bands are identified. Best example are the results concerning Lu-Hf isotopes, where more



FIGURE 2.31: **Left:** PES for  $^{135}\text{Pr}$ . The figure is taken from the work of Frauendorf et al. [9]. **Right:** PES for the odd- $A$  isotope  $^{163}\text{Lu}$  evaluated at a fixed spin  $I = 53/2$  with positive parity and positive signature. The red dot corresponds to a global minimum for normal deformed structure, while the blue diamonds represent two additional minima which correspond to strong deformation. This figure is adapted from Ref. [65].

than 20 such bands were experimentally confirmed [66]. It is interesting that the nuclei with even  $N$  (especially the Lu isotopes) have ground TSD bands emerging from a configuration based on the  $\pi = i_{13/2}$  nucleon. In fact, Ødegård et al. [57] point out the fact that nuclei with proton number  $Z \approx 71$  and neutron number  $N \approx 94$  have stable triaxial shapes around the values  $(\beta_2, \gamma) = (0.38, \pm 20^\circ)$ . Now that the stability of asymmetric nuclear shapes has been visualized in terms of energy surfaces and deformation parameters, it is instructive to understand how one can identify triaxial nuclei (both experimentally and theoretically). This will be done in the following section.

### 2.3.5 Fingerprints of Triaxiality

Within recent years, it has been shown that triaxiality plays an important role on features such as:

- Calculating nucleon separation energies [56]
- Protonic emission probabilities [67, 68]
- Determination of fission barrier height [69, 70]

- Nuclear fragmentation [71]

On the experimental side, a tremendous effort was made in order to construct setups that can study nuclei at very high spins (where collective phenomena previously discussed appear). Unfortunately, measuring triaxiality directly is still quite challenging [38, 55]. Over the last 25 years, with the advance in technology of detectors [72], some large facilities were built, with the sole purpose of studying with great degree of precision high-spin states of nuclei. Facilities such as the EUROBALL [73] or GAMMASPHERE [74] opened *new frontiers* on the nuclear physics at high-spin; being able to measure excited spectra of nuclei having angular momentum within the range  $60 - 80\hbar$ . Regarding the reactions involved, most of the measurements of highly excited (and rapidly rotating) are obtained through *Fusion-Evaporation Reactions*. Since this work does not focus on the experimental setups and procedures, only some literature covering these reactions are mentioned [21, 66, 72, 75–78].

Even though stable triaxiality is an elusive phenomenon, *two clear fingerprints* are known to pinpoint asymmetric nuclear shapes: **wobbling motion** and **chiral symmetry breaking**. There has been an extensive study of these two phenomena, and both indicate a clear lack of symmetry for the underlying nuclei. Since wobbling is the main focus of this work, a brief introduction for chiral symmetry breaking will be made below, while a separated chapter will be devoted to the experimental evidence and theoretical studies regarding wobbling motion.

### 2.3.6 Chiral motion

Firstly introduced by Frauendorf [79], it concerns nuclei in which the nucleonic configurations lead to a system that lacks *chiral symmetry*, meaning that the *left-handed* version is not identical with the *right-handed* one. The two systems can be transformed into each other via the chiral operator by combining a rotation with the time-reversal operator:  $\chi_{\text{chiral}} = \mathcal{T}\mathcal{R}(\pi)$ . The left/right handedness of the nuclear system comes from the coupling of three different angular momenta, typically a valence proton, a valence neutron, and a rotational core. As such, the chiral symmetry breaking is expected to appear in odd-odd nuclei.

In that pioneering work, Frauendorf showed that for a triaxial nucleus, the collective angular momentum  $\mathbf{R}$  will align along the intermediate ( $m$ ) axis of the

deformed ellipsoid (note that the  $m$ -axis is also the axis with largest MOI). The energy is minimized when the triaxial system rotates about the largest MOI, and for irrotational-like flow this corresponds to the  $m$ -axis. Regarding the valence nucleons (particles or holes), the location of their corresponding Fermi level will influence the alignment with the ellipsoid [79, 80]. For a valence proton located in the bottom part of the high- $j$  subshell, its a.m. will align with the short  $s$ -axis of the ellipsoid. Furthermore, a valence neutron located in the upper part of the shell will align its a.m. with the long  $l$ -axis. This type of alignment is related to the overlap between the quasi-particle wave-function and that of the triaxial core. For the particle + core coupling, a *maximal overlap of their wave-functions will minimize the interaction energy*, hence the particle will align its a.m. with the short axis. On the other hand, for the hole + core coupling, *the energy is minimized for a minimal overlap of the wave-functions*, meaning that the hole will tend to align its a.m. with the long axis. A further discussion on the overlap will be detailed in the next chapter.

When the chiral symmetry is broken in the intrinsic frame of reference (body-fixed frame), the restoration of the symmetry in the laboratory frame (through quantum tunnelling [81]) will manifest itself as the emergence of two (almost) degenerate doublet bands with  $\Delta I = 1\hbar$  [79]. This interesting behavior has been drawing a lot of attention lately, with most of the experimental identifications around the transitional nuclei  $A \approx 130$ . Over the years, a great amount of research towards a complete spectroscopy of chiral nuclei has been done in Refs. [80, 82–84] and Refs. [85–90]. Examples of experimental chiral doublets for some odd-odd nuclei are shown in Figs. 2.32 - 2.33.

The geometrical interpretation of the left-handed and right-handed systems can be seen in Fig. 2.34, where the ellipsoid is ‘surrounded’ by the two valence nucleons, each with its aligned angular momentum. Regarding axes labelling, it is fully consistent with the one from Ref. [95] (i.e., see Table I therein).

### 2.3.7 Wobbling Motion

The second fingerprint of triaxiality is the main topic of this work, and it will be discussed in detail in the next chapter. A great amount of progress in understanding nuclear phenomena at high spin has been made by studying this effect. Going back to the discussion about the triaxial shapes and their asymmetry between the

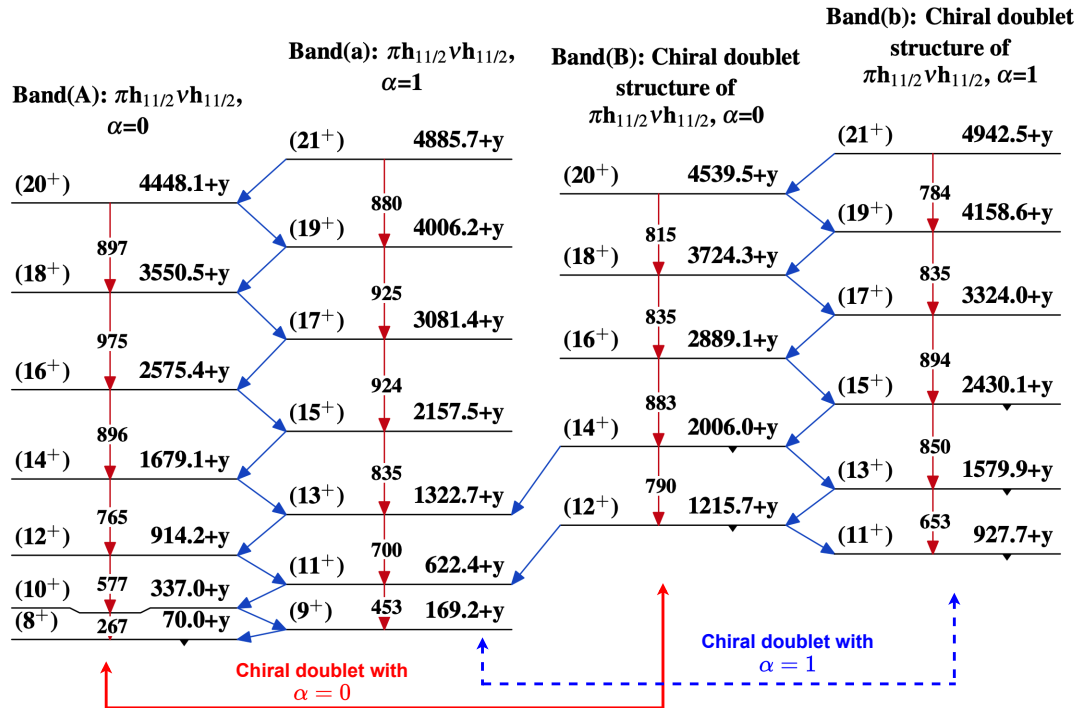


FIGURE 2.32: The energy spectra for the odd-odd  $^{136}\text{Pm}$  isotope, in which the chiral doublet built on the configuration  $\pi h_{11/2} \otimes \nu h_{11/2}$  appears. Experimental data is from Ref. [91] and the level scheme is adapted from Ref. [92].

MOI, this key feature leads to the possibility of defining a rotation about any of the three axis. Although most of rotational motion will be around the axis with the largest MOI (since this is energetically *the cheapest* [12]), the other two axes will contribute to a ‘total’ (superimposed) rotation such that the angular momentum  $\mathbf{I}$  of the system will precess around a steady position. The precessional motion has oscillator-like behavior, meaning that  $\mathbf{I}$  will not only precess, but its projection around the principal axes will oscillate around a steady position. The easiest way of understanding wobbling motion is through the classical analog of the *spinning asymmetric top*. However, the spinning motion for a nucleus is *quantized* and a typical phonon number will be attributed to the system.

As it will be shown in the following chapter, treating the wobbling phenomenon in a ‘classical’ picture will lead to very good results concerning the physical quantities of interest. Moreover, there are many attempts (albeit quantum mechanical or semi-classical approximations) at describing wobbling motion in which the parameters used to describe the Hamiltonian have clear physical meaning, keeping thus a close contact with well-defined concepts regarding system dynamics.



FIGURE 2.33: The energy spectra for the odd-odd  $^{132}\text{La}$  isotope, in which the chiral doublet built on the configuration  $\pi h_{11/2} \otimes \nu h_{11/2}$  appears. Experimental data is taken from Refs. [93, 94].

Other classical analogies for the nuclear wobbling motion can be seen in celestial bodies such as planets. Indeed, Earth has a precession given by its rotation and a small amplitude polar motion. As a result, the Earth's 'angular momentum' will oscillate with respect to one of the body's fixed axis.

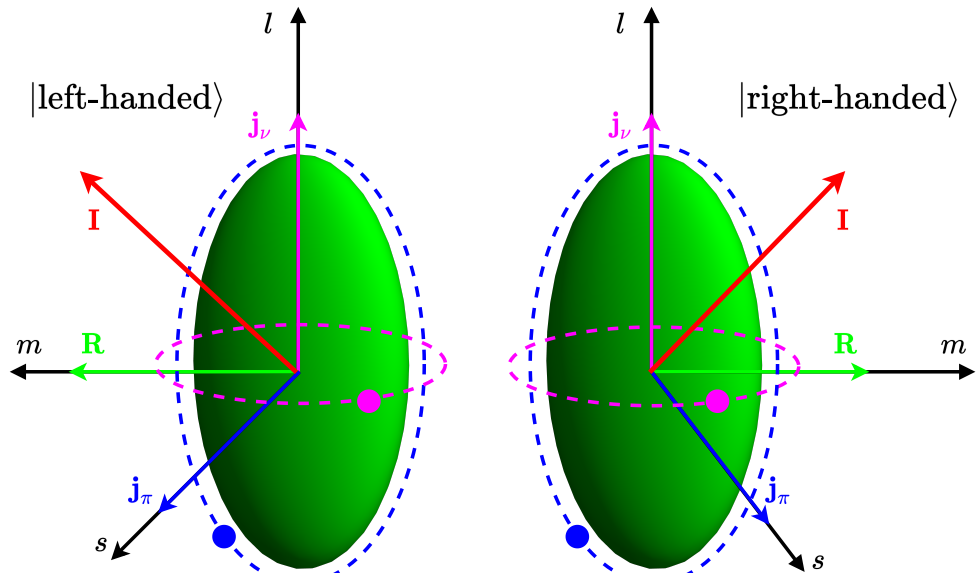


FIGURE 2.34: Left- and right-handed chiral systems for a triaxial odd-odd nucleus, indicating the mutually perpendicular angular momentum vectors. The two valence nucleons are colored with blue (proton) and magenta (neutron). These figures were inspired from [80]. Considering the discussion regarding alignments, the proton a.m.  $\mathbf{j}_\pi$  is aligned with the  $s$ -axis, the neutron a.m.  $\mathbf{j}_\nu$  with the  $l$ -axis, and the even-even core a.m.  $\mathbf{R}$  with the  $m$ -axis of the ellipsoid.

The alignments for the core and the particles are described in text.



# Chapter 3

## Wobbling Motion in Nuclei

The pioneering work of Bohr and Mottelson [1], which was done more than 50 years ago, lead to some interesting features regarding the collective phenomena in triaxial nuclei. Namely, they pointed out that a specific precessional motion of the nucleus's spin will take place when the rotational energy is sufficient. The angular momentum for triaxial nuclei is not aligned to any of the principal axes of the ellipsoid, but it *precesses* and *wobbles* around one of these axes. They called this phenomenon **wobbling motion** (w.m.). The asymmetry of the three MOI makes the rotation (in the quantum mechanical sense) to be possible around any of the three axes.

As such, a *main* rotation around the axis with the largest MOI will be the most energetically favorable, but the other two directions will also contribute to this main rotation, leading to a unique characteristic of triaxial nuclei. The non-uniformity nature of w.m. was firstly studied for the ‘pure’ rigid-rotators that correspond to the even-even nuclei. In this case, the w.m. can be treated as small amplitude oscillations of the total angular momentum  $\mathbf{I}$  around the axis with the largest MOI.

### 3.1 Wobbling Motion in Even-Even Nuclei

The analytical expressions for wobbling excitations were firstly evaluated by Bohr and Mottelson using the so-called *Harmonic Approximation* (HA). This approximation can be described as a small-amplitude limit for the Triaxial Rigid Rotor

Hamiltonian, which was discussed in Chapter 2 (see Section 2.3.2). In this limit, the projection of the total angular momentum onto the axis with largest MOI is  $I_3 \approx I$ , meaning that the nucleus will mostly rotate around the 3-axis, with some ‘disturbances’ from the other two principal axes of the triaxial rotor. For the description of this simple wobbler, one can consider the case when the 3-axis has the largest MOI and:

$$\mathcal{I}_3 > \mathcal{I}_2 > \mathcal{I}_1 \text{ or } A_3 < A_2 < A_1 . \quad (3.1)$$

Following this ordering, the Hamiltonian can be written as:

$$\hat{H}_{\text{rot}} = \textcolor{red}{A_3} \textcolor{red}{I_3^2} + (\textcolor{blue}{A_1} I_1^2 + \textcolor{blue}{A_2} I_2^2) , \quad (3.2)$$

where the different colors try to emphasize *a main rotation around the 3-axis* (represented by red color) and *the precession + oscillation of the total angular momentum* (represented by blue color).

The wobbling excitations causing oscillations with small amplitudes for  $\mathbf{I}$  about the 3-axis are assumed to have a harmonic-like behavior, meaning that the final energy spectrum will have the typical  $\hbar\omega(n + 1/2)$  behavior. The oscillatory motion can be explained as the ‘vibration’ of the total angular momentum around a steady position, where each wobbling excitation consists of an additional vibrating phonon. Therefore, the Hamiltonian can be expressed in terms of *boson* creation and annihilation operators [1]:

$$b^\dagger = \frac{1}{\sqrt{2I}} I_+ , \quad b = \frac{1}{\sqrt{2I}} I_- , \quad [b, b^\dagger] \approx 1 . \quad (3.3)$$

This initial quantization allows one to write Eq. (3.2) as the sum of a *rotational term* and a *wobbling-specific term*:

$$\hat{H}_{\text{rot}} = \textcolor{red}{A_3} \textcolor{red}{I_3^2} + \textcolor{blue}{H_w} , \quad (3.4)$$

$$\textcolor{blue}{H_w} = t_1 \left( n + \frac{1}{2} \right) + \frac{1}{2} t_2 (b^\dagger b^\dagger + b b) , \quad (3.5)$$

where the *number of boson excitations* is denoted by  $n$ , and it is given by  $n = b^\dagger b$ . The two factors  $t_{1,2}$  are expressed in terms of the inertial parameters as [1]:

$$t_1 = I(A_2 + A_1 - 2A_3) , \quad (3.6)$$

$$t_2 = I(A_2 - A_1) , \quad (3.7)$$

with a linear dependence of the two parameters on the total angular momentum. Moreover, depending on the values of  $A_k$ , the contribution of  $t_{1,2}$  can be negative. Their behavior is shown within the right inset of Fig. 3.3. Although the Hamiltonian  $H_w$  is considered to have an oscillatory-like behavior, its general expression does not look like a harmonic Hamiltonian. Nevertheless, Eq. (3.5) can be brought to a diagonalized form by introducing a new set of boson creation and annihilation operators. These operators will be written as linear combinations of  $(b^\dagger, b)$  [1]:

$$c^\dagger = w_1 b^\dagger - w_2 b , \quad (3.8)$$

$$c = w_1 b - w_2 b^\dagger , \quad (3.9)$$

where the two coefficients  $w_{1,2}$  are defined in terms of  $t_{1,2}$  as [1]:

$$\begin{aligned} w_1 &= \left[ \frac{1}{2} \left( \frac{t_1}{\sqrt{t_1^2 - t_2^2}} + 1 \right) \right]^{1/2} , \\ w_2 &= \left[ \frac{1}{2} \left( \frac{t_1}{\sqrt{t_1^2 - t_2^2}} - 1 \right) \right]^{1/2} . \end{aligned} \quad (3.10)$$

The terms  $w_{1,2}$  verify the condition  $w_1^2 - w_2^2 = 1$ , and they make the ‘dangerous’ products  $b^\dagger b^\dagger$  and  $bb$  vanish [96]. Note that  $w_{1,2}$  are constant functions of spin, unlike the coefficients  $t_{1,2}$ . In addition, by introducing a number operator  $\hat{n} = c^\dagger c$  and an excitation quanta  $\hbar\omega_w$  defined as [1]:

$$\hbar\omega_w = \sqrt{t_1^2 - t_2^2} = 2I\sqrt{(A_1 - A_3)(A_2 - A_3)} , \quad (3.11)$$

then the final harmonic-like expression of  $H_w$  can be given:

$$H_w = \hbar\omega_w \left( \hat{n} + \frac{1}{2} \right) . \quad (3.12)$$

In this expression, the quanta  $\hbar\omega_w$  defined in Eq. (3.11) in terms of  $t_{1,2}$  is called

*wobbling frequency*, and it is increasing linearly with the total angular momentum. Accordingly, Eq. (3.4) can be re-written with the wobbling Hamiltonian defined in Eq. (3.12):

$$\hat{H}_{\text{rot}} = A_3 I(I+1) + \hbar\omega_w \left( \hat{n} + \frac{1}{2} \right). \quad (3.13)$$

The eigenvalues of the rotor Hamiltonian can be expressed in terms of a *wobbling phonon number*  $n_w$  (the eigenvalue of the number operator  $\hat{n} = c^\dagger c$ ) and a *wobbling frequency* (defined in Eq. (3.11)):

$$E_{I,n_w} = A_3 I(I+1) + \hbar\omega_w \left( n_w + \frac{1}{2} \right). \quad (3.14)$$

The spectrum of an even-even wobbling nucleus is finally represented in Eq. (3.14). Notice again the two colored terms that illustrate the energies coming from the rotation around the 3-axis and the disturbed motion with small oscillations around the other two axes. Consequently, the wobbling character of the system will be generated by the latter harmonic term. The wobbling phonon number  $n_w$  is related to the ‘strength’ of the tilting for  $\mathbf{I}$ , suggesting that an increasing number for  $n_w$  will result in oscillations with larger amplitudes around the other two axes. The phonon number takes only integer values  $n_w = 0, 1, \dots$ . Inset *b*) from Fig. 3.1, shows a sketch with the tilting effect that the wobbling phonon number has on the total angular momentum vector. For completeness, the collective structure of two wobbling bands generated through phonon excitations is exemplified in inset *a*) from Fig. 3.1.

An alternative way of depicting the wobbling term  $H_w$  from Eq. (3.5) (or Eq. (3.12)) would be to express it more generally in terms of  $I_1$  and  $I_2$ . When doing so, one achieves the following form (assuming that rotation is around the 3-axis) [96]:

$$H_w = (A_1 - A_3)I_1^2 + (A_2 - A_3)I_2^2 = T_{\text{kin}} + T_{\text{pot}}, \quad (3.15)$$

where according to Ref. [59], one could group the terms into purely *kinetic* and *potential* components. This way of expressing  $H_w$  is instructive because it keeps a close contact with the classical picture of understanding the total energy. An



FIGURE 3.1: **Left:** A typical wobbling structure for even-even nuclei. The yrast band contains even angular momenta since the band has signature  $\alpha = 0$ , while the first excited band has odd spins and  $\alpha = 1$ . **Right:** The increase of tilting angle between the rotational axis (the 3-axis in this case) and the total angular momentum  $\mathbf{I}$ . With each wobbling phonon number, the total angular momentum generates a ‘stronger’ precessional motion (illustrated by the colored ellipses).



FIGURE 3.2: The kinetic and potential terms from Eq. (3.15) are graphically represented as function of  $I_1$  and  $I_2$ , respectively. The a.m. components vary from 0 to  $10\hbar$ . The MOI for each curve are as follows:  $\mathcal{I}_1 : \mathcal{I}_2 : \mathcal{I}_3 = 10 : 25 : 20$  (red),  $\mathcal{I}_1 : \mathcal{I}_2 : \mathcal{I}_3 = 10 : 25 : 40$  (blue),  $\mathcal{I}_1 : \mathcal{I}_2 : \mathcal{I}_3 = 10 : 25 : 60$  (black),  $\mathcal{I}_1 : \mathcal{I}_2 : \mathcal{I}_3 = 30 : 25 : 10$  (magenta). The unit for MOI is  $\hbar^2 \text{MeV}^{-1}$ .

example with the behavior of  $T_{\text{kin}}$  and  $T_{\text{pot}}$  with respect to  $I_1$  and  $I_2$ , respectively, can be seen in Fig. 3.2 for different MOI ratios.

As a qualitative analysis of the wobbling frequency and the rotor energy, one can take three arbitrary values for the moments of inertia and study the behavior of



FIGURE 3.3: **Left:** The energy spectrum for an even-even triaxial nucleus, with the main rotation around the 3-axis, according to Eq. (3.14). **Right:** The wobbling frequency (as per Eq. (3.11)) plotted together with the linear terms  $t_1$  and  $t_2$  (Eq. (3.7)), which are used to express  $\hbar\omega_w$ . The unit for  $I_k$ ,  $k = 1, 2, 3$  is  $\hbar^2 \text{ MeV}^{-1}$ .

both  $E_{I,n}$  and  $\hbar\omega_w$  with increasing angular momentum and wobbling phonon number. Keep in mind that depending on the value of the wobbling phonon number, different spin sequences will be allowed. More precisely, from the invariance of the rotor w.r.t. rotations by  $\pi$  about the principal axes for even-even nuclei, the signature quantum number  $\alpha$  can take the values 0 and 1. Each wobbling band will have an alternating signature, starting with  $\alpha = 0$  for  $n_w = 0$  then  $\alpha = 1$  for  $n_w = 1$  and so on: even spin sequences appear for even values of  $n_w$  and odd spin sequences appear for odd values of  $n_w$  (see Fig. 3.3).

The rotor energy from Eq. (3.14) is graphically represented for an arbitrary set of moments of inertia as a function of the nuclear angular momentum  $I$  in the left inset of Fig. 3.3. This pedagogical example contains rotational bands up to  $n_w = 5$  in the wobbling phonon number. From Fig. 3.3, one can see the quadratic and linear behavior for the energy  $E$  and the wobbling frequency, respectively, both with increasing trends.

Another instructive study would be the evolution of the components of  $\mathbf{I}$  expressed



FIGURE 3.4: The geometrical representation of the first and second component of the total angular momentum  $\mathbf{I}$  as functions of the polar angles, according to Eq. (3.18).

in polar coordinates. Indeed, by expressing the three angular momentum components in terms of the polar and azimuthal angles  $\theta, \varphi$ :

$$I_1 = I' \sin \theta \cos \varphi , \quad (3.16)$$

$$I_2 = I' \sin \theta \sin \varphi , \quad (3.17)$$

$$I_3 = I' \cos \theta , \quad (3.18)$$

where  $I' = \sqrt{I(I+1)}$ , then one can make a set of graphical representations. In Fig. 3.4, the quantities  $I_1$  and  $I_2$  are represented in the  $(\theta, \varphi)$  plane for a fixed spin value  $I = 10\hbar$ . Since the third component  $I_3$  is independent of the azimuthal angle  $\varphi$ , it has been dismissed.

Other relevant observables that can be calculated for simple wobbler are the two quadrupole moments  $Q_{20;22}$  and the intraband/interband  $B(E2)$  transition probabilities. The quadrupole components are expressed in terms of the intrinsic

quadrupole moment  $Q_0$  and the triaxiality parameter as [97]:

$$Q_{20} = Q_0 \cos \gamma, \quad Q_{22} = \frac{1}{\sqrt{2}} Q_0 \sin \gamma. \quad (3.19)$$

These components can be furthermore used to determine the intraband  $B(E2)$  transition probabilities [59]:

$$B(E2; (n, I) \rightarrow (n, I - 2)) = \frac{5}{16\pi} Q_{22}^2, \quad (3.20)$$

and also the interband transitions:

$$B(E2; (n, I) \rightarrow (n - 1, I - 1)) = \frac{5}{16\pi} \frac{n}{I} \left( \sqrt{3} Q_{20} w_1 + \sqrt{2} Q_{22} w_2 \right)^2, \quad (3.21)$$

$$B(E2; (n, I) \rightarrow (n + 1, I - 1)) = \frac{5}{16\pi} \frac{n+1}{I} \left( \sqrt{3} Q_{20} w_2 + \sqrt{2} Q_{22} w_1 \right)^2. \quad (3.22)$$

Notice that for the intraband transitions, going from the state  $I$  to  $I - 2$  will only depend on the quadrupole component  $Q_{22}$  squared (Eq. (3.19)), thus making the transitions spin-independent.

### 3.1.1 Triaxial rotor energy vs. wobbling energy

An important discussion regarding the nomenclature of the energy should be made. As it was shown in Eq. (3.14), the energy spectrum for a simple wobbler can be determined for every phonon number and spin sequences. However, that is the full (i.e., ‘absolute’) spectrum of the wobbler, which is composed of the *yrast* band with  $n_w = 0$  and the *excited band* having  $n_w = 1, 2, \dots$ . On the other hand, for every state  $I$  within the collective bands, a set of quantities can be determined from the absolute energies ( $E_{I,n}$ ) by following the rules [59]:

$$E_{\text{wob}}(I_{\text{even}}) = E_{I,n} - E_{I,0}, \quad (3.23)$$

$$E_{\text{wob}}(I_{\text{odd}}) = E_{I,n} - \frac{1}{2} (E_{I-1,0} + E_{I+1,0}), \quad (3.24)$$

to which the community refers to as *wobbling energies*. But often in literature, the energies calculated via Eq. (3.14) are also referred to as wobbling energies, which is not the same as Eqs. (3.23) - (3.24), so a distinction should be made clear.

### 3.1.2 Testing the Harmonic Approximation

It is worth going further and apply the HA formalism in even-even nuclei for an existing nucleus. As it will be discussed in a follow-up section, it turns out that experimental observations for wobbling structures in even-mass isotopes have been very scarce. Nevertheless, very recently, Petrache et al. identified a large collection of band structures in  $^{130}\text{Ba}$  [98]. Two of them are reported to be of wobbling nature [99]. As such, one can take  $^{130}\text{Ba}$  as a testing sample and check if the energy formula given in Eq. (3.14) can be applied successfully.

The technique is based on a *fitting procedure*, where a set of parameters extracted from the expression of  $E_{I,n}$  will be adjusted such that the experimental data are best reproduced by the theoretical model. This kind of approach works pretty good for ‘well-behaved’ model functions and also if the input data is large enough. More often than not, if the model function contains parameters with a clear physical meaning, then this method becomes a suitable tool. In fact, in the following chapters, the developed formalism will verify the experimental data through similar fitting procedures.

Looking at the energy formula from Eq. (3.14), two fitting parameters would seem relevant, namely the largest moment of inertia  $\mathcal{I}_3$  and the wobbling frequency  $\hbar\omega$ . However, the wobbling frequency is furthermore dependent on the other two moments of inertia (as per Eq. (3.11)), meaning that one can use the set  $\mathcal{P}_{\text{fit}} = [\mathcal{I}_1, \mathcal{I}_2, \mathcal{I}_3]$  as appropriate fitting parameters. The wobbling phonon number  $n_w$  is attributed as follows:  $n_w = 0$  for the yrast band (denoted throughout calculations with B1) and  $n_w = 1$  for the first excited band (denoted with B2). The band B1 has signature  $\alpha = 0$ , so it has even spins, while B2 has odd spins. The experimental data regarding spins and energies for the two bands correspond to the measurements done in Ref. [98].

#### 3.1.2.1 Energy Spectrum

Indeed, by following the fitting method described above, a set  $\mathcal{P}_{\text{fit}}$  is obtained. The parameters, i.e., the three moments of inertia are shown in Table 3.1. Remarking the fact that the largest MOI is the one corresponding to the 3-axis. With these parameters, the theoretical energies are determined numerically and the two bands are compared to the measured data in Fig. 3.5. Concerning the fitted energies,

TABLE 3.1: The parameter set  $\mathcal{P}_{\text{fit}}$  obtained from the fitting procedure of the excitation energies of the two wobbling bands (B1 and B2) for  $^{130}\text{Ba}$ . The model function corresponds to the energy of a simple wobbler (see Eq. (3.14)).

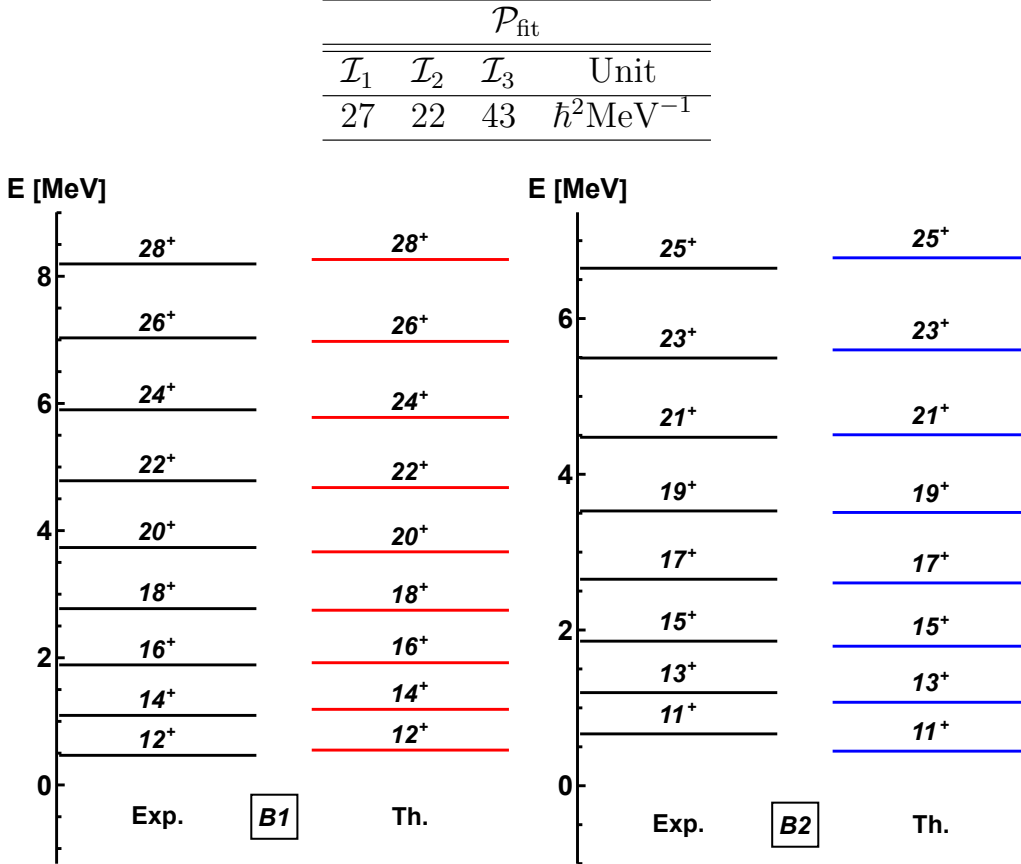


FIGURE 3.5: Comparison between the experimental and theoretical excitation energies (Eq. (3.25)) for the two wobbling bands of  $^{130}\text{Ba}$  (B1 and B2). Experimental data are taken from Ref. [98]. The theoretical data was obtained by fitting Eq. (3.14) as described in text, with the parameters defined in Table 3.1. Note that the band-head  $I^\pi = 10^+$  state from B1 is missing from the spectrum, since it was subtracted from each level.

instead of working with the ‘absolute energies’ (Eq. (3.14)), the *excitation energies* were used [39, 100, 101]. These are determined by subtracting the band-head energy of B1 (that is the  $I_b = 10^+$  level) from every excited state of B1 and B2. By doing so, the accuracy of the results will be improved. The excitation energy for a spin state  $I$  is given as:

$$E(I) = E_{\text{abs}}(I) - E_{\text{abs}}(I_b) , \quad (3.25)$$

where ‘abs.’ signifies the absolute value for  $E$  at that particular spin state ( $I > I_b$ ) and  $I_b$  is the band-head state within the yrast band.



FIGURE 3.6: **Left:** The wobbling energies for  $^{130}\text{Ba}$  calculated with Eq. (3.24) (see text for explanation on the green region). For the first state of B2, the energy was determined as  $E_{\text{wob}}(11^+) = E_{\text{B2}}(11^+) - \frac{1}{2}E_{\text{B1}}(12^+)$  since the band-head state of B1 is zero (as per the definition of excitation energy given in Eq. (3.25)). **Right:** The rotational frequencies for the two wobbling bands of  $^{130}\text{Ba}$ , calculated using Eq. (2.44).

Besides the excited spectrum obtained in Fig. 3.5, other quantities such as the rotational frequency (Eq. (2.44)) for the two bands in  $^{130}\text{Ba}$  are compared with experimental values in Fig. 3.6, and the obtained results agree with the measured data quite well. Note that both frequencies are increasing functions of angular momentum, although for B1, at spin  $I \geq 24\hbar$ , there seems to be less of an increase, which is not fully reproduced by the fitted values. Moreover, having the excitation energies for the two bands, one can evaluate the theoretical wobbling energies as defined in Eq. (3.24) and compare them with the experimental values. The two quantities are graphically represented in Fig. 3.6. Remarking the fact that there is an opposite behavior for the two curves, namely the experimental wobbling energies decrease with angular momentum, while the theoretical ones are constantly increasing. Unfortunately, it turns out that by using the Hamiltonian for a *simple wobbler* is not enough to completely describe the collective motion in this isotope.

### 3.1.2.2 Transition Probabilities

Another step is the calculation of electromagnetic transition probabilities. Firstly, the reduced transition probabilities  $B(E2)$  (both the interband and the intraband) depend on the components  $Q_{20}$  and  $Q_{22}$  of the quadrupole moment. These two can be evaluated numerically using the expressions from Eq. (3.19), while the

TABLE 3.2: The numerical values for the quantities which are required to determine the quadrupole transition probabilities  $B(E2)$  defined in Eqs. (3.20) - (3.22). The parameter set  $\mathcal{P}_{\text{fit}}$  was obtained through the fitting procedure and the values are shown in Table 3.1. The intraband transition probabilities  $B(E2)$  are evaluated for states  $(n, I) \rightarrow (n, I - 2)$ .

Parameters	Calculated values	Observations
$\beta_2$	0.24	Taken from Ref. [99]
$\gamma$	$21.4^\circ$	Taken from Ref. [99]
$w_1$	1.008	Evaluated with $\mathcal{P}_{\text{fit}}$
$w_2$	0.132	Evaluated with $\mathcal{P}_{\text{fit}}$
$Q_0$	$390.376 \times 10^{-2}$ eb	As per Eq. (2.50)
$Q_{20}$	$363.213 \times 10^{-2}$ eb	As per Eq. (3.19)
$Q_{22}$	$101.168 \times 10^{-2}$ eb	As per Eq. (3.19)
$B(E2)_{\text{in}}$	$0.0509 \text{ (eb)}^2$	Eq. (3.20)

intrinsic quadrupole moment is furthermore evaluated using Eq. (2.50). From the microscopic calculations performed by Chen et al. in Ref. [99], they have determined that this isotope has a stable triaxial minimum located at  $(\beta_2, \gamma) = (0.24, 21.5^\circ)$ . This set of deformation parameters will be used within the following computations. Taking the value of  $\beta_2 = 0.24$ , the intrinsic quadrupole moment  $Q_0$  is readily obtained from Eq. (2.50). The transition probabilities from Eqs. (3.20), (3.21), and (3.22) also depend on the two factors  $w_{1,2}$  defined in Eq. (3.10), which are functions of the three moments of inertia. Thus, the quality of the fitting procedure will also be reflected in the results for transition probabilities. The numerical values for  $Q_0$ ,  $w_{1,2}$ , and  $Q_{20,22}$  are presented in Table 3.2.

Having the deformation parameters, the  $w_{1,2}$  terms, and the quadrupole components, one can further evaluate the reduced transition probabilities. The graphical representation from Fig. 3.7 shows the interband transition probabilities  $B(E2)_{\text{out}}$  for states  $(n_w = 1, I) \rightarrow (n_w = 0, I - 1)$ . These values are determined with the parameters defined in Table 3.2. A constant decrease with spin can be observed, and an overall agreement with theoretical calculations from Ref. [99] is observed (see inset *a* from Fig. 4 in [99]).

Considering the interband transitions  $B(E2)_{\text{out}}$  and the constant value for  $B(E2)_{\text{in}}$  (typical for the HA), the ratios  $B(E2)_{\text{out}}/B(E2)_{\text{in}}$  can be assessed. In Table 3.3, the obtained ratios are compared with the experimental ones, where a good agreement can be seen. Additionally, a decreasing trend with respect to the angular momentum is observed.



FIGURE 3.7: The interband quadrupole transition probabilities (Eq. (3.21)) from the first excited wobbling band (B2) to the yrast band (B1) for  $^{130}\text{Ba}$ .

TABLE 3.3: The ratios  $B(E2)_{\text{out}}/B(E2)_{\text{in}}$  for  $^{130}\text{Ba}$ . The interband transitions signify the change from a state  $I$  in band B2 to a state  $I - 1$  in band B1. The experimental data (where available) are taken from Ref. [98, 99].

$I$	$B(E2)_{\text{out}}/B(E2)_{\text{in}}$	
	Experimental	Calculated
11		0.37
13	0.32	0.32
15	0.36	0.27
17	0.22	0.24
19	0.22	0.21
21	0.41	0.19
23		0.18
25		0.16

### 3.1.2.3 General Discussion

The spectrum of this even-even nucleus has been quantitatively reproduced quite well. Moreover, the obtained values for the tree MOI indicate a triaxial nucleus with main rotation around the third axis. However the approximation should not be considered a ‘realistic’ tool in describing  $^{130}\text{Ba}$ . This is because in another work, Chen et al. [99] (and also followed quickly by Wang et al. [102]) found through microscopic calculations that the wobbling motion does not occur as per a pure triaxial rotator, but it emerges from the coupling of two quasi-particles  $\pi(h_{11/2})^2$  with a triaxial core. In fact, their work shows that  $^{130}\text{Ba}$  is the first nucleus in which a configuration with two quasi-particles generates stable triaxial deformation in an even-even nucleus. Consequently, the implementation adopted here only shows that  $^{130}\text{Ba}$  does behave as a wobbler, but this pure triaxial rotator

model *hides* contributions coming from single-particle configuration in the final Hamiltonian. This translates to the fact that Eq. (3.14) contains the effect of the two  $h_{11/2}$  protons hidden within  $\hbar\omega_w$ . In fact, looking back at  $E_{\text{wob}}$  from Fig. 3.6, the discrepancy of the two lines is a clear indicator that some other terms should be taken into account. The experimental wobbling energy from Fig. 3.6 does show an increasing trend for large spins ( $I \geq 23\hbar$ ) which is also matched by the theoretical model (the green region marked inside the plot), suggesting a *transition* with respect to the motion of the nucleus. The transition between decreasing/increasing behavior will be discussed on the next section, dedicated to the odd-mass nuclei.

A quenching factor was necessary for the calculation of the transition probabilities in order to compensate for the magnitude of  $w_{1,2}$ . Nevertheless, this simple and straightforward formalism proves to be a decent tool. The calculations presented here are unique to this research, and they will be considered towards a separate forthcoming publication.

Concluding this section on wobbling motion of even-even nuclei, a final sketch is depicted in Fig. 3.8, where the main axes of the triaxial ellipsoid are represented and denoted with  $m$ ,  $s$ , and  $l$ -axis (medium, short and long, respectively). The precession motion of the total angular momentum (the a.m. of the core itself) will be around the  $m$ -axis, having the largest moment of inertia.

## 3.2 Wobbling Motion in Odd-Mass Nuclei

The previous discussion regarding the *simple wobbler* was specific to nuclei with even number of nucleons. However, wobbling motion also occurs in odd-mass isotopes. In fact, it turns out that across the chart of nuclides, most of the wobblers are odd- $A$ . The reason for this has to do with the triaxial nature of a nucleus. In simple terms, it is ‘easier’ for a (non-axial) deformed system to achieve stability if there is a valence nucleon in a high- $j$  shell which couples to a triaxial core and then drives the entire system to large deformation.

As an example, stable triaxial shapes with large deformations  $\beta_2 \approx 0.4$  can emerge for nuclei in the region  $N \approx 94$ . These are built on the configuration of an odd nucleon (i.e., the  $i_{13/2}$  proton) that couples to a triaxial even-even core. This highly aligned nucleon will play a crucial role in generating wobbling excitations



FIGURE 3.8: A schematic representation of a *simple wobbler*, where the total angular momentum is doing a precessional motion about the axis with the largest MOI. In this particular sketch, the axis with the largest MOI is denoted by  $m$  for intermediate/medium. The long and short axes are labelled  $l$  and  $s$ , respectively. The small-amplitude oscillations of  $\mathbf{R}_\phi$  are depicted with the (black) encircled sine wave. Notation of the angular momentum is consistent with Table 3.4. This figure was adapted from Ref. [103] and inspired from Ref. [104].

for these nuclei, by driving the nuclear shape towards large deformations and stabilizing the TSD structure. Based on this, the description for wobbling motion in an odd-mass system will require the usage of a typical Particle-Rotor-Model. The model Hamiltonian can be expressed as [9]:

$$\hat{H}_{\text{QTR}} = H_{\text{coupl}} + \sum_{k=1}^3 A_k (\hat{I}_k - \hat{j}_k)^2 , \quad (3.26)$$

where  $\hat{I}_k - \hat{j}_k$  are the core's angular momentum components. The term  $H_{\text{coupl}}$  defines the interacting forces between the valence nucleon and the core. This model is known as *Quasi-Particle Triaxial Rotor* (QTR) and it has been developed by Frauendorf et al. in Ref. [9]. The Hamiltonian given in Eq. (3.26) is treated by Frauendorf in the so-called *Frozen Alignment* (FA) approximation. The idea behind FA is that the a.m. for the quasi-particle is rigidly aligned along one of the principal axes of the core. An interesting result was obtained from the description of the QTR Hamiltonian within this approximation. Namely, two possible wobbling modes can occur: the *longitudinal wobbling* and *transverse wobbling*. These two scenarios arise from the alignment of the quasi-particle with the axis having the largest MOI. The quasi-particle + core system is regarded as a valence nucleon

TABLE 3.4: The adopted notations for describing odd- $A$  nuclei by means of particles and angular momenta. These symbols will be used throughout the rest of the work.

Object	Notation	Angular momentum
quasi-particle	$\mathcal{Q}$	$\mathbf{j}_{\mathcal{Q}}$
q-p with <i>particle</i> character	$\mathcal{Q}_p$	$\mathbf{j}_{\mathcal{Q}_p}$
q-p with <i>hole</i> character	$\mathcal{Q}_h$	$\mathbf{j}_{\mathcal{Q}_h}$
triaxial even-even core	$\mathcal{C}$	$\mathbf{R}_{\mathcal{C}}$
total system	$\mathcal{Q} + \mathcal{C}$	$\mathbf{I}$

moving in a quadrupole deformed mean-field generated by the core, so the coupling term  $H_{\text{coupl}}$  can be considered a single-particle term, such as the one presented in Eqs. (2.61) - (2.63) or Eq. (2.66).

In order to avoid repeating certain words, some notations will be adopted throughout the following sections and chapters. Namely, a quasi-particle will be denoted with  $\mathcal{Q}$ . Additionally, a quasi-particle with *hole* character will be referred to as  $\mathcal{Q}_h$  while a quasi-particle with *particle* character will be labelled as  $\mathcal{Q}_p$ . Finally, the core will be denoted with  $\mathcal{C}$ . These notations can be seen in Table 3.4.

The existence of minima within the energy function signify stable structures in the nucleus (see discussion on PES given in Section 2.3.4). In order to minimize the system's energy, a  $\mathcal{Q}_p$  ( $\mathcal{Q}_h$ ) will tend to create a specific coupling with  $\mathcal{C}$ , such that their density distribution overlap becomes maximal (minimal). A maximal (minimal) overlap for  $\mathcal{Q}_p + \mathcal{C}$  ( $\mathcal{Q}_h + \mathcal{C}$ ) will minimize the attractive (repulsive) short-range interaction between the two. In terms of the coupling, one can have [9]:

- the angular momentum for a high- $j$   $\mathcal{Q}_p$  (i.e.,  $\mathbf{j}_{\mathcal{Q}_p}$ ) will align itself with the short (*s*-axis) of  $\mathcal{C}$
- the angular momentum for a high- $j$   $\mathcal{Q}_h$  (i.e.,  $\mathbf{j}_{\mathcal{Q}_h}$ ) will make an alignment with the long (*l*-axis) of  $\mathcal{C}$
- the angular momentum for any  $\mathcal{Q}$  (i.e.,  $\mathbf{j}_{\mathcal{Q}}$ ) from a half-filled high- $j$  shell will align itself with the intermediate (*m*-axis) of  $\mathcal{C}$

Going back to the discussion on longitudinal and transverse wobbling modes, it is the  $\mathcal{Q} + \mathcal{C}$  coupling that dictates what wobbling mode will arise. More precisely,

if the a.m. for  $\mathcal{Q}$  aligns itself *along* the  $m$ -axis, then the motion is considered *longitudinal wobbling* (LW). On the other hand, if the a.m. for  $\mathcal{Q}$  aligns itself *perpendicular* to the  $m$ -axis, then the motion is considered as *transverse wobbling* (TW). One can encounter two different situations that could lead to transverse wobbling. If a  $\mathcal{Q}_p$  comes from the bottom of a deformed  $j$ -shell, it will align its a.m. with the  $s$ -axis (i.e.,  $s \perp m$ ). Moreover, if a  $\mathcal{Q}_h$  comes from the top of a deformed  $j$ -shell, it will tend to align its a.m. with the  $l$ -axis (i.e.,  $l \perp m$ ), which is consistent with the discussion made in Section 2.3.6. These three scenarios are summarized in three *workflow diagrams* that depict wobbling motion (stable triaxial structures), starting from the quasi-particle position within a  $j$ -shell and ending with the emerging wobbling behavior. The TW is shown in Figs. 3.9-3.10, while the same analogy is presented in Fig. 3.11 for LW.

For increasing rotating motion, the Coriolis effect kicks in, trying to align the angular momentum of  $\mathcal{Q}$  with the axis of rotation (i.e., the  $m$ -axis). This creates a change from  $(s) \rightarrow (m)$ -axis for  $\mathcal{Q}_p$  and a realignment  $(l) \rightarrow (m)$ -axis for  $\mathcal{Q}_h$ . This realignment will result in a transition from one wobbling regime to another, meaning that the system will undergo a phase transition. The transition takes place at some ‘critical’ value of  $I$ . In a recent work made by this team [103, 105] such a transition is discussed within a semi-classical approach. However, the FA approximation makes a constraint on the quasi-particle, meaning that its angular momentum is always aligned along one of the principal axes of the triaxial ellipsoid. Consequently, the Coriolis effect is left out when discussing TW or LW behavior.

Returning to the QTR Hamiltonian from Eq. (3.26), if one applies a small-amplitude limit for wobbling vibrations about the three-axis (i.e., a Harmonic Approximation such as the one used for the simple wobbler), and also the quasi-particle  $\mathcal{Q}$  is fixed along the three-axis (making it *frozen*), then the Hamiltonian will acquire the following form:

$$\hat{H} = A_3(\hat{I}_3 - j)^2 + A_1\hat{I}_1^2 + A_2\hat{I}_2^2 . \quad (3.27)$$

The subscript ‘QTR’ from Eq. (3.26) will be dismissed hereafter. By using such a constraint in the QTR Hamiltonian, the angular momentum for  $\mathcal{Q}$  becomes just a number (i.e.,  $\mathbf{j}_{\mathcal{Q}} \rightarrow j$ ). Regarding the angular momentum components, these can



FIGURE 3.9: The workflow of a quasi-particle with particle character  $Q_p$  in its coupling with a triaxial rotor  $\mathcal{C}$ . Each of the five ‘steps’ represents a characteristic involved in the wobbling motion, as described in text. Namely, for  $Q_p$  coming from the bottom of a  $j$ -shell and coupling with the  $s$ -axis of the even-even core  $\mathcal{C}$  (1) will maximize the density overlap (2), which will minimize their interaction (3), minimizing the total energy (4), and finally stabilizing the triaxial structure (5) to a TW. The long  $l$ -axis has been ignored within the drawings. In the bottom-most picture, the precessional cone of the total a.m. is shown, oscillating along the  $s$ -axis.



FIGURE 3.10: The workflow of a quasi-particle with hole character  $\mathcal{Q}_h$  in its coupling with a triaxial rotor  $\mathcal{C}$ . Each of the five ‘steps’ represents a characteristic involved in the wobbling motion, as described in text. Namely, for  $\mathcal{Q}_h$  coming from the top of a  $j$ -shell and coupling with the  $l$ -axis of the even-even core  $\mathcal{C}$  (1) will minimize the density overlap (2), which will minimize their interaction (3), minimizing the total energy (4), and finally stabilizing the triaxial structure (5) to a TW. The short  $s$ -axis has been ignored within the drawings. In the bottom-most picture, the precessional cone of the total a.m. is shown, oscillating along the  $l$ -axis.

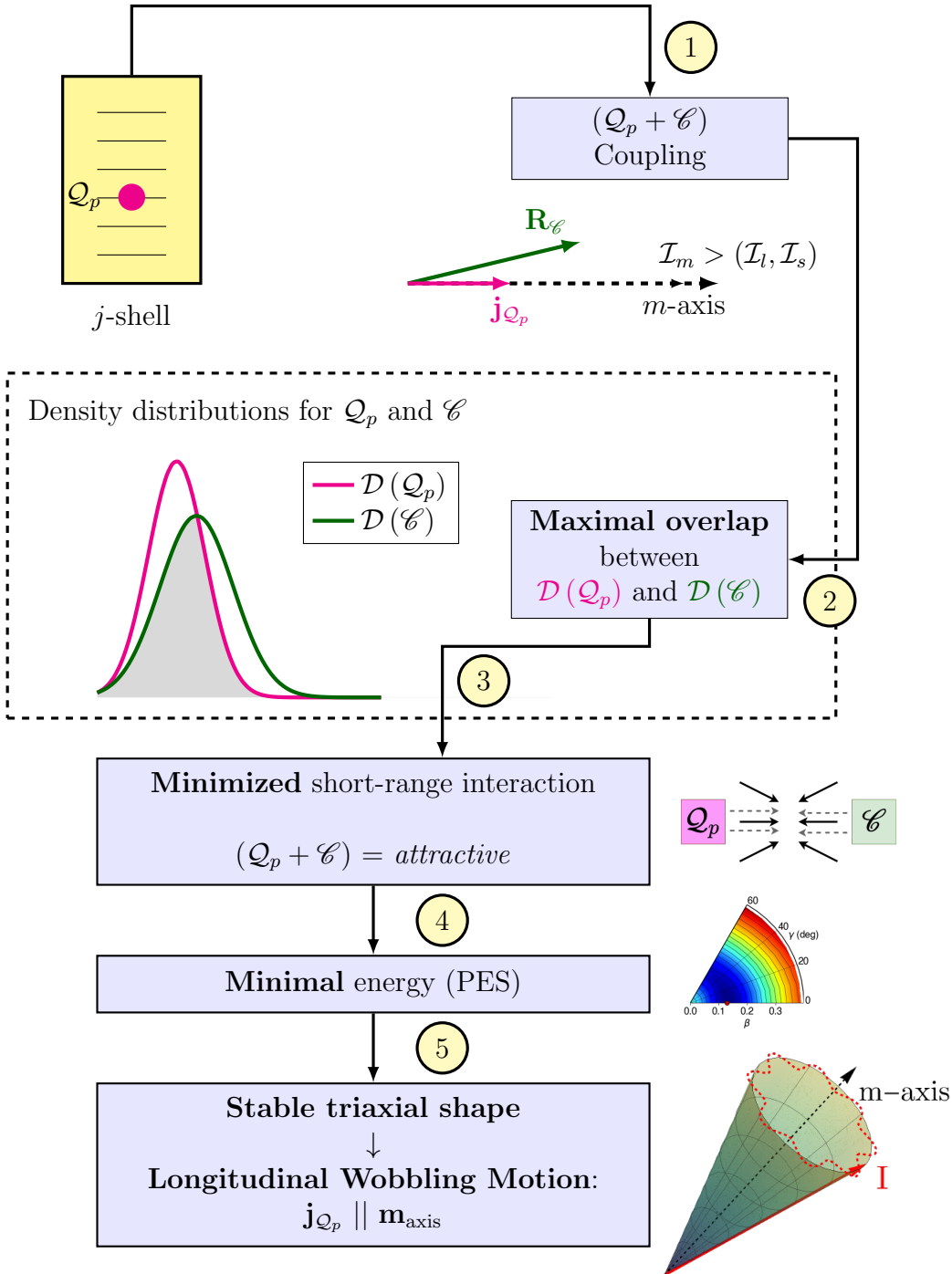


FIGURE 3.11: The workflow of a particle  $\mathcal{Q}_p$  in its coupling with a triaxial rotor  $\mathcal{C}$  within LW mode. Each of the five ‘steps’ represents a characteristic involved in the wobbling motion, as described in text. Namely, for  $\mathcal{Q}_p$  coming from the middle of a *j*-shell and coupling with the *m*-axis of the even-even core  $\mathcal{C}$  (1) will maximize the density overlap (2), which will minimize their interaction (3), minimizing the total energy (4), and finally stabilizing the triaxial structure (5). In the bottom-most picture, the precessional cone of the total a.m. is shown, oscillating along the *m*-axis.

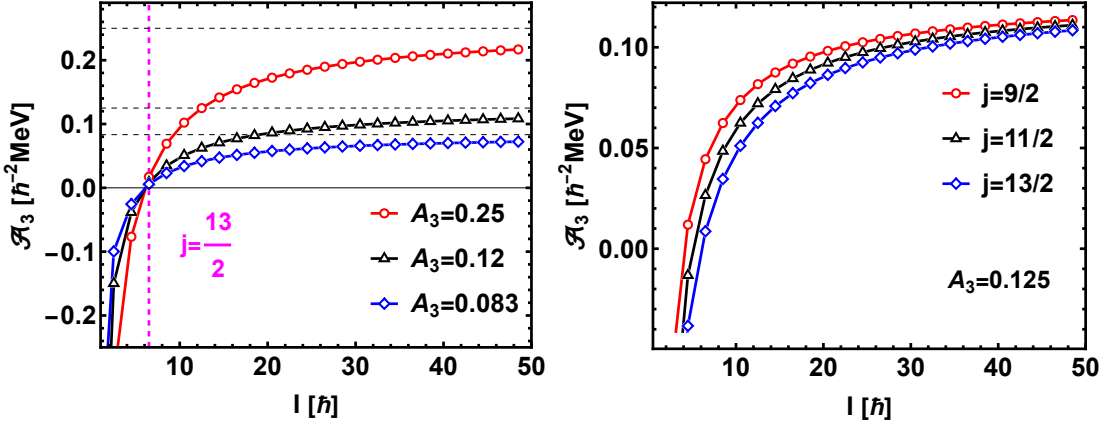


FIGURE 3.12: The reduced inertia parameter defined in Eq. (3.29) as a function of spin. **Left:** The angular momentum of the quasi-particle is fixed (i.e.,  $j = 13/2$ ) and different values for  $A_3$  are attributed. The vertical grid-line corresponds to the spin value at which  $\mathcal{A}_3$  becomes positive. The horizontal dashed lines correspond to the numerical values of  $A_3$  indicated in the legend.

**Right:** The value of  $A_3$  is fixed and different values for  $j$  are considered.

be re-written as:

$$\hat{I}_3 = \sqrt{\mathcal{J}^2 - \hat{I}_1^2 - \hat{I}_2^2} \approx \mathcal{J} - \frac{1}{2} \left( \frac{\hat{I}_1^2}{\mathcal{J}} + \frac{\hat{I}_2^2}{\mathcal{J}} \right) , \quad (3.28)$$

where  $\mathcal{J}$  are the eigenvalues of the total angular momentum, and they are defined as  $\mathcal{J} = \sqrt{I(I+1)}$ . If the factor  $A_3$  is also expressed in terms of  $j$  and  $\mathcal{J}$  through the introduction of a so-called *reduced* inertia parameter:

$$\mathcal{A}_3 = A_3 \left( 1 - \frac{j}{\mathcal{J}} \right) , \quad (3.29)$$

then the QTR Hamiltonian acquires the following form:

$$\hat{H} = A_3(\mathcal{J} - j)^2 + (A_1 - \mathcal{A}_3)\hat{I}_1^2 + (A_2 - \mathcal{A}_3)\hat{I}_2^2 . \quad (3.30)$$

The reduced inertia parameter  $\mathcal{A}_3$  is graphically represented in Fig. 3.12, where the evolution w.r.t. spin is studied for different values of  $A_3$  and  $j$ . Keep in mind that the value of the spin  $I$  defines the quantity  $\mathcal{J}$  which enters in Eq. (3.29).

The Hamiltonian for an odd- $A$  triaxial nucleus has an expression quite similar to the simple wobbler (Eq. (3.2)), except that the coefficients of the first and second components  $\hat{I}_{1,2}$  contain a contribution coming from the quasi-particle itself (through the reduced inertia parameter  $\mathcal{A}_3$  given in Eq. (3.29)). It is important to

mention the fact that one can typically apply HA method for the QTR Hamiltonian only when  $\hat{I}_1^2 + \hat{I}_2^2 \ll I(I+1)$  [1, 9]. As it was the case for the simple wobbler (recall Eq. (3.11)), a wobbling frequency can be deduced from Eq. (3.30) by following a similar procedure. Thus, through an analogy with Eq. (3.11), the QTR frequency is:

$$\hbar\omega_w = 2\mathcal{J}\sqrt{(A_1 - \mathcal{A}_3)(A_2 - \mathcal{A}_3)} , \quad (3.31)$$

or in terms of the three moments of inertia:

$$\hbar\omega_w = \frac{j}{\mathcal{I}_3} \sqrt{\left[1 + \frac{\mathcal{J}}{j} \left(\frac{\mathcal{I}_3}{\mathcal{I}_1} - 1\right)\right] \left[1 + \frac{\mathcal{J}}{j} \left(\frac{\mathcal{I}_3}{\mathcal{I}_2} - 1\right)\right]} . \quad (3.32)$$

For a longitudinal wobbler, the wobbling frequency requires the condition:

$$\mathcal{I}_3 > (\mathcal{I}_1, \mathcal{I}_2) \equiv A_3 < (A_1, A_2) , \quad (3.33)$$

meaning that the total system rotates around the 3-axis (intermediate axis with largest MOI as  $\mathcal{I}_3 = \mathcal{I}_m$ ). For LW, both  $(\mathcal{I}_3/\mathcal{I}_1 - 1)$  and  $(\mathcal{I}_3/\mathcal{I}_2 - 1)$  are positive, meaning that the wobbling frequency increases with  $I$ . For the transverse wobbling, the MOI condition requires:

$$\mathcal{I}_3 > \mathcal{I}_1 \text{ and } \mathcal{I}_3 < \mathcal{I}_2 , \quad (3.34)$$

or, equivalently:

$$A_3 < A_1 \text{ and } A_3 > A_2 . \quad (3.35)$$

The wobbling frequency is thus an increasing function of  $\mathcal{J}$  for the longitudinal regime, while for the transverse behavior it increases until it reaches a maximum value  $\hbar\omega_w^{\max}$  and then it starts to *decrease*. It eventually reaches zero at a *critical spin value*  $\mathcal{J}_{\text{crit}} = j \cdot \mathcal{I}_2 / (\mathcal{I}_2 - \mathcal{I}_3)$ . In Fig. 3.13, the behavior of  $\hbar\omega_w$  with respect to spin is plotted for a typical longitudinal wobbler (left inset) and a transverse wobbler (right inset). The maximum value for the frequency in TW regime is achieved at:

$$\mathcal{J} = \frac{j}{2} \left( \frac{\mathcal{I}_1}{\mathcal{I}_1 - \mathcal{I}_3} + \frac{\mathcal{I}_2}{\mathcal{I}_2 - \mathcal{I}_3} \right) . \quad (3.36)$$

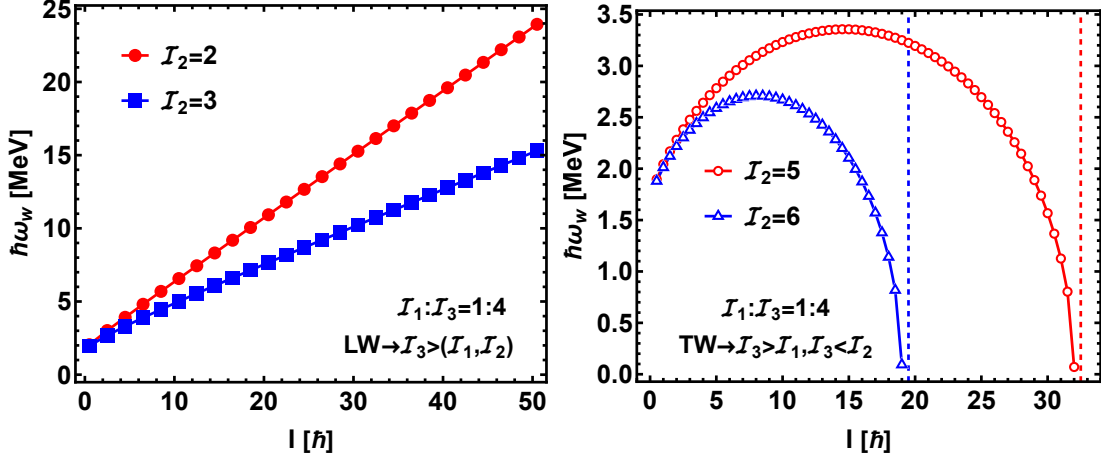


FIGURE 3.13: The wobbling frequency for an odd- $A$  nucleus with  $j = 13/2$ . **Left:** The *longitudinal wobbler* case with two sets of MOI, where only  $\mathcal{I}_2$  changes. **Right:** The *transverse wobbler* case with two sets of MOI, where only  $\mathcal{I}_2$  is different. Note the vertical grid-lines in the right inset that signify the critical angular momentum where the wobbling frequency reaches zero. The maximum value reached in the TW regime is given by Eq. (3.36). The unit for MOI is  $\hbar^2 \text{MeV}^{-1}$ .

In the same manner as for the simple wobbler, geometrical representations for the coupling schemes in the longitudinal and transverse wobbling motion are implemented and shown in Fig. 3.14.

In this section, the collective motion specific to triaxial structures was treated, starting from an initial rotor Hamiltonian amended with a single-particle term. It was shown that based on the  $\mathcal{Q}+\mathcal{C}$  coupling scheme, two scenarios might emerge (i.e., Fig. 3.14). Some workflow diagrams were created for transverse and longitudinal wobbling in Figs. 3.9 - 3.11, which explain how these two modes appear. Furthermore, the LW regime is characterized by an increase in wobbling energy with spin, while the opposite is true for TW regime. By keeping the quasi-particle's a.m. fixed along a principal axes, the expression for  $\hat{H}$  was obtained via Eq. (3.27), which is quite close to the case of even-even nuclei (see Eq. (3.2)). The wobbling frequencies were also expressed in Eqs. (3.31) - (3.32) and their behavior is analyzed with respect to spin in Fig. 3.13. Lastly, the reduced inertia factor  $\mathcal{A}_3$  introduced in Eq. (3.29) is studied w.r.t. the total spin  $I$ , and its evolution was shown in Fig. 3.12.



FIGURE 3.14: Geometrical representation with the alignment scheme for a longitudinal wobbler and a transverse wobbler. The a.m. vectors for the quasi-particle, the core, and the total system are represented by  $\mathbf{j}_Q$ ,  $\mathbf{R}_C$ , and  $\mathbf{I}$ , respectively. Note that the precessional motion with oscillator-like behavior of  $\mathbf{I}$  is illustrated with the encircled sine wave (black color). The resulting motion of the total a.m. will consist in a precessional cone that is properly depicted in Figs. 3.9-3.11.

### 3.3 Wobbling Nuclei - A Complete Catalog

In this section, an inventory of all the known wobbling nuclei will be made. It is worth mentioning that there are ongoing debates regarding the experimental measurements and their ‘validity’ for some of these isotopes, implying that wobbling phenomenon might not be present in some of them. Any existing conjecture will be mentioned where needed. For each wobbler, the band structure, the deformation parameters, and other important observations are mentioned. Knowing the deformation parameters, one can also categorize the isotopes within regions of *normal deformation* (ND structures) or *strong deformation* (SD structure).

Although WM was predicted theoretically more than 50 years ago by Bohr and Mottelson [1], the first experimental observation of this collective mode has been confirmed in 2001. Moreover, the predictions were initially made for even-even nuclei, but the first discovery was for the odd- $A$   $^{163}\text{Lu}$  nucleus [57]. The advance in technological equipment that allows high-resolution and precise measurements has been persistent over the last two decades, resulting in a large number of investigations for the nuclear matter at very high angular momentum ( $I \approx 50\hbar$  or even  $I \approx 80\hbar$ ). In the following subsections, the known wobblers are categorized



FIGURE 3.15: The experimental wobbling energy, defined through the Eq. (3.24), for nuclei within the  $A \approx 100$  mass region.

based on the atomic mass  $A$ , whereas a final diagram is mapped at the end of the section. The mapping procedure is a useful and unique feature in this work, since it provides an easy and reliable source for retrieving information related to deformed nuclei.

### 3.3.1 Wobbling around A=100

In this region, recent measurements show that  $^{105}\text{Pd}$  [106] has two rotational bands as wobbling excitations. The odd quasi-particle is a neutron from the  $h_{11/2}$  orbital that is coupling to the even-even core. The  $\mathcal{Q} + \mathcal{C}$  coupling in which the valence nucleon is a neutron represents a rare example across the nuclide chart. The even-even nucleus  $^{112}\text{Ru}$  [107] is also considered to have three wobbling bands (one yrast and two excited). Additionally, some measurements on  $^{114}\text{Pd}$  [108] (an isotone of the previous nucleus) show that the two bands with different signature ( $\alpha = 0$  and  $\alpha = 1$ ) have similar behavior with the ones from  $^{112}\text{Ru}$  (the excitation energies as function of angular momentum vary in the same fashion). However, the determination of mixing ratios and transition probabilities between levels was not possible, so the interpretation of these structures as wobbling bands cannot be fully ascertained [109]. The behavior of the wobbling energy  $E_{\text{wob}}$  as defined in Eq. (3.24) is calculated for all the mentioned nuclei, using the available experimental data, and the results are shown in Fig. 3.15.

### 3.3.2 Wobbling around A=130

Chakraborty et al. [110] identified some wobbling bands in the odd- $A$   $^{127}\text{Xe}$  isotope. The collective states are built on the odd  $\nu h_{11/2}$  nucleon configuration, leading to the apparition of four bands, two decoupled bands (i.e., favored  $\alpha = -1/2$  and un-favored  $\alpha = 1/2$ ) with zero-phonon number, and two excited ( $n_w = 1, 2$ ) wobbling bands. The wobbling energies (as defined in Eq. (3.24)) are increasing with angular momentum, indicating that  $^{127}\text{Xe}$  behaves as a longitudinal wobbler.

Another presumably longitudinal wobbler is the nucleus  $^{133}\text{La}$  [111] with two wobbling bands  $n_w = 0$  and  $n_w = 1$  that exhibit enhanced  $E2$  transition probabilities and mixing ratios (which are considered hallmarks of wobbling motion). The neighboring nucleus  $^{135}\text{Pr}$  was also investigated, and three wobbling bands of TW character are reported (the yrast and  $n_w = 1$  bands in [112], and  $n_w = 2$  in [113]). The transition from LW to TW between  $^{133}\text{La}$  and its close neighbor  $^{135}\text{Pr}$  is a remarking feature in this mass region. An insight into this change in motion will be discussed at the end of the section.

Although there is inconclusive evidence regarding transition probabilities and mixing ratios [114, 115], the yrast band from  $^{131}\text{Ba}$ , which is built on the  $h_{11/2}$  neutron hole (i.e.,  $Q_h$ ), has an excited wobbling band with negative parity spins ranging from  $13/2$  to  $29/2$  [116]. If precise measurements for the transition probabilities  $B(E2)$  will show enhanced values, then indication of transverse wobbling will be experimentally ascertained.

The isotope  $^{133}\text{Ba}$  is another odd-mass nucleus in which three wobbling bands have been identified by Devi et al. [117]. Besides the excited  $n_w = 1$  and  $n_w = 2$ , the yrast  $n_w = 0$  band has a signature partner band. All four bands are of negative parity. Devi et al. found out that the wobbling energies and the alignment behave quite similarly to  $^{135}\text{Pr}$ , concluding that this nucleus is a transverse wobbler. The remarking characteristic of this nucleus is that a hole-like particle  $Q_h$  couples to the core  $\mathcal{C}$ . Indeed, the odd  $h_{11/2}$  neutron aligns itself with the long axis of the core, causing the TW regime to appear.

Within the last couple of years, a set of measurements brought light upon several even-even wobblers, although more precise measurements are required for ascribing triaxiality to this collective phenomenon. An example is the isotope that was

studied in Section 3.1.2, namely  $^{130}\text{Ba}$  [98, 99, 102]. This nucleus exhibits wobbling via the coupling of two protons  $\pi(h_{11/2})^2$  with the core  $\mathcal{C}$ . Such a coupling corresponds to a two-quasi-particle configuration in the nucleus, denoted here by  $2\mathcal{Q}_h$  for holes and  $2\mathcal{Q}_p$  for particles. Since the measurements of the transition probabilities show enhanced values and the wobbling energies decrease with spin, the isotope is regarded as a clear transverse wobbler.

Petrache et al. also discovered wobbling motion within some nuclei that were heavily studied in terms of chirality (i.e., the Nd and Ce isotopes). In their research, it was found that  $^{134}\text{Ce}$  has two sets of wobbling bands [118]. The first set is based on a  $2\mathcal{Q}_h$  configuration with two neutron holes  $\nu(h_{11/2})^2$ , which align with the long axis. Here the exponent signifies the number of holes relative to the notation  $\mathcal{Q}_h$ , and it is equivalent to the alternative notation  $\nu(h_{11/2})^{-2}$  used in [119–121]. The  $n_w = 0$  and  $n_w = 1$  bands possess negative triaxiality, meaning that is  $\gamma < 0$ . Similarly, two more bands emerge from the coupling of the same  $2\mathcal{Q}_h$  with the core, but their a.m. is aligned along the short axis of  $\mathcal{C}$ , and the triaxiality parameter  $\gamma$  becomes positive. Both sets behave as transverse wobblers, but the latter set has a higher quadrupole deformation. The isotope  $^{136}\text{Nd}$  has been confirmed as a transverse wobbler in the same work. Remarking the fact that this nucleus also has two sets of wobbling bands. The first set (zero- and one-phonon wobbling bands) is built on the same neutron holes, where  $\mathbf{j}_{\mathcal{Q}_h}$  aligns with the long axis, giving the entire system a negative triaxiality and low quadrupole deformation. The second set has three bands (one yrast and two excited) that are built on two 2 protons  $\pi(h_{11/2})^2$ , which align their a.m. with the short axis, driving the system to positive  $\gamma$  and a larger quadrupole deformation.

Lastly, the isotope  $^{138}\text{Nd}$  was investigated by Petrache et al. [119], and some remarks about a possible wobbling behavior in the measured spectra were made. There is one excited band (labelled  $L7$ ) that decays to the yrast band ( $L6$ ), however, the configuration of the wobbling band is different than the yrast partner. Namely, the  $L7$  band is built on a  $2\mathcal{Q}_h$  neutron pair  $\nu(h_{11/2})^2$ , which aligns with the long axis (due to the hole character). The behavior of the wobbling energy  $E_{\text{wob}}$  as defined in Eq. (3.24) is calculated for all the mentioned nuclei, and the results are shown in Fig. 3.16. Exception is the isotope  $^{138}\text{Nd}$ , where a plot showing both the absolute energies is used instead. For  $^{135}\text{Pr}$ , the transition from a TW regime to LW which was identified in [113] is marked by two colored regions (green for TW and red for LW).



FIGURE 3.16: The experimental wobbling energy, defined through the Eq. (3.24), for nuclei within the  $A \approx 130$  mass region. For  $^{134}\text{Ce}$ , the two abbreviations denote the bands with lower deformation (L.D.) and higher deformation (H.D.), respectively. For  $^{136}\text{Nd}$ , the two configurations are represented by  $2-Q_h$  for the neutron holes and  $2-Q_p$  for the protons that couple with the core. See text for more details.

### 3.3.3 Wobbling around $A=160$

Experimentally, this is the *richest* region within the chart of nuclides characterized by wobbling motion. The first ever nucleus in which this phenomenon has been observed was  $^{163}\text{Lu}$  [57]. With a huge infrastructure available at the Euroball detector [73], two *triaxial strongly deformed* bands (TSD1 and TSD2) were measured. Both bands were built on the configuration of a  $Q_p$  proton which belongs to the  $i_{13/2}$  orbital. In fact, along the  $A \approx 160$  region, this *intruder* will cause stability of the triaxial structures. One year later, a second excited wobbling band (TSD3) was confirmed [58], and in a recent work by Raduta et al. (i.e., the current team) the third excited phonon band (TSD4) was ascribed to the wobbling character [39, 101]. The measurements indicate large quadrupole values, positive



FIGURE 3.17: The experimental wobbling energy, defined through the Eq. (3.24), for nuclei within the  $A \approx 160$  mass region.

triaxiality, and enhanced quadrupole transitions. Furthermore, quantities such as alignment, dynamic moment of inertia, and excitation energies relative to a reference show similarities across each of the four bands, with higher magnitudes than other neighboring (coexisting) normally-deformed structures [122]. This is a clear indicator that stable triaxial structures exist in  $^{163}\text{Lu}$ . After this discovery, a large number of wobbling bands with large deformation were identified in  $^{161}\text{Lu}$  [123],  $^{165}\text{Lu}$  [124],  $^{167}\text{Lu}$  [125], and  $^{167}\text{Ta}$  [126].

It is worth mentioning that the isotopes have large spins, meaning that they are also rapidly rotating. When fast rotation occurs, both the core as well as the particle angular momentum will align with the intermediate axis, meaning that these wobblers behave as longitudinal wobblers. However, qualitatively, the wobbling energies have a decreasing trend with spin  $I$ , typical for a transverse-like character. Keep in mind that for large angular momentum values, the TW/LW description becomes unstable. For the high-spin region, the wobbling mechanism is explained through a ‘top-on-top’ model [5, 127] (analogy with the classical asymmetric top). The behavior of the wobbling energy  $E_{\text{wob}}$  as defined in Eq. (3.24) is calculated for all the mentioned nuclei, using the available experimental data, and the results are shown in Fig. 3.17.

### 3.3.4 Wobbling around A=180

A set of new measurements show wobbling structures in the heavy-nuclei region, such as the isotopes  $^{183}\text{Au}$  [128] and  $^{187}\text{Au}$  [78, 104]. In the former, two wobbling bands were identified, one built on a positive parity proton  $i_{13/2}$  and one built on a negative parity proton  $h_{9/2}$ . The remarkable feature of this nucleus is that even though both protons align perpendicular to the intermediate axis (typical to a TW regime) the wobbling energies exhibit a decrease (the  $n_w = 1$  band built on the positive parity proton). As a matter of fact, Nandi et al. speculate that these states represent the initial increasing part of the wobbling energy as function of spin for a transverse wobbler. Remember that the wobbling frequency of a TW system (Eqs. (3.31) - (3.32)) has an increasing part in the low-spin region and only after a critical  $\mathcal{J}$  value (i.e., Eq. (3.36)) the frequency starts to decrease (according to Fig. 3.13). Moreover, an interesting remark is raised, suggesting that the increasing/decreasing trend of the wobbling energies must not be considered as the sole indicator for LW/TW regime (this discussion is also emphasized in a recent work done by Poenaru and Raduta [103, 105]). The  $^{187}\text{Au}$  nucleus exhibits longitudinal wobbling motion, having one yrast and one excited band, both built on the  $h_{9/2}$  proton, located at the middle of the shell, exhibiting longitudinal behavior (since the  $Q$  will align its a.m. along the  $m$ -axis of the core). The behavior of the wobbling energy  $E_{\text{wob}}$  as defined in Eq. (3.24) is calculated for the two nuclei using the available experimental data, and the results are shown in Fig. 3.18.

### Evidence Against Wobbling Motion

For collective excitations, the dominant E2 character of the linking transitions between the  $n_w = 1$  and yrast bands must have mixing ratios larger than unity. Keep in mind that the mixing ratio for a particular  $\Delta I = 1$  transition is typically defined as [64, 129]:

$$\delta = c \cdot E_\gamma \frac{\langle I_f | |\mathcal{M}(E2)| |I_i \rangle}{\langle I_f | |\mathcal{M}(M1)| |I_i \rangle}, \quad (3.37)$$

where  $E_\gamma = E(I_i) - E(I_f)$ ,  $\mathcal{M}(E2)$  is the reduced matrix element corresponding to the electric quadrupole moment, and  $\mathcal{M}(M1)$  is the matrix element of the magnetic dipole moment. The mixing ratio is expected to be  $\delta > 1$  for wobbling



FIGURE 3.18: The experimental wobbling energy, defined through the Eq. (3.24), for nuclei within the  $A \approx 180$  mass region. Data are taken from references cited in text for each isotope. Note that for  $^{183}\text{Au}$ , there are two configurations which cause wobbling motion, namely, the protons  $\pi i_{13/2}$  (positive parity) and  $\pi h_{9/2}$  (negative parity). Nandi et al. [128] suspect that the behavior of the former band is justified by a transverse-like wobbling frequency which increases up to a certain spin before it starts to decrease. This is illustrated via the small inset inside the first figure, where the wobbling frequencies for a TW nucleus are sketched (according to Eq. (3.32) and Fig. 3.13).

excitations. Apparently, after new measurements (re-evaluations) performed on  $^{105}\text{Pd}$ ,  $^{135}\text{Pr}$ ,  $^{133}\text{La}$ ,  $^{133}\text{Ba}$ ,  $^{135}\text{Pr}$ , the mixing ratios are in fact  $\delta < 1$ , meaning that the magnetic transitions are more enhanced. The magnetic dominance would rule out wobbling mode. These newly conducted measurements lead to mixing ratios less than one, which is in favor of an entire re-evaluation, in particular for  $^{133}\text{La}$  [130] and  $^{135}\text{Pr}$  [131, 132].

Besides the wobbling motion, other collective phenomena can arise in the yrast and excited bands of triaxial nuclei. One example is the so-called Tilted-Axis-Precession (TiP) [133], which is a very recent description for the rotational properties of non-axial nuclei. Lawrie et al. showed that tilted precession behaves quite similarly to wobbling motion, and at low spins there can be a ‘competition’ between the two. Remarking the fact that TiP effect implies a precession of the total angular momentum which does not require the quantization of the energy in terms of vibrational phonons. Moreover, the precession does not have to be around one of the principal axes of the triaxial ellipsoid. This interesting process was in fact used to describe the motion in  $^{135}\text{Nd}$  [134] and it seems to be drawing a lot of attention lately.

## The Transition Between Wobbling Regimes

The already discussed isotopes  $^{133}\text{La}$  and  $^{135}\text{Pr}$  show an interesting phenomenon, where the former exhibits an increasing wobbling energy, while the latter (with only two extra nucleons) reveals a decreasing trend. This rather ‘abrupt’ change in the  $\mathcal{Q} + \mathcal{C}$  coupling, (i.e., parallel alignment of  $\mathcal{Q}$  with the core in the first case, and perpendicular alignment in the second) was explained by Biswas et al. [111]. Indeed, in both nuclei the  $\mathcal{Q}_p$  ( $h_{11/2}$  proton) is expected to align with the  $s$ -axis, such that the two isotones must exhibit transverse wobbling. But the situation can be understood in the following way: the  $\mathcal{Q}_p$  in  $^{135}\text{Pr}$  aligns its a.m. with the short axis of the triaxial core, and a TW will arise since the  $m$ -axis has the largest MOI. However, for  $^{133}\text{La}$ , besides the  $h_{11/2}$  proton, an extra pair of protons (positive-parity) will align gradually with the  $s$ -axis of the triaxial density distribution. It is this additional alignment that increases the effective MOI of the short axis, which achieves a higher magnitude than the one along the  $m$ -axis. This re-arrangement will finally result in the LW behavior of the isotope.

The LW/TW behavior within the two nuclei can also be understood in terms of angular momentum behavior w.r.t. the rotational frequency (i.e., the backbending curves, such as the ones presented in Figs. 2.20 - 2.21). For  $^{133}\text{La}$ , there is a rather constant and gradual increase in spin with the rotational frequency. On the other hand,  $^{135}\text{Pr}$  shows a strong backbend with increasing spin, although rather late. Additionally, both nuclei show rotation around the short axis close to the yrast line (since the proton will align its a.m. with that axis). For  $^{135}\text{Pr}$ ,  $\mathcal{I}_s$  is smaller than  $\mathcal{I}_m$ , and with increasing spin it becomes convenient to add more and more collective angular momentum on the  $m$ -axis. Consequently, the wobbling frequency will start to decrease with increasing spin and so does the final wobbling energy. Such a mechanism clearly leads to a transverse regime. At the same time, the ratio  $\mathcal{I}_s/\mathcal{I}_m$  is closer to 1 for  $^{133}\text{La}$ , meaning that the medium axis is no longer preferred by the collective rotation, and the  $s$ -axis will start to gain angular momentum. The increase of collective a.m. along the short axis causes the wobbling frequency to increase with spin, which is specific to the longitudinal character. The evolution with rotational frequency of the total angular momentum in both nuclei can be seen in Fig. 3.19. Notice the gradual increase of the yrast band for  $^{133}\text{La}$  vs. the sharp backbend present in  $^{135}\text{Pr}$ .

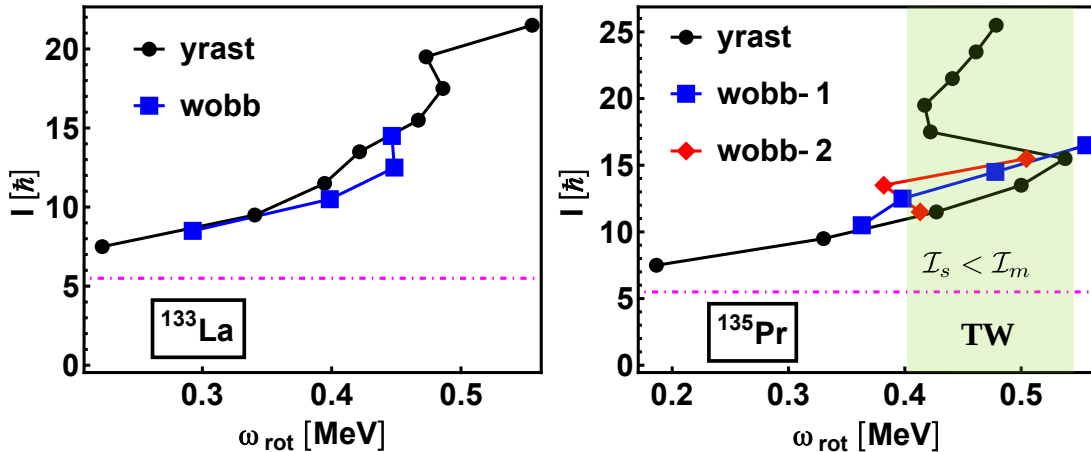


FIGURE 3.19: The angular momentum evolution with respect to the (experimental) rotational frequency  $\omega_{\text{rot}}$  for  $^{133}\text{La}$  (left) and  $^{135}\text{Pr}$  (right). The back-bending region for the latter nucleus is illustrated within the colored sector. Since the MOI of the  $s$ -axis is smaller, more and more collective a.m. will be added to this axis, causing a decrease in the wobbling frequency (TW). The dotted magenta line represents the angular momentum value for the odd proton.

### 3.3.5 Wobbling Motion - Experimental Chart

All the currently known wobblers were grouped in four main regions based on their masses, namely,  $A \approx 100, 130, 160$  and  $180$ . Following up, a chart showing all wobblers with some important values will be constructed. Values such as the quadrupole deformation parameter, triaxiality parameter, and wobbling regime are indexed. This is an inedited representation of the nuclides and the first *unified depiction* of wobbling nuclei in terms of their deformation parameters. The scheme can be seen in Fig. 3.21, however, the reader should firstly refer to Fig. 3.20 that acts as a legend.

## 3.4 Concluding Remarks

Concluding this chapter, the important discussions need to be pointed out. Firstly, the formalism for wobbling motion in even-even nuclei was described, obtaining the wobbling frequency and the energy spectrum for a simple triaxial rotor (recall Eq. (3.11) and Eq. (3.14)). The geometrical representation of the angular momentum components in terms of the polar angles  $(\theta, \varphi)$  was also realized for a given value of  $I$  (see Fig. 3.4). The Harmonic Approximation (HA) was tested for a



FIGURE 3.20: Example of a wobbling nucleus that appears in the chart shown in Fig. 3.21. This particular case is for  $^{187}\text{Au}$ . Experimental  $E_{\text{wob}}$  are calculated according to Eq. (3.24).

known wobbler, i.e., the  $^{130}\text{Ba}$  isotope. Results concerning the excitation energies, quadrupole moments, and transition probabilities were evaluated and compared with the available experimental data. The agreement with the experimental data is quite good, representing a new and original set of results concerning wobbling nuclei. The next step consisted in the analysis of an odd- $A$  triaxial nucleus using the Quasi-Particle Triaxial Rotor model (QTR), whose model Hamiltonian was given by Eq. (3.26). Two possible wobbling motions were portrayed at low spins, namely the transverse and longitudinal wobbling. The difference between the two was explained in terms of particle-rotor coupling.

Additionally, three workflow diagrams were illustrated in Figs. 3.9 - 3.11, required for understanding how alignments of the odd quasi-particle ( $Q$ ) with the triaxial core ( $\mathcal{C}$ ) are realized in terms of their density distribution overlap. A wobbling frequency for the odd- $A$  case was obtained via Eq. (3.32) through a harmonic approximation, and its behavior with angular momentum was quantitatively described for both wobbling regimes (see Fig. 3.12). Another set of geometrical representations were made for the wobbling modes, showing how the precession of each individual vector (i.e., the core a.m.  $\mathbf{R}_{\mathcal{C}}$ , quasi-particle a.m.  $\mathbf{j}_Q$ , and total a.m.  $\mathbf{I}$ ) behaves relative to the entire ellipsoid (see Figs. 3.8 and 3.14). Lastly, an inventory with all the known wobbling nuclei was developed in a unified diagram (Fig. 3.21), which is a first within literature.

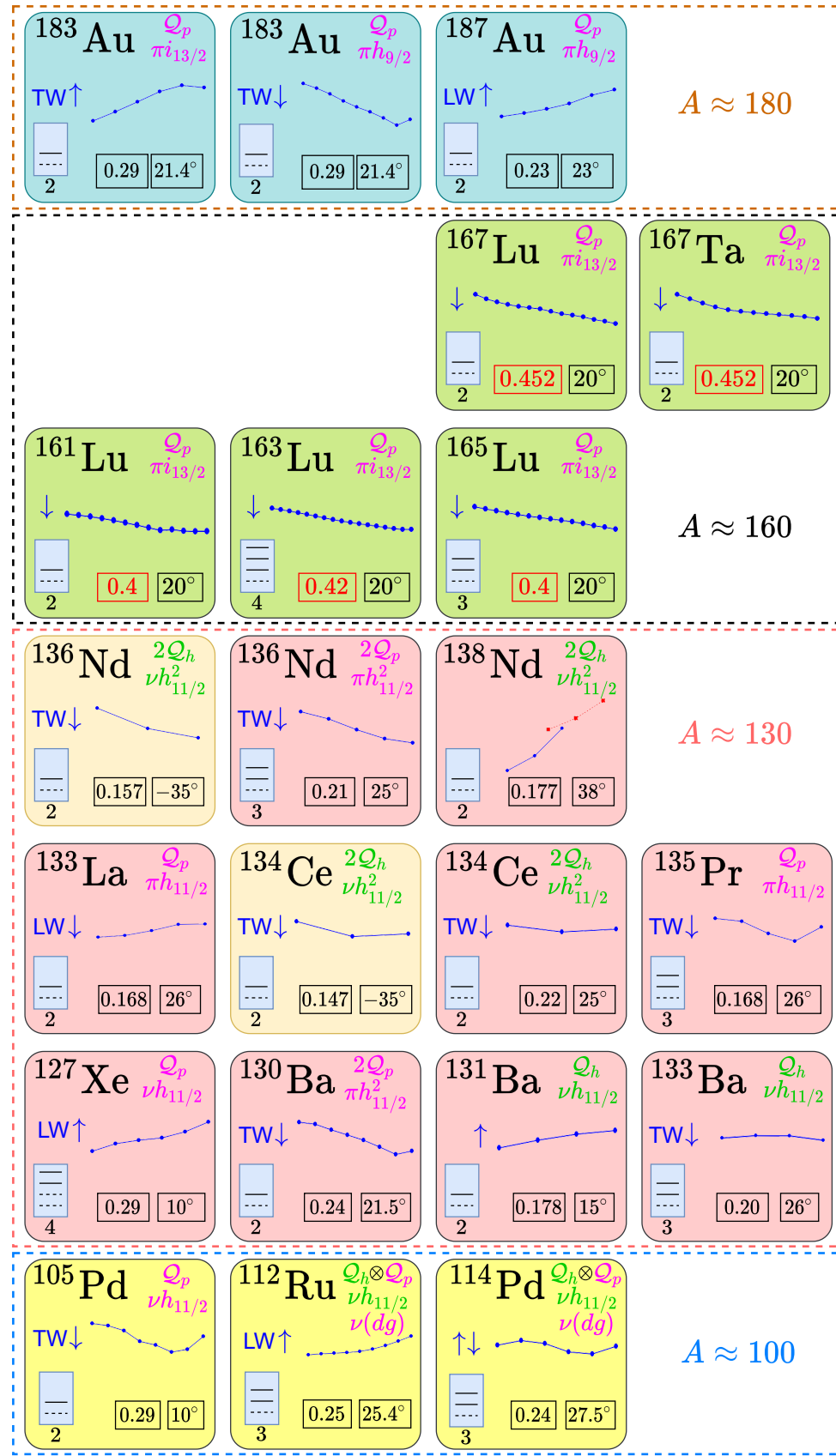


FIGURE 3.21: Unified chart showing all the currently known wobblers. See Fig. 3.20 for legend. *Strong deformation* is marked with red color for  $\beta_2$ .

With the concept of wobbling motion fully explained from a theoretical standpoint, the next step is to study the wobbling motion in odd- $A$  nuclei in detail, by using a formalism based on the Particle-Rotor Model. Analytical results for the relevant quantities will be given, with discussions and important observations when necessary.

# Chapter 4

## New Theoretical Formalism

In this chapter, a formalism describing the wobbling properties in odd- $A$  nuclei will be presented. The model was developed recently by the current team (i.e., Raduta and Poenaru) and applied to  $^{135}\text{Pr}$  [135], the ‘family’ of Lu isotopes  $^{161,165,167}\text{Lu}$  [136], and  $^{163}\text{Lu}$  [101, 103, 105, 136, 137]. This framework is an original contribution to the field of nuclear structure, with a focus on the theoretical aspects of collective phenomena in nuclei.

### 4.1 Previous Work - Foundation

From a development standpoint, it is instructive to review some previous ‘stages’ that lead to the current work, since the description of odd- $A$  nuclei achieved in here is strongly connected with former calculations done by the team. Consequently, in this section, a brief overview of the wobbling motion in  $^{163}\text{Lu}$  done by Raduta et al. in 2017 [39] will be given. Indeed, by using a *semi-classical* approach, the wobbling properties of this odd-mass isotope were accurately described.

The semi-classical approaches tend to be very useful when applied to problems having a *quantal* Hamiltonian that contains quantities behaving as in the *classical limit*, when certain constraints or approximations are made. Moreover, these methods always keep the dynamics of the system in close contact with known classical features, which in principle are easier to interpret (i.e., a clear physical meaning). For this reason, the collective properties of  $^{163}\text{Lu}$  were characterized by such a method. Dealing with an odd nucleus it makes sense to adopt a Particle +

Rotor Model, where the odd quasi-particle couples to an even-even core. From the total Hamiltonian  $H = H_{\text{rot}} + H_{\text{sp}}$  (recall discussion on the PRM model 2.60 and also QTR Hamiltonian 3.26), one obtained the energy spectrum of the four wobbling bands in this nucleus. There is another debate regarding the ‘true’ nature of the fourth triaxial strongly-deformed band. For example, Jensen et al. [122] suspect this band as being built from single-particle excitations, meaning that the states do not show wobbling mechanism. On the other side, Tanabe et al. [138] is in favor of attributing  $n_w = 3$  for TSD4. More details on the interpretation of TSD4 will be discussed in the following sections.

After the Hamiltonian problem was established, the classical equations of motion that fully describe  $\mathcal{Q}$  and  $\mathcal{C}$  (recall notations from Table 3.4, which are still used throughout the remaining chapters) are obtained through the Variational Principle (VP) by following a textbook procedure. The VP translates into a *dequantization* of an initial Hamiltonian, thus making the change from a quantal space  $S_{\text{qt}}$  to a classical space  $S_{\text{cls}}$ . The two  $S$  notations are used hereafter just to signify the difference between a ‘classical’ and a ‘quantal’ picture of the system, having no mathematical significance.

This kind of transition  $S_{\text{qt}} \rightarrow S_{\text{cls}}$  was also used previously for describing collective phenomena [55, 139, 140]. In order to keep a short overview of the foundational stage, the VP is skipped for now, but it will be detailed in a subsequent section. Furthermore, the classical equations of motions were solved with several restrictions, and the energy spectrum was analytically obtained (see Eq. 3.23 from Ref. [39]). The excited bands TSD2, TSD3, and TSD4 were constructed via a phonon operator acting every state  $I$  (denoted by  $\Gamma_1^\dagger$  in Eq. 3.43 from Ref. [39]). This approach makes it possible to have  $n_w = 3$  phonon excitations that are obtained by applying the phonon operator three times on the spin states belonging to the yrast band TSD1. In fact, since the states from TSD4 have negative parity, they are obtained by applying twice  $\Gamma_1^\dagger(\pi = +1)$  and once  $\Gamma_1^\dagger(\pi = -1)$ , where the former phonon has positive parity and the latter has a negative parity. A schematic representation with the mechanism of action for the phonon operator from this formalism is shown in Fig. 4.1.

From the seminal work from 2017 of the team, several features should be emphasized:

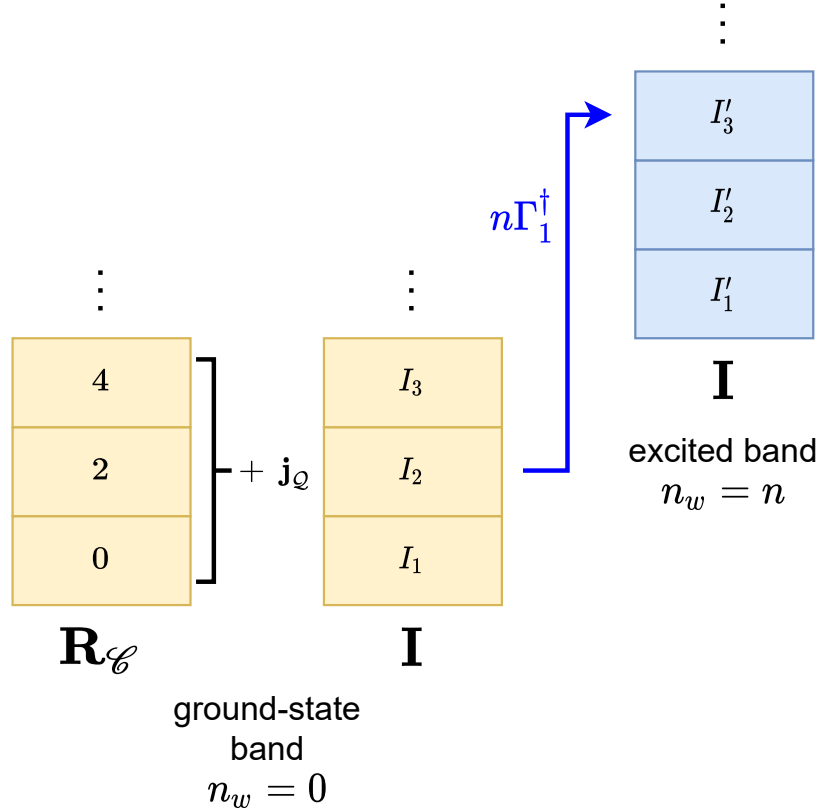


FIGURE 4.1: The mechanism of action for the phonon operator introduced in Ref. [39]. The operator is creating excited states with a given angular momentum from the ground state bands. The angular momentum of the core is defined as  $\mathbf{R}_C$ , while the quasi-particle a.m. is denoted by  $\mathbf{j}_Q$ . The ground-state band emerges from the coupling of these two, giving rise to a series of spins  $I_i = R_i + j$  (where  $R = \{\dots, R_i - 2, R_i, R_i + 2, \dots\}$ ). Acting with  $\Gamma_1^\dagger$   $n$ -times on any of these states, an excited level in the  $n_w = n$  wobbling band is obtained. In this example a rotational core having even spin states has been chosen, however the same principle applies if the spin states are odd.

- The four TSD bands are considered as zero-, one-, two-, and three-wobbling phonon bands for TSD1, TSD2, TSD3, and TSD4, respectively
- Each excited band is obtained by acting on the yrast - TSD1 - band with one-, two-, and three-phonons, respectively (e.g., a state  $I$  from TSD2 is obtained by acting with the wobbling-phonon operator on a state  $I - 1$  from TSD1 and so on), according to Fig. 4.1
- Wobbling structure for the group TSD1-3 emerged from a proton  $i_{13/2}$  ( $Q_p$ ) where all spin states have positive parity
- The band TSD4 has spin states with negative parity, and it is built on a proton from the  $h_{9/2}$  orbital (also a  $Q_p$ )

- In the expression of the rotor Hamiltonian, the rigid-like MOI were adopted (see Eq. (2.30)), which depend on  $\gamma$  and  $\mathcal{I}_0$ . Moreover, the model assumes the same set of MOI across all four bands
- Deformation parameters  $\beta_2$  and  $\gamma$  were a priori fixed (taken from literature)
- Analytical expressions for the energies were expressed in terms of total spin and wobbling phonon numbers
- Experimental data was reproduced through a fitting procedure, with the free parameters  $\mathcal{I}_0^{-1}$  (rotor part) and a *scaling factor*  $s = V \cdot \mathcal{I}_0$  (single-particle part).

Later on, the team also analyzed the wobbling properties of two more isotopes:  $^{165,167}\text{Lu}$  [100], and the model showed again that it was an useful tool in providing a realistic description of the wobbling motion in odd-mass nuclei. Hereafter, when referring to the procedure realized by Raduta and Poenaru in [39] and [100], the term  $\mathbf{W}_0$  will be used. Throughout the remaining chapters, comparison between the newly developed theory and  $\mathbf{W}_0$  will be made when necessary, in order to point out the key differences.

## 4.2 Re-interpretation of the Wobbling Motion

The  $\mathbf{W}_0$  formalism can be regarded as a cornerstone in the description of an odd- $A$  particle-triaxial-rotor system. In a follow-up work (2020) done by Raduta and Poenaru [101, 136], a new interpretation of the wobbling bands was made, relative not only to  $^{163}\text{Lu}$ , but to an entire set of wobblers. The way of obtaining yrast and excited states within the collective spectrum turned out to be a first within literature. The model starts with the typical QTR Hamiltonian:

$$\hat{H} = \hat{H}_{\text{rot}} + \hat{H}_{\text{sp}} , \quad (4.1)$$

where  $\hat{H}_{\text{sp}}$  represents the quasi-particle that moves inside the quadrupole mean-field as described in Eq. (A.15) from Appendix A and Eq. (2.63) (also recall Sections 2.3.2 - 2.3.3):

$$\hat{H}_{\text{sp}} = \epsilon_j + \frac{V}{j(j+1)} \left[ \cos \gamma \left( 3\hat{j}_3^3 - \mathbf{j}_{\mathcal{Q}}^2 \right) - \sqrt{3} \sin \gamma \left( \hat{j}_1^2 - \hat{j}_2^2 \right) \right] , \quad (4.2)$$

with  $\epsilon_j$  as the intrinsic energy of the particle from the corresponding  $j$ -shell (as it was discussed in Section 2.3.3). The total angular momentum of the core + odd-particle system is  $\mathbf{I} = \mathbf{R}_{\mathcal{C}} + \mathbf{j}_{\mathcal{Q}}$ . The components of the total angular momentum are  $\mathbf{I} = \{\hat{I}_1, \hat{I}_2, \hat{I}_3\}$  and the a.m. components for  $\mathcal{Q}$  are  $\mathbf{j}_{\mathcal{Q}} = \{\hat{j}_1, \hat{j}_2, \hat{j}_3\}$ . The labelling of the axes for the triaxial ellipsoid is  $k = (1, 2, 3)$ . Knowing this, one can express the rotor part as [136]:

$$\hat{H}_{\text{rot}} = \sum_{k=1}^3 A_k (\hat{I}_k - \hat{j}_k)^2 , \quad (4.3)$$

where the inertial factors  $A_k$  are expressed in terms of the three MOI:  $A_k = 1/(2\mathcal{I}_k)$ . Note that the Hamiltonian from Eq. (4.3) is just as the one expressed in Eq. (2.55), except that here the components of  $\mathbf{R}_{\mathcal{C}}$  are given in terms of  $\mathbf{I}$  and  $\mathbf{j}_{\mathcal{Q}}$ .

Obviously, the next task would be to obtain the eigenvalues of the Hamiltonian, thus finding the energies of the system. One can proceed with the diagonalization technique of  $\hat{H}$  using a set of states that manifest the invariance to rotations by  $\pi$  around a particular axis (the  $D_2$  symmetry [1]). However, it is more practical to describe the system only through a few variables that have a classical counterpart, where the system's dynamics will keep a classical analogy to that of a rotating body lacking axial symmetry. The approach that best fits this requirement is the Variational Principle (VP), to which one associates the Time-Dependent Variational Equation (TDVE). When applying the VP on an initial problem, it is necessary to have a variational state embedding all the relevant degrees of freedom for the underlying physics. Furthermore, the VP will induce a time dependence on the variables comprising the variational state itself [55]. For each variable (usually complex) parametrizing the state, the TDVE will yield its equation of motion, marking the ‘connection’ between the initial quantal variable (belonging to  $S_{\text{qt}}$ ) and the classical variable (belonging to  $S_{\text{cls}}$ ).

### 4.2.1 Variational Principle

The discussion regarding the VP and TDVE from the previous subsection can therefore be summarized in the following equation, which must be associated to

the quantal Hamiltonian defined in Eq. (4.1):

$$\delta \int_0^t \langle \Psi_{IM;j} | \hat{H} - i \frac{\partial}{\partial t'} | \Psi_{IM;j} \rangle dt' = 0 . \quad (4.4)$$

Obviously, the variational state  $|\Psi_{IM;j}\rangle$  (also known as the *trial function*) must be chosen in such a way that it comprises the entire space of the original quantal Hamiltonian. This can be achieved if the function is a *coherent state* [141], which due to its *completeness* property will span all the basis vector states from  $S_{\text{qt}}$ . Keep in mind that for  $S_{\text{qt}}$  the states belong to the Hilbert space of  $\hat{H}$ . For the present case, the trial function is defined as [39]:

$$\Psi_{\text{trial}} \equiv |\Psi_{IM;j}\rangle = \mathcal{N} e^{z\hat{I}_-} e^{s\hat{j}_-} |IMI\rangle |jj\rangle , \quad (4.5)$$

where the ladder operators for the total and single-particle a.m. are represented by  $\hat{I}_-$  and  $\hat{j}_-$ , respectively. The subscript separated by ‘;’ in  $IM;j$  adopted here indicates the two different momenta involved in the description of the odd-mass systems (namely  $\mathbf{I}$  and  $\mathbf{j}_{\mathcal{Q}}$ ). The factor  $\mathcal{N}$  is the normalization constant keeping the trial function normalized to unity. Its value is specified according to Refs. [135, 139] as:

$$\mathcal{N} = (1 + |z|^2)^{-I} (1 + |s|^2)^{-j} . \quad (4.6)$$

The states  $|IMK\rangle$  from  $\Psi_{\text{trial}}$  represent the Wigner-D functions (eigenstates of  $\hat{I}^2$  and  $\hat{I}_3$ ), while  $|j\Omega\rangle$  are wave-functions of the odd quasi-particle (eigenstates of  $\hat{j}^2$  and  $\hat{j}_3$ ). Notice that the trial function is explicitly given in terms of the *extremal states*, i.e., the two projections are maximal  $K = I$  and  $\Omega = j$ . The normalized states for the total angular momentum are expressed in terms of the Wigner-D functions [11]:

$$|IMK\rangle = \sqrt{\frac{2I+1}{8\pi^2}} \mathcal{D}_{MK}^I . \quad (4.7)$$

The vector states  $|j\Omega\rangle$  describe general wave-functions for a particle  $\chi$  having the structure [142]:

$$|\chi\rangle = \sum_{j\Omega} c_{j\Omega} |j\Omega\rangle , \quad (4.8)$$

where the coefficients  $c_{j\Omega}$  should be a priori known.

### 4.2.2 Classical Equations of Motion

Returning to the trial function  $|\Psi_{IM;j}\rangle$  from Eq. (4.5), its expression must be further discussed in terms of the variables  $z$  and  $s$ , which represent complex functions of time. They are associated to the motion of the core and the odd-particle, respectively [55]:

$$z = \rho e^{i\varphi}, \quad s = \sigma e^{i\psi}. \quad (4.9)$$

The averages of  $\hat{H}$  with the variational state  $|\Psi_{IM;j}\rangle$  is given as:

$$\langle \hat{H} \rangle = \langle \Psi_{IM;j} | \hat{H} | \Psi_{IM;j} \rangle, \quad (4.10)$$

and its analytical form was evaluated in Ref. [39] with respect to the  $z$  and  $s$ . However, here it would be more useful to change  $\rho$  and  $\sigma$  in the following way:

$$\begin{aligned} \rho &\rightarrow r = \frac{2I}{1 + \rho^2}, \quad 0 \leq r \leq 2I, \\ \sigma &\rightarrow f = \frac{2j}{1 + \sigma^2}, \quad 0 \leq f \leq 2j. \end{aligned} \quad (4.11)$$

These two new variables keep the same correspondence, meaning that  $r$  is related to the core, while  $f$  is related to the odd-particle. Moreover, by doing such a transformation, the TDVE (Eq. (4.4)) will provide the equations of motion in a *canonical form*. In fact, this is the reason behind the change of variable employed in Eq. (4.11). The set of equations of motion is [136]:

$$\begin{aligned} \frac{\partial \mathcal{H}}{\partial r} &= \dot{\varphi}, \quad \frac{\partial \mathcal{H}}{\partial \varphi} = -\dot{r}, \\ \frac{\partial \mathcal{H}}{\partial f} &= \dot{\psi}, \quad \frac{\partial \mathcal{H}}{\partial \psi} = -\dot{f}, \end{aligned} \quad (4.12)$$

where  $\mathcal{H}$  is just the average of  $\hat{H}$  with the trial function, as defined in Eq. (4.10). It now plays the role of *classical energy function* (CEF) and, moreover, it is a constant of motion. Remarking the fact that the *classical image* of the initial problem (i.e., the Hamiltonian of an odd- $A$  triaxial nucleus) is now properly reached through the canonical equations of motion (Eq. (4.12)). The explicit form of the equations

of motion attained by the VP are [136]:

$$\begin{aligned}\dot{\varphi} &= \frac{2I-1}{I}(I-r)(A_1 \cos^2 \varphi + A_2 \sin^2 \varphi - A_3) - \\ &\quad - 2\sqrt{\frac{f(2j-f)}{r(2I-r)}}(I-r)(A_1 \cos \varphi \cos \psi + A_2 \sin \varphi \sin \psi) + 2A_3(j-f), \\ \dot{\psi} &= \frac{2j-1}{j}(j-f)(A_1 \cos^2 \psi + A_2 \sin^2 \psi - A_3) - \\ &\quad - 2\sqrt{\frac{r(2I-r)}{f(2j-f)}}(j-f)(A_1 \cos \varphi \cos \psi + A_2 \sin \varphi \sin \psi) + 2A_3(I-r) - \\ &\quad - V \frac{2j-1}{j^2(j+1)}(j-f)\sqrt{3}(\sqrt{3} \cos \gamma + \sin \gamma \cos 2\psi),\end{aligned}\tag{4.13}$$

for the *canonical coordinates*  $(\varphi, \psi)$ , and [136]:

$$\begin{aligned}-\dot{r} &= \frac{2I-1}{2I}r(2I-r)(A_2 - A_1) \sin 2\varphi + \\ &\quad + 2\sqrt{rf(2I-r)(2j-f)}(A_1 \sin \varphi \cos \psi - A_2 \cos \varphi \sin \psi), \\ -\dot{f} &= \frac{2j-1}{2j}f(2j-f)(A_2 - A_1) \sin 2\psi + \\ &\quad + 2\sqrt{rf(2I-r)(2j-f)}(A_1 \cos \varphi \sin \psi - A_2 \sin \varphi \cos \psi) + \\ &\quad + V \frac{2j-1}{j^2(j+1)}f(2j-f)\sqrt{3} \sin \gamma \sin 2\psi,\end{aligned}\tag{4.14}$$

for the *canonical momenta*  $(r, f)$ , respectively. It results that *classical coordinates* encompassed in  $S_{\text{cls}}$  are the generalized momentum and generalized coordinates, which are represented by  $(r, f)$  and  $(\varphi, \psi)$ . Keep in mind that the two sets of equations of motion and canonical variables correspond to the core and the single-particle. Thus, the dequantization procedure was described, obtaining the classical dynamics of the system.

### 4.2.3 Classical Energy Function (CEF)

Regarding the structure of the CEF, its expression in terms of the canonical variables is given as:

$$\begin{aligned}\mathcal{H} \equiv \langle \Psi_{IM;j} | \hat{H} | \psi_{IM;j} \rangle &= \\ &= \frac{I}{2}(A_1 + A_2) + A_3 I^2 + \frac{2I - 1}{2I} r(2I - r) \mathcal{A}_\varphi + \frac{j}{2}(A_1 + A_2) + A_3 j^2 + \\ &\quad + \frac{2j - 1}{2j} f(2j - f) \mathcal{A}_\psi - 2\sqrt{rf(2I - r)(2j - f)} \mathcal{A}_{\varphi\psi} + \\ &\quad + A_3 [r(2j - f) + f(2I - r)] - 2A_3 I j + V \frac{2j - 1}{j + 1} \mathcal{A}_\gamma.\end{aligned}\quad (4.15)$$

Since the expression is quite lengthy, some *canonical factors* were introduced in Eq. (4.15), namely  $\mathcal{A}_\varphi$ ,  $\mathcal{A}_\psi$ ,  $\mathcal{A}_{\varphi\psi}$ , and  $\mathcal{A}_\gamma$ . They depend on the canonical coordinates as follows:

$$\begin{aligned}\mathcal{A}_\varphi &= A_1 \cos^2 \varphi + A_2 \sin^2 \varphi - A_3, \\ \mathcal{A}_\psi &= A_1 \cos^2 \psi + A_2 \sin^2 \psi - A_3, \\ \mathcal{A}_{\varphi\psi} &= A_1 \cos \varphi \cos \psi + A_2 \sin \varphi \sin \psi, \\ \mathcal{A}_\gamma &= \cos \gamma - \frac{f(2j - f)}{2j^2} \sqrt{3} (\sqrt{3} \cos \gamma + \sin \gamma \cos 2\psi).\end{aligned}\quad (4.16)$$

#### 4.2.3.1 Canonical Factors - Qualitative Analysis

It is worth analyzing the behavior of the canonical factors defined in Eq. (4.16), since their evolution with respect to the generalized coordinates and MOI ordering will provide a better understanding regarding the behavior of the CEF. Firstly, the factor  $\mathcal{A}_\varphi$  is graphically represented in Fig. 4.2 for different orderings of  $A_k$ . Because  $\mathcal{A}_\varphi$  and  $\mathcal{A}_\psi$  have similar expressions (only the coordinate is changed), the plots are equivalent.

For the mixed term  $\mathcal{A}_{\varphi\psi}$  from Eq. (4.16) it is more suitable to create a contour plot, as it depends on both canonical coordinates  $(\varphi, \psi)$ . As such, representations with different MOI orderings have been depicted in Fig. 4.3, by letting the coordinates vary inside the interval  $[0, \pi]$ .

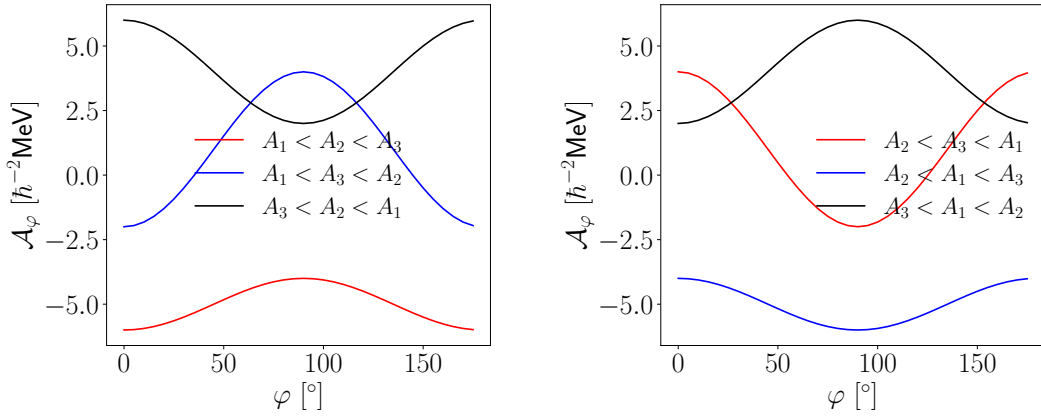


FIGURE 4.2: The evolution of  $A_\varphi$  with respect to the generalized coordinate  $\varphi$ , at different MOI orderings. The values 1, 3, 7 were chosen and they are interchanged between the three inertia factors. This figure is equivalent for  $A_\psi$ .

Lastly, the factor  $A_\gamma$  must also be represented as a contour plot, because it depends on the canonical coordinates of the single-particle, namely the set  $(f, \psi)$ . Its graphical representation for a few values of  $\gamma$  shown in Fig. 4.4.

From the representations shown in Figs. 4.2 - 4.4, one can interpret the results as possible conditions for the stability of an odd- $A$  system in regards to the wobbling regime. More precisely, smaller values of  $A$  will correspond to a lower total energy. Keep in mind that all these canonical factors take part in the structure of the CEF, meaning that lower energies could imply a greater degree of stability to some extent.

#### 4.2.3.2 Critical Region

Given the general expression of the CEF from Eqs. (4.15) - (4.16), one can group the terms in a part that is independent on the coordinates, a part that depends only on the core's coordinates  $(r, \varphi)$ , a third part that depends on the single-particle's coordinates  $(f, \psi)$ , and finally a *mixed* term, which contains both sets of classical coordinates. As a result,  $\mathcal{H}$  can be summarized (coloring is just to emphasize the grouping of the terms):

$$\mathcal{H}(r, \varphi; f, \psi) = \mathcal{H}_{\text{free}} + \mathcal{H}_c(r, \varphi) + \mathcal{H}_Q(f, \psi) + \mathcal{H}_{\text{mixed}}(r, \varphi; f, \psi) . \quad (4.17)$$

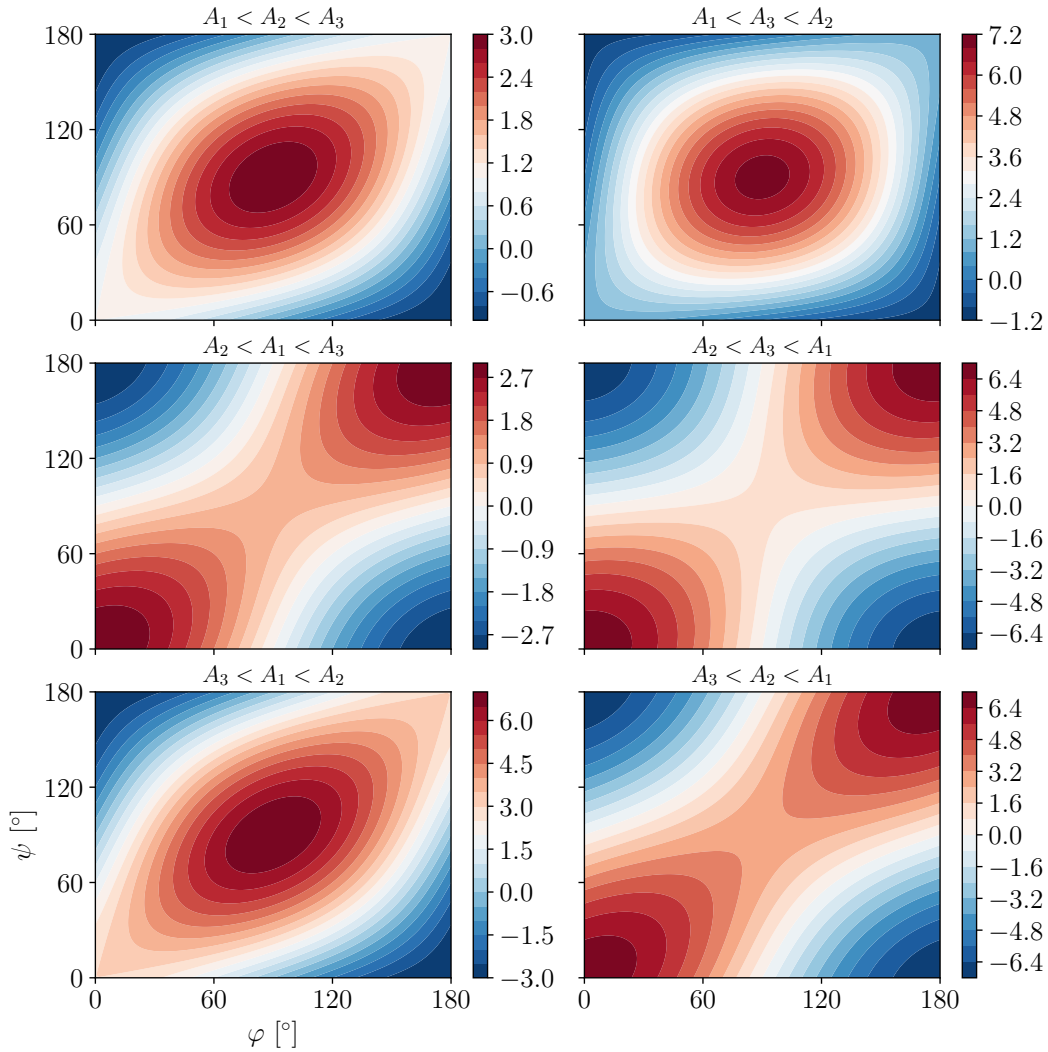


FIGURE 4.3: The mixed canonical factor  $\mathcal{A}_{\varphi\psi}$  from Eq. (4.16), as function of the coordinates  $\varphi$  and  $\psi$ . Both coordinates vary within the interval  $[0, \pi]$ . All insets share common labelling for the OX and OY axes.

From the critical conditions associated to the classical energy function, namely:

$$\begin{aligned} \left( \frac{\partial \mathcal{H}}{\partial r} \right) &= 0 , \quad \left( \frac{\partial \mathcal{H}}{\partial \varphi} \right) = 0 , \\ \left( \frac{\partial \mathcal{H}}{\partial f} \right) &= 0 , \quad \left( \frac{\partial \mathcal{H}}{\partial \psi} \right) = 0 , \end{aligned}$$

it is possible to obtain the points at which  $\mathcal{H}$  is *minimal* (provided by the sign of its corresponding Hessian). In order to meet such a criteria for  $\mathcal{H}$ , one needs to set an ordering of the three inertia factors. Choosing the largest MOI to be around the 3-axis and  $\mathcal{I}_3 > \mathcal{I}_2 > \mathcal{I}_1$  (or, equivalently  $A_1 < A_2 < A_3$ ), the function



FIGURE 4.4: The canonical factor  $\mathcal{A}_\gamma$  from Eq. (4.16), as a function of the coordinates  $(f, \psi)$  corresponding to the single-particle  $\mathcal{Q}$ . The  $j$ -shell has been fixed to  $j = 13/2$ . In terms of the two variables,  $f$  varies within  $[0, 2j]$  while  $\psi$  is inside the interval  $[0, \pi]$ . All insets share a common labelling for the OX and OY axes.

achieves a minimum value at:

$$p_0 = (I, 0; j, 0) . \quad (4.18)$$

#### 4.2.4 Wobbling Frequencies

By performing a linearization procedure on the classical equations of motion (from Eq. (4.12) or explicitly in Eqs. (4.13) - (4.14)) around the minimum point of  $\mathcal{H}$  (i.e., point  $p_0$ ), an algebraic equation of fourth degree will show up, with a new variable which will be denoted with  $\Omega$ . Reasoning behind this labelling will become

clear later on. For now, the equation for  $\Omega$  is given generally as [101]:

$$\Omega^4 + B\Omega^2 + C = 0 , \quad (4.19)$$

where the coefficient  $B$  is [136]:

$$B = - \left\{ [(2I-1)(A_3 - A_1) + 2jA_1][(2I-1)(A_2 - A_1) + 2jA_1] + 8A_2A_3Ij + \right. \\ \left. + \left[ (2j-1)(A_3 - A_1) + 2IA_1 + V \frac{2j-1}{j(j+1)} \sqrt{3} (\sqrt{3} \cos \gamma + \sin \gamma) \right] \times \right. \\ \left. \times \left[ (2j-1)(A_2 - A_1) + 2IA_1 + V \frac{2j-1}{j(j+1)} 2\sqrt{3} \sin \gamma \right] \right\} , \quad (4.20)$$

and the coefficient  $C$  is [136]:

$$C = \left\{ [(2I-1)(A_3 - A_1) + 2jA_1] \left[ (2j-1)(A_3 - A_1) + 2IA_1 + \right. \right. \\ \left. \left. + V \frac{2j-1}{j(j+1)} \sqrt{3} (\sqrt{3} \cos \gamma + \sin \gamma) \right] - 4IjA_3^2 \right\} \left\{ [(2I-1)(A_2 - A_1) + 2jA_1] \times \right. \\ \left. \times \left[ (2j-1)(A_2 - A_1) + 2IA_1 + V \frac{2j-1}{j(j+1)} 2\sqrt{3} \sin \gamma \right] - 4IjA_2^2 \right\} . \quad (4.21)$$

In a work done by Raduta et al [39], a similar equation as the one from Eq. (4.19) was obtained via a Random Phase Approximation (RPA) method applied to another (quantized) energy function. It is of crucial importance to extract from Eq. (4.19) only those solutions that are real and positive, meaning that one has to study the stability conditions for the equation. Obviously, the general solutions are:

$$\Omega_1 \rightarrow \left( \frac{-B - \sqrt{B^2 - 4C}}{2} \right)^{1/2}, \quad \Omega_2 \rightarrow \left( \frac{-B + \sqrt{B^2 - 4C}}{2} \right)^{1/2}, \\ \Omega_3 \rightarrow - \left( \frac{-B - \sqrt{B^2 - 4C}}{2} \right)^{1/2}, \quad \Omega_4 \rightarrow - \left( \frac{-B + \sqrt{B^2 - 4C}}{2} \right)^{1/2}. \quad (4.22)$$

Because of the positivity condition, only  $\Omega_1$  and  $\Omega_2$  will be taken into consideration. The conditions where Eq. (4.19) has vanishing solutions will be now analyzed in terms of  $B$  and  $C$ .

*Case i)  $B > 0$  and  $C = 0$*

The situation  $C = 0$  imposes that the terms (or at least one) inside the curly

brackets from Eq. (4.21) will equate to zero. In order to simplify the calculations, some notations should be introduced. Firstly, from the definition of  $A_k = 1/(2\mathcal{I}_k)$ , one can exploit that the MOI (both in rigid and irrotational representation) are typically expressed in terms of  $\beta_2$ ,  $\gamma$ , and a common factor (recall Eq. (2.30)):

$$\mathcal{I}_k = \mathcal{I}_0 \cdot h(\beta_2, \gamma; k) , \quad (4.23)$$

where  $h$  is a trigonometric function defining moments of inertia either in the rigid or the irrotational picture. Going back to the inertia factors, it results that:

$$A_k = \frac{1}{2\mathcal{I}_k} = \frac{1}{\mathcal{I}_0} \cdot h'(\beta_2, \gamma; k) \equiv \frac{1}{\mathcal{I}_0} \bar{A}_k . \quad (4.24)$$

Using Eq. (4.24) it is possible to rewrite each sub-term from  $B$  and  $C$  with the following notations:

$$\begin{aligned} P_{31} &= (2I - 1)(\bar{A}_3 - \bar{A}_1) + 2j\bar{A}_1 , \quad P_{21} = (2I - 1)(\bar{A}_2 - \bar{A}_1) + 2j\bar{A}_1 , \\ Q_{31} &= (2j - 1)(\bar{A}_3 - \bar{A}_1) + 2I\bar{A}_1 , \quad Q_{21} = (2j - 1)(\bar{A}_2 - \bar{A}_1) + 2I\bar{A}_1 , \\ G_1 &= \frac{2j - 1}{j(j + 1)} \sqrt{3} (\sqrt{3} \cos \gamma + \sin \gamma) , \quad G_2 = \frac{2j - 1}{j(j + 1)} 2\sqrt{3} \sin \gamma . \end{aligned} \quad (4.25)$$

This transformation is very useful because the constant  $1/\mathcal{I}_0$  can be factored out from both  $B$  and  $C$ , leaving only one ‘independent variable’ within the equations, i.e.,  $S = \mathcal{I}_0 V$ , which will be considered a *scaling factor*. Getting back to  $C = 0$ , after some rearrangement one gets:

$$\begin{aligned} P_{31}G_1S + P_{31}Q_{31} - 4Ij\bar{A}_3^2 &= 0 , \\ P_{21}G_2S + P_{21}Q_{21} - 4Ij\bar{A}_2^2 &= 0 . \end{aligned} \quad (4.26)$$

Indeed, the above formulas represent a set of linear equations in the newly introduced variable  $S$ , which are of the form  $aS + b = 0$ . As a physical interpretation for  $S$ , it is remarkable the fact that it comprises a rotational part of the odd-mass system (through  $\mathcal{I}_0$ ) and also single-particle contribution (through the potential strength  $V$ ), embedding both the collective rotation and deformation effects. By a straightforward manipulation of Eq. (4.26), the two solutions that provide vanishing a  $C$  term are:

$$S_{01} = \frac{4Ij\bar{A}_3^2 - P_{31}Q_{31}}{P_{31}G_1} \text{ and } S_{02} = \frac{4Ij\bar{A}_2^2 - P_{21}Q_{21}}{P_{21}G_2} . \quad (4.27)$$

*Case ii)  $B = 0$  and  $C = \text{arbitrary}$*

When  $B$  must vanish, a second-degree algebraic equation for the variable  $S$  will appear. Using the same notations that were introduced in the case *i)* for the sub-terms involved in  $C$ , it results the following:

$$P_{31}P_{21} + 8Ij\bar{A}_2\bar{A}_3 + (Q_{31} + SG_1)(Q_{21} + SG_2) = 0 ,$$

or, after some manipulation:

$$G_1G_2S^2 + (Q_{21}G_1 + Q_{31}G_2)S + P_{31}P_{21} + 8Ij\bar{A}_2\bar{A}_3 = 0 . \quad (4.28)$$

The solutions of this second-degree equation are:

$$\begin{aligned} S_{11} &= -\frac{\sqrt{(G_1Q_{21} + G_2Q_{31})^2 - 4G_1G_2(8Ij\bar{A}_2\bar{A}_3 + P_{21}P_{31})} + G_1Q_{21} + G_2Q_{31}}{2G_1G_2} , \\ S_{12} &= \frac{\sqrt{(G_1Q_{21} + G_2Q_{31})^2 - 4G_1G_2(8Ij\bar{A}_2\bar{A}_3 + P_{21}P_{31})} - G_1Q_{21} - G_2Q_{31}}{2G_1G_2} . \end{aligned} \quad (4.29)$$

Gathering the outcomes of Eqs. (4.27) and (4.29), four solutions for the variable  $S$  are obtained, i.e.,  $S = \{S_{01}, S_{02}, S_{11}, S_{12}\}$ . Returning to the case *i)* that provides a vanishing  $C$  term, it would be instructive to see for what values of  $\mathcal{I}_0$  and  $V$  the left-hand sides from Eq. (4.26) equate to zero. Denoting the first left-hand side with  $f_1 = f_1(\mathcal{I}_0, V)$  and the second one with  $f_2 = f_2(\mathcal{I}_0, V)$ , a contour plot in the  $(\mathcal{I}_0, V)$  space can be developed, where any contour line would depict a region at which  $f_1$  and  $f_2$  are null. This is graphically represented in the left inset of Fig. 4.5, revealing that for  $\mathcal{I}_0 \in [0, 60]$ , the value of  $V$  does not change. Also noteworthy are the contours that only consist of straight lines. In order to distinguish the positive/negative regions of  $f_1$  and  $f_2$ , a 50:50 ratio of red-blue colors has been chosen relative to the width of the plot. Nevertheless, both terms cover the entire range of values provided for  $V$  and  $\mathcal{I}_0$ .

Furthermore, the left-hand side of Eq. (4.28) from case *ii)* can also be zero for certain intervals of  $\mathcal{I}_0$  and  $V$ . A restriction on  $V$  to only have positive values is adopted throughout the formalism (to be consistent with the literature [137, 143, 144]). This forces only a single contour (denoted with  $F = 0$ ) to appear above the



FIGURE 4.5: **Left:** Contour lines showing the values of  $\mathcal{I}_0$  and  $V$  at which both lhs from Eq. (4.26) vanish (denoted here by  $f_1$  and  $f_2$ , respectively). **Right:** The contour  $F = 0$  (lhs of Eq. (4.28)) as function of the parameters  $\mathcal{I}_0$  and  $V$ . **Both:** Darker (lighter) color corresponds to negative (positive) values. The calculations were done for fixed values of  $I, j, \gamma, A_1, A_2, A_3$ . Units are  $\hbar^2 \text{MeV}^{-1}$  for  $\mathcal{I}_0$  and  $\text{MeV}$  for  $V$ .

TABLE 4.1: The positivity conditions for the two solutions  $\Omega_{1,2}$  given in Eq. (4.22). The trivial solution  $B = C = 0$  has been dismissed.

Solution	Positive square root
$\Omega_1$	$B < 0$ and $0 \leq C \leq B^2/4$
$\Omega_2$	$(B \leq 0 \text{ and } C \leq B^2/4) \text{ or } (B < 0 \text{ and } C \leq 0)$

OX axis. A representation showing this line is done in the right inset of Fig. 4.5, where  $V \in [0, 5]$ .

Taking a look at the regions portrayed in Fig. 4.5, one can assume that they represent a clear indicator concerning the stability of Eq. (4.19). Obviously, when the values of  $(\mathcal{I}_0, V)$  lie near the contours lines, then the equation reaches instability and no real solutions emerge.

Regarding the solutions given in Eq. (4.22), the selected ones are  $\Omega_1$  and  $\Omega_2$ . Considering their structure, it is important to retrieve all the conditions that grant positive square roots. These conditions are sketched in Table 4.1.

Going back to the CEF shown in Eq. (4.17), the free term  $\mathcal{H}_{\text{free}}$  is the one that does not depend on any canonical variable. The other three terms (depicted by red color) have a dependence on either the core  $(r, \varphi)$  or particle  $(f, \psi)$  coordinates. However, the remarkable feature is that all these terms are comprised in the two

solutions  $\Omega_1$  and  $\Omega_2$ . In fact, one expects such a thing because  $\Omega_1$  and  $\Omega_2$  emerge from the linearization of the equations of motion around the minimum point  $p_0 = (r_0 = I, \varphi_0 = 0 ; f_0 = j, \psi_0 = 0)$ . As it was shown in **W<sub>0</sub>** and also Refs. [135, 136], the solutions  $\Omega_{1,2}$  give the ‘final’ terms in the total energy spectrum for an odd-mass system. More precisely, the CEF from 4.17 combined with the two real and positive solutions of Eq. (4.19) will result in the spectrum [103]:

$$E_{I,n_1,n_2} = \epsilon_j + \mathcal{H}_{\min}^I + \mathcal{F}_{n_{w_1}n_{w_2}}^I , \quad (4.30)$$

where the free term given in Eq. (4.17) becomes the *minimal energy*  $\mathcal{H}_{\min}^I$  and the *phonon* term  $\mathcal{F}_{n_{w_1}n_{w_2}}^I$  is the sum of the two solutions  $\Omega_{1,2}$  [103]:

$$\mathcal{F}_{n_{w_1}n_{w_2}}^I = \hbar\Omega_1^I \left( n_{w_1} + \frac{1}{2} \right) + \hbar\Omega_2^I \left( n_{w_2} + \frac{1}{2} \right) . \quad (4.31)$$

The term from Eq. (4.31) can be regarded as originating from  $\mathcal{H}_{\mathcal{C}} + \mathcal{H}_{\mathcal{Q}} + \mathcal{H}_{\text{mixed}}$ . This was obtained from the linearization procedure mentioned at the start of the section. The energy of the odd-particle belonging to a particular  $j$ -shell (as per  $\hat{H}_{\text{sp}}$  from Eq. (4.2)) is represented by  $\epsilon_j$  and it is adopted as a constant. The coloring from Eq. (4.30) is consistent with the one from Eq. (4.17) such that the analogy between each component can be clearly viewed. Putting together Eq. (4.30) and Eq. (4.31), the general spectrum of an odd-mass triaxial nucleus will be:

$$E_{I,n_1,n_2} = \epsilon_j + \mathcal{H}_{\min}^I + \hbar\Omega_1^I \left( n_{w_1} + \frac{1}{2} \right) + \hbar\Omega_2^I \left( n_{w_2} + \frac{1}{2} \right) . \quad (4.32)$$

The conditions of existence and positivity for  $\Omega_{1,2}$  were summarized in Table 4.1. The physical interpretation of  $\Omega_1$  and  $\Omega_2$  from Eq. (4.32) is a remarkable feature of this formalism. Indeed, here  $\Omega$  represents a wobbling frequency in the same sense as for the simple wobbler (recall Eq. (3.14)) and the odd- $A$  case discussed in Section 3.2 from Chapter 3. The advantage of using the TDVE approach is that the Hamiltonian is separated and two distinct wobbling frequencies emerge: one for the core and one for the odd particle. This semi-classical approach is very useful for visualizing the two interacting systems, which can be seen directly from the analytical expression of the spectrum (that is Eq. (4.32)). Concerning the two numbers from Eq. (4.32), i.e.,  $n_{w_1} = 0, 1, \dots$  and  $n_{w_2} = 0, 1, \dots$ , they are the

wobbling phonon numbers, which are also separated in terms of the core and the single-particle.

#### 4.2.5 An Alternative Approach

In this section, a different description for the phonon term  $\mathcal{F}_{n_{w_1}n_{w_2}}^I$  from Eq. (4.31) will be made. This method provides similar results for  $\Omega_1$  and  $\Omega_2$ , but it will help to better understand the definition of the wave-functions of the triaxial bands. Starting again with the CEF from Eq. (4.17) and expanding it around  $p_0$  up to second order, the obtained equation will be [136]:

$$\begin{aligned} \mathcal{H} = & \mathcal{H}_{\min}^I + \\ & + \left\{ \frac{1}{2I} [(2I-1)(A_3 - A_1) + 2jA_1] r'^2 + \frac{I}{2} [(2I-1)(A_2 - A_1) + 2jA_1] \varphi'^2 + \right. \\ & + \frac{1}{2j} \left[ (2j-1)(A_3 - A_1) + 2IA_1 + V \frac{2j-1}{j(j+1)} \sqrt{3} (\sqrt{3} \cos \gamma + \sin \gamma) \right] f'^2 + \\ & + \frac{j}{2} \left[ (2j-1)(A_2 - A_1) + 2IA_1 + V \frac{2j-1}{j(j+1)} 2\sqrt{3} \sin \gamma \right] \psi'^2 - \\ & \left. - 2A_3 r' f' - 2Ij A_2 \varphi' \psi' \right\}. \end{aligned} \quad (4.33)$$

where the primed coordinates  $r', \varphi', f', \psi'$  are the deviations from the minimum point  $p_0 = (r_0, \varphi_0; f_0, \psi_0)$ , which are expressed as:

$$\begin{aligned} r' &= (r - r_0), \quad \varphi' = (\varphi - \varphi_0), \\ f' &= (f - f_0), \quad \psi' = (\psi - \psi_0). \end{aligned} \quad (4.34)$$

Note that the curly braces from Eq. (4.33) are used to emphasize the three terms  $\mathcal{H}_C(r, \varphi) + \mathcal{H}_Q(f, \psi) + \mathcal{H}_{\text{mixed}}(r, \varphi; f, \psi)$ , so that one can clearly see the terms with both separated and mixed canonical variables. Again, one illustrates the grouped factors as per Eq. (4.17) through a similar coloring. It is clear from this expression that  $\mathcal{H}_{\min}^I$  is the free term  $\mathcal{H}_{\text{free}}$ .

*i) Non-coupling terms* Ignoring the coupling terms from Eq. (4.33), the CEF will consist in the sum of two independent harmonic oscillators with the

frequencies:

$$\begin{aligned}\omega_1 &= \{(2I-1)(A_3 - A_1) + 2jA_1\}[(2I-1)(A_2 - A_1) + 2jA_1]\}^{1/2}, \\ \omega_2 &= \left[ (2j-1)(A_3 - A_1) + 2IA_1 + V \frac{2j-1}{j(j+1)} \sqrt{3} (\sqrt{3} \cos \gamma + \sin \gamma) \right]^{1/2} \\ &\cdot \left[ (2j-1)(A_2 - A_1) + 2IA_1 + V \frac{2j-1}{j(j+1)} 2\sqrt{3} \sin \gamma \right]^{1/2}. \quad (4.35)\end{aligned}$$

In order to obtain real solutions for  $\omega_1$ , the following conditions for the three inertia factors must hold:

$$\begin{aligned}A_3 > SA_1 \text{ and } A_2 > SA_1, \\ \text{while: } A_3 > A_2 \text{ or } A_3 < A_2, \quad (4.36)\end{aligned}$$

while for the second frequency, the following restrictions must hold:

$$A_3 > S'A_1 - VT \text{ and } A_2 > S'A_1 - VT'.$$

The terms  $S$ ,  $S'$ ,  $T$ , and  $T'$  are defined as:

$$\begin{aligned}S &= \frac{2I-1-2j}{2I-1}, \quad S' = \frac{2j-2I-1}{2j-1}, \\ T &= \frac{1}{j(j+1)} \sqrt{3} (\sqrt{3} \cos \gamma + \sin \gamma), \quad T' = \frac{1}{j(j+1)} 2\sqrt{3} \sin \gamma. \quad (4.37)\end{aligned}$$

Ensuring positivity for  $V$  guarantees that the prescribed conditions for  $\omega_2$  are consistently met.

*ii) Coupling terms* For treating the terms from the expansion given in Eq. (4.33) that contain products of the type  $r' \cdot f'$  and  $\varphi' \cdot \psi'$ , a *quantization* should be employed on the canonical variables. Indeed, from the classical coordinates (obtained via the TDVE) of the phase space  $S_{\text{cls}}$ , one can also go back to a quantum  $S_{\text{qt}}$  space, where each coordinate will have a corresponding (quantal) operator defined in that space. Such a change was properly implemented in [136], resulting in the following transformations:

$$\begin{aligned}\varphi &\rightarrow \hat{q}_1, \quad r \rightarrow \hat{p}_1, \quad [\hat{q}_1, \hat{p}_1] = i, \\ \psi &\rightarrow \hat{q}_2, \quad f \rightarrow \hat{p}_2, \quad [\hat{q}_2, \hat{p}_2] = i. \quad (4.38)\end{aligned}$$

The notation of the operators is consistent with the fact that  $(\varphi, \psi)$  represent the canonical coordinates and  $(r, f)$  depict the canonical momenta. Furthermore, each set has a corresponding creation and annihilation operator defined as:

$$a^\dagger = \frac{1}{\sqrt{2}k_1} (k_1^2 \hat{q}_1 + i\hat{p}_1) , \quad a = \frac{1}{\sqrt{2}k_1} (k_1^2 \hat{q}_1 - i\hat{p}_1) , \quad (4.39)$$

for the variables  $(r, \varphi)$  of the core and:

$$b^\dagger = \frac{1}{\sqrt{2}k_2} (k_2^2 \hat{q}_2 + i\hat{p}_2) , \quad b = \frac{1}{\sqrt{2}k_2} (k_2^2 \hat{q}_2 - i\hat{p}_2) , \quad (4.40)$$

for the single-particle variables  $(f, \psi)$ . Using the terms defined in Eqs. (4.39) - (4.40), the operators  $(\hat{q}_1, \hat{p}_1)$  and  $(\hat{q}_2, \hat{p}_2)$  will acquire the following form:

$$\begin{aligned} \hat{q}_1 &= \frac{1}{\sqrt{2}k_1} (a^\dagger + a) , \quad \hat{p}_1 = \frac{i k_1}{\sqrt{2}} (a^\dagger - a) , \\ \hat{q}_2 &= \frac{1}{\sqrt{2}k_2} (b^\dagger + b) , \quad \hat{p}_2 = \frac{i k_2}{\sqrt{2}} (b^\dagger - b) . \end{aligned} \quad (4.41)$$

The transformations that go from  $(\hat{q}_1, \hat{p}_1)$  and  $(\hat{q}_2, \hat{p}_2)$  to  $(a^\dagger, a)$  and  $(b^\dagger, b)$  are *canonical*. The two constant factors  $k_1$  and  $k_2$  that appear in Eqs. (4.39) - (4.41) are called *canonicity factors* [39], and they are fixed such that ‘dangerous’ terms like  $(a^\dagger)^2 + a^2$  and  $(b^\dagger)^2 + b^2$  do not appear in the two frequencies. One should not confuse them with the canonical factors  $\mathcal{A}$ , which were defined in Eq. (4.16) as a way of expressing the CEF. The expressions for  $k_1$  and  $k_2$  are [136]:

$$\begin{aligned} k_1 &= \left[ \frac{(2I-1)(A_2 - A_1) + 2jA_1}{(2I-1)(A_3 - A_1) + 2jA_1} \cdot I^2 \right]^{1/4} \\ k_2 &= \left[ \frac{(2j-1)(A_2 - A_1) + 2IA_1 + V \frac{2j-1}{j(j+1)} 2\sqrt{3} \sin \gamma}{(2j-1)(A_3 - A_1) + 2IA_1 + V \frac{2j-1}{j(j+1)} \sqrt{3} (\sqrt{3} \cos \gamma + \sin \gamma)} \cdot j^2 \right]^{1/4} . \end{aligned} \quad (4.42)$$

It can be seen that the canonicity factors from Eq. (4.42) exhibit a behavior  $f(x) \propto x^{1/2}$  with respect to the total and single-particle angular momentum, respectively. Moreover, the triaxiality parameter and the single-particle potential strength only affect  $k_2$ . In a similar fashion as for the calculations done in Eqs.

(4.26) and (4.28), one can introduce a set of additional notations:

$$\begin{aligned}\Delta_{31} &= (2I - 1)(A_3 - A_1) + 2jA_1 , \quad \Delta_{21} = (2I - 1)(A_2 - A_1) + 2jA_1 , \\ \Sigma_{31} &= (2j - 1)(A_3 - A_1) + 2IA_1 , \quad \Sigma_{21} = (2j - 1)(A_2 - A_1) + 2IA_1 ,\end{aligned}\quad (4.43)$$

where the factors  $G_1$  and  $G_2$  from Eq. (4.25) will be kept the same. Compared to the calculations from Eqs. (4.26) - (4.28), no prior factorization for the inertia factors is made here. With the notations given in Eq. (4.43), the two oscillator frequencies and the canonicity factors achieve a more practical shape, namely:

$$\begin{aligned}\omega_1 &= (\Delta_{31} \cdot \Delta_{21})^{1/2} , \\ \omega_2 &= (\Sigma_{31} + VG_1)^{1/2} \cdot (\Sigma_{21} + VG_2)^{1/2} ,\end{aligned}\quad (4.44)$$

for the wobbling frequencies, and:

$$\begin{aligned}k_1 &= \left( \frac{\Delta_{21}}{\Delta_{31}} \cdot I^2 \right)^{1/4} \\ k_2 &= \left[ \frac{\Sigma_{21} + VG_2}{\Sigma_{31} + VG_1} \cdot j^2 \right]^{1/4} ,\end{aligned}\quad (4.45)$$

for the two canonicity factors. Notice the single-particle strength appearing explicitly for  $\omega_2$  and also  $k_2$ .

From the quantization made in Eq. (4.38), the operators  $(a^\dagger, a; b^\dagger, b)$  defined in Eqs. (4.39) - (4.40), and the factors defined in Eq. (4.42), this *new quantal representation* of the classical energy  $\{S_{\text{cls}} \supset \mathcal{H}\} \rightarrow \{\hat{H} \subset S_{\text{qt}}\}$  will achieve the following form:

$$\begin{aligned}\hat{H} = \mathcal{H}_{\min}^I + \left\{ \omega_1 \left( a^\dagger a + \frac{1}{2} \right) + \omega_2 \left( b^\dagger b + \frac{1}{2} \right) + A_3 k_1 k_2 (a^\dagger b^\dagger + ba - a^\dagger b - b^\dagger a) - \right. \\ \left. - IjA_2 \frac{1}{k_1 k_2} (a^\dagger b^\dagger + ba + a^\dagger b + b^\dagger a) \right\} .\end{aligned}\quad (4.46)$$

Since  $\mathcal{H}_{\min}^I$  does not depend on the canonical variables, its structure will stay unchanged. The next two terms are the harmonic oscillators with the two frequencies of oscillation  $\omega_1$  and  $\omega_2$ , while the last two contain mixed products of creation/annihilation operators from both the core and single-particle degrees of freedom. Indeed, this structure can be regarded in a similar way as the grouped terms from Eq. (4.17) or Eq. (4.33), depicted here by the blue and red colors. The Hamiltonian defined in Eq. (4.46) will have the following commutation rules

with the creation and annihilation operators:

$$\begin{aligned} [\hat{H}, a^\dagger] &= \omega_1 a^\dagger + A_3 k_1 k_2 (b - b^\dagger) - Ij A_2 \frac{1}{k_1 k_2} (b + b^\dagger) , \\ [\hat{H}, a] &= -\omega_1 a - A_3 k_1 k_2 (b^\dagger - b) + Ij A_2 \frac{1}{k_1 k_2} (b^\dagger + b) , \\ [\hat{H}, b^\dagger] &= \omega_2 b^\dagger + A_3 k_1 k_2 (a - a^\dagger) - Ij A_2 \frac{1}{k_1 k_2} (a + a^\dagger) , \\ [\hat{H}, b] &= -\omega_2 b - A_3 k_1 k_2 (a^\dagger - a) + Ij A_2 \frac{1}{k_1 k_2} (a^\dagger + a) . \end{aligned} \quad (4.47)$$

One can see that Eq. (4.47) forms a linear system, which can be solved with the introduction of a special *phonon operator* [39, 100]:

$$\Gamma^\dagger = X_1 a^\dagger - Y_1 a + X_2 b^\dagger - Y_2 b . \quad (4.48)$$

The four *phonon amplitudes*  $(X_1, Y_1)$  and  $(X_2, Y_2)$  are complex numbers defined in such a way that the following restrictions (commutation rules) hold true:

$$[\hat{H}, \Gamma^\dagger] = \Omega \Gamma^\dagger , \quad [\Gamma, \Gamma^\dagger] = 1 , \quad (4.49)$$

and they verify the relation:

$$|X_1|^2 - |Y_1|^2 + |X_2|^2 - |Y_2|^2 = 1 . \quad (4.50)$$

The amplitudes were firstly calculated in Ref. [139] and their expressions as functions of  $\omega_{1,2}$ ,  $k_{1,2}$ , and  $\Omega$  can be seen in Appendix B therein. Furthermore, the factor  $\Omega$  from Eq. (4.49) turns out to be the wobbling frequency obtained in the previous section. Indeed, one finds that the system of equations given in Eq. (4.47) verifies:

$$\Omega^4 + B' \Omega^2 + C' = 0 , \quad (4.51)$$

where the two primed coefficients are [136]:

$$\begin{aligned} B' &= -(\omega_1^2 + \omega_2^2 + 8A_2 A_3 Ij) , \\ C' &= (\omega_1 \omega_2)^2 - 4 \left[ A_3^2 (k_1 k_2)^2 + A_2^2 \frac{(Ij)^2}{(k_1 k_2)^2} \right] (\omega_1 \omega_2) + 16(A_2 A_3 Ij)^2 . \end{aligned} \quad (4.52)$$

Manipulating the obtained terms from Eq. (4.52), it can be shown that they are

actually equivalent with the factors  $B$  and  $C$  defined in Eq. (4.20) and Eq. (4.21), respectively. Notice the fact that the first term does not contain any canonicity factors (i.e., neither  $k_1$  nor  $k_2$ ), however,  $C'$  depends quadratically on the product  $k_1 k_2$ . Moreover, the contribution from both oscillator frequencies attained when the coupling terms were ignored (Eq. (4.35)) comes into play for both terms. Obviously, in reference to the core and single-particle degrees of freedom, there is an interplay between them in  $B'$  but also  $C'$  (through the fact that  $\omega_2$  contains the single-particle potential strength  $V$  and the triaxiality parameter  $\gamma$  parameters).

Prior to conclude this section, some graphical representations of the oscillator frequencies ( $\omega_1, \omega_2$ ) and the canonicity factors ( $k_1, k_2$ ) will be made, in order to get a qualitative interpretation of their behavior with respect to certain parameters. As such, in the left inset of Fig. 4.6 the oscillator frequencies are shown as function of the total angular momentum and for arbitrary values of the single particle potential  $V$ , triaxiality parameter  $\gamma$  and single-particle  $j$ -shell. Notice that the two quantities vary linearly with spin (recall Eq. (4.35)), and they also intersect at a particular spin  $I'$ , depending on the magnitude of the three inertia factors  $A_k$ . Moreover, the region with  $I \leq j$  is captured too (marked by the hatched gray area), although one should keep in mind that usually the wobbling bands have band-heads which lie higher than that. The plot was made only for a single ordering of the three inertia factors, given that reversing  $A_2$  and  $A_3$  will not produce significant modifications of the figures (i.e.,  $\omega_1$  stays the same and  $\omega_2$  changes only very slightly). In the right inset of Fig. 4.6 a different approach is taken into consideration for  $\omega_2$ . Since this quantity depends on both parameters  $\gamma$  and  $V$ , a contour plot within this space is provided, while the other relevant parameters are kept constant. From this representation, one can notice the rather constant grow in magnitude for  $\omega_2$  when the single-particle potential  $V$  increases. Additionally, for a given  $V$ , the frequency does not vary too much across the  $\gamma$  range, particularly for  $V < 2$ . The rather abrupt changes only happen in the low  $\gamma$  and  $V > 2$  region. Throughout the contour representations,  $V$  was kept in the interval [0, 5] MeV and  $\gamma$  in  $[0^\circ, 60^\circ]$  and arbitrary values were specified for the three inertia factors ( $A_3 > A_2 > A_1$ ), the total spin, and the single-particle angular momentum.

Concerning the canonicity factors, they are represented separately in Fig. 4.7. The plots show the evolution of both quantities with respect to the total angular momentum and at different  $A_k$  orderings. For the calculations, the factors  $A_k$



FIGURE 4.6: **Left:** The oscillator frequencies  $\omega_1$  and  $\omega_2$  from Eq. 4.35. For this particular example,  $j = 13/2$  and the ordering  $A_3 > A_2 > A_1$  is chosen, according to the conditions of existence for  $\omega_1$  and  $\omega_2$ . The intersection point between  $\omega_1$  and  $\omega_2$  is marked by the red vertical line around  $I \approx 24\hbar$ . See text for details on the two colored regions split by the black vertical line. **Right:** The oscillator frequency  $\omega_2$  from Eq. (4.35) within the  $(\gamma, V)$  plane. The value of  $\gamma = 25^\circ$  is marked with the dashed vertical line just to guide the eye. Each contour line represents an energy difference of about 0.20 MeV.

remain unchanged but only  $A_2$  and  $A_3$  are reversed. Remarkable the fact that for  $k_2$ , reversing the factors  $A_{2,3}$  will change the behavior with respect to spin from an increasing one ( $A_3 > A_2$ ) to a decreasing type ( $A_2 > A_3$ ). The same cannot be said about  $k_1$ , where both orderings give an increasing trend w.r.t. spin. Note that just for a pedagogical purpose, the plots contain the regions where  $I \leq j$ , similarly as per Fig. 4.6.

Since the structure of  $k_2$  is dependent on the triaxiality parameter and the single-particle potential strength, a set of contour plots within this plane can also be created, in a similar fashion as the one obtained for  $\omega_2$  from Fig. 4.6. For this case though, by reversing  $A_2$  and  $A_3$  will produce significant changes on the values of  $k_2$  (recall Fig. 4.7 where the condition  $A_2 > A_3$  gave decreasing behavior for the canonicity factor). Consequently, two such contour plots are depicted in Fig. 4.8.

This alternative procedure in obtaining a set of solutions that describe a harmonic motion of the core  $\mathcal{C}$  and the odd single-particle  $\mathcal{Q}$  comprised a) the required steps in acquiring analytical results for the energy spectra and b) qualitative analyses of some quantities that emerged from calculations. Furthermore, by quantizing the classical variables obtained from TDVE, it is possible to attain a new CEF, which



FIGURE 4.7: The canonicity factors from Eq. (4.42) are graphically represented as function of spin  $I$  for arbitrary MOI,  $V$  and  $\gamma$ . The single-particle angular momentum is set to  $j = 13/2$ . For the calculations, the two  $A_k$  orderings kept the same numerical values and only  $A_2$  and  $A_3$  were interchanged. The regions where  $I \leq j$  (hatched area) and  $I \geq j$  (green area) that are split by the vertical dashed line are pointed out as well.



FIGURE 4.8: The canonicity factor  $k_2$  from Eq. (4.42) in the  $(\gamma, V)$  plane, evaluated at fixed inertia factors and angular momenta. The value of  $\gamma = 25^\circ$  is marked by the vertical dashed line just to guide the eye.

can be summarized in the following way: *The CEF is composed of 1) a term that is independent of any canonical variable and 2) two harmonic vibrators with the phonon energies  $\{\Omega_1, \Omega_2\}$ , portraying the precessional motion of the core and the odd particle.* The oscillators arise from the solutions of a fourth degree algebraic equation (Eq. (4.19)), whose origin was presented in a ‘quantized manner’ from Eq. (4.38). This is indeed a remarkable feature of the current model, since the dequantization of the initial Hamiltonian and also further *re-quantization* of  $\mathcal{H}$  can be done consistently without any loss of the underlying system dynamics and

degrees of freedom. The final form of the energy spectrum is defined analytically in Eq. (4.30).

Regarding the energy spectrum  $E_{I,n_{w_1},n_{w_2}}$  obtained in Eq. (4.30) and Eq. (4.32), when both wobbling phonon numbers are zero, it simply reflects the *zero-point-motion* for the system, i.e., the true ground state. Even when  $n_{w_1} = n_{w_2} = 0$ , the core and particle will contribute to the total energy of the system, through the smallest ‘quantum fluctuations’ characterized by  $\Omega_1/2$  and  $\Omega_2/2$ , which is consistent with the harmonic description of the triaxial rigid rotators. This will be crucial when the real wobbling spectrum of the studied nuclei will be interpreted.

### 4.3 A New Band Structure in Lu Isotopes

Following up to the team’s work in regards to the so-called **W<sub>0</sub>** approach outlined in Section 4.1, two more research papers were devoted to the study of wobbling motion in Lu isotopes (see Refs. [101, 136]), but with a different perspective in reference to the band structure. In what follows, the new interpretation (hereafter referred to as **W<sub>1</sub>**) will be described, while also pointing out key distinctions between it and **W<sub>0</sub>**.

Recalling the mechanism that generates the wobbling states via **W<sub>0</sub>**, this was depicted in Fig. 4.1, and it was shown that from the ground states (calculated variationally according to Eq. (4.4)), one can obtain energy levels for bands  $n_w = 1, 2, \dots$  by acting with a phonon operator once, twice, and so on, on a given spin state  $I$ . Moreover, a spin state  $I$  from a band  $n_w = n'$  emerged by means of the phonon operator acting on  $I - 1$  from the band  $n_w = n' - 1$ . The formalism **W<sub>0</sub>** clearly shows the fact that the variational method can be applied to the ground-band and furthermore get excited bands through an additional term (i.e., the phonon operator). On the other hand, **W<sub>1</sub>** changes this landscape by aiming at a more *compact* method in attaining the wobbling spectrum. In order to better understand this procedure, a specific case-study for <sup>163</sup>Lu will be employed in the following subsection, and a generalization to other isotopes can be inherently adopted later on.

TABLE 4.2: The spin, parity, and signature assignments for  $^{163}\text{Lu}$  taken from experimental measurements [145]. Concerning the notation  $\pi(l_j)$ , it signifies an odd proton in the  $l$ -orbital with angular momentum  $j$ . The last two columns represent the key difference between the formalisms  $\mathbf{W}_0$  and  $\mathbf{W}_1$ .

Band	Spins	$\pi$	$\alpha$	$\pi(l_j)$	$\mathbf{W}_0: \mathcal{C} + \mathcal{Q}_p$	$\mathbf{W}_1: \mathcal{C} + \mathcal{Q}_p$
TSD1	13/2, 17/2 ... 97/2	+	+1/2	$\pi(i_{13/2})$	$0^+, 2^+, 4^+, \dots$	$0^+, 2^+, 4^+, \dots$
TSD2	27/2, 31/2 ... 91/2	+	-1/2	$\pi(i_{13/2})$	$\text{TSD1} + 1\Gamma^\dagger$	$1^+, 3^+, 5^+, \dots$
TSD3	33/2, 37/2 ... 85/2	+	+1/2	$\pi(i_{13/2})$	$\text{TSD1} + 2\Gamma^\dagger$	$\text{TSD2} + \Gamma^\dagger$
TSD4	47/2, 51/2 ... 83/2	-	-1/2	$\pi(h_{9/2})$	$\text{TSD1} + 3\Gamma^\dagger$	$1^+, 3^+, 5^+, \dots$

### 4.3.1 Variational States

The isotope  $^{163}\text{Lu}$  has been studied successfully by the team within  $\mathbf{W}_0$  and also through the current  $\mathbf{W}_1$  model. In both approaches one considered the wobbling spectrum as being composed of four TSD bands. In  $\mathbf{W}_0$  the bands were one ground (TSD1) and three excited (TSD2, TSD3, TSD4), which were ‘in line’ with other studies on this isotope [122, 124, 138]. The general characteristics of the four triaxial bands and their particle + core structure were already described at the beginning of the chapter from the perspective of  $\mathbf{W}_0$ . Experimentally, the collective structure of  $^{163}\text{Lu}$  is summarized in Table 4.2.

Within the *renormalization* of  $\mathbf{W}_1$  for the nucleus  $^{163}\text{Lu}$ , one applies the variational principle (i.e., Eq. (4.4)) for all states in TSD1 and TSD2. Additionally, since the coupling scheme  $\mathcal{Q} + \mathcal{C}$  is different for TSD4 (i.e., the  $j = 9/2$  proton couples with the even-even core, as opposed to the  $j = 13/2$  proton for the other bands), then another VP will be employed for TSD4 as well. The states from TSD3 are excited wobbling states formed by the action of a phonon operator on TSD2. Indeed, this *successive application of TDVE in obtaining variational states is a remarkable aspect of  $\mathbf{W}_1$* .

All the states from TSD1 are produced by coupling the  $j = 13/2$  odd proton from  $i_{13/2}$ -shell with a triaxial even-even core having the spin sequence  $\mathcal{C}_1 = 0, 2, 4, \dots$ , forming a zero-phonon wobbling band. Both the core and the single-particle have positive parity. On the other hand, all states in TSD2 are built by the same odd-particle, but with a different core:  $\mathcal{C}_2 = 1, 3, 5 \dots$ , which also has positive parity. Notice the even/odd dissimilarity between the two angular momentum sequences of the cores  $\mathcal{C}_1$  and  $\mathcal{C}_2$  that are specified in Table 4.2 and compared to the previous  $\mathbf{W}_0$  theory. The wobbling bands TSD1 and TSD2 from  $^{163}\text{Lu}$  can be explained by means of a semi-classical model through an even-odd staggering

of states  $(0^+, 1^+)$ ,  $(2^+, 3^+)$ , ... of collective nature. They are in fact *Signature Partner Bands* [136]: two sequences of states that differ with  $\Delta I = 2\hbar$  inside the bands and  $\Delta I = 1\hbar$  for spins belonging to adjacent bands, each having opposite signature but similar parity. In Ref. [101] it was proven that TSD2 is the signature partner of TSD1. The negative parity states belonging to the band TSD4 are explored semi-classically via TDVE with the collective core  $\mathcal{C}_2 = 1, 3, 5 \dots$  coupled to a negative parity proton  $j^\pi = 9/2^-$ . Recall that the signature quantum number was described in Appendix C (see Section C.2) and its definition provided by Eq. (C.10).

In terms of quasi-particle + triaxial core coupling, it is remarkable the fact that the ‘final picture’ for  $^{163}\text{Lu}$  is regarded as a positive parity core of even spin states that generates the band TSD1 (i.e.,  $\mathcal{C}_1$ ), a core with odd spin states of positive parity states forming TSD2 and TSD4 (i.e.,  $\mathcal{C}_2$ ), and finally the one-phonon states in TSD3, which are activated from the ground band TSD2. This is emphasized within the last two columns of Table 4.2. One can encapsulate this current renormalization under the following set of *equalities*:

$$\begin{aligned} \{TSD1\} &\equiv \{\mathcal{C}_1 [0^+, 2^+, 4^+, \dots] \otimes \mathcal{Q}_1[j^\pi = 13/2^+]\} , \\ \{TSD2\} &\equiv \{\mathcal{C}_2 [1^+, 3^+, 5^+, \dots] \otimes \mathcal{Q}_1[j^\pi = 13/2^+]\} , \\ \{TSD4\} &\equiv \{\mathcal{C}_2 [1^+, 3^+, 5^+, \dots] \otimes \mathcal{Q}_2[j^\pi = 9/2^-]\} , \end{aligned} \quad (4.53)$$

for TSD1-2-4 and:

$$\{TSD3 [\dots, I^+, (I+2)^+, \dots]\} \equiv \{TSD2 [\dots, (I-1)^+, (I+1)^+, \dots] + \Gamma^\dagger\} , \quad (4.54)$$

for TSD3. The two odd protons from Table 4.3 are denoted with  $\mathcal{Q}_1$  and  $\mathcal{Q}_2$  in Eqs. (4.53) - (4.54), and these notations will be used hereafter. Thus, the two equations establish the renormalization of  $\mathbf{W}_1$ , which is successfully applied to  $^{163}\text{Lu}$  and (later on) to other isotopes.

With the Eqs. (4.53) - (4.54) as ‘recipes’, one can obtain the wobbling energies for  $^{163}\text{Lu}$  as per Eq. (4.32) by adopting the spins and wobbling phonon numbers of each band. These values are provided in Table 4.3. Notice that for TSD1-2-4, the pair of phonon numbers are  $(0, 0)$  due to them being ground states. Moreover, the TSD3 states are activated only by the wobbling-phonon number  $n_{w_1}$  (i.e.,  $n_{w_2} = 0$ ), which is consistent with the theory from  $\mathbf{W}_0$ . As it will be seen, all four bands

TABLE 4.3: The wobbling phonon numbers ( $n_{w_1}, n_{w_2}$ ) and the phonon term  $\mathcal{F}_{n_{w_1} n_{w_2}}^I$  are provided in the first three columns for  $^{163}\text{Lu}$ . The first ( $I_0$ ) and terminus ( $I_t$ ) states of each band are given in the next two columns. Last column contains the quasi-particles involved in the particle + rotor coupling, which are denoted according to Eqs. (4.53) - (4.54).

Bands	$n_{w_1}$	$n_{w_2}$	$\mathcal{F}_{n_{w_1} n_{w_2}}^I$	$I_0$	$I_t$	$\mathcal{Q}$
TSD1	0	0	$\mathcal{F}_{00}^I = \frac{1}{2} (\Omega_1^I + \Omega_2^I)$	$13/2^+$	$97/2^+$	$j^\pi = 13/2^+ \stackrel{\text{not}}{\equiv} \mathcal{Q}_1$
TSD2	0	0	$\mathcal{F}_{00}^I = \frac{1}{2} (\Omega_1^I + \Omega_2^I)$	$27/2^+$	$91/2^+$	$j^\pi = 13/2^+ \stackrel{\text{not}}{\equiv} \mathcal{Q}_1$
TSD3	1	0	$\mathcal{F}_{10}^{I-1} = \frac{3}{2} \Omega_1^{I-1} + \frac{1}{2} \Omega_2^{I-1}$	$33/2^+$	$85/2^+$	$j^\pi = 13/2^+ \stackrel{\text{not}}{\equiv} \mathcal{Q}_1$
TSD4	0	0	$\mathcal{F}_{00}^I = \frac{1}{2} (\Omega_1^I + \Omega_2^I)$	$47/2^-$	$83/2^-$	$j^\pi = 9/2^- \stackrel{\text{not}}{\equiv} \mathcal{Q}_2$

have the wobbling frequency  $\Omega_2$  in the zero-point energy, that is  $\frac{1}{2}\Omega_2^I$ . In reference to TSD3, given that the band is obtained as one-phonon excitations built on top of TSD2, then by acting with the operator on a state  $I$  from TSD2 it will increase the angular momentum by one unit. Consequently, for a state  $I \in \{\text{TSD3}\}$  the phonon operator is indeed  $\mathcal{F}_{10}^{I-1}$ , where  $I-1 \in \{\text{TSD2}\}$ .

Taking the information comprised in Table 4.3 and using the general energy formula obtained in Eq. (4.32), one can determine the wobbling spectrum of  $^{163}\text{Lu}$  through the following set of equations:

$$\begin{aligned}
 E_{I,0,0}^{\text{TSD1}} &= \epsilon_{13/2} + \mathcal{H}_{\min}^I + \mathcal{F}_{00}^I = \epsilon_{13/2} + \mathcal{H}_{\min}^I + \frac{1}{2} (\Omega_1^I + \Omega_2^I) , \\
 E_{I,0,0}^{\text{TSD2}} &= \epsilon_{13/2} + \mathcal{H}_{\min}^I + \mathcal{F}_{00}^I = \epsilon_{13/2} + \mathcal{H}_{\min}^I + \frac{1}{2} (\Omega_1^I + \Omega_2^I) , \\
 E_{I,1,0}^{\text{TSD3}} &= \epsilon_{13/2} + \mathcal{H}_{\min}^{I-1} + \mathcal{F}_{10}^{I-1} = \epsilon_{13/2} + \mathcal{H}_{\min}^{I-1} + \frac{1}{2} (3 \cdot \Omega_1^{I-1} + \Omega_2^{I-1}) , \\
 E_{I,0,0}^{\text{TSD4}} &= \epsilon_{9/2} + \mathcal{H}_{\min}^I + \mathcal{F}_{00}^I = \epsilon_{9/2} + \mathcal{H}_{\min}^I + \frac{1}{2} (\Omega_1^I + \Omega_2^I) ,
 \end{aligned} \tag{4.55}$$

where  $\epsilon_{13/2}$  and  $\epsilon_{9/2}$  are the single-particle shell energies for  $\mathcal{Q}_1$  and  $\mathcal{Q}_2$ , respectively. For each band, the spins are the ones from Table 4.2. Keep in mind that the wobbling frequencies and the minimal energy both depend on the single-particle angular momentum  $j$  as well, so it must be properly inserted for each band as per Table 4.3.

The obtained set of energies from Eq. (4.55) represents the *absolute energies*. As such, they will be subtracted from the band-head energy of  $^{163}\text{Lu}$ , obtaining a spectrum of *excitation energies* (recall Eq. (3.25)). The band-head energy  $E_{13/2,0,0}^{\text{TSD1}}$  is the energy corresponding to the ground-state  $I_b = 13/2$  from TSD1. Its

expression is as follows:

$$E_{13/2,0,0}^{\text{TSD1}} = \epsilon_{13/2} + \mathcal{H}_{\min}^{13/2} + \mathcal{F}_{00}^{13/2} = \epsilon_{13/2} + \mathcal{H}_{\min}^{13/2} + \frac{1}{2} (\Omega_1^{13/2} + \Omega_2^{13/2}) . \quad (4.56)$$

An important aspect when working with the excitation energies is that the single-particle energies will practically cancel out. Only for TSD4 there will be the constant term  $\epsilon_{9/2} - \epsilon_{13/2} = -0.344$  MeV [101], which is just the difference between the two spherical shell model states of  $\mathcal{Q}_2$  and  $\mathcal{Q}_1$ . Regarding the two wobbling frequencies, in the case of  $^{163}\text{Lu}$  their expressions are:

$$\Omega_{1,2} = \left[ \frac{1}{2} (-B \mp \sqrt{B^2 - 4C}) \right]^{1/2} , \quad (4.57)$$

such that the ordering  $\Omega_1 < \Omega_2$  holds true. The minimal energy term  $\mathcal{H}_{\min}^I$ , which firstly appeared in Eq. (4.30), has the structure [103]:

$$\mathcal{H}_{\min}^I = (A_2 + A_3) \frac{I+j}{2} + A_1(I-j)^2 - V \frac{2j-1}{j+1} \sin \left( \gamma + \frac{\pi}{6} \right) . \quad (4.58)$$

### 4.3.2 Fitting Parameters

A compact analytical structure for the wobbling spectrum of  $^{163}\text{Lu}$  is obtained with the help of Eq. (4.55). Additionally, the base rule in calculating the excitation energies (by the subtraction of Eq. (4.56) from each level) gives the primary step in the fitting procedure. As for the components comprising the energy itself, the term  $\mathcal{H}_{\min}^I$  is taken according to Eq. (4.58) and the wobbling frequencies  $\Omega_{1,2}$  are granted by Eq. (4.57).

In order to get numerical results for the excitation energies, a set of free parameters will be employed in the fitting method, such that by fixing these values, the theoretical data are achieved. From the classical energy function (or even the initial quantal Hamiltonian) it can be seen that the rotational term is expressed in terms of the inertia factors  $A_k$  and the single-particle term is explicitly specified through the single-particle strength  $V$  and triaxiality  $\gamma$ . Therefore, it is well suited to pick the following quantities as fitting parameters throughout the numerical computations: moments of inertia:  $\mathcal{I}_1, \mathcal{I}_2, \mathcal{I}_3$ , single-particle potential strength  $V$ , and

triaxiality parameter  $\gamma$ . Going further, these values will be denoted as:

$$\mathcal{P}_{\text{fit}} = [\mathcal{I}_1, \mathcal{I}_2, \mathcal{I}_3, V, \gamma] . \quad (4.59)$$

The actual fitting technique consists of finding the set  $\mathcal{P}_{\text{fit}}$  that best reproduces the experimental data concerning the wobbling spectrum. The numerical implementation aims at determining  $\mathcal{P}_{\text{fit}}$  such that the  $\chi^2$ -function [103] :

$$\chi^2 = \frac{1}{N_T} \sum_i \frac{\left( E_{\text{exp}}^{(i)} - E_{\text{th}}^{(i)} \right)^2}{E_{\text{exp}}^{(i)}} , \quad (4.60)$$

is *minimal*. Here  $N_T$  represents the total number of states for the isotope. In the case of  $^{163}\text{Lu}$ , the  $\chi^2$ -function will contain all states belonging to TSD1-3 and TSD4. Obviously  $E_{\text{exp}}^{(i)}$  represents the *experimental excitation energy*, which is evaluated by subtracting the band-head level (having an energy of 1.738 MeV) from each state. From a computational standpoint, the problem thereby consists of a minimization process that has to be tackled on the  $\chi^2$ -function.

This new approach is different than  $\mathbf{W}_0$  in the sense that the moments of inertia are now considered as separate (independent) ‘free’ values, whereas in [39] one of the parameters was the scaling factor  $1/\mathcal{I}_0$  emerging from the adoption of the rigid-body MOI (see Eq. (2.30)). Moreover, in the present model the three moments of inertia have no angular momentum dependence, i.e., they are fixed and remain constant across the entire spin range of each isotope. On the other side, unlike  $\mathbf{W}_0$  where  $\gamma$  and  $\beta$  were fixed with values from literature, this re-interpretation obtains  $\gamma$  self-consistently right from the fitting procedure. Both approaches consider  $V$  as a free parameter.

The argument in favor of using a set of free MOI is that the *real* moments of inertia for the nucleus are neither irrotational nor rigid, but they satisfy the relation  $\mathcal{I}^{\text{irr}} < \mathcal{I}^{\text{exp}} < \mathcal{I}^{\text{rig}}$  (recall discussion in Chapter 2.2 and Eq. (2.31)). A study of the three moments of inertia in regards to a possible change in magnitude at higher spins due to Coriolis or even pairing interaction is excluded within this approach, as the initial quantal Hamiltonian does not contain such terms. Lastly, the quadrupole deformation parameter does not appear explicitly throughout the description, since it is somewhat *encoded* in the potential strength  $V$  (see Eqs. (2.61) and (2.62)).

## 4.4 Numerical Results in Lu Isotopes

In the previous section, one formulated: i) the renormalization procedure that is the cornerstone of the  $\mathbf{W}_1$  formalism via Eqs. (4.53) - (4.54) ii) a set of analytical expressions for the wobbling bands in  $^{163}\text{Lu}$  provided by Eq. (4.55) iii) the free parameter set  $\mathcal{P}_{\text{fit}}$  via Eq. (4.59), and finally iv) the actual fitting procedure, which will be employed as application (minimization of  $\chi^2$  from Eq. (4.60)). The team's work with the  $\mathbf{W}_1$  formalism concluded in two research papers, where in addition to the study of the wobbling properties in  $^{163}\text{Lu}$  [101], several other Lu isotopes were examined [136]. Herein, the results obtained for  $^{161,163,165,167}\text{Lu}$  will be presented, providing data for quantities like:

1. excitation energies
2. alignments
3. dynamic moments of inertia
4. energies relative to a reference rotor

Naturally, calculations concerning the transition probabilities for every nucleus will be provided as well, making a comparison with the available experimental data. The first step is to numerically reproduce the general spectrum depicted in Eq. (4.32). This is realized by following the rules that were outlined for  $^{163}\text{Lu}$  in Eqs. (4.55) - (4.60), and then apply them to the other isotopes. However, prior knowledge of the two wobbling phonon numbers, the quasi-particle + core coupling scheme, the spins, and parities is required. The  $\mathbf{W}_1$  model considers TSD1 and TSD2 from  $^{163}\text{Lu}$  as being ground-states obtained variationally by coupling an odd particle with two different cores (recall  $\mathcal{C}_1$  and  $\mathcal{C}_2$  defined in Eqs. (4.53) - (4.54)). A remarkable feature of this theory is that the same principle can be used to the other isotopes: namely the pair (TSD1, TSD2) is regarded as zero-phonon bands having different core + particle couplings. Furthermore, some fitting considerations should be taken into account for every isotope in order to have a consistency throughout the numerical implementations. These can be summarized in the following way:

- $^{161}\text{Lu}$

- There are only two bands generated by the coupling of  $\mathcal{Q}_1$  with an even-even core
- In regards to their nature, both bands are ground-states (zero-phonon)
- The core in TSD1 has even spins (i.e.,  $\mathcal{C}_1$ ) and in TSD2 it has odd spin spins (i.e.,  $\mathcal{C}_2$ )
- $^{163}\text{Lu}$ 
  - Four TSD bands with the structure described in Table 4.2
  - Three different core + odd-particle couplings:  $(\mathcal{Q}_1 + \mathcal{C}_1) \rightarrow \text{TSD1}$ ,  $(\mathcal{Q}_1 + \mathcal{C}_2) \rightarrow \text{TSD2}$ , and  $(\mathcal{Q}_2 + \mathcal{C}_1) \rightarrow \text{TSD4}$
- $^{165}\text{Lu}$ 
  - The three TSD bands are created from a single quasi-particle (i.e., the proton  $\mathcal{Q}_1$ ), which couples to a core of even states (TSD1) and a core with odd states (TSD2).
  - TSD1-2 are ground-bands
  - TSD3 is a one-phonon band that is obtained as wobbling excitations built on top of TSD2
- $^{167}\text{Lu}$ 
  - treated in a similar fashion as the  $^{161}\text{Lu}$  isotope

The characteristics of each isotope mentioned above are condensed into a set of tables where, for the sake of completeness, the spin and parity are also indicated. These are sketched in Tables 4.4 - 4.6. Since the previous section contains the relevant data for  $^{163}\text{Lu}$  (recall Tables 4.2 and 4.3), it has been omitted here. It is worth to point out that besides TSD4 from  $^{163}\text{Lu}$ , every nucleus has wobbling excitations emerging from the coupling of the  $\mathcal{Q}_1$  single-particle with an even-even core. Indeed, the coupling in TSD4 is between the proton  $\mathcal{Q}_2$  of negative parity and the core  $\mathcal{C}_1$  of positive parity.

Putting together the set of absolute energies from Eq. (4.55) and the discussion in reference to the excitation energy for a state  $I$ , one can define a general formula that will illustrate the systematics of the wobbling states to be used within the

TABLE 4.4: Spin and parity assignments for  $^{161}\text{Lu}$ , which are required for the excitation energy calculations (first column). The single-particle and the core states are shown in the third and fourth column. The wobbling phonon numbers from Eq. (4.31) are shown in the penultimate column. The band-head  $I_b$  of this isotope is also given in the last column.

Band	Spins	$\mathcal{Q}$	$\mathcal{C}$	$(n_{w_1}, n_{w_2})$	$I_b$
TSD1	$21/2^+, 25/2^+, \dots, 89/2^+$	$j^\pi = 13/2^+$	$4^+, 6^+, 8^+ \dots$	$(0, 0)$	21/2
TSD2	$31/2^+, 35/2^+, \dots, 79/2^+$	$j^\pi = 13/2^+$	$9^+, 11^+, 13^+ \dots$	$(0, 0)$	

TABLE 4.5: Spin and parity assignments for  $^{165}\text{Lu}$ , which are required for the excitation energy calculations (first column). The single-particle and the core states are shown in the third and fourth column. The wobbling phonon numbers from Eq. (4.31) are shown in the penultimate column. The band-head  $I_b$  of this isotope is also given in the last column.

Band	Spins	$\mathcal{Q}$	$\mathcal{C}$	$(n_{w_1}, n_{w_2})$	$I_b$
TSD1	$25/2^+, 29/2^+, \dots, 89/2^+$	$j^\pi = 13/2^+$	$6^+, 8^+, 10^+ \dots$	$(0, 0)$	
TSD2	$35/2^+, 39/2^+, \dots, 91/2^+$	$j^\pi = 13/2^+$	$11^+, 13^+, 15^+ \dots$	$(0, 0)$	25/2
TSD3	$41/2^+, 45/2^+, \dots, 81/2^+$	$j^\pi = 13/2^+$	$\text{TSD2} + \Gamma^\dagger$	$(1, 0)$	

TABLE 4.6: Spin and parity assignments for  $^{167}\text{Lu}$ , which are required for the excitation energy calculations (first column). The single-particle and the core states are shown in the third and fourth column. The wobbling phonon numbers from Eq. (4.31) are shown in the penultimate column. The band-head  $I_b$  of this isotope is also given in the last column.

Band	Spins	$\mathcal{Q}$	$\mathcal{C}$	$(n_{w_1}, n_{w_2})$	$I_b$
TSD1	$25/2^+, 29/2^+, \dots, 89/2^+$	$j^\pi = 13/2^+$	$6^+, 8^+, 10^+ \dots$	$(0, 0)$	25/2
TSD2	$35/2^+, 39/2^+, \dots, 91/2^+$	$j^\pi = 13/2^+$	$11^+, 13^+, 15^+ \dots$	$(0, 0)$	

fitting procedure:

$$E_{I_b}^{\text{TSD1}}(^A\text{Lu} ; \text{abs}) = \epsilon_{13/2} + \mathcal{H}_{\min}^{I_b} + \mathcal{F}_{00}^{I_b}, \quad (4.61)$$

$$E_{I, n_{w_1}, n_{w_2}}^{\text{TSD}N} (^A\text{Lu} ; \text{exc}) = \left( \epsilon_j + \mathcal{H}_{\min}^I + \mathcal{F}_{n_{w_1} n_{w_2}}^I \right) - E_{I_b}^{\text{TSD1}}(^A\text{Lu} ; \text{abs}), \quad (4.62)$$

where  ${}^A\text{Lu}$  represents the isotope that is evaluated (i.e.,  $A \in \{161, 163, 165, 167\}$ ),  $I$  is the state belonging to a triaxial band  $N$  from  ${}^A\text{Lu}$  ( $I \in \text{TSD}N$ ,  $I > I_b$ ), and the labels ‘abs/exc’ symbolize the absolute/excitation energy, respectively. Additionally,  $I_b$  is the band-head of the corresponding nucleus, and it is given explicitly in the last column of Tables 4.4 - 4.6. The value  $\epsilon_j$  denotes the single-particle proton’s energy for either  $\mathcal{Q}_1$  ( $j = 13/2$ ) or  $\mathcal{Q}_2$  ( $j = 9/2$ ). The energy from Eq. (4.61) corresponds to the absolute energy of the band-head, which was firstly provided for  ${}^{163}\text{Lu}$  in Eq. (4.56). For simplicity, the subscripts  $n_{w_1}$  and  $n_{w_2}$  appearing in  $E_{I_b}^{\text{TSD1}}(^A\text{Lu} ; \text{abs})$  have been dropped entirely because TSD1 has



FIGURE 4.9: The overall workflow for solving the minimization of the  $\chi^2$ -function (Eq. (4.60)). Initially, the absolute energy of the band-head  $I_b$  (Eq. (4.61) - red color) is subtracted from every state  $I$  (Eq. (4.30) - black color) in order to obtain the excitation energy (Eq. (4.62) - blue color). This is applied to the entire spectrum. Next, the inputs from Tables 4.2 - 4.6 are used in the minimization of  $\chi^2$ . The fitting function returns the set of parameters  $\mathcal{P}_{\text{fit}}$  (Eq. (4.59)), finalizing thus the numerical procedure.

$n_{w_1} = n_{w_2} = 0$ . It can be seen now that by using Eq. (4.62), the single-particle energy for bands TSD1-3 across all isotopes simply vanish, while only for TSD4 in  $^{163}\text{Lu}$  the quantity  $\epsilon_{9/2} - \epsilon_{13/2}$  shows up.

Concluding the current section, Eq. (4.62) provides the final ingredient towards the determination of the energy spectra for the whole group of nuclides. Indeed, the  $\chi^2$ -function can be minimized using  $E_{I,n_w1,n_w2}^{TSDN}(^A\text{Lu}; \text{exc})$  as a model, with the data from Tables 4.4 - 4.6 as input. The full workflow is depicted in Fig. 4.9 as a diagram.

#### 4.4.1 Numerical Parameters

With the theoretical and experimental excitation energies attributed to each nucleus, the minimization procedure of Eq. (4.60) can be readily applied. Note

TABLE 4.7: The fitting parameters  $\mathcal{P}_{\text{fit}}$ , i.e., the moments of inertia, the single-particle potential strength, and the triaxiality  $\gamma$  for each Lu isotope. The number of wobbling states (n.o.s.) and the root-mean-square error are also given in the last two columns.

Isotope	Bands	$\mathcal{I}_1 [\hbar^2/\text{MeV}]$	$\mathcal{I}_2 [\hbar^2/\text{MeV}]$	$\mathcal{I}_3 [\hbar^2/\text{MeV}]$	$V [\text{MeV}]$	$\gamma [^\circ]$	n.o.s	$E_{\text{rms}} [\text{MeV}]$
$^{161}\text{Lu}$	TSD1-2	87.555	2.773	22.744	2.933	20	29	0.168
$^{163}\text{Lu}$	TSD1-3	63.2	20	10	3.1	17	52	0.264
	TSD4	67	34.5	50	0.7	17	10	0.057
$^{165}\text{Lu}$	TSD1-3	77.295	16.184	4.399	1.673	20	42	0.125
$^{167}\text{Lu}$	TSD1-2	87.032	10.895	3.758	8.167	19.48	30	0.165

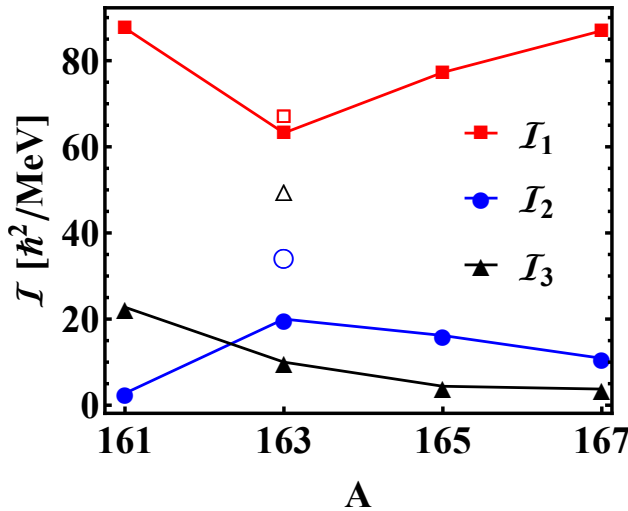


FIGURE 4.10: The fitted MOI (see Table 4.7) plotted as a function of the mass number  $A$ . The unfilled symbols represent the band TSD4 from  $^{163}\text{Lu}$ . This figure was taken as is from Ref. [136].

that since the variational states from TSD4 are obtained from a different core + particle polarization, a separate fit for the states of this band will be made [101]. Results are presented in Table 4.7, where in order to appraise the quality of the fits, the root-mean-square error (RMS) [146] for all bands is also shown. Based on the achieved statistics, it can be concluded that the current description of the excitation energies is quite good across the entire mass region.

To evidentiate the dependence of the three MOI with respect to the atomic mass  $A$ , the numerical values of  $\mathcal{I}_k$  from Table 4.7 are graphically represented in Fig. 4.10, where one remarks a switch in their ordering at  $A = 163$ . Such a change can be regarded as a *phase transition*. Moreover, there is a similar ordering concerning  $\mathcal{I}_2$  and  $\mathcal{I}_3$  between  $^{161}\text{Lu}$  and TSD4 from  $^{163}\text{Lu}$ , while the same order is reversed for the other nuclides.

From the obtained MOI, one sees that the maximal value is corresponding to

the 1-axis. As per the discussion regarding wobbling regime from Chapter 3, the interaction between the core and the odd particle seems to drive the system to a longitudinal-like motion. However, in the ‘final picture’, one is unable to assert that these isotopes behave as transverse or longitudinal wobblers. This is due to the fact that within the current model, the MOI do not have angular momentum dependence, thus it is impossible to pinpoint regions across the range of  $I$  where transitions from transverse to longitudinal wobbling might occur. Certainly, it could be that at a slow rotational motion the ordering is  $\mathcal{I}_2 > \mathcal{I}_1 > \mathcal{I}_3$ , and then gradually shift to  $\mathcal{I}_1 > \mathcal{I}_{2,3}$  (decrease of  $\mathcal{I}_2$  due to pairing interaction and increase of  $\mathcal{I}_1$  due to alignment). Nevertheless,  $\mathbf{W}_1$  only shows the normalized MOI as a *final* and not a *full* picture of the wobbling behavior. Therefore, through this formalism, a possible transverse regime near the low-spin limit for the Lu isotopes is not excluded.

In the section dedicated to experimental findings regarding wobbling structures (recall Section 3.3 from Chapter 3), which concluded with Fig. 3.21, it was shown that  $\gamma \approx 20^\circ$  for all Lu isotopes. Looking back at Table 4.7, it can be seen that except for  $^{163}\text{Lu}$ , the agreement between the experimental values and fitted results is indeed remarkable. Also noteworthy is the fact that the bands in  $^{163}\text{Lu}$  have similar triaxiality, although their MOI differ in magnitude. The single-particle potential strength given by the fit is also graphically shown for each nucleus in Fig. 4.11. There is a sharp increase in  $V$  for  $^{167}\text{Lu}$  from its neighbor  $^{165}\text{Lu}$ , which can be explained by means of collectiveness. Surely, it is possible that the two extra neutrons could induce a stronger quadrupole field that is *experienced* by the odd-particle. Furthermore, this *structural* change of the field can be enforced by the drastic evolution in the shape of the triaxial ellipsoid (i.e., the values of  $\mathcal{I}_{2,3}$  decrease while  $\mathcal{I}_1$  increases compared to neighboring nuclei). Additional comments concerning the single particle potential strength  $V$  will be made in a separate discussion.

#### 4.4.2 Energies

The excitation energies for all isotopes can be calculated straightforwardly using the parameters provided in Table 4.7. In this subsection, these energies are evaluated and compared with the experimental data. For  $^{161}\text{Lu}$ , the results are shown in Fig. 4.12. The four triaxial bands of wobbling nature in  $^{163}\text{Lu}$  are plotted in

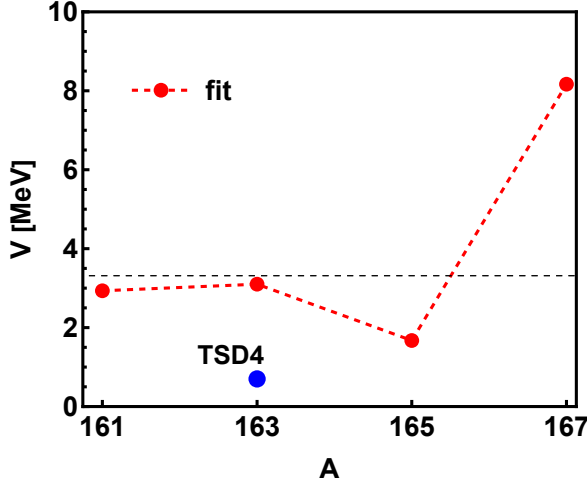


FIGURE 4.11: Fitted values for the single particle potential strength  $V$  as function of the mass number  $A$ . The separate procedure for TSD4 in  $^{163}\text{Lu}$  is marked by the blue dot. For an illustrative purpose, the average value across the entire mass region is also represented by the dashed horizontal line. The actual numerical values of  $V$  are specified in Table 4.7.

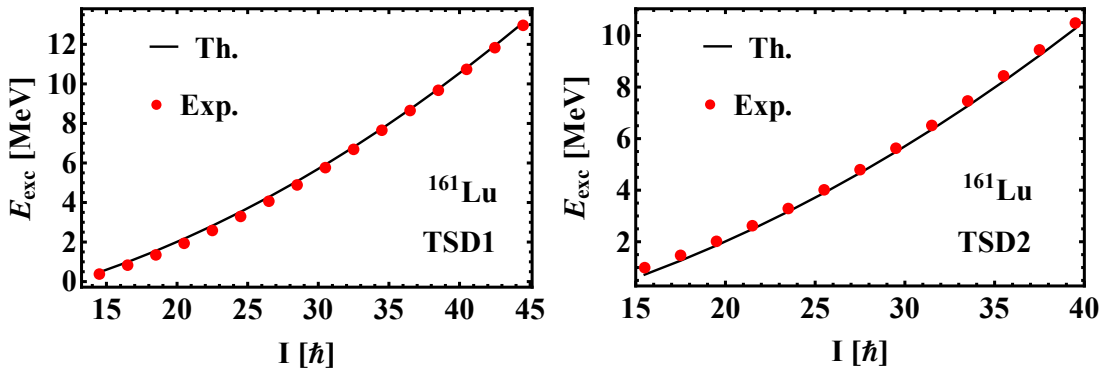


FIGURE 4.12: The experimental and theoretical excitation energies provided by Eq. (4.62) for the two wobbling bands in  $^{161}\text{Lu}$ . Experimental data are taken from Ref [123]. The figures are taken from Ref. [136].

Fig. 4.13, where an agreement with the experimental data can be seen across the entire spin range. When comparing the results from here with the ones of  $\mathbf{W}_0$  [39], there is a clear improvement of the present semi-classical model. A graphical representation showing the wobbling bands of  $^{165}\text{Lu}$  is depicted in Fig. 4.14 as function of the angular momentum. It can be seen that the two ground-bands and the one-wobbling-phonon band are fairly well reproduced through the current model. Lastly, the two wobbling bands for  $^{167}\text{Lu}$  are shown in Fig. 4.15 for which the experimental data are qualitatively well described by the  $\mathbf{W}_1$  formalism. Based on the results summarized in Figs. 4.12 - 4.15, it can be concluded that the renormalization applied in  $\mathbf{W}_1$  was indeed a realistic approximation.

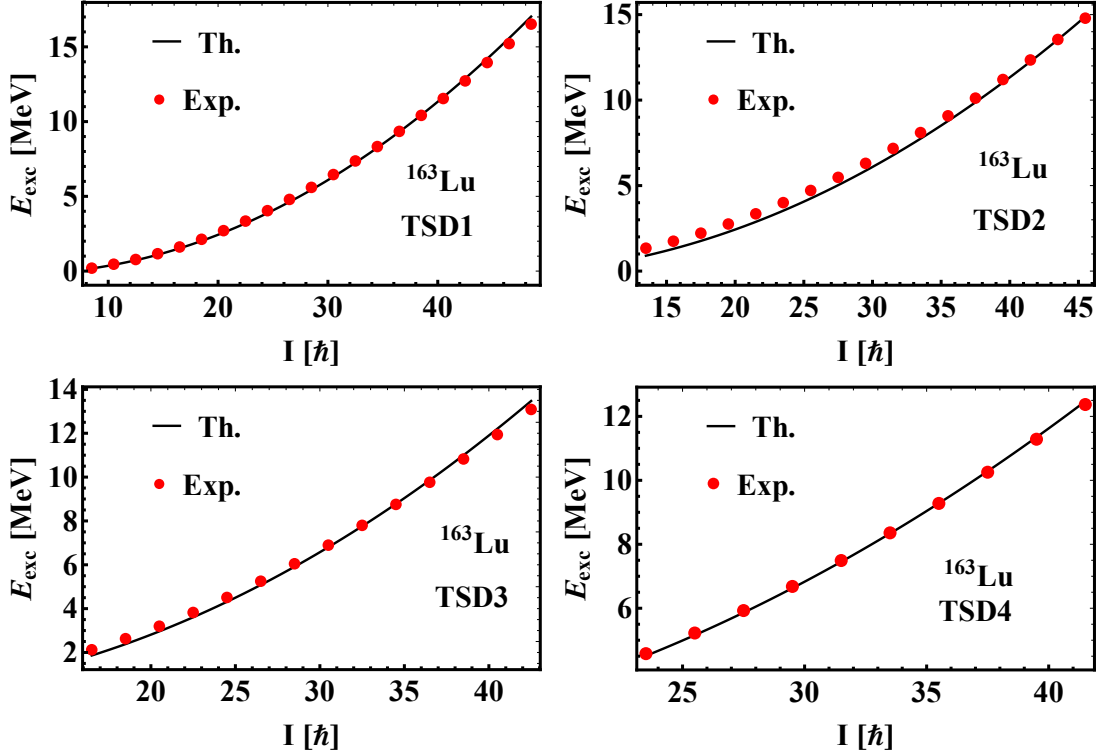


FIGURE 4.13: The experimental and theoretical excitation energies provided by Eq. (4.62) for the two wobbling bands in  $^{163}\text{Lu}$ . Experimental data are taken from Ref [145]. The figures are taken from Ref. [136].



FIGURE 4.14: The experimental and theoretical excitation energies provided by Eq. (4.62) for the three wobbling bands in  $^{165}\text{Lu}$ . Experimental data are taken from Ref [124]. The figures are taken from Ref. [136].

In what follows a remark about the transverse/longitudinal wobbling regimes should be made. Indeed, recalling the behavior of the wobbling energy defined in Eq. (3.24) for the  $A \approx 160$  region, all isotopes show a decreasing trend with respect to the total angular momentum. Such a decrease would indicate a transverse-like regime for every isotope. The evaluation of  $E_{\text{wob}}$  from Eq. (3.24) implies that the  $n_w = 1$  band is always the first band above the yrast line. By contrast, in this approach, the  $n_w = 1$  band only appears for  $^{163,165}\text{Lu}$  nuclides due to them having states activated by the phonon operator. Consequently, a direct comparison between the experimental and theoretical values can be made solely for the

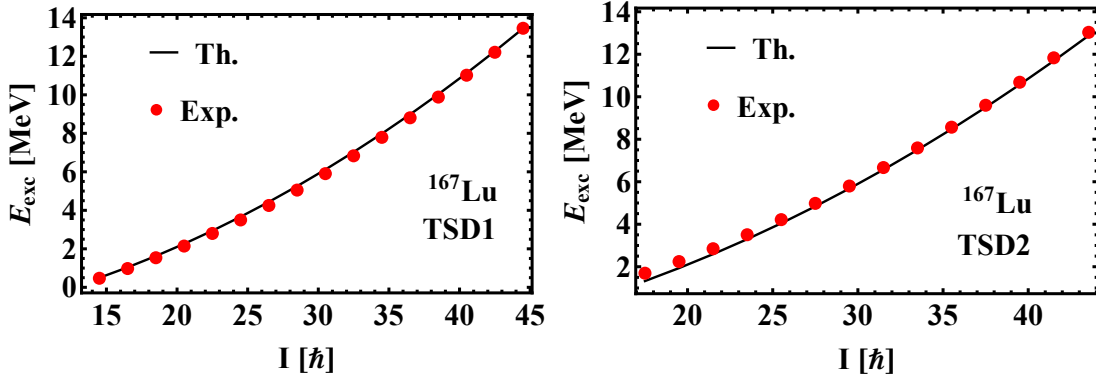


FIGURE 4.15: The experimental and theoretical excitation energies provided by Eq. (4.62) for the three wobbling bands in  $^{167}\text{Lu}$ . Experimental data are taken from Ref [125]. The figures are taken from Ref. [136].

set of states  $\text{TSD3} \rightarrow \text{TSD2}$ , meaning that the standard definition for the wobbling energy is now properly adjusted to the  $\mathbf{W}_1$  formalism, and the corresponding graphical representation is done in Fig. 4.16. Based on the plots, it can be seen that the experimental wobbling energy is increasing from 0.144 MeV to 0.170 MeV within the spin range  $33/2 - 77/2$ , and then it decreases for the last two spin states. Interesting the fact that both isotopes have a rather similar behavior for the experimental  $E_{\text{wob}}$ , although in the high-spin limit the decrease in magnitude is unexpected, because the core and the quasi-particle's a.m. must point in the same direction, leading to a longitudinal-like motion. Additionally, the current theory predicts the increasing part and it even shows a slight quenching when  $I \geq 40\hbar$ . Besides that, there is an almost constant shift between the calculated and experimental values for  $E_{\text{wob}}$  of about  $\approx 0.3$  MeV and  $\approx 0.15$  MeV in  $^{163}\text{Lu}$  and  $^{165}\text{Lu}$ , respectively. One may conclude that the present model properly describes the wobbling motion, which is also consistent with microscopic studies done in Ref. [147].

#### 4.4.3 Alignment

Going further with the study of the triaxial properties in odd-mass nuclei in  $\mathbf{W}_1$ , other relevant quantities are calculated. The *alignment* (or aligned angular momentum) is defined as the total spin minus a reference value. Usually the reference value is a function that depends on rotational frequency  $\hbar\omega$ . Namely the alignment

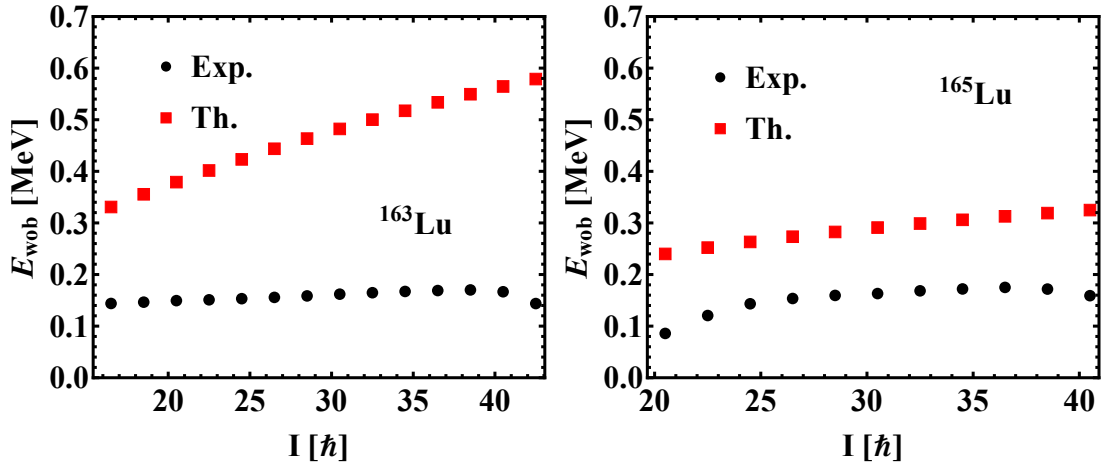


FIGURE 4.16: The theoretical wobbling energies as per Eq. (3.24) compared with the experimental ones for  $^{163}\text{Lu}$  (**left**) and  $^{165}\text{Lu}$  (**right**). Note that the  $n = 1$  and  $n = 0$  bands are TSD3 and TSD2 within the current description.

The figures are taken from Ref. [136].

and its reference value are given as:

$$\begin{aligned} i_x &= I - I_{\text{ref}}, \\ I_{\text{ref}} &= \mathcal{I}_0 \omega + \mathcal{I}_1 \omega^3, \end{aligned} \quad (4.63)$$

where the coefficients  $\mathcal{I}_0$  and  $\mathcal{I}_1$  are obtained by a least square procedure fit. Within literature, these values are also known as the Harris parameters [44]. The linear term from Eq. (4.63) is involved in the spherical symmetry and the second term is related to the axial symmetry. Consequently, the alignment gives a measure of triaxiality for the isotopes. The comparison between the theoretical and the experimental alignments is done for each isotope with the Harris parameters set to  $(\mathcal{I}_0, \mathcal{I}_1) = (30, 40)$  in units of  $\hbar^2 \text{MeV}^{-1}$ , and the results can be seen in Fig. 4.17 for  $^{163}\text{Lu}$ , Fig. 4.18 for  $^{165}\text{Lu}$ , and lastly Fig. 4.19 for  $^{161,167}\text{Lu}$ .

Taking a closer look at Figs. 4.17 - 4.19, a good agreement between the theory and experiment can be inferred, especially for  $A = 167$ . There are however a few discrepancies between the results for  $^{163}\text{Lu}$  in the high-frequency limit (i.e.,  $\hbar\omega \geq 0.45$  MeV), where the experimental data shows a rather linear increase while the theoretical points suffer a quenching and a slight down-bending. In fact, one might extract three regions, each with its different character regarding the angular momentum: a) one linearly increasing region at small frequencies ( $\hbar\omega \in [0, 0.3]$ ), b) a saturation region at medium frequencies ( $\hbar\omega \in [0.3, 0.55]$ ), and finally c) a decreasing function at high frequencies ( $\hbar\omega \geq 0.6$ ). It seems that  $\mathbf{W}_1$  can be



FIGURE 4.17: The theoretical and experimental alignments for  $^{163}\text{Lu}$ , according to Eq. (4.63), as function of the rotational frequency (Eqs. (2.42) - (2.44)). The figures are taken from Ref. [136].

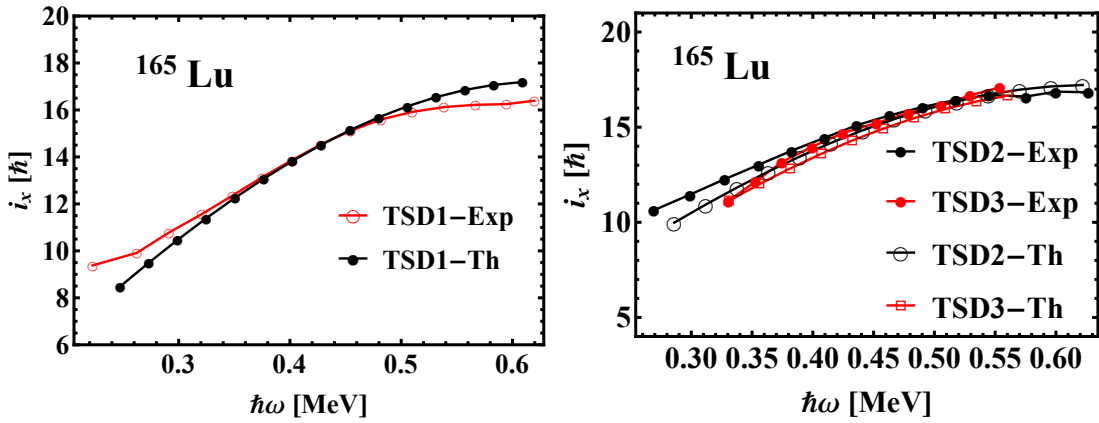


FIGURE 4.18: The theoretical and experimental alignments for  $^{165}\text{Lu}$ , according to Eq. (4.63), as function of the rotational frequency (Eqs. (2.42) - (2.44)). The figures are taken from Ref. [136].



FIGURE 4.19: The theoretical and experimental alignments for  $^{161}\text{Lu}$  (**left**) and  $^{167}\text{Lu}$  (**right**), according to Eq. (4.63), as function of the rotational frequency (Eqs. (2.42) - (2.44)). The figures are taken from Ref. [136].

further improved if the alignment is properly adjusted (e.g., by amending it with a linear term having large contribution only in the upper  $\hbar\omega$ -limit).

Comparing the curves relative to the entire mass region, based on their similarities and the fact that they are quite close to each other indeed reflects the wobbling character. Using  $\mathbf{W}_0$ , some alignment values were evaluated for  $^{165}\text{Lu}$  and  $^{167}\text{Lu}$  [100], where the bands TSD2 and TSD3 were one- and two-wobbling phonons. This new approach theory shows a clear improvement over the previous model.

#### 4.4.4 Reference Energy

Another useful quantity illustrating the wobbling behavior across neighboring isotopes is the excitation energy relative to a spherical rigid rotor. This is evaluated with an *effective* moment of inertia and it is graphically represented as a function of the total angular momentum. This reference energy is a typical rotor expression defined in terms of the squared angular momentum as  $E_{\text{ref}} = \alpha I(I+1)$ . The value of  $\alpha$  can be indeed regarded as an effective inverse MOI, which is usually determined by fitting the experimental reference energies. Moreover,  $\alpha$  can differ from isotope to isotope but here one kept the same value across all nuclei. Throughout these calculations, the reference energy was fixed to  $E_{\text{ref}} = 0.0075I(I+1)$  MeV. The results are depicted in Fig. 4.20 for  $^{161}\text{Lu}$ , Fig. 4.21 for  $^{165}\text{Lu}$ , and Fig. 4.22 for  $^{167}\text{Lu}$ . The four wobbling bands in  $^{163}\text{Lu}$  are plotted separately in Fig. 4.23.



FIGURE 4.20: The excitation energy relative to a rotor reference  $E_{\text{ref}} = 0.0075I(I + 1)$  as function of the total angular momentum, for  $^{161}\text{Lu}$ . The figures are taken from Ref. [136].



FIGURE 4.21: Comparison between theoretical and experimental excitation energy relative to a rotor reference  $E_{\text{ref}} = 0.0075I(I + 1)$  for  $^{165}\text{Lu}$ , as function of the total angular momentum. The zero- and one-wobbling-phonon bands TSD2-3 are plotted on the same figure. The figures are taken from Ref. [136].

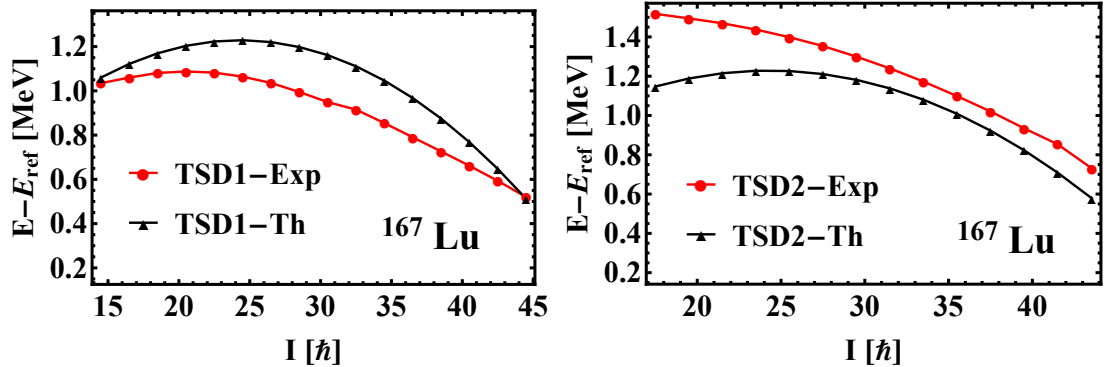


FIGURE 4.22: Comparison between theoretical and experimental excitation energy relative to a rotor reference  $E_{\text{ref}} = 0.0075I(I + 1)$  for  $^{167}\text{Lu}$ , as function of the total angular momentum. The figures are taken from Ref. [136].



FIGURE 4.23: The excitation energy relative to a rotor reference  $E_{\text{ref}} = 0.0075I(I + 1)$  as function of the total angular momentum, for  $^{163}\text{Lu}$ . The figures are taken from Ref. [136].

Concerning the graphical representations from Figs. 4.20 - 4.23, some remarks should be highlighted. Firstly, each experimental curve shows a decreasing trend with angular momentum. Some bands exhibit a stronger behavior than others. For example, TSD2 of  $^{163}\text{Lu}$  is almost constant in the range  $I \in (15 - 17) \hbar$  and only starts to get smaller beyond when  $I \geq 30\hbar$ . The same can be observed for TSD3 from  $^{165}\text{Lu}$ . On the other hand, TSD3 from  $^{163}\text{Lu}$  or TSD2 from  $^{167}\text{Lu}$  are decreasing rather rapidly across the entire spin range. The reduction of  $E - E_{\text{ref}}$  indicates that the contribution of the rotor part becomes more and more significant, leading to a diminishing effect of triaxiality when angular momentum reaches large values. The theoretical curves do reproduce the overall trends, showing some striking similarities for TSD4 from  $^{163}\text{Lu}$  or TSD3 in  $^{165}\text{Lu}$ . Remarking that the obtained numerical data for TSD1-3 from  $^{163}\text{Lu}$  show a decrease within a *convex* manner, whereas the experimental sets behave as *concave* functions. The deviation from the experimental set for TSD3 in the same nucleus increases by about 0.3 MeV for  $I \geq 35\hbar$ . Otherwise, it can be concluded that the current model does reproduce the dominance of a rotor-like behavior over triaxiality at large angular momentum for the studied isotopes. Improvements in the quality of the figures



FIGURE 4.24: The theoretical dynamic moment of inertia defined in Eq. (2.47) for the isotopes  $^{161}\text{Lu}$  (left) and  $^{167}\text{Lu}$  (right) is compared with the experimental data. The rotational frequency is defined as  $\hbar\omega_I = dE/dI = E_\gamma(I \rightarrow I - 2)/2$ . The figures are taken from Ref. [136].

can be observed when comparing with the calculations made using the previous approach  $\mathbf{W}_0$  [100].

#### 4.4.5 Dynamic MOI

The dynamic moment of inertia  $\mathcal{I}^{(2)}$  was introduced in Chapter 2 (recall Eqs. (2.47) - (2.48) from Section 2.2.9.3), where it was shown that this quantity is directly related to the energy differences for the  $I + 2, I, I - 2$  levels, respectively. Usually  $\mathcal{I}^{(2)}$  is represented as a function of the rotational frequency or even the total angular momentum. In the current formalism, the graphical representations are made with respect to the rotational frequency, and the data for  $^{161,167}\text{Lu}$  can be seen in Fig. 4.24. For  $^{163}\text{Lu}$ , the comparison between theory and experiment is depicted in Fig. 4.25. Lastly, the three bands from  $^{165}\text{Lu}$  are sketched in Fig. 4.26.

Usually the dynamic MOI is sensitive to single-particle effects, such as spin alignment of nucleons or even interaction between orbitals. Thus, it could be an indicator of triaxiality and wobbling motion, since the nucleus can suffer structural changes as its angular momentum (or rotational frequency) increases. Looking at Figs. 4.24 - 4.26 some interesting features appear. Firstly, regarding the theoretical calculations, the  $\mathbf{W}_1$  formalism predicts constant values for this quantity, meaning that the dynamic MOI is a constant function of  $\hbar\omega$  and furthermore the rotational frequency is linear in  $I$ . This can be seen throughout the plots, where

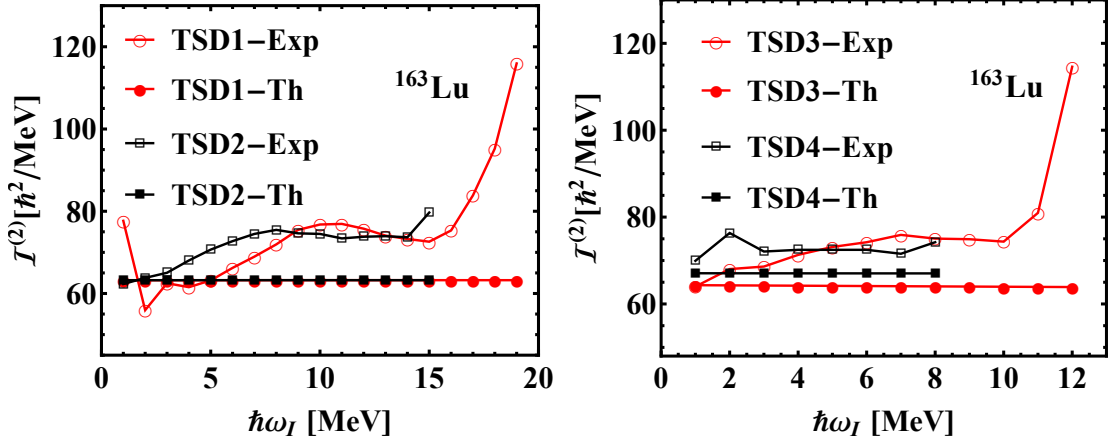


FIGURE 4.25: The dynamic moment of inertia defined in Eq. (2.47) for  $^{163}\text{Lu}$ . The rotational frequency is defined as  $\hbar\omega_I = dE/dI = E_\gamma(I \rightarrow I - 2)/2$ . The figures are taken from Ref. [136].

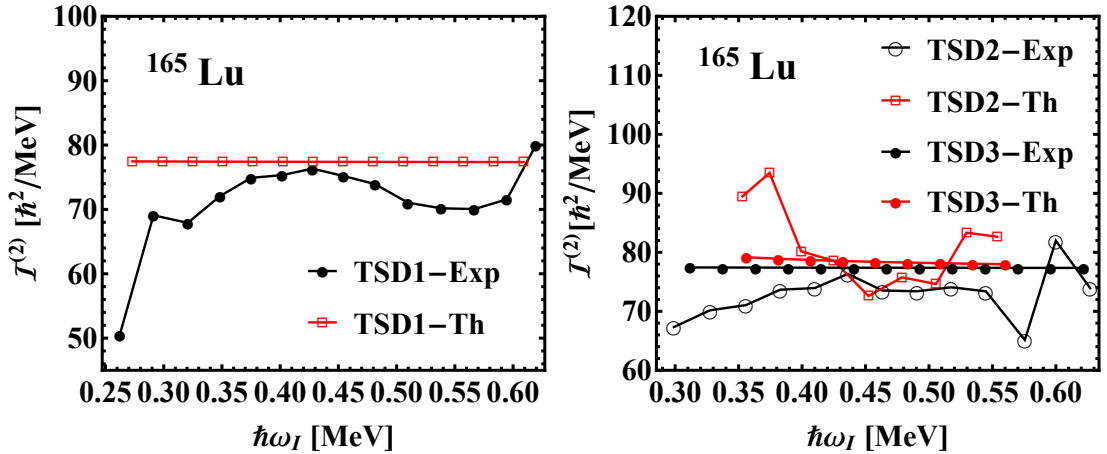


FIGURE 4.26: The dynamic moment of inertia defined in Eq. (2.47) for  $^{165}\text{Lu}$  showing the band TSD1 (left) and the bands TSD2-3 (right). The rotational frequency is defined as  $\hbar\omega_I = dE/dI = E_\gamma(I \rightarrow I - 2)/2$ . The figures are taken from Ref. [136].

each TSD band has a constant  $\mathcal{I}^{(2)}$  for the entire range of  $\hbar\omega$ . Nonetheless, if one compares the averaged data, then the theoretical and measured lines would lie quite close to each other. On the other side, the experimental data exhibits some staggering (e.g., band TSD1 from  $^{161}\text{Lu}$ ) and even sharp changes in magnitude, as it is the case for TSD2 from  $^{161}\text{Lu}$  and  $^{165}\text{Lu}$ . In  $^{161}\text{Lu}$ , the abrupt increase is caused by the alignment of the odd-proton angular momentum, showing up at  $\hbar\omega = 0.45$  MeV. The staggering behavior appearing in the low  $\hbar\omega$  region is caused by the interaction between states from strongly deformed bands and their neighboring normally deformed structures. Remarkable the fact that TSD1 from  $^{165}\text{Lu}$  exhibits a rather constant dynamic MOI (just as the theoretical value) except for

the first two states. Comparing the present calculations with the results from Ref. [100], an overall improvement in the agreement with the experimental data can be observed.

#### 4.4.6 Electromagnetic Transitions

The electromagnetic transitions for  $^{161,163,165,167}\text{Lu}$  will be calculated within the **W<sub>1</sub>** formalism, and then compared with the experimental data. For collective phenomena, one usually expects two ‘main’ characteristics to arise: *a*) the transitions between neighboring bands to be predominantly of E2 character and *b*) the states have large quadrupole moments. In fact, as it was discussed in Chapters 2 and 3, the large quadrupole moments and large mixing ratios are regarded as essential ‘tests’ for wobbling behavior.

For the numerical application, the electric quadrupole E2 transitions will be examined in the first part, while the magnetic dipole M1 transitions are addressed in the second part. Concerning the transitions, the *intraband* as well as the *interband* ones need to be evaluated. Because of the collective nature of the wobbling bands, the spin difference within a band is  $\Delta I = 2\hbar$ , while two states from adjacent bands only differ by  $\Delta I = 1\hbar$  (recall Fig. 3.1 from the discussion in Section 3.1). The difference between interband/intraband transitions can be seen in Fig. 4.27. Therein, the E2 transitions are sketched for levels belonging to the same band and levels from different bands. The allowed spin sequences for each band are also exemplified. The magnetic transitions for wobbling states have a dipole nature. Experimental observations point out that in collective spectra these M1 transitions are typically quite small when compared with the E2 case. Moreover, the ‘competition’ between E2 and M1 for a state  $I$  is reflected in the mixing ratio  $\delta$ , which is expected to be large for the studied isotopes.

The transition probabilities between states that comprise excited spectra are determined from the matrix elements (m.e.) of the *transition operators* (recall discussion in Section 2.2.9.4 from Chapter 2.2). The calculations are made in the laboratory (lab) system, meaning that the multipole operators must be expressed in terms of the *intrinsic* ones via the Wigner- $\mathcal{D}$  functions [1, 148]:

$$\mathcal{M}(\lambda, \mu) = \sum_{\nu} \mathcal{D}_{\mu\nu}^{\lambda} \mathcal{M}(\lambda, \nu) , \quad (4.64)$$

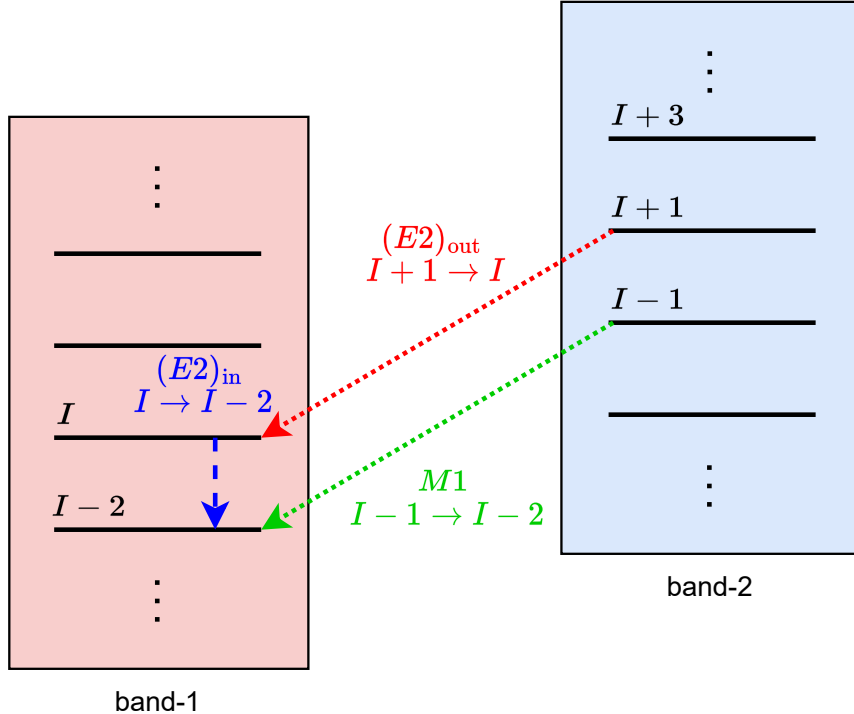


FIGURE 4.27: Schematic representation with the electric quadrupole and magnetic dipole transitions occurring in wobbling spectra of nuclei. The *intraband* values ( $E2_{in}$ ; blue) represent the transitions between an initial state  $I_i$  and a final state  $I_f$  belonging to the same band, which are characterized by  $\Delta I = I_i - I_f = 2\hbar$ . On the other hand, the *interband* values ( $E2_{out}$ ; red) take place between states belonging to two contiguous bands, and they are characterized by  $\Delta I = 1\hbar$ . Lastly, the magnetic transitions are marked by the green  $M1$  arrow.

where  $\mathcal{M}(\lambda, \mu)$  represents the lab operator and  $\mathcal{M}(\lambda, \nu)$  is the intrinsic multipole operator. The quantities of interest here are  $\mathcal{M}(E2, \mu)$  for the electric quadrupole transitions and  $\mathcal{M}(M1, \mu)$  for the magnetic dipole transitions. Each case will be treated individually in the following subsections, starting with the analytical expressions and finally providing the numerical results.

#### 4.4.6.1 E2 Transitions

For the E2 transitions, one has to replace  $\lambda = 2$  in Eq. (4.64) and the *quadrupole transition operator* becomes [101, 148]:

$$\mathcal{M}(E2, \mu) = [\mathcal{D}_{\mu 0}^2 Q_0 - (D_{\mu 2}^2 + D_{\mu -2}^2) Q_2] + e \sum_{\nu=-2,0,2} \mathcal{D}_{\mu \nu}^2 r^2 Y_2^\nu . \quad (4.65)$$

The spherical harmonics appear in Eq. (4.65) according to the textbook expression of the electric multipole operator  $\mathcal{M}(E\lambda, \mu)$ , which is proportional to  $r^\lambda Y_\lambda^\mu$  [54]. The two (intrinsic) quadrupole moments  $Q_0$  and  $Q_2$  represent a measure of deformation and asymmetry of the nuclear shape, marking a *departure* from spherical symmetry. They are expressed in terms of the deformation parameters  $\beta$  and  $\gamma$  as [100]:

$$Q_0 = \frac{3}{4\pi} Z R^2 \beta \cos \gamma , \quad Q_2 = \frac{3}{4\pi} Z R^2 \beta \sin \gamma / \sqrt{2} . \quad (4.66)$$

These are quite similar with the quantities given in Eqs. (2.50) and (3.19) from Chapters 2 and 3, respectively. Since the triaxial system can be regarded as a collective core + a single particle, the electric transition operator defined in  $\mathbf{W}_1$  can be described as an operator that is separated into a *collective* term and a *single-particle* term. As a matter of fact, it can be seen from Eq. (4.65) that the term inside squared brackets is the collective one, while the products  $r^2 Y_2^\nu$  comprise the odd-proton contribution. These two terms can be further condensed into [136]:

$$\mathcal{M}(E2, \mu) \equiv T_{2\mu}^{\text{coll}} + T_{2\mu}^{\text{sp}} . \quad (4.67)$$

Besides the electric transition operator, the wave-functions for the wobbling bands considered in the current picture are also needed. The ground-bands are attained from the variational principle (the trial function sketched in Eqs. (4.4) - (4.5)):

$$\begin{aligned} |\Psi_{IM;j}\rangle &= \mathcal{N} e^{z\hat{I}_-} e^{s\hat{j}_-} |IMI\rangle |jj\rangle = \\ &= \sum_{K=-I}^I \sum_{\Omega=-j}^j \sqrt{\frac{(2I)!}{(I-K)!(I+K)!}} \sqrt{\frac{(2j)!}{(j-\Omega)!(j+\Omega)!}} \times \\ &\quad \times \frac{z^{I+K}}{(1+|z|^2)^I} \frac{s^{j+\Omega}}{(1+|s|^2)^j} |IMK\rangle |j\Omega\rangle , \end{aligned} \quad (4.68)$$

where the summation in terms of the  $K$  and  $\Omega$  components is consistent with the one employed in Ref. [83]. Note that the complex variables  $(z; s)$  correspond to the classical coordinates  $(r, \varphi; f, \psi)$  via the transformations employed in Section 4.2.2 (see Eqs. (4.9), and (4.11) - (4.12)). The set  $(r, \varphi; f, \psi)$  brought the equations of motion to a canonical form and were explicitly given in Eq. (4.13) - 4.14. Through Eq. (4.18) it was shown that the CEF from Eq. (4.15) is minimal in the point  $p_0$ .

Evaluating the wave-function specified in Eq. (4.68) around this minimum point, the expression of  $|\Psi_{IM;j}\rangle$  turns out to be [101, 136]:

$$|\Psi_{IM;j}\rangle|_{p_0} = \sum_{K\Omega} C_{IK} C_{j\Omega} |IMK\rangle |j\Omega\rangle |\emptyset\rangle_I , \quad (4.69)$$

with the two factors  $C_{IK}$  and  $C_{j\Omega}$  expressed in terms of the binomial coefficients as in Ref. [39]:

$$C_{IK} = \frac{1}{2^I} \binom{2I}{I-K}^{1/2}, \quad C_{j\Omega} = \frac{1}{2^j} \binom{2j}{j-\Omega}^{1/2}, \quad (4.70)$$

and  $|\emptyset\rangle_I$  being the vacuum state for the boson creation and annihilation operators  $(a^\dagger, a; b^\dagger, b)$  that emerged by means of the re-quantization procedure applied in Eqs. (4.38) - (4.41) for the classical coordinates  $(r, \varphi; f, \psi)$ .

Regarding the wave-functions that will be utilized for the numerical calculations of  $B(E2)$  and  $B(M1)$  in the **W<sub>1</sub>** picture, these can be constructed from the expansion of  $|\Psi_{IM;j}\rangle$  up to first-order (abbreviated ‘1st or.’) in the coordinates  $(r, \varphi; f, \psi)$  around the point  $p_0$ , and then perform re-quantization of the coordinates, which results in Eq. (4.69) acquiring the new structure [39, 101, 136]:

$$\begin{aligned} |\Psi_{IM;j}\rangle|_{p_0}^{\text{1st or.}} \equiv & \left| \Psi_{IM;j}^{(1)} \right\rangle = \sum_{K\Omega} C_{IK} C_{j\Omega} |IMK\rangle |j\Omega\rangle \times \\ & \times \left\{ 1 + \frac{i}{\sqrt{2}} \left[ \left( \frac{K}{I} k_1 + \frac{I-K}{k_1} \right) a^\dagger + \left( \frac{\Omega}{j} k_2 + \frac{j-\Omega}{k_2} \right) b^\dagger \right] \right\} |\emptyset\rangle_I . \end{aligned} \quad (4.71)$$

Looking at Eq. (4.71) it can be seen that the first-order expansion is reflected through the presence of  $a^\dagger$  and  $b^\dagger$  as independent variables (that is, no mixed or quadratic components). The canonicity factors  $k_1, k_2$  defined in Eq. (4.42) also show up for every coordinate. Lastly,  $K, \Omega$  are the projections onto the rotational axis of the total and single-particle angular momentum vectors in the intrinsic coordinate system, respectively.

With the expressions of the E2 transition operator granted by Eq. (4.65) and wave-functions from Eq. (4.71), the matrix elements of  $\mathcal{M}(E2, \mu)$  can be finally constructed. The reduced transition probabilities are defined more generally as

[148]:

$$\begin{aligned} B(E2; I_i \rightarrow I_f) &= \sum_{M_i M_f \mu} |\langle \Psi_{I_i M_i; j} | \mathcal{M}(E2, \mu) | \Psi_{I_f M_f; j} \rangle|^2 = \\ &= |\langle \Psi_{I_i} | \mathcal{M}(E2) | \Psi_{I_f} \rangle|^2 . \end{aligned} \quad (4.72)$$

The initial and final states from Eq. (4.72) are represented by  $I_i$  and  $I_f$ , respectively. Moreover, the subscript signifying the single-particle angular momentum and the superscript ‘(1)’ that appear in  $|\Psi_{I-1 M-1; j}^{(1)}\rangle$  were dropped. The last term of the equality has no dependence on the projections  $M$ , and it was obtained by applying the Wigner-Eckart theorem:

$$\langle \Psi_{I_i M_i; j} | \mathcal{M}(\lambda, \mu) | \Psi_{I_f M_f; j} \rangle = C_{M_f \mu M_i}^{I_f \lambda I_i} \langle \Psi_{I_i} | \mathcal{M}(\lambda) | \Psi_{I_f} \rangle . \quad (4.73)$$

From the structure of  $\mathcal{M}(E2, \mu)$  given in Eq. (4.67) and the probabilities specified in Eq. (4.72), it results that there will be two sets of reduced matrix elements, i.e.,  $\langle \Psi_{I_i} | T_2^{\text{coll}} | \Psi_{I_f} \rangle$  and  $\langle \Psi_{I_i} | T_2^{\text{sp}} | \Psi_{I_f} \rangle$ , respectively. Their analytical expressions are given explicitly in Appendix D from [39]. The matrix element  $\langle \Psi_{I_i} | \mathcal{M}(E2) | \Psi_{I_f} \rangle$  is calculated in units of  $e \cdot \text{fm}^2$  or  $e \cdot b$ , such that  $B(E2)$  is measured in  $e^2 \cdot b^2$ . Recall that when  $B(E2)$  was firstly discussed (Section 2.2.9.4 with Eq. (2.52)) there was no inference on the transition operator’s matrix elements, while here one finally adopts them.

Because the formalism **W<sub>1</sub>** uses a set of free MOI by fitting Eq. (4.60), no assumption on their actual nature (that is neither hydrodynamical nor rigid) is made. Moreover, the calculated parameters  $\mathcal{P}_{\text{fit}}$  shown in Table 4.7 indicate that the maximal MOI is  $\mathcal{I}_1$  for each isotope. Accordingly, the quadrupole components  $Q_0$  and  $Q_2$  give the degree of elongation and asymmetry of the charge/mass distribution with respect to this axis. In order to keep a consistent numerical procedure, the two quadrupole moments should also be considered as free quantities when computing the transition probabilities (Eq. (4.72)). Consequently, the components are evaluated per each isotope by fixing one intraband transition from TSD1 (first excited to yrast) and one interband transition TSD2  $\rightarrow$  TSD1 (first state  $I$  in TSD2 to  $I - 1$  in TSD1). With this method, the values  $Q_0 = 18.43 \text{ eb}$  and  $Q_2 = 19.81 \text{ eb}$  are determined for  $^{163}\text{Lu}$ . The results for the other isotopes are collected and graphically represented in Fig. 4.28, where a change of ordering between the two quadrupole components can be observed at  $^{165}\text{Lu}$ . Besides that,



FIGURE 4.28: The calculated quadrupole moments  $Q_0$  and  $Q_2$  from 4.65. The unit for  $Q$  is  $e \cdot b$ . See text for details on their numerical determination. Figure is taken as is from Ref. [136].

the magnitude of the components drops quite low compared to the neighboring nuclei. Remarking the fact that the isotope  $^{167}\text{Lu}$  has an almost identical set of quadrupole moments.

The *quadrupole transition moment*  $Q_I$  can be also calculated for a state  $I$  in terms of the reduced transition probability  $B(E2; I \rightarrow I - 2)$ . Their unusually large values (measured in units of  $b$ ) are a clear indicator for triaxial deformations. The probability of the transition  $I \rightarrow I - 2$  is expressed in terms of the moment  $Q_I$  as [149]:

$$B(E2; I \rightarrow I - 2) = \frac{5}{16\pi} (C_{K0K}^{I2I-2})^2 Q_I^2 , \quad (4.74)$$

meaning that one can extract  $Q_I$  for every state from a band using the following definition:

$$Q_I = \sqrt{\frac{16\pi}{5}} \cdot \frac{\langle \Psi_I | |\mathcal{M}(E2)| | \Psi_{I-2} \rangle}{C_{K0K}^{I2I-2}} , \quad (4.75)$$

which will be adopted throughout the calculations. Keep in mind that in practice, this quantity cannot be inferred self-consistently, but only through the already known  $B(E2)$  transition probabilities (or equivalently, the reduced m.e.). As such, when the experimental  $Q_I$  values are addressed, they are in fact obtained directly from the experimental  $B(E2)$  quantities.

In addition to the quadrupole moment for in-band transitions  $I \rightarrow I - 2$ , the *static quadrupole moment* (SQM) can be studied [1]. It gives a measure of nuclear charge distribution associated with the collective rotational motion of the nucleus [150, 151], and it arises as the diagonal m.e. of  $\mathcal{M}(E2)$  (that is  $I_i = I_f$ , unlike  $Q_I$ , where  $\Delta I_{i \rightarrow f} = 2$ ). The SQM is nothing else than the measured quadrupole moment introduced in Section 2.2.9.4, having Eq. (2.51) as a general expression. From Eq. (4.72) and Eqs. (4.74) - (4.75), it results that the SQM can be expressed straight from the transition quadrupole moment via the relation [1]:

$$Q_{\text{SQM}}(I) = C_{K0K}^{I2I} C_{I0I}^{I2I} Q_I . \quad (4.76)$$

In order to test the validity of the current interpretation, the reduced transition probabilities  $B(E2)$  are calculated using Eq. (4.72) and compared with the experimental data for each isotope. The numerical results for the intraband transitions in TSD1 and TSD2 are shown in Table 4.8. Furthermore, Table 4.9 shows the interband transitions  $I \rightarrow I - 1$ , which were evaluated as  $B(E2; I \rightarrow I - 1) = |\langle \Psi_I | \mathcal{M}(E2) | \Psi_{I-2} \rangle|^2$ . Both the transition quadrupole moment  $Q_I$  (Eq. (4.75)) and the SQM (Eq. (4.76)) are compared with the experimental data in Table 4.10.

Concerning the static quadrupole moments presented in Table 4.10, by keeping the value of  $K$  fixed across each state, then for sufficiently large spins  $Q_{\text{SQM}}(I) \approx -Q_I/2$  [1]. Such a behavior translates to the total a.m. becoming perpendicular to the 1-axis. When  $K = I$ , any shape fluctuation emerging due to rotational motion will become negligible and  $Q_{\text{SQM}}(I) \rightarrow Q_I$  [1]. Two graphical representations showing  $Q_{\text{SQM}}(I)$  with fixed  $K = 1/2$  are made for TSD1 and TSD2 from  $^{163}\text{Lu}$  in Figs. 4.29 and 4.30, respectively. The two figures also depict the limits  $-Q_I/2$  and  $Q_I$ , which are provided by replacing the experimental set of  $Q_I$  with an average value  $\langle Q_I \rangle$  in both bands. Remarking the fact that the theoretical points are below the  $-\langle Q_I \rangle/2$  line when  $K$  is kept fixed, but they lie above the  $\langle Q_I \rangle$  when  $K = I$ .

Unfortunately, experimental data are only available for  $^{163}\text{Lu}$ , meaning that the quality of the model cannot be tested directly by comparisons of the transition probabilities in the other nuclei. Nevertheless, from the similarities of the isotopes in regards to the collective quantities assessed throughout the previous sections (e.g., dynamical MOI, alignments, and so on) one expects an agreement across the electromagnetic transitions as well.

TABLE 4.8: The reduced intraband transition probabilities for  $^{161,163,165,167}\text{Lu}$  obtained through Eq. (4.72) are compared with the experimental data (where available) taken from Ref. [145].

$B(E2; I \rightarrow I - 2)$ [e <sup>2</sup> · b <sup>2</sup> ]				$B(E2; I \rightarrow I - 2)$ [e <sup>2</sup> · b <sup>2</sup> ]			
TSD1	$I$	Theory	Experiment	TSD2	$I$	Theory	Experiment
$^{161}\text{Lu}$	41/2	2.80	-	$^{161}\text{Lu}$	47/2	2.84	-
	45/2	2.83	-		51/2	2.86	-
	49/2	2.85	-		55/2	2.88	-
	53/2	2.87	-		59/2	2.89	-
	57/2	2.88	-		63/2	2.54	-
	61/2	2.90	-		67/2	2.51	-
	65/2	2.91	-		71/2	2.49	-
	69/2	2.92	-				
$^{163}\text{Lu}$	41/2	2.80	3.45	$^{163}\text{Lu}$	47/2	2.71	2.56
	45/2	2.74	3.07		51/2	2.66	2.67
	49/2	2.69	2.45		55/2	2.62	2.81
	53/2	2.64	2.84		59/2	2.58	2.19
	57/2	2.60	2.50		63/2	2.54	2.25
	61/2	2.56	1.99		67/2	2.51	1.60
	65/2	2.53	1.95		71/2	2.49	1.61
	69/2	2.50	2.10				
$^{165}\text{Lu}$	41/2	3.63	-	$^{165}\text{Lu}$	47/2	3.68	-
	45/2	3.66	-		51/2	3.71	-
	49/2	3.69	-		55/2	3.73	-
	53/2	3.72	-		59/2	3.75	-
	57/2	3.77	-		63/2	3.77	-
	61/2	3.76	-		67/2	3.78	-
	65/2	3.77	-		71/2	3.79	-
	69/2	3.79	-				
$^{167}\text{Lu}$	41/2	2.80	-	$^{167}\text{Lu}$	47/2	2.84	-
	45/2	2.83	-		51/2	2.86	-
	49/2	2.85	-		55/2	2.88	-
	53/2	2.87	-		59/2	2.89	-
	57/2	2.88	-		63/2	2.90	-
	61/2	2.90	-		67/2	2.92	-
	65/2	2.91	-		71/2	2.93	-
	69/2	2.92	-				

TABLE 4.9: The reduced interband transition probabilities for connecting states  $I \in \text{TSD2} \rightarrow I - 1 \in \text{TSD1}$ . Experimental data are taken from Ref. [145].

Nucleus	$B(E2; I \rightarrow I - 1)$			Nucleus	$B(E2; I \rightarrow I - 1)$		
	$[e^2 \cdot b^2]$		Exp		$[e^2 \cdot b^2]$		Exp
	$I$	Th	Exp		$I$	Th	Exp
$^{161}\text{Lu}$	$47/2$	0.54	-	$^{165}\text{Lu}$	$47/2$	0.37	-
	$51/2$	0.47	-		$51/2$	0.34	-
	$55/2$	0.42	-		$55/2$	0.32	-
	$59/2$	0.37	-		$59/2$	0.29	-
	$63/2$	0.33	-		$63/2$	0.27	-
$^{163}\text{Lu}$	$47/2$	0.54	0.54	$^{167}\text{Lu}$	$39/2$	0.66	-
	$51/2$	0.49	0.54		$47/2$	0.54	-
	$55/2$	0.44	0.70		$51/2$	0.49	-
	$59/2$	0.34	0.65		$55/2$	0.45	-
	$63/2$	0.36	0.66		$59/2$	0.41	-
					$63/2$	0.38	-

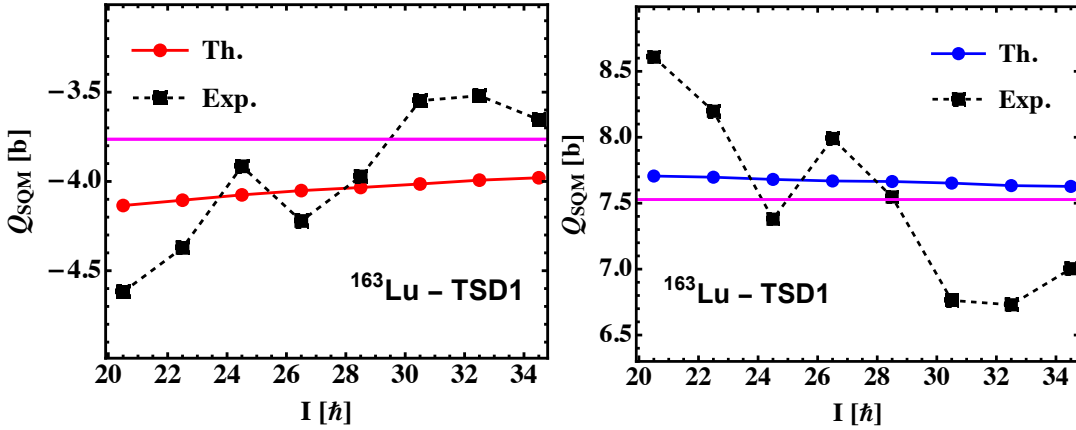


FIGURE 4.29: The static quadrupole moment from Eq. (4.76) graphically represented as a function of total spin  $I$  for the first band in  $^{163}\text{Lu}$ . **Left:** Calculations are done with  $K = 1/2$ . **Right:** Calculations are done with  $K = I$ . The magenta lines represent the limits  $-\langle Q_I \rangle / 2$  (left inset) and  $\langle Q_I \rangle$  (right inset).

#### 4.4.6.2 M1 Transitions

In what follows, the results concerning the magnetic transition probabilities will be analyzed. For the magnetic transitions within wobbling states, the corresponding operator is expressed as a collective plus a single-particle components, keeping thus a consistency with Eq. (4.67):

$$\mathcal{M}(M1; \mu) = M_{1\mu}^{\text{coll}} + M_{1\mu}^{\text{sp}} . \quad (4.77)$$

TABLE 4.10: The quadrupole transition moment  $Q_I$  (Eq. (4.75)) and the static quadrupole moment  $Q_{\text{SQM}}$  (Eq. (4.76)). For the calculation of  $Q_{\text{SQM}}$ ,  $K$  was fixed to  $K = 1/2$ . The experimental data are taken from Refs. [65, 145, 152]. The unit of measure is consistent with the one employed by Görgen et al. [152].

		$Q_I$ [b]		$Q_{\text{SQM}}$ [b]				$Q_I$ [b]		$Q_{\text{SQM}}$ [b]	
TSD1	$I$	Th	Exp	Th	Exp	TSD2	$I$	Th	Exp	Th	Exp
$^{161}\text{Lu}$	41/2	8.89	-	-4.13	-	$^{161}\text{Lu}$	47/2	8.92	-	-4.15	-
	45/2	8.91	-	-4.17	-		51/2	8.93	-	-4.18	-
	49/2	8.92	-	-4.20	-		55/2	8.95	-	-4.21	-
	53/2	8.94	-	-4.23	-		59/2	8.96	-	-4.24	-
	57/2	8.95	-	-4.25	-		63/2	8.97	-	-4.26	-
	61/2	8.96	-	-4.27	-		67/2	8.98	-	-4.28	-
	65/2	8.97	-	-4.28	-		71/2	8.98	-	-4.29	-
	69/2	8.98	-	-4.30	-						
$^{163}\text{Lu}$	41/2	8.89	9.93	-4.71	-4.62	$^{163}\text{Lu}$	47/2	8.71	8.51	-4.76	-3.99
	45/2	8.77	9.34	-4.75	-4.37		51/2	8.62	8.67	-4.80	-4.09
	49/2	8.66	8.32	-4.78	-3.92		55/2	8.53	8.88	-4.83	-4.21
	53/2	8.57	8.93	-4.81	-4.22		59/2	8.46	7.82	-4.85	-3.72
	57/2	8.50	8.37	-4.84	-3.97		63/2	8.39	7.91	-4.87	-3.77
	61/2	8.43	7.45	-4.86	-3.55		67/2	8.34	6.66	-4.89	-3.19
	65/2	8.36	7.37	-4.88	-3.52		71/2	8.28	6.68	-4.90	-3.20
	69/2	8.31	7.63	-4.90	-3.65						
$^{165}\text{Lu}$	41/2	10.12	-	-4.71	-	$^{165}\text{Lu}$	47/2	10.15	-	-4.76	-
	45/2	10.14	-	-4.75	-		51/2	10.17	-	-4.80	-
	49/2	10.16	-	-4.78	-		55/2	10.19	-	-4.83	-
	53/2	10.18	-	-4.81	-		59/2	10.20	-	-4.85	-
	57/2	10.19	-	-4.84	-		63/2	10.21	-	-4.87	-
	61/2	10.21	-	-4.86	-		67/2	10.22	-	-4.89	-
	65/2	10.22	-	-4.88	-		71/2	10.23	-	-4.90	-
	69/2	10.23	-	-4.90	-						
$^{167}\text{Lu}$	41/2	8.90	-	-4.13	-	$^{167}\text{Lu}$	47/2	8.92	-	-4.15	-
	45/2	8.91	-	-4.17	-		51/2	8.94	-	-4.18	-
	49/2	8.92	-	-4.20	-		55/2	8.95	-	-4.21	-
	53/2	8.94	-	-4.23	-		59/2	8.96	-	-4.24	-
	57/2	8.95	-	-4.25	-		63/2	8.97	-	-4.26	-
	61/2	8.96	-	-4.27	-		67/2	8.98	-	-4.28	-
	65/2	8.97	-	-4.28	-		71/2	8.98	-	-4.29	-
	69/2	8.98	-	-4.30	-						

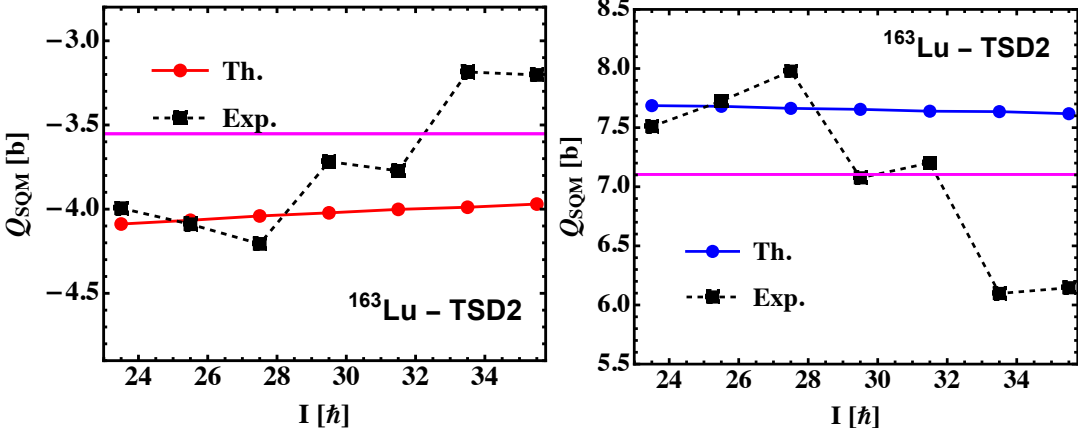


FIGURE 4.30: The static quadrupole moment from Eq. (4.76) graphically represented as a function of total spin  $I$  for the band TSD2 in  $^{163}\text{Lu}$ . **Left:** Calculations are done with  $K = 1/2$ . **Right:** Calculations are done with  $K = I$ . The magenta lines represent the limits  $-\langle Q_I \rangle / 2$  (left inset) and  $\langle Q_I \rangle$  (right inset).

The magnetic transition operator adopted in the present formalism is defined as:

$$\mathcal{M}(M1, \mu) = \sqrt{\frac{3}{4\pi}} \mu_N \sum_{\nu=-1,0,1} \mathcal{D}_{\mu\nu}^1 [g_R R_\nu + q g_j j_\nu] , \quad (4.78)$$

which is in accordance to the general definition from Ref. [148]. The factor  $\mu_N$  from Eq. (4.78) represents the nuclear magneton  $\mu_N = e\hbar/2m_p c$ ,  $g_R = Z/A$  is the gyromagnetic factor for the core,  $g_j$  is the proton's free gyromagnetic factor ( $g$ -factor) [153] and  $\mathcal{D}_{\mu\nu}^1$  is the Wigner- $\mathcal{D}$  function expressing the magnetic operator in the lab system. The spherical components  $R = \{R_{-1}, R_0, R_{+1}\}$  and  $j = \{j_{-1}, j_0, j_{+1}\}$  are defined in terms of the cartesian ones via the relations outlined in Ref. [154]. In these calculations, the single-particle  $g$ -factor is quenched by the constant value  $q = 0.430$  in order to take into account the polarization effects, which are not included in the free factor. Indeed, such a quenching is necessary due to the interaction of the odd-proton with the currents that are distributed inside the core. The same quenching factor is applied to every isotope. The wave-functions involved in the m.e. of the  $\mathcal{M}(M1)$  transition operator are expressed in terms of the angular momenta for the collective core  $\mathbf{R}_\mathcal{C}$  and the odd proton  $\mathbf{j}_Q$ , leading to the structure:

$$|\Phi_{IM;j}\rangle = \frac{1}{\sqrt{2j+1}} \sum_{M_R \Omega} C_{M_R \Omega M}^{RjI} C_{RK} |RM_RK\rangle |j\Omega\rangle , \quad (4.79)$$

where  $M_R$  is the projection of the core a.m. onto the quantization axis (in the lab

frame). The quantum numbers  $K$  and  $\Omega$  still signify the projections of  $\mathbf{I}$  and  $\mathbf{j}_{\mathcal{Q}}$  onto the quantization axis (in the intrinsic frame). Obviously, the term  $C_{RK}$  is equivalent with the factors given in Eq. (4.70). Note that this wave-function has a different shape than the one from Eq. (4.71), where the summation was in terms of the state vectors  $|IMK\rangle$  and not  $|RM_RK\rangle$ . The reduced  $B(M1)$  transition probabilities can be formulated now as [39]:

$$\begin{aligned} B(M1; I_i \rightarrow I_f) &= \sum_{M_i M_f \mu} |\langle \Phi_{I_i M_i} | \mathcal{M}(M1, \mu) | \Phi_{I_f M_f} \rangle|^2 = \\ &= |\langle \Phi_{I_i} | \mathcal{M}(M1) | \Phi_{I_f} \rangle|^2 . \end{aligned} \quad (4.80)$$

Similarly as it was the case for  $\mathcal{M}(E2)$ , the m.e. of  $\mathcal{M}(M1)$  are treated separately as  $\langle \Phi_{I_i} | |M_1^{\text{coll}}| | \Phi_{I_f} \rangle$  for  $M_{1\mu}^{\text{coll}}$  and  $\langle \Phi_{I_i} | |M_1^{\text{sp}}| | \Phi_{I_f} \rangle$  for  $M_{1\mu}^{\text{sp}}$ , respectively. Their expressions are given in Appendix C of Ref. [39]. With the reduced matrix elements of  $\mathcal{M}(E2)$  and  $\mathcal{M}(M1)$  one can determine the mixing ratio, which shows the *competition* between E2 and M1 transitions from states belonging to TSD2 and TSD1 [129, 148]:

$$\delta = 8.87 \cdot 10^{-4} E_{if} \frac{\langle I_i | | \mathcal{M}(E2) | | I_f \rangle}{\langle I_i | | \mathcal{M}(M1) | | I_f \rangle} , \quad (4.81)$$

where the  $E2$  m.e. has units of  $e \cdot \text{fm}^2$  and  $M1$  m.e. has units of  $e \cdot \text{fm}$ . The transition energy between the initial and final state is represented by  $E_{if}$  and its unit is MeV. Results obtained with the current formalism for the reduced transition probabilities  $B(M1)$  and the mixing ratios  $\delta$  are shown in Table 4.11 for  $^{161,163,165,167}\text{Lu}$ . Looking at the data concerning the  $B(M1)$  values for  $^{163}\text{Lu}$ , the theoretical results agree with the experimental data quite well. Indeed, there is an increase with angular momentum  $I$ , and it is more pronounced for the measured values. Regarding the mixing ratios, it seems that the current model reproduces the sign, but the calculated ratios are almost half the observed ones. Nevertheless,  $\delta$  is much larger than 1, which is in agreement with the signature of wobbling nature for these bands.

Knowing the  $E2$  transition probabilities, one can determine the branching ratios  $B(E2)_{\text{out}}/B(E2)_{\text{in}}$  for the TSD2 states. Experimentally, the data are evaluated from lifetime measurements or spin polarization assessments [78, 106, 155]. The  $E2$  branching ratio practically shows the predominant character of the transition within a band, i.e., whether they decay to a neighboring band via  $I - 1$  transitions

TABLE 4.11: The numerical results for the reduced  $M1$  transitions between states  $I \in \text{TSD2} \rightarrow I - 1 \in \text{TSD1}$ . The calculated mixing ratio  $\delta(E2/M1)$  (Eq. (4.81)) are also shown in comparison with the experimental data, which are taken from Refs. [65, 145, 152].

		$B(M1)$		$\delta(E2/M1)$				$B(M1)$		$\delta(E2/M1)$			
		$[\mu_N^2]$		[MeV · fm]				$[\mu_N^2]$		[MeV · fm]			
		$I$	Th	Exp	Th	Exp			$I$	Th	Exp	Th	Exp
$^{161}\text{Lu}$	$47/2$	0.018	-	-1.55	-		$47/2$	0.017	0.017	1.55	-3.1		
	$51/2$	0.018	-	-1.56	-		$51/2$	0.018	0.017	-1.58	-3.1		
	$55/2$	0.019	-	-1.57	-	$^{163}\text{Lu}$	$55/2$	0.019	0.024	-1.61	-3.1		
	$59/2$	0.019	-	-1.58	-		$59/2$	0.019	0.023	-1.64	-3.1		
	$63/2$	0.020	-	-1.59	-		$63/2$	0.020	0.024	-1.66	-		
$^{165}\text{Lu}$	$47/2$	0.018	-	-1.32	-		$39/2$	0.016	-	-1.67	-3.1		
	$51/2$	0.018	-	-1.34	-		$47/2$	0.018	-	-1.65	-5.1		
	$55/2$	0.019	-	-1.36	-	$^{167}\text{Lu}$	$51/2$	0.018	-	-1.65	-3.9		
	$59/2$	0.019	-	-1.38	-		$55/2$	0.019	-	-1.65	-		
	$63/2$	0.020	-	-1.40	-		$59/2$	0.019	-	-1.65	-		
							$63/2$	0.020	-	-1.65	-		

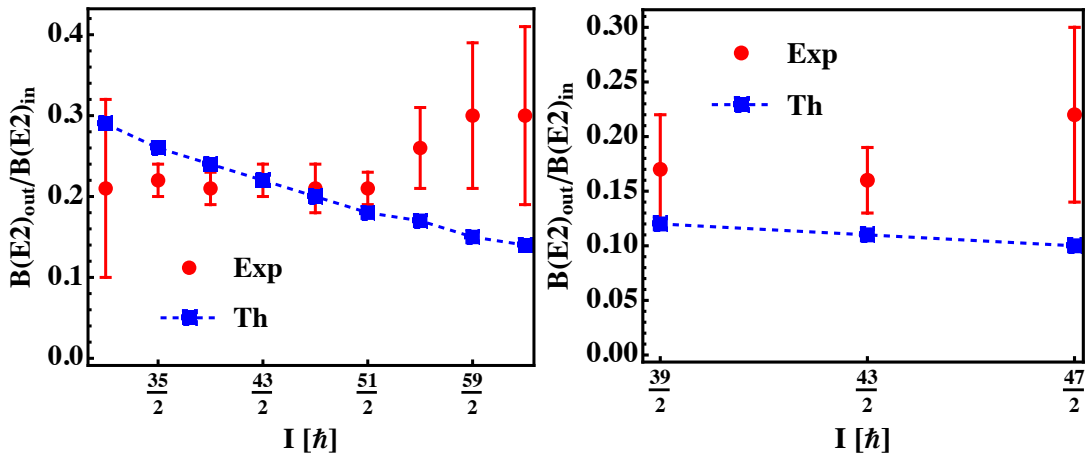


FIGURE 4.31: The branching ratio for E2 transitions in  $^{163}\text{Lu}$  (left) and  $^{165}\text{Lu}$  (right). The spin states belong to TSD2 in both isotopes. Experimental data are taken from Refs. [58, 156, 157] ( $A = 163$ ) and Ref. [124] ( $A = 165$ ).

or to a lower  $I - 2$  in the same band. These results are shown in Fig. 4.31 for  $^{163,165}\text{Lu}$  and the left inset of Fig. 4.32 for  $^{167}\text{Lu}$ .

Additionally, the ratios  $B(M1)/B(E2)_{\text{out}}$  are evaluated for a few known levels from  $^{163}\text{Lu}$ , and a comparison between the theoretical and experimental data is depicted in the right inset of Fig. 4.32. These ratios are considered as essential information, since for collective excitations it is expected to be smaller than unity (E2 character prevails). Experimentally, they can be extracted from the angular distributions and angular correlations [155] (which are beyond the scope of this

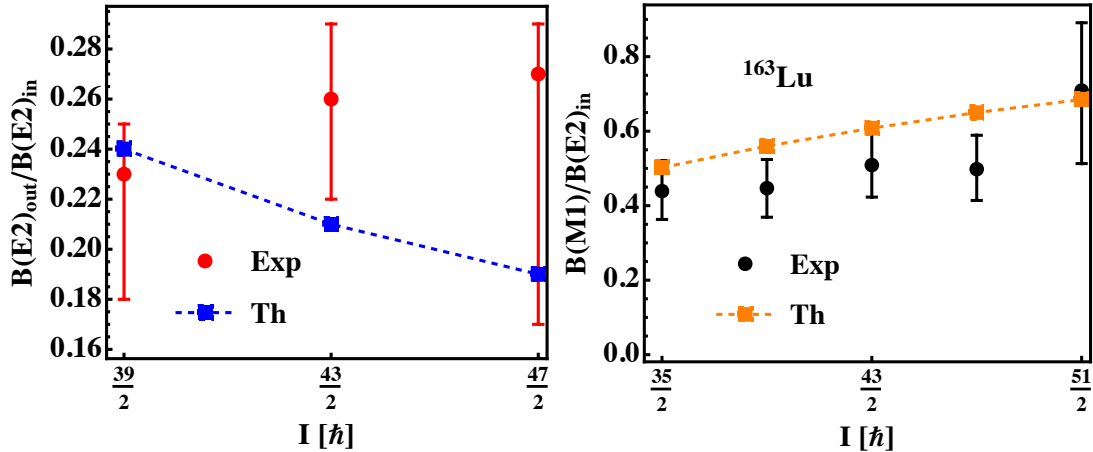


FIGURE 4.32: **Left:** The calculated branching ratio for E2 transitions in  $^{163}\text{Lu}$  are compared with the experimental data of Ref. [125]. **Right:** The ratio  $B(M1)/B(E2)_{\text{in}}$  measured in units of  $\mu_N^2/(e^2 b^2)$  for a few states connecting TSD2 and TSD1 from  $^{163}\text{Lu}$ . Experimental data are taken from Ref. [145].

work).

Taking a look at the branching ratios illustrated in Figs. 4.31 - 4.32, it is remarkable that the model shows a decrease of the values with increasing spin, while the experimental points out the opposite behavior. This is even more emphasized in  $^{163}\text{Lu}$ , where the calculated ratios decrease from 0.3 at  $I = 31/2$  to about 0.1 at  $I \geq 59/2$ . A similar result was obtained in Frauendorf in Ref. [9], where by using the QTR model, a decreasing  $B(E2)_{\text{out}}/B(E2)_{\text{in}}$  ratio emerged, although his model also showed some magnitudes larger than 0.4 for  $I \leq 15$ . Nevertheless, the agreement with the measured data is reproduced very well by both **W<sub>1</sub>** and Ref. [9]. *This shows that the current semi-classical formalism is on par with other descriptions of the wobbling motion available within the literature.* Conversely, the  $B(M1)/B(E2)_{\text{in}}$  ratios from Fig. 4.32 do show the same increasing trend with angular momentum, and besides the  $I = 39/2$  and  $I = 47/2$  states, all the other evaluations lie within the experimental uncertainties.

Besides the reduced transition probabilities, the *static magnetic moments*  $\mu_I$  can be evaluated in accordance with the definition given by Bohr [1]:

$$\mu_I = g_R I + g' \frac{K^2}{I+1} , \quad (4.82)$$

where  $g'$  is directly extracted from  $B(M1; I \rightarrow I-1)$  transitions, while the projection  $K$  remains unchanged from  $I$  to  $I-1$ . The factor  $g_R$  is the same as the one from Eq. (4.78), i.e.,  $g_R = Z/A$ . It follows that the expression of  $g'$  is given

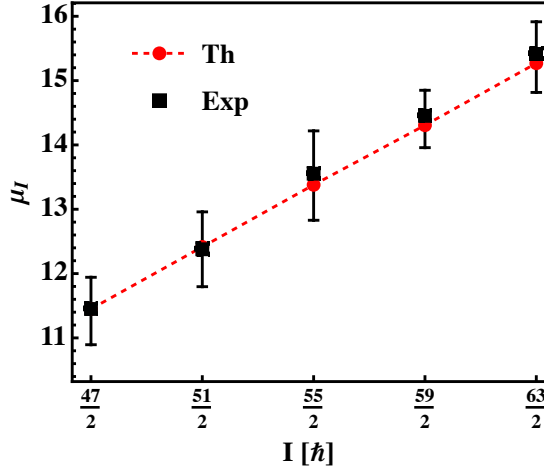


FIGURE 4.33: The static magnetic moment  $\mu_I$  for  $^{163}\text{Lu}$ , calculated according to Eq. (4.82). The value of  $K$  was fixed to  $K = I - 1$  for every  $I$  state belonging to TSD2 decaying to  $I - 1 \in \text{TSD1}$ .

by the following rule [1]:

$$g' = \sqrt{\frac{4\pi}{3}} \frac{1}{\mu_N} \left[ \frac{B(M1; I \rightarrow I-1)}{K^2 (C_{K0}^{I-1} C_{K0}^{I-1})^2} \right]^{1/2}. \quad (4.83)$$

By firstly evaluating  $g'$ , then the static moments from Eq. (4.82) can be determined. Some results for TSD2 from  $^{163}\text{Lu}$  are shown in comparison with the experimental estimates in Fig. 4.33, where obviously the good agreement is verified due to the consistency across the  $B(M1)$  values (see Table 4.11).

Concluding this section on electromagnetic transitions, several points should be outlined concerning the  $\mathbf{W}_1$  formalism. Indeed, starting with the definition of the general multipole operator (Eq. (4.64)), the electric quadrupole transition operator  $\mathcal{M}(E2, \mu)$  (Eq. (4.65)) and the magnetic dipole transition operator  $\mathcal{M}(M1, \mu)$  (Eq. (4.78)) were analyzed. Remarking the fact that they are composed of a term describing the collective core and a term related to the odd proton. Their matrix elements were required in order to obtain the transition probabilities between the wobbling states. In the case of  $E2$  transitions, the wave-function used for determining  $\langle \Psi_{I_i} | |\mathcal{M}(E2)| | \Psi_{I_f} \rangle$  was constructed in terms of  $|IMK\rangle$  and  $|j\Omega\rangle$  (see definition in Eq. (4.71)). For  $M1$  transitions, the wave-function from  $\langle \Phi_{I_i} | |\mathcal{M}(M1)| | \Phi_{I_f} \rangle$  was expressed in terms of the collective core  $\mathbf{R}_{\mathcal{C}}$  by following Eq. (4.79). The results for the transition probabilities were thus evaluated numerically and listed in Tables 4.8 - 4.11. The static quadrupole moments were evaluated using Eq. (4.76), and they are graphically represented in Figs. 4.29 -

4.30. Mixing ratios (Eq. (4.81)), branching ratios, and  $B(M1)/B(E2)_{\text{in}}$  were also compared with the experimental data (where available) in Table 4.11 and Figs. 4.31 - 4.32. Lastly, by using the definition of the static magnetic moment employed in Eq. (4.82), the theoretical values were compared to the experimental ones in Fig. 4.33. A reasonable agreement for all quantities is observed, which together with the results regarding the excitation energies indicate that the  $\mathbf{W}_1$  formalism proves to be an effective and accurate tool in studying the wobbling motion in a semi-classical picture.

## 4.5 Concluding Remarks

Some final remarks on the  $\mathbf{W}_1$  formalism portrayed throughout this chapter are worth emphasizing before continuing with the rest of the work. As mentioned,  $\mathbf{W}_0$  was the foundational part that lead to the development of a model which accurately characterizes the energy spectra of wobbling nuclei. From the variational principle (Eq. (4.4)) applied on the ground-band TSD1 and then the successive application of phonon operators on these states to generate TSD2,3,... (recall Fig. 4.1), one changed the methodology by introducing the renormalization of the bands (Eqs. (4.53) - (4.54)). Thereafter, the trial function in  $\mathbf{W}_1$  (Eq. (4.5)) is given as a product of two coherent states: one associated to the core and one to the odd proton. The initial Hamiltonian (Eq. (4.1)) was dequantized through the VP, and the Classical Energy Function emerged (Eq. (4.15)). Performing a linearization procedure on the equations of motion (Eqs. (4.12) - (4.14)) around the minimum point of the CEF, two wobbling frequencies are obtained:  $\Omega_1$  and  $\Omega_2$  (defined in Eq. (4.57)). The two frequencies define the motion of the core and the single particle, respectively. An alternative way of obtaining them was described in Section 4.2.5. Having the minimal term  $\mathcal{H}_{\min}$  (Eq. (4.58)) and  $\Omega_{1,2}$ , the general spectrum can be formed by following Eqs. (4.31) - (4.32). The fitting procedure of the renormalization uses the excitation energies instead of the absolute energies (recall Eq. (4.62) and the diagram from Fig. 4.9). Once the free parameters  $\mathcal{P}_{\text{fit}}$  are attained by minimizing the  $\chi^2$ -function (Eq. (4.60)), the calculation of several quantities can be performed, followed by the comparison with real data. An overall good agreement was achieved across the nuclides. Finally, calculations of the transition probabilities for  $^{161,163,165,167}\text{Lu}$  were performed, reproducing the experimental measurements quite well.

The concept of Signature Partner Bands was introduced for TSD1 and TSD2, where TSD2 is the unfavored partner of TSD1 and both bands have the phonon numbers  $n_{w_1} = n_{w_2} = 0$ . The Signature Partner argument holds here since, energetically, the states from TSD1 lie quite close to TSD2 ones. Keep in mind that the unfavored nature of TSD2 causes an upward shift relative to the ones from TSD1. Moreover, the calculation of the potential energies performed by the team in Ref. [39] shows similar properties between both bands as the minima are deep and comprise all states.

For the sake of completeness, the signature quantum number will be discussed in terms of the trial function adopted in  $\mathbf{W}_1$ . The Hamiltonian of a rigid rotor is invariant to rotations with  $\pi$  about an axis perpendicular to the symmetry axis [1]. The same invariance is true for triaxial nuclei, even though a symmetry axis cannot be assigned in these systems. In addition, the wave-functions that describe the degrees of freedom must also be invariant to rotations with  $\pi$  about the rotation axis. If one picks  $x$ -axis as the rotation and also the quantization axis (in a system labelled  $\{x, y, z\}$ ), then the ladder operators for the a.m. operator will acquire the form:

$$\hat{I}_{\mp} = \hat{I}_y \pm i\hat{I}_z ; \quad \hat{j}_{\mp} = \hat{j}_y \pm i\hat{j}_z , \quad (4.84)$$

and the rotation operator in the particle + rotor system must be constructed in terms of the angular momenta  $\hat{I}_x$  and  $\hat{j}_x$ , respectively. As such, the  $\mathcal{R}_x(\pi)$  operator is expressed as:

$$\mathcal{R}_x(\pi) = e^{-i\pi\hat{I}_x} \otimes e^{-i\pi\hat{j}_x} . \quad (4.85)$$

Acting with  $\mathcal{R}_x(\pi)$  on the trial function defined in Eq. (4.5) will make the change:

$$(\rho, \varphi; \sigma, \psi) \rightarrow (\rho, \varphi + \pi; \sigma, \psi + \pi) . \quad (4.86)$$

The complex variables  $z$  and  $s$  were expressed in terms of the classical coordinates as per Eq. (4.9). Because the CEF is invariant to Eq. (4.86), so must be the trial function  $|\Psi_{IM;j}\rangle$ . The eigenvalues of  $\mathcal{R}_x(\pi)$  acting on  $|\Psi_{IM;j}\rangle$  are  $r_x(\pi) = e^{-i\pi(I+j)}$ , meaning that  $r_x(\pi) = \pm i$ . The signature quantum number shows the invariance of the wave-function under this rotation, and in the case of odd-mass nuclei it is either  $\alpha = +1/2$  or  $\alpha = -1/2$ . The spin sequence  $\frac{13}{2}, \frac{17}{2}, \frac{21}{2}, \dots$  corresponds

to  $\alpha = 1/2$  and  $\frac{15}{2}, \frac{19}{2}, \frac{23}{2}, \dots$  to  $\alpha = -1/2$  (recall data depicted in Table 4.2). Indeed, the first set would correspond to TSD1 while the second set is identified with TSD2. This shows that the assignment of Signature Partner Bands for TSD1 and TSD2 is valid in the current formalism, since the wave-function describing the odd- $A$  nuclei admits states of both positive ( $+1/2$ ) and negative ( $-1/2$ ) signature.

With the formalism **W<sub>1</sub>** fully described in terms of a semi-classical spectrum that verifies the experimental data in a realistic fashion, one can now proceed to another description of the wobbling phenomenon. By using an *iteration* of **W<sub>1</sub>** several new concepts will be adopted through this extension, with the aim of obtaining a unified and consistent view of the wobbling motion for <sup>163</sup>Lu.



# Chapter 5

## Novel Description of the Wobbling Bands

A unique picture for the description of wobbling bands in odd nuclei will be developed in this chapter. This formalism is based on the  $\mathbf{W}_1$  approach, which was systematically treated in the previous chapter. Its validity was shown through the comparison with the experimental measurements for different quantities. The newly developed model adheres to a semi-classical framework with the aim of comprehensively describing the wobbling spectra of nuclei that exhibit admixtures of positive- and negative-parity bands. As such, the model will be applied to  $^{163}\text{Lu}$  for testing purposes, given that its fourth wobbling band (TSD4) comprises states of negative parity.

The work that will be depicted here is in fact based on three papers published by the team. Indeed, in Ref. [137], the key concept standing behind this interpretation was pointed out and new results concerning the excitation energies were obtained, while in Refs. [103, 105], the authors took the model even further to calculate other quantities such as Routhians, rotational frequencies, and wobbling energies. Moreover, the geometrical interpretation of the *Classical Energy Function* (CEF) was extensively studied in terms of its behavior near the critical points, meaning that interest is devoted to finding stable/unstable wobbling motion. On top of that, graphical representations with two constants of motion, i.e., the total energy and the total angular momentum are realized for this nucleus, pointing out the *allowed* classical trajectories of the system. As it will be shown, the information retrieved from these figures proves to be an efficient way of understanding

this collective phenomenon unique to triaxial nuclei. The classical study of the wobbling picture for  $^{163}\text{Lu}$  in [105] is a remarkable characteristic of the model, as the alternative treatments from the literature are based on quantal pictures that do not have a clear and ‘easy-to-grasp’ physical meaning regarding the system dynamics. In addition, the study of collective motion in terms of stability diagrams in relation to a classical set of coordinates is another first within the literature.

This chapter will be structured as follows: 1) a part that will cover the energy spectrum of  $^{163}\text{Lu}$  (as per Ref. [103]) and 2) a part that will be centered on the classical view of the stability and trajectories (according to the investigations from Ref. [105]). More concisely, part 1) will cover:

- introduction of *Signature Partner + Parity Partner Bands*
- new analytical formula for the wobbling spectrum for  $^{163}\text{Lu}$
- numerical calculations for the excitation energies
- interpretation of the free parameters in relation to other studies

while part 2) will be focused on:

- formalism of the energy function employed in the context of Parity Partner Bands
- analytical expressions for CEF in the critical regions
- contour plots are constructed with the obtained CEF(s)
- *nuclear trajectories* (i.e., intersection curves of the energy and angular momentum)

Obviously, for both parts some general discussions will be made, emphasizing the main results that emerge from the considerations.

## 5.1 Parity Partner Bands

Recalling the main features that were adopted in the  $\mathbf{W}_1$  formalism for the odd- $A$   $^{163}\text{Lu}$  nucleus, all its wobbling properties were described through the TDVE - Eq.

(4.4)) - used in the bands TSD1-2 and TSD4. The band TSD3 was interpreted as the one-wobbling-phonon band built as an excitation on top of TSD2. On the other hand, TSD1-2 were considered Signature Partner Bands, with the *favored* signature for the former and the *unfavored* signature for the latter. They are created by the odd proton  $i_{13/2}$  ( $\mathcal{Q}_1$  from Table 4.3), where the valence proton will couple to an even-even core  $\mathcal{C}_1 = 0^+, 2^+, 4^+, \dots$  for TSD1 and  $\mathcal{C}_2 = 1^+, 3^+, 5^+, \dots$  for TSD2. To maintain consistency, the notations utilized in  $\mathbf{W}_1$  will be retained. Both  $\mathcal{C}_1$  and  $\mathcal{C}_2$  exhibit positive parity according to the renormalization from Eq. (4.53).

Even if the variational principle was applied to TSD4 as a ground-state with zero-wobbling-phonon numbers, a different valence nucleon was coupled with the rotational core. More precisely, the  $h_{9/2}$  proton ( $\mathcal{Q}_2$  from Table 4.3) coupled with the core  $\mathcal{C}_2$ . Obviously, the total parity for the nucleus was given in terms of the positive parity of the core states and the proton's negative parity. In the wobbling bands of  $^{163}\text{Lu}$ , the parity can be summarized as:

$$\begin{aligned} \pi_{\text{TSD1}} &= \pi_{\mathcal{C}_1} \pi_{\mathcal{Q}_1} = + , \\ \pi_{\text{TSD2}} &= \pi_{\mathcal{C}_2} \pi_{\mathcal{Q}_1} = + , \\ \pi_{\text{TSD3}} &= \pi_{\text{TSD2}} \pi_{\Gamma^\dagger} = + , \\ \pi_{\text{TSD4}} &= \pi_{\mathcal{C}_2} \pi_{\mathcal{Q}_2} = - , \end{aligned} \quad (5.1)$$

where the positive parity of TSD3 can be attributed to the invariance of parity upon the application of the phonon operator to TSD2, despite an increase in spin by one unit.

Although the  $\mathbf{W}_1$  model effectively accounts for the wobbling phenomenon in tri-axial nuclei, it exhibits a significant inconsistency within its formalism: namely, the emergence of *two distinct quasi-particles in the coupling mechanism characteristic of a Particle-Rotor-Model*. While other studies have also employed such couplings (e.g., Ref. [128] utilizes the  $\mathcal{Q}_{1,2}$  quasi-particles to investigate the wobbling mechanism in  $^{183}\text{Au}$ ), establishing a unified coupling scheme would render this model a more robust tool for studying odd-mass triaxial nuclei. It is worth investigating if instead of dealing with two valence nucleons (one for TSD1-3 and one for TSD4) all bands can be created by the same nucleon. This would result in a single fitting procedure for the excited spectrum, which will be shown later.

Since the intruder  $i_{13/2}$  causes the triaxiality in TSD1-3, and because of the similarities between this group with TSD4, the quasi-particle  $\mathcal{Q}_1$  seems to be a proper candidate for the new coupling renormalization. Indeed, adopting only the  $i_{13/2}$  proton, the coupling schemes in  $^{163}\text{Lu}$  will be expressed in a compact form as [103]:

1. Coupling  $C'_1$ : the  $\mathcal{Q}_1$  proton aligns itself with the (positive) core of even spin states  $\mathcal{C}_1 = 0^+, 2^+, 4^+, \dots$
2. Coupling  $C'_2$ : the  $\mathcal{Q}_1$  proton couples with the (positive) core of odd spin states  $\mathcal{C}_2^+ = 1^+, 3^+, 5^+, \dots$
3. Coupling  $C'_3$ : the  $\mathcal{Q}_1$  proton couples with the (negative) core of odd spin states  $\mathcal{C}_2^- = 1^-, 3^-, 5^-, \dots$

Here, the two cores used in  $C'_2$  and  $C'_3$ , respectively, are labeled with the superscripts + and - in order to distinguish them by the opposite parity. Obviously, these new couplings  $\{C'_1, C'_2, C'_3\}$  preserve the rules outlined in Eq. (5.1). It is conspicuous that  $C'_1$  corresponds to TSD1,  $C'_2$  to the band TSD2, and lastly  $C'_3$  defines the band TSD4. No changes are applied to TSD3, which is the one-wobbling-phonon band. Hereafter, this new formalism will be referred to as **W<sub>2</sub>**, to be differentiated from **W<sub>1</sub>**. In Appendix A of Ref. [105], several workflow diagrams are available, illustrating the formalisms **W<sub>1</sub>** and **W<sub>2</sub>** as well as the coupling schemes described above (see Figs. 9 - 11 for reference).

Even though TSD4 is now considered a zero-phonon band generated by the quasi-particle  $\mathcal{Q}_1$ , a relationship with its other neighboring bands must be established. In **W<sub>1</sub>** it was proven [136] that signature is a good quantum number, and that the wave-function admits states with both positive and negative signatures (recall discussion from Appendix C and Eq. (C.10)). This led to TSD1 and TSD2 being signature partners since their similar properties and spin differences pointed towards this consideration. Looking at the two sequences  $\mathcal{C}_2^+$  and  $\mathcal{C}_2^-$  that were assigned as triaxial even-even cores to TSD2 and TSD4, it could suggest that they are *Parity Partner Bands* [137]. This idea assumes that two rotational structures can co-exist near the same deformation region. Additionally, the two partners have  $\Delta I = 2$  between states belonging to the same band and  $\Delta = 1$  for adjacent states, with energy states following a  $\propto I(I + 1)$  trend and opposite parity.

### 5.1.1 Parity of the wave-function

Since the renormalization of the band TSD4 is based on the idea that it is the parity partner of TSD2, a discussion about the parity quantum number within this semi-classical picture should be in order. Namely, one has to check how the trial function employed in the VP (Eq. (4.4)) behaves under a parity transformation. The parity transformation in quantum mechanics (also called *space reflection*) is the operation through which the coordinate axes change sign. An example of such a general transformation can be given in terms of the Cartesian system:

$$(x, y, z) \xrightarrow{\hat{P}} (-x, -y, -z) \quad (5.2)$$

The wave function can at most change a sign under the parity transformation, meaning that one can have:

$$\hat{P}\Psi(\mathbf{r}) = \Psi(-\mathbf{r}) = \Psi(\mathbf{r}) , \quad (5.3)$$

for the *positive parity states* and:

$$\hat{P}\Psi(\mathbf{r}) = \Psi(-\mathbf{r}) = -\Psi(\mathbf{r}) , \quad (5.4)$$

for the *negative parity states*. In the case of the core, the parity transformation (parity operator) is defined as the product between the complex conjugation operator and a rotation of angle  $\pi$  around the quantization axis. Moreover, the total parity of an odd-mass nucleus can be defined as the product between the parity operator of the core and the single-particle one:

$$\hat{P}_T = \hat{P}_{\text{core}} \otimes \hat{P}_{\text{sp}} . \quad (5.5)$$

The trial function was defined in terms of the set of variables  $(z, s)$  through Eq. (4.9), which were further expressed using  $(r, \varphi; f, \psi)$  according to the transformations Eq. (4.11). When acting with the parity operator defined in Eq. (5.5) on this trial function, the change of coordinates follows the rule:

$$\hat{P}_T\Psi_{IM;j}(r, \varphi; f, \psi) = \Psi_{IM;j}(r, \varphi + \pi; f, \psi + \pi) \equiv \bar{\Psi} , \quad (5.6)$$

and the invariance of the classical energy function to rotations with  $\pi$  around the quantization axis gives:

$$\mathcal{H}(r, \varphi; f, \psi) = \mathcal{H}(r, \varphi + \pi; f, \psi + \pi). \quad (5.7)$$

The remarkable feature of the last two equations is that the wave function describing the triaxial system and its image through the action of  $\hat{P}_T$  form a set of two linearly dependent functions, which differ only by a multiplicative constant  $p$ , where  $|p| = 1$ . Consequently,  $p$  can either be  $+1$  or  $-1$  resulting in the following relationship:

$$\begin{aligned} \bar{\Psi} &= p\Psi, \\ \bar{\Psi}(r, \varphi; f, \psi) &= \pm \Psi(r, \varphi; f, \psi). \end{aligned} \quad (5.8)$$

This important result shows that the triaxial rotor admits eigenfunctions with positive and negative parity, so the trial function describes wobbling bands with both types of parities. For the case of  $\Psi(r, \varphi; f, \psi)$  and the Hamiltonian describing  $^{163}\text{Lu}$ , *TSD4 band can emerge from the coupling of the same odd proton as the other bands TSD1, TSD2, and TSD3*. Concluding this discussion, it was shown that parity is a good quantum number and the bands TSD2 and TSD4 can, indeed, be considered parity partners, i.e., they are generated by the coupling of a triaxial even-even core with an identical odd quasi-particle. Another interesting characteristic coming out from this work is related to the energies in both bands, where the states of TSD2 lie lower than those of its negative partner. New experimental data on wobbling nuclei comprising both positive and negative parity bands could encourage pursuing a study on the relative energy spacings between the partners and see if a general pattern can be inferred.

### 5.1.2 Redefined Energy Spectrum

The Hamiltonian of the triaxial system remains unchanged in  $\mathbf{W}_2$  and the Variational Principle from Eq. (4.4) keeps the same structure. However, instead of obtaining an energy spectrum for the TSD bands as the one defined in Eq. (4.32) and Eq. (4.55), a different class of equations has to be used. From the phonon term  $\mathcal{F}_{n_{w_1} n_{w_2}}^I$  (Eq. (4.31)) and the minimal energy  $\mathcal{H}_{\min}^I$  (Eq. (4.58)), the modified

spectrum of  $^{163}\text{Lu}$  is given as [137]:

$$\begin{aligned} E_{I,0,0}^{\text{TSD1}} &= \epsilon_{13/2} + \mathcal{H}_{\min}^I + \mathcal{F}_{00}^I, \quad I^\pi = 13/2^+, 17/2^+, 21/2^+ \dots, \\ E_{I,0,0}^{\text{TSD2}} &= \epsilon_{13/2}^1 + \mathcal{H}_{\min}^I + \mathcal{F}_{00}^I, \quad I^\pi = 27/2^+, 31/2^+, 35/2^+ \dots, \\ E_{I,1,0}^{\text{TSD3}} &= \epsilon_{13/2} + \mathcal{H}_{\min}^{I-1} + \mathcal{F}_{10}^{I-1}, \quad I^\pi = 33/2^+, 37/2^+, 41/2^+ \dots, \\ E_{I,0,0}^{\text{TSD4}} &= \epsilon_{13/2}^2 + \mathcal{H}_{\min}^I + \mathcal{F}_{00}^I, \quad I^\pi = 47/2^-, 51/2^-, 55/2^- \dots, \end{aligned} \quad (5.9)$$

where one kept a consistent notation with the previous approach. The analytical terms from Eq. (5.9) contain different single-particle energies, which is in contrast to  $\mathbf{W}_1$ . This renormalization implies a change in the particle + core interaction, in the sense that the single-particle mean-field of the unfavored partner states (TSD2) and negative partner states (TSD4) are affected by the alternating signature between TSD1-2 (signified by the red color in Eq. (5.9)) and parity change  $\pi = +1 \rightarrow \pi = -1$  for TSD4 (signified by blue color in Eq. (5.9)) [103, 105, 137]. Actually, the two corrections come at the cost of the *unified* fitting procedure that is now applied to  $^{163}\text{Lu}$ , as compared to  $\mathbf{W}_1$ . Looking at the spectrum of Eq. (5.9), it is obvious that the same fitting parameters from Eq. (4.59) will be used here.

## 5.2 Numerical Results

Proceeding with the workflow illustrated in Fig. 4.9, a new numerical implementation should be performed. The results and discussions are presented in the current section. Because  $^{163}\text{Lu}$  is the only isotope to have positive and negative parity bands in the same collective structure, the model is tested on this nucleus.

Firstly, the normalization adopted in  $\mathbf{W}_2$  is sketched in Table 5.1, and with the information from this table, one can proceed with the minimization of the  $\chi^2$ -function. The validity of the theory will be checked by calculating the excitation energies as per Eq. (4.62) and the wobbling energies defined according to Eq. (3.24).

TABLE 5.1: Details for the normalization employed in  $\mathbf{W}_2$ . From the second left-most column one has: the number of energy states  $n_s$  within each wobbling band of  $^{163}\text{Lu}$ , the valence nucleon  $j^\pi = 13/2^+$ , the a.m. for the core  $\mathbf{R}_{\mathcal{C}}$ , the total a.m.  $\mathbf{I}$ , and the corresponding coupling scheme as per Section 5.1.

Band	$n_s$	$\mathbf{j}_{\mathcal{Q}}$	$\mathbf{R}_{\mathcal{C}}$ - Sequence	$\mathbf{I}$ - Sequence	Coupling
TSD1	21	$\mathcal{Q}_1$	$\mathcal{C}_1 = 0^+, 2^+, 4^+, \dots$	$13/2^+, 17/2^+, 21/2^+, \dots$	$C'_1$
TSD2	17	$\mathcal{Q}_1$	$\mathcal{C}_2^+ = 1^+, 3^+, 5^+, \dots$	$27/2^+, 31/2^+, 35/2^+, \dots$	$C'_2$
TSD3	14	$\mathcal{Q}_1$	1-phonon exc.	$33/2^+, 37/2^+, 41/2^+, \dots$	
TSD4	11	$\mathcal{Q}_1$	$\mathcal{C}_2^- = 1^-, 3^-, 5^-, \dots$	$47/2^-, 51/2^-, 55/2^-, \dots$	$C'_3$

TABLE 5.2: The parameter set  $\mathcal{P}$  of Eq. (4.59) obtained by minimizing the  $\chi^2$ -function for  $^{163}\text{Lu}$  in the renormalization of  $\mathbf{W}_2$ . A unique fitting was applied for all four TSD bands of the isotope.

$\mathcal{I}_1 [\hbar^2/\text{MeV}]$	$\mathcal{I}_2 [\hbar^2/\text{MeV}]$	$\mathcal{I}_3 [\hbar^2/\text{MeV}]$	$\gamma$ [deg.]	$V$ [MeV]
72	15	7	22	2.1

### 5.2.1 Energy spectrum

In what follows, the spectrum of excitation energies will be analyzed. Table 5.2 shows the results of the fitting method in the  $\mathbf{W}_2$  formalism, where the three moments of inertia, the single particle potential strength, and the triaxiality parameter are provided.

The root mean square error for the excitation energy is  $E_{\text{rms}} \approx 79$  keV, while the formalism  $\mathbf{W}_1$  gave  $E_{\text{rms}} \approx 240$  keV [101]. In fact, this is the first semi-classical study of  $^{163}\text{Lu}$  within the literature achieving an agreement of under 100 keV with the experimental measurements for the wobbling spectrum [103]. Note that there is a three-fold improvement in the theoretical calculations, as opposed to  $\mathbf{W}_1$ .

In reference to the excitation energies, when the band-head  $E_{13/2}^{\text{TSD1}}$  is subtracted, the single-particle mean-field corrections present in Eq. (5.9) become  $\epsilon_{13/2}^1 - \epsilon_{13/2}$  and  $\epsilon_{13/2}^2 - \epsilon_{13/2}$  for TSD2 and TSD4, respectively. These corrections are slightly varied such that consistency with the measured data is maintained. Throughout the calculations, the two quantities are  $\epsilon_{13/2}^1 - \epsilon_{13/2} = 0.3$  MeV and  $\epsilon_{13/2}^2 - \epsilon_{13/2} = 0.6$  MeV. Evaluating the signature splitting between the first two states and the terminus states in TSD2 (i.e.,  $E_{27/2}^{\text{TSD2}} - E_{25/2}^{\text{TSD2}}$  and  $E_{91/2}^{\text{TSD2}} - E_{89/2}^{\text{TSD2}}$ ) with the parameter set  $\mathcal{P}_{\text{fit}}$ , the values 0.492 MeV and 0.936 MeV are obtained, which agree with the estimates made by Jensen et al. [65].

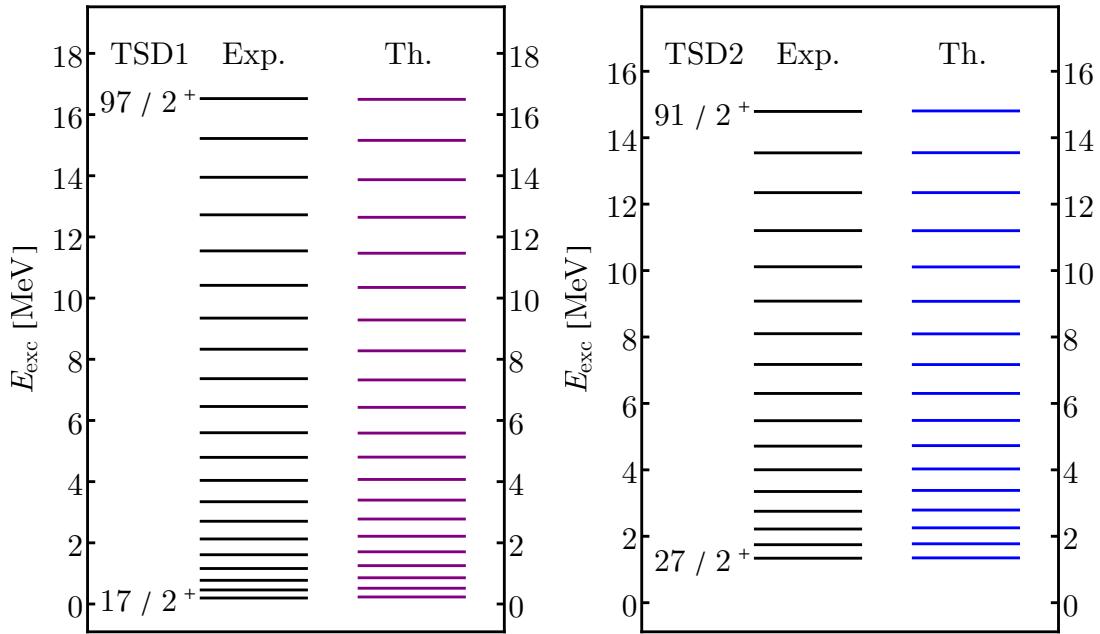


FIGURE 5.1: The excitation energies (Eq. (4.62)) of  $^{163}\text{Lu}$  for the bands TSD1 and TSD2, obtained in the  $\mathbf{W}_2$  formalism using Eq. (5.9). Calculations were done with the parameters presented in Table 5.2.

The excitation energies are graphically represented in Figs. 5.1 - 5.2, where only the first and last spin values are labeled for each band. Remarkable are the very small differences across the states belonging to TSD1-3, while for TSD4 there is a small downward shift in the region  $47/2 \leq I \leq 55/2$  and an upward shift when  $I \geq 75/2$ . A possible reason for the over-estimation of high-spin states might be the *ad-hoc* mean-field correction that was adopted for TSD4 (recall Eq. (5.9)). On the other hand, the classical energy function provided by the VP seems to have a steep minimum, causing the system to be more cranked near  $I = 47/2$ .

Regarding the wobbling energy given as relative differences between the first excited band and the yrast one, the results are represented in Fig. 5.3. The first excited band is in fact TSD3 and the yrast partner is TSD2. From the evolution of  $E_{\text{wob}}$ , it can be seen that the calculated values reflect an increasing trend with angular momentum, suggesting that  $^{163}\text{Lu}$  behaves as a longitudinal wobbler. This is in contrast to other interpretations that show a decreasing w.r.t. to  $I$  [9, 158, 159]. However, within these studies, the wobbling energies are obtained from TSD2 (first excited band) and TSD1 (yrast band), and such a consideration does not hold here since TSD2 is obtained variationally as a ground band. Still, by analyzing the experimental data from Fig. 5.3, a slight increase in spin can

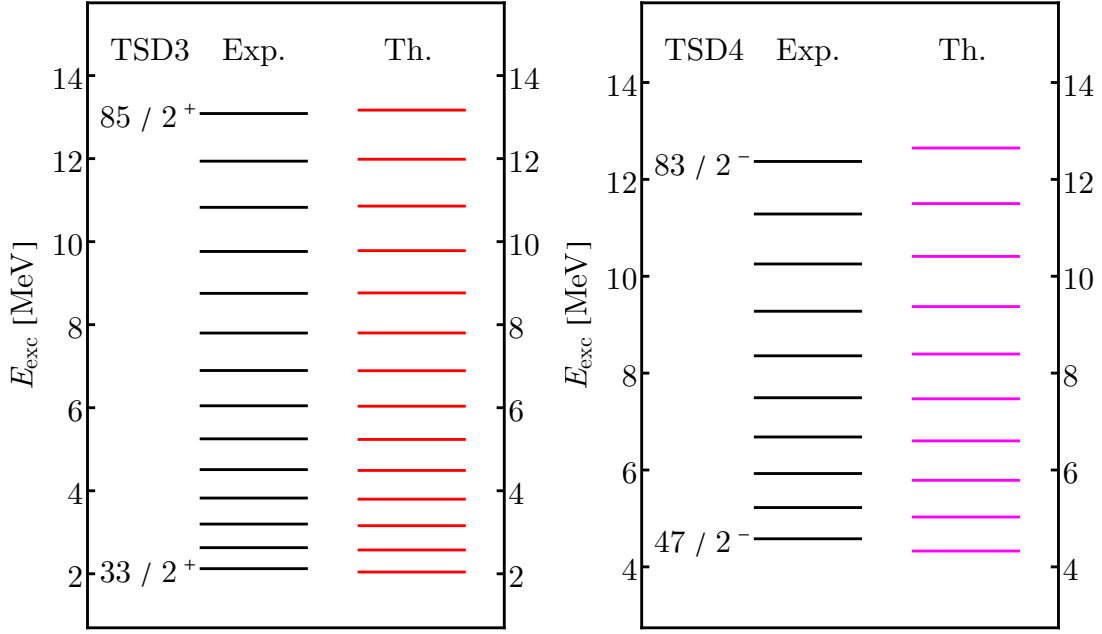


FIGURE 5.2: The excitation energies (Eq. (4.62)) of  $^{163}\text{Lu}$  for the bands TSD3 and TSD4 , obtained in the  $\mathbf{W}_2$  formalism using Eq. (5.9). Calculations were done with the parameters presented in Table 5.2.

be observed. Certainly, from the lower spin limit and up to  $I \approx 37/2$ , the energy is increasing, but after a *critical value*  $I \geq 39/2$  it starts to decrease. The identification of a critical region in which the nucleus might change its wobbling regime is a remarkable feature of the current research. The increasing behavior of the theoretical data also shows a quenching in the high-spin limit, pointing out the change in the wobbling regime as well.

Also worth discussing is the difference  $\delta_{42} = E_I^{\text{TSD4}} - E_I^{\text{TSD2}}$ , where the almost constant value  $\delta_{42} \approx 0.3$  MeV is observed, suggesting that the states with the same angular momentum from TSD2 and TSD4 might emerge from the parity projection of a single wave-function lacking reflection symmetry (hence the change  $\pi = + \rightarrow \pi = -$ ). For the sake of completeness, the two wobbling frequencies  $\Omega_{1,2}$  that comprise the phonon term  $\mathcal{F}_{n_{w_1} n_{w_2}}^I$  defined in Eq. (4.31) are represented as a function of the total angular momentum in Fig. 5.4. It can be seen that the solution  $\Omega_2$  is much larger over the entire spin range, indicating that the odd proton's a.m. exhibits a more pronounced precessional motion than that of the core. Indeed, the difference is only about 1.5 – 2 MeV for low  $I$  and it goes to 3.5 – 4 MeV in the large spin limit. Nevertheless, this is expected because the condition  $\Omega_2 > \Omega_1$  was fixed in Eq. (4.22).

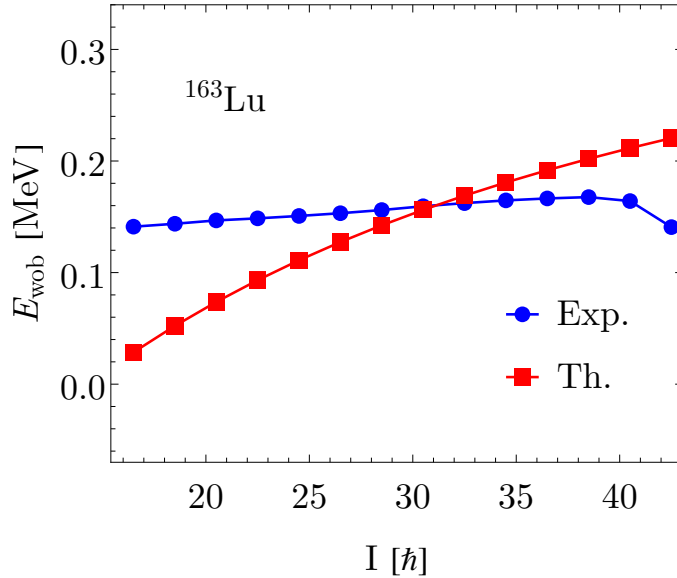


FIGURE 5.3: Wobbling energy for  $^{163}\text{Lu}$  obtained in the  $\mathbf{W}_2$  formalism and compared with the experimental results. The theoretical values were calculated with Eq. (3.24).



FIGURE 5.4: The wobbling frequencies, i.e., the two solutions of Eq. (3.13) as a function of the total spin. Calculations are made with the parameter set provided in Table 5.2.

### 5.2.2 Interpretation of the parameter set

The set  $\mathcal{P}_{\text{fit}}$  attained after the minimization procedure of the  $\chi^2$ -function is given in Table 5.2. However, the fitting method only gives the numerical values, without providing context on the physical interpretation of the results themselves. As such, in this subsection, one should make a quantitative analysis of the five parameters and see how the current model compares with existing studies. Concerning the magnitudes of the three moments of inertia, it is clear that the system rotates around the 1-axis, as the largest MOI corresponds to this axis. Moreover, the 1-axis MOI is much larger than the other two, signifying the nature of small-amplitude vibrations that are typical to a triaxial rotor (i.e., large rotational motion around  $\mathcal{I}_1$  and a fluctuation generated by the anisotropy of  $\mathcal{I}_{2,3}$ ). A graphical representation where the three moments of inertia are compared with the  $\mathbf{W}_1$  formalism is shown in Fig. 5.5. Looking at the plot, it can be seen that  $\mathcal{I}_1$  is the largest across all the fitting procedures, although  $\mathbf{W}_2$  provides the largest one. It should be pointed out that these are *effective* MOI of the system, that is the particle + triaxial-rotor. There is no spin dependence inferred for the three quantities, so a possible change in their ordering cannot be studied with the current description. Since the current approach is not a microscopic one, no presumptions on what causes the MOI ordering can be stated (e.g., orbital mixing and so on). As a matter of fact, the nature of the three MOI for a real nucleus is neither rigid nor irrotational (see discussion from Chapter 2.2 and Eq. (2.31)).

Taking the moments of inertia given by the  $\mathbf{W}_2$  model, a direct comparison with the rigid and hydrodynamical (irrotational) ones is made in Fig. 5.6. The rigid values are calculated using the first formula from Eq. (2.30) and the hydrodynamical values are attained using the second formula. It is noteworthy that the MOI provided by the fit suggest an irrotational-like behavior rather than a rigid-like for the triaxial system since there is a larger discrepancy between the MOI of the 2- and 3-axes in the rigid case.

Going further with the analysis of the parameters, a value of  $\gamma = 22^\circ$  is obtained. The agreement with the predicted minimum of  $^{163}\text{Lu}$  [65, 122] is quite good, as the experimental minimum for the TSD structures is identified at  $(\beta, \gamma) = (0.38, 20^\circ)$  (recall Fig. 2.31). Other studies that describe the wobbling properties of  $^{163}\text{Lu}$  take the triaxiality parameter fixed a priori (see Refs. [127, 144] for example), but the current approach determines  $\gamma$  self-consistently. Remarkable is the fact that

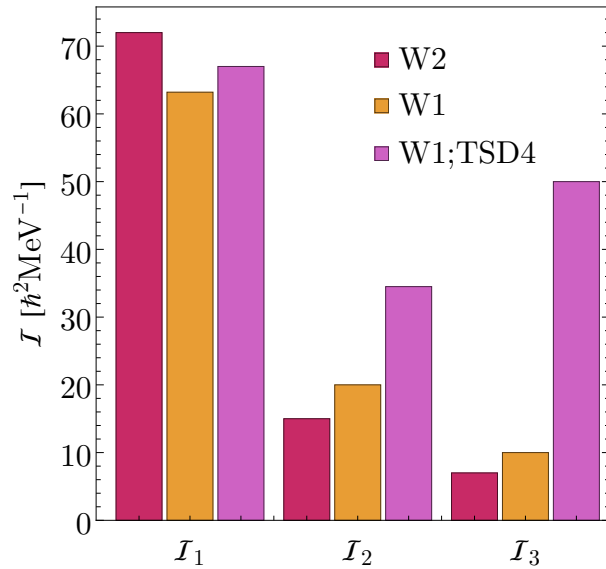


FIGURE 5.5: Comparison between the MOI obtained in the approach **W<sub>2</sub>** (current chapter) and **W<sub>1</sub>** (as per Chapter 4). Note that there was a separate minimization of the  $\chi^2$ -function for TSD4 within the previous formalism. The numerical values for  $\mathcal{I}_{1,2,3}$  are taken from Tables 4.7 and 5.2.

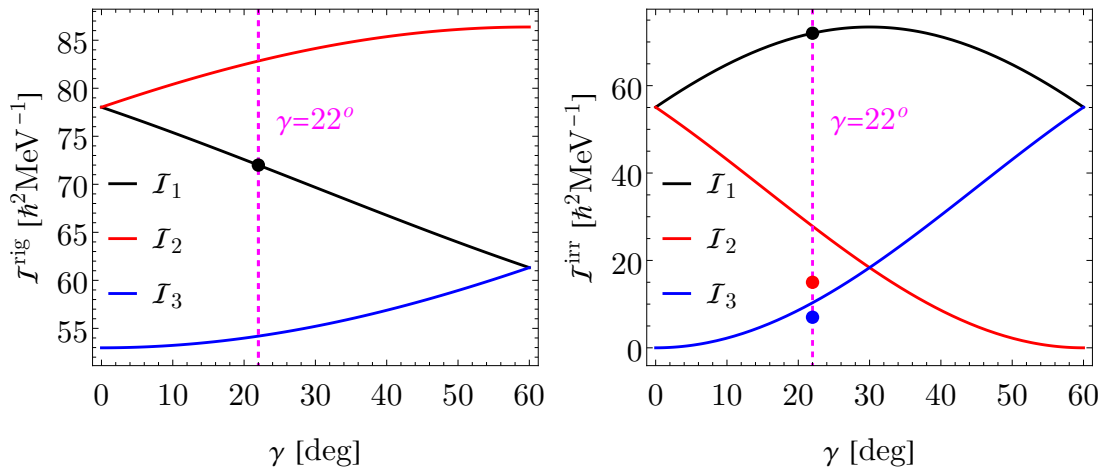


FIGURE 5.6: The rigid (**left**) and hydrodynamical (**right**) MOI as function of  $\gamma$ . The scaling factors for both types of MOI are determined by fixing  $\mathcal{I}_1^{\text{rig}}$  and  $\mathcal{I}_1^{\text{irr}}$  to the fitted  $\mathcal{I}_1$  with the deformation parameters  $(\beta, \gamma) = (0.38, 22^\circ)$ . The black, red, and blue points represented the numerical values of  $\mathcal{I}_1$ ,  $\mathcal{I}_2$ , and  $\mathcal{I}_3$  from Table 5.2, respectively. The value  $\gamma = 22^\circ$  from the fit is marked with the dashed magenta line just to guide the eye.

the obtained value is slightly bigger than the one from  $\mathbf{W}_1$  ( $\gamma = 17^\circ$ ). This might be caused by the larger ratios for  $\mathcal{I}_1/\mathcal{I}_2 = 4.8$  and  $\mathcal{I}_1/\mathcal{I}_3 = 10.2$  in  $\mathbf{W}_2$  than the ones from  $\mathbf{W}_1$  ( $\mathcal{I}_1/\mathcal{I}_2 = 3.1$  and  $\mathcal{I}_1/\mathcal{I}_3 = 6.3$ , respectively), which also indicate a larger triaxiality.

Lastly, the single-particle potential strength should be discussed. It has a value of  $V = 2.1$  MeV and in  $\mathbf{W}_1$  this parameter was  $V^{\text{TSD}1,2,3} = 3.1$  MeV and  $V^{\text{TSD}4} = 0.7$  MeV. An explanation for its decrease in the present case might be due to the upward shift in the energy caused by the unfavored partner, or due to the energetic shift of the parity partner. Nevertheless, a quenching effect on the quadrupole deformation of the triaxial system due to either the signature splitting or the parity symmetry breaking is observed. Still, the obtained value seems to be consistent with the previous calculations, as  $V$  is close to the average value of the two  $V$ 's from  $\mathbf{W}_1$ . Other interpretations developed using a similar single-particle term in the Hamiltonian adopted values around  $V = 1.6$  MeV [144], however, that was for an isotope with smaller quadrupole deformation  $\beta_2 = 0.18$ .

According to the structure described at the beginning of this chapter, the above sections conclude part 1) of the research, which was supposed to describe the concept of Parity Partners, to re-define the excitation energy spectrum and apply it to  $^{163}\text{Lu}$ , and finally to give some context on the interpretation of the free parameters. Since all points were properly covered, one can go further to part 2) of this study, where the classical energy function must be re-evaluated under the assumptions of the  $\mathbf{W}_2$  approach.

### 5.3 Classical Energy Function (CEF)

From the Hamiltonian given by Eq. (4.1) (i.e., the sum of the single-particle term in Eq. (4.2) and the rotor term in Eq. (4.3)), one obtained the classical energy function by taking the Hamiltonian's average on the trial function (Eq. (4.5)). The structure of the CEF was firstly given in Section 4.2.3 and even a qualitative analysis of its sub-terms has been employed in Figs. 4.2 - 4.4. The minimum point of  $\mathcal{H}$  was found to be  $p_0 = (0, I; 0, j)$  (recall Eq. (4.18)). These considerations are still important here. Adopting the polar coordinate system  $(\theta, \varphi)$ , the Cartesian

components of the total angular momentum can be expressed as:

$$\mathbf{I} = \{I_1, I_2, I_3\} \equiv \{x_1, x_2, x_3\} , \\ x_1 = I \sin \theta \cos \varphi , x_2 = I \sin \theta \sin \varphi , x_3 = I \cos \theta , \quad (5.10)$$

where the quantization axis is chosen as the 3-axis. Going back to the expression of  $\mathcal{H}$  from Eq. (4.15) and evaluating it in the minimum point using the new coordinate system, a compact form is achieved [105]:

$$\mathcal{H} |_{p_0} = I \left( I - \frac{1}{2} \right) \sin^2 \theta \cdot \mathcal{A}_\varphi - 2A_1 I j \sin \theta + T_{\text{core}} + T_{\text{sp}} , \quad (5.11)$$

where the last two terms are independent of the polar angles  $(\theta, \varphi)$  and they are defined as [105]:

$$T_{\text{core}} = \frac{I}{2} (A_1 + A_2) + A_3 I^2 , \\ T_{\text{s.p.}} = \frac{j}{2} (A_2 + A_3) + A_1 j^2 - V \frac{2j-1}{j+1} \sin \left( \gamma + \frac{\pi}{6} \right) . \quad (5.12)$$

It would be instructive to see how  $T_{\text{core}}$  behaves under different  $A_k$  orderings and also how the single-particle term evolves for different  $j$ . Two such comparisons are depicted in Fig 5.7. It can be seen that the variations of  $T_{\text{sp}}$  at different  $j$  values are not significant. On the other hand, the  $A_k$  ordering affects  $T_{\text{core}}$  with a large amount, especially for higher spins.

### 5.3.1 CEF - Stability Regions

The classical energy function from Eq. (5.11) is expressed by classical coordinates that relate to the dynamics of the core (i.e.,  $r, \varphi$ ) and the valence nucleon (i.e.,  $f, \psi$ ). However,  $\mathcal{H}(r, \varphi; f, \psi)$  is nothing else than the average of  $\hat{H}$  with the trial function. Thus, going back into the quantal picture, the physical interpretation of Eq. (5.11) is *the expectation value of the Hamiltonian* or, equivalently, *the allowed energy states of the system*. For this reason, analyzing the CEF around the critical points is crucial for identifying the stability of the system.

In this subsection, such calculations will be performed, namely the critical points of  $\mathcal{H}$  will be identified and then graphical representations in the polar plane  $(\theta, \varphi)$  will be made. If there are extremal points with minimum character present, then



FIGURE 5.7: **Right:** The term  $T_{\text{core}}$  from Eq. (5.12) as function of the angular momentum  $I$  at different orderings for  $A_k$  (the arbitrary values  $0.05, 0.025, 0.011 \hbar^{-2}\text{MeV}$  were interchanged between each factor). The magenta line is for the inertia factors provided by the fit. **Left:** The term  $T_{\text{sp}}$  from Eq. (5.12), evaluated for three different single-particle angular momenta using the potential strength and the three MOI from Table 5.2.

TABLE 5.3: The minimum points of  $\mathcal{H}$  for a fixed ordering of the inertia factors. The orderings are chosen in agreement with the fit parameters from Table 5.2.

Minimal point	$\theta$ [rad]	$\varphi$ [rad]	$A_k$ ordering
$m_1$	$\pi/2$	0	$A_3 > A_2 > A_1$
$m_2$	$\pi/2$	$\pi$	$A_3 > A_2 > A_1$
$m_3$	$\pi/2$	$2\pi$	$A_3 > A_2 > A_1$

the so-called regions of stability could be pinpointed. These regions should indicate if there are any allowed rotational states for the system.

Firstly, all the critical points for  $\mathcal{H}$  with minimum character are given in Table 5.3. The intervals of variation for  $\theta$  and  $\varphi$  are fixed to  $\theta \in [0, \pi]$  and  $\varphi \in [0, 2\pi]$ , respectively. Some numerical evaluations for the CEF can be realized in this coordinate space. These are sketched as *contour plots* for different spins in  $^{163}\text{Lu}$ . For the sake of completeness, contour plots for two spin states from each band will be constructed and the critical points from Table 5.3 are also drawn in these figures. The plots are shown in Figs. 5.8 - 5.11.

Looking at the set of graphics depicted in Figs. 5.8 - 5.11, some remarking features emerge. They have some similarities, suggesting resembling collective properties, but also some discrepancies, caused by the different depths of the minima. A primary common feature consists of the set of *equi-energy* curves that surround a sole minimum point for the low values of  $\mathcal{H}(\theta, \varphi)$ . Around the minimum point  $m_2$

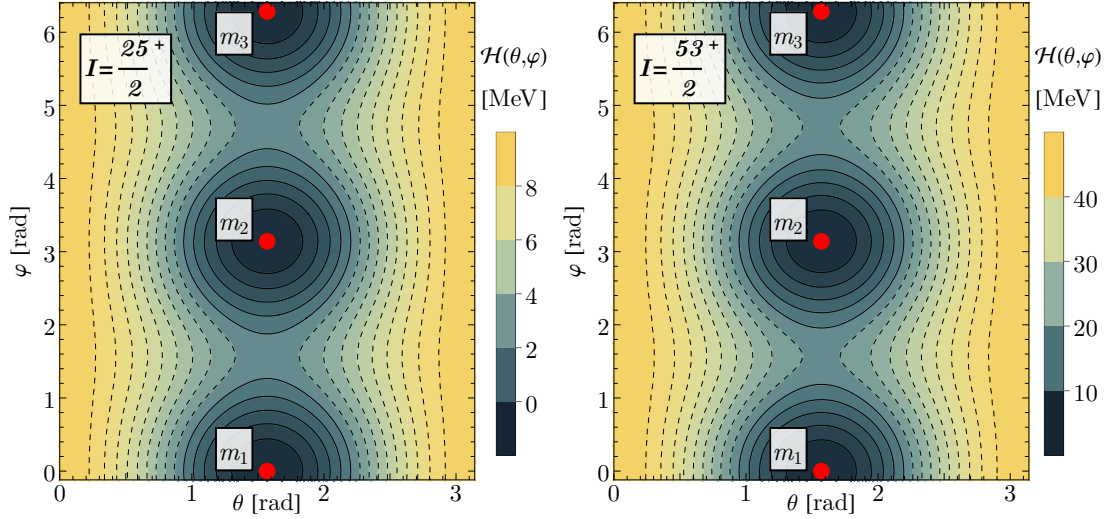


FIGURE 5.8: The classical energy function (Eq. (5.11)) as a function of the polar coordinates for two states from TSD1 (i.e.,  $I = 25/2^+$  and  $53/2^+$ ), evaluated using the fit parameters from Table 5.2. The minimum points of  $\mathcal{H}$  are marked by the red dots. See the text for an explanation of the dashed contour styling.

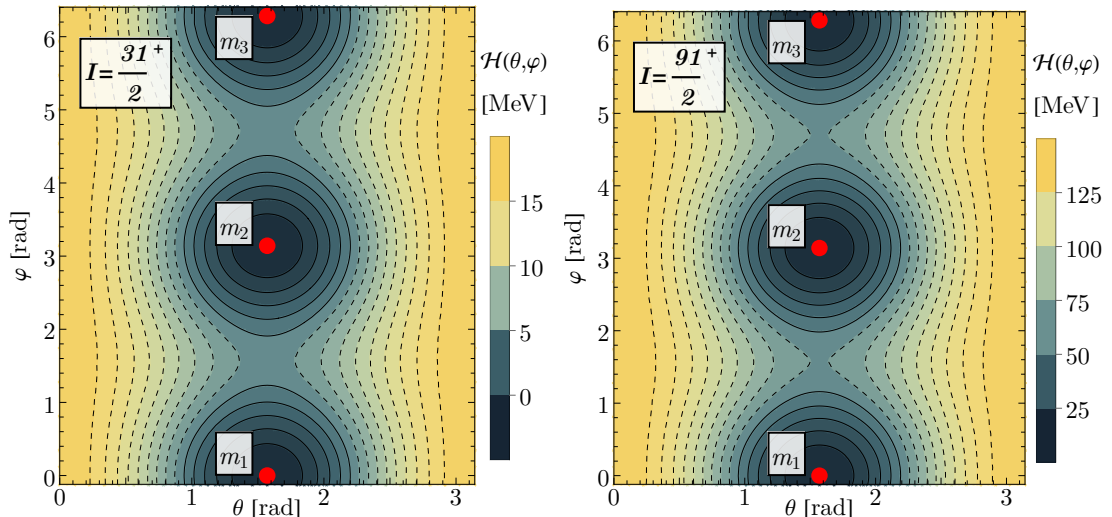


FIGURE 5.9: The classical energy function (Eq. (5.11)) as a function of the polar coordinates for two states from TSD2 (i.e.,  $I = 31/2^+$  and  $91/2^+$ ), evaluated using the fit parameters from Table 5.2. The minimum points of  $\mathcal{H}$  are marked by the red dots. See the text for an explanation of the dashed contour styling.

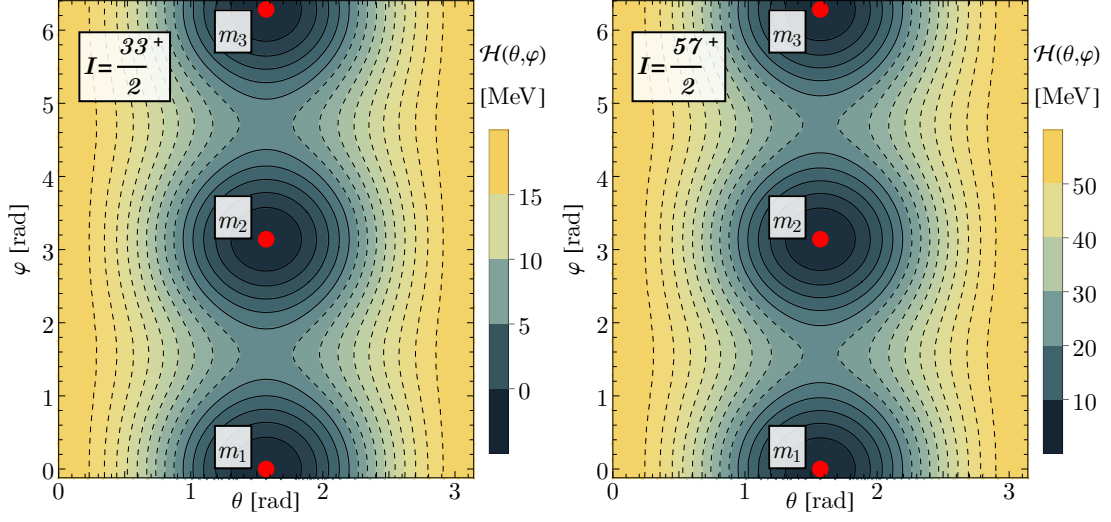


FIGURE 5.10: The classical energy function (Eq. (5.11)) as a function of the polar coordinates for two states from TSD3 (i.e.,  $I = 33/2^+$  and  $57/2^+$ ), evaluated using the fit parameters from Table 5.2. The minimum points of  $\mathcal{H}$  are marked by the red dots. See the text for an explanation of the dashed contour styling.

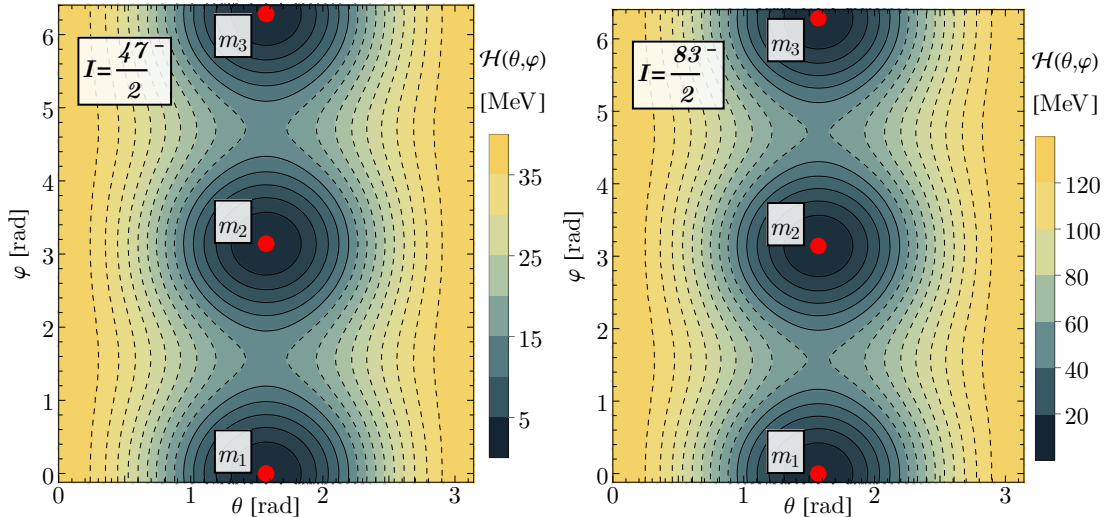


FIGURE 5.11: The classical energy function (Eq. (5.11)) as a function of the polar coordinates for two states from TSD4 (i.e.,  $I = 47/2^-$  and  $83/2^-$ ), evaluated using the fit parameters from Table 5.2. The minimum points of  $\mathcal{H}$  are marked by the red dots. See the text for an explanation of the dashed contour styling.

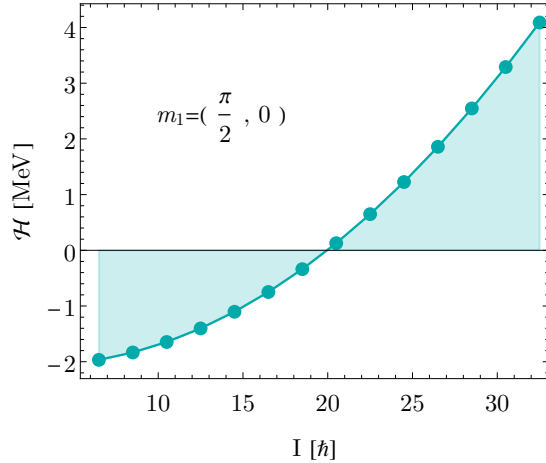


FIGURE 5.12: The CEF from Eq. (5.11) is evaluated in one of its minimum points ( $m_1 = (\pi/2, 0)$  given in Table 5.3) and plotted with respect to the angular momentum. The calculations are done using the fitting parameters from Table 5.2.

there are closed trajectories (marked by the solid black lines) and as the energy increases (keeping the angular momentum fixed) there is a *critical region* at which the orbits surround all minima (highlighted by the dashed lines). The lack of localization for these orbits indicates an *unstable motion* of the nucleus and they could be related to a phase transition, where the system undergoes a sudden change in its rotational character. Indeed, examining Fig. 5.9, which has quite deep minima (as the maximal values reach  $\approx 120$  MeV), there are about five stable trajectories that surround  $m_{1,2,3}$ . Beyond those trajectories, the wobbling motion becomes unstable. From an equilibrium standpoint, such ‘excited’ states cannot be reached by the nucleus, hence the rotational motion occurs near the minimum points. Discussion on the stability of the wobbling motion will be reiterated in the next section, but it is worth mentioning that such a description of the dynamics of a nucleus in terms of classical orbits is a unique feature of this research.

Additionally, the CEF is studied quantitatively in one of its minimum points (i.e., the  $m_1 = (\pi/2, 0)$  point from Table 5.3) w.r.t. the total angular momentum. As the depth of the contour plots changes across the different spin states, it would be instructive to see how these modifications are affected by  $I$ . As a result, a graphical representation of  $\mathcal{H}$  in the point  $m_2$  has been sketched in Fig. 5.12. As a final step in this analysis, Fig. 5.13 shows the behavior of  $\mathcal{H}$  with respect to different values of  $I$ , by keeping one polar coordinate fixed and varying the other. The fixed values are taken to coincide with the minimum point  $m_1$ .



FIGURE 5.13: The evolution of  $\mathcal{H}$  for different values of  $I$ , obtained by keeping one polar coordinate fixed and letting the other one vary in its normal interval.

**Left:** The coordinate  $\theta$  is fixed to  $\theta = \pi/2$  and  $\varphi = [0, 2\pi]$ . **Right:** The coordinate  $\varphi$  is fixed to  $\varphi = 0$  and  $\theta = [0, \pi]$ .

By expressing the classical energy function in terms of the polar coordinates, an analytical structure of Eq. (5.11) is properly obtained. This function provides an insight into the precessional motion of the angular momentum, which according to the calculations made for  $^{163}\text{Lu}$  in the **W<sub>2</sub>** approach, is the 1-axis (largest MOI is  $\mathcal{I}_1$ ). The representations shown in Figs. 5.8 - 5.11 depict three regions, i.e., i) one where the triaxial ellipsoid could behave as a wobbler, having closed circular orbits around  $m_{1,2,3}$  ii) a criticality region and iii)  $\mathcal{H} > \mathcal{H}_{\text{critical}}$  beyond which the orbits become non-localized and surround all three minima. This critical value can be extracted from the left inset of Fig 5.13 as the peak value. A simple sketch where all these regions can be clearly differentiated is made in Fig. 5.14. Identification of a phase transition between a well-defined motion around the 1-axis and an unstable rotor is a remarkable feature in the current model.

### 5.3.2 Classical 3D Trajectories

In the previous section, a study of the wobbling motion in  $^{163}\text{Lu}$  has been performed in terms of the classical energy function. However, the analysis was only elaborated in the space generated by the set of polar coordinates (Eq. (5.10)), restricting the geometrical interpretation of the system dynamics to a two-dimensional picture. In two recent publications [103, 105], the team successfully gave a 3-dimensional representation of the classical energy function. In the following, the numerical recipe for obtaining this geometry will be presented.



FIGURE 5.14: A schematic illustration showing the three regions that can be identified for a triaxial nucleus within the  $\mathbf{W}_2$  formalism. The stable motion is characterized by the closed orbits around the minimal points  $m_{1,2,3}$  suggesting the precession of  $\mathbf{I}$  around the 1-axis. Furthermore, for a fixed angular momentum, a critical value of  $\mathcal{H}$  is marked by the thick orange lines. Beyond this region, the rotational motion becomes unstable, marking a phase transition.

From the classical equations of motion depicted in Chapter 4, it results that the system admits two constants of motion, i.e., the total energy and the total angular momentum. These two quantities are obviously expected to be conserved. The angular momentum can be written as the squared sum of its components:

$$I^2 = x_1^2 + x_2^2 + x_3^2 . \quad (5.13)$$

Using the initial CEF provided in Eq. (5.11), one can aim at expressing it in terms of  $x_1$ ,  $x_2$ , and  $x_3$ , respectively. This would imply that the energy function explicitly contains the angular momentum components. Changing from the polar coordinates to the cartesian ones  $\mathcal{H}(\theta, \varphi) \rightarrow E(x_1, x_2, x_3)$ , the following formula

for the energy is obtained [105]:

$$\begin{aligned} E = & \left(1 - \frac{1}{2I}\right) A_1 x_1^2 + \left(1 - \frac{1}{2I}\right) A_2 x_2^2 + \left[\left(1 - \frac{1}{2I}\right) A_3 + A_1 \frac{j}{I}\right] x_3^2 \\ & - I \left(I - \frac{1}{2}\right) A_3 - 2A_1 I j + T_{\text{rot}} + T_{\text{sp}} . \end{aligned} \quad (5.14)$$

where  $E$  is now called the *energy surface* [105]. In the expression of  $E$ , one can notice the three coordinates  $x_k$  that appear as squared terms. If some notations are introduced and some algebraic manipulations are performed, the energy surface acquires the compact form:

$$E' = \frac{x_1^2}{s_1} + \frac{x_2^2}{s_2} + \frac{x_3^2}{s_3} , \quad (5.15)$$

where  $E'$  is the energy after the  $x_k$ -free terms in the r.h.s. of Eq. (5.14) have been subtracted from  $E$ . The structure of Eq. (5.15) resembles a general ellipsoid (hence the name *energy surface*):

$$\frac{x_1^2}{a^2} + \frac{x_2^2}{b^2} + \frac{x_3^2}{c^2} = 1 , \quad (5.16)$$

where  $a, b, c$  are the semi-axes of different lengths, which for the triaxial ellipsoid become:

$$\begin{aligned} a &\rightarrow \sqrt{E's_1} , \\ b &\rightarrow \sqrt{E's_2} , \\ c &\rightarrow \sqrt{E's_3} . \end{aligned} \quad (5.17)$$

The semi-axes lengths depend on the three inertia factors  $A_k$ , meaning that the fit quality will be reflected in the geometrical shape of  $E'$  through the parameter set  $\mathcal{P}_{\text{fit}}$ . Putting together Eq. (5.13) (i.e., a sphere of radius  $r = I$ ) and Eq. (5.15) (an ellipsoid with semi-axes given by Eq. (5.17)), their intersection can be made in the 3-dimensional space generated by the angular momentum components  $\{x_1, x_2, x_3\}$ . These overlapping surfaces will give the *classical trajectories*, defined as a collection of points in this space along which the total angular momentum  $\mathbf{I}$  is orbiting, making a precessional motion. These trajectories will play a crucial role in characterizing the motion of the nucleus, as they will be oriented along one of the three axes  $x_k$ ,  $k = 1, 2, 3$ , suggesting rotations around a particular direction



FIGURE 5.15: The nuclear trajectories for the state  $I = 25/2^+$  from TSD1 in  $^{163}\text{Lu}$ . The left inset shows the trajectory of the system corresponding to the real energy of the spin (i.e., the red ellipses that surround  $x_1$ ). The rotational axis is marked by the red color, signifying that the nucleus wobbles around it.

preferred by the system.

When the PRM Hamiltonian (Eq. (4.1)) is diagonalized for a given  $I$ , a set of  $2I + 1$  energies are obtained. Thus, it is mandatory to study the evolution of these trajectories when the energy increases and see their behavior with respect to the angular momentum and also energy. The intersection curves of the two constants of motion Eq. (5.13) and Eq. (5.14) are represented as manifolds in Figs. 5.15 - 5.18, where each figure represents a rotational state within one of the four bands of  $^{163}\text{Lu}$ . Every representation contains three insets that reveal different nuclear phases. The first inset (left) shows the trajectory of the system given by the intersection of the angular momentum  $I$  and the real energy of this state (according to the experimental data from Figs. 5.1 - 5.2). Therefore, it can be regarded as the ‘real’ nuclear trajectory. It is remarkable the fact that all the real trajectories are observed around the  $x_1$ -axis. The invariance of  $\hat{H}$  to rotations with  $\pi$  about  $x_1$  makes it possible to have two distinct (although symmetrical) paths around  $x_1$ , i.e., one for the positive and one for the negative direction, which are depicted with red ellipses. Keep in mind that the energy surface is evaluated using the parameters  $\mathcal{P}_{\text{fit}}$ , therefore one expects  $x_1$  to be the rotational axis.

For low-lying states, the two orbits lie quite close to the  $x_1$ -axis, making the rotation more pronounced around the  $x_1$  and  $-x_1$  directions. As the energy increases, the precession of  $\mathbf{I}$  increases as well, making the two trajectories approach each other, resulting in a *tilted rotation* of the system. The tilt implies that the rotational axis is misaligned and it is moving away from its *equilibrium point* [105]. Increasing the energy even further will make the two trajectories intersect with



FIGURE 5.16: The nuclear trajectories for the state  $I = 27/2^+$  from TSD2 in  $^{163}\text{Lu}$ . The left inset shows the trajectory of the system corresponding to the real energy of the spin (i.e., the red ellipses that surround  $x_1$ ). The rotational axis is marked by the red color, signifying that the nucleus wobbles around it.

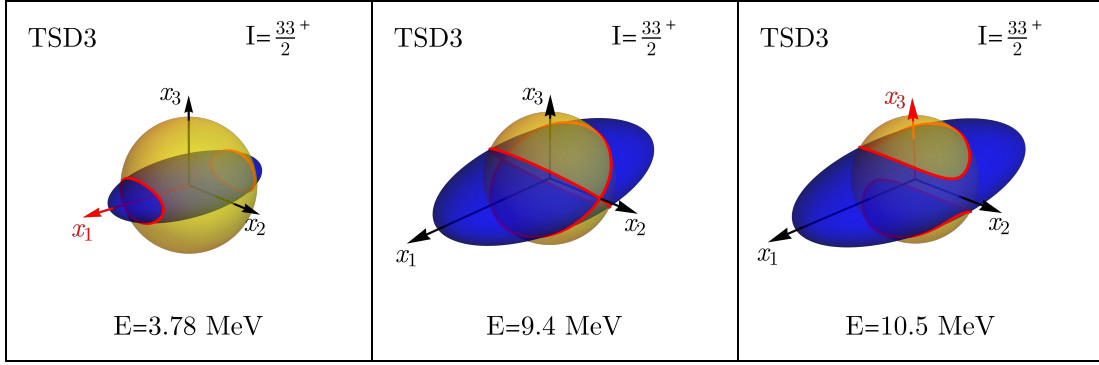


FIGURE 5.17: The nuclear trajectories for the state  $I = 33/2^+$  from TSD3 in  $^{163}\text{Lu}$ . The left inset shows the trajectory of the system corresponding to the real energy of the spin (i.e., the red ellipses that surround  $x_1$ ). The rotational axis is marked by the red color, signifying that the nucleus wobbles around it.

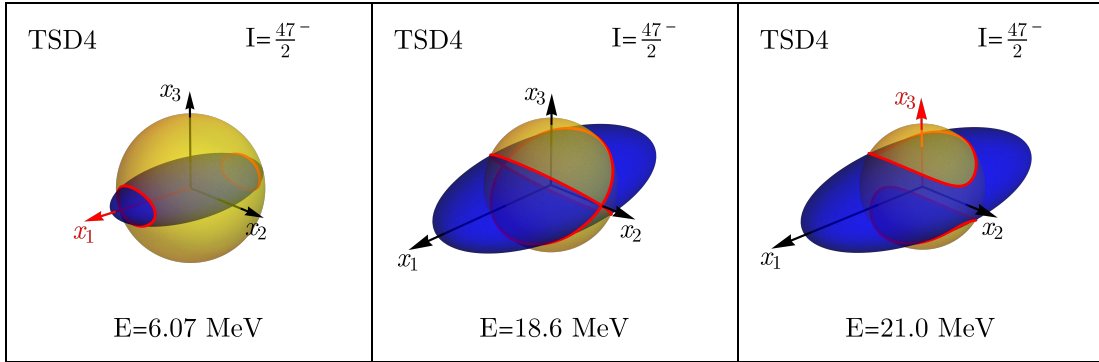


FIGURE 5.18: The nuclear trajectories for the state  $I = 47/2^-$  from TSD4 in  $^{163}\text{Lu}$ . The left inset shows the trajectory of the system corresponding to the real energy of the spin (i.e., the red ellipses that surround  $x_1$ ). The rotational axis is marked by the red color, signifying that the nucleus wobbles around it.

each other, marking a *critical point* where the wobbling motion becomes unstable. This is represented by the middle inset throughout Figs. 5.15 - 5.18. Lastly, if the energy increases beyond the critical point, a different picture emerges, where the rotational axis changes from  $x_1$  to  $x_3$ . Such a transition is shown in the right inset of each figure, where two symmetric paths are visible along the  $x_3$  and  $-x_3$  directions. However, the energies at which the nucleus could undergo a change in the rotational axis are way too large for a phase transition to occur naturally in  $^{163}\text{Lu}$ . Concisely, the state  $I = 25/2^+$  from TSD1 has a real energy of about 2.6 MeV, while the critical value requires twice that amount. Nonetheless, this is another remarkable aspect of the current formalism, showing that phase transitions between rotational modes can be identified.

Comparing the description of the wobbling motion made in the 3-dimensional space and the one from the previous subsection, both are able to pinpoint regions where phase transitions for the nuclear wobbling motion can take place. Identifying the changes in the rotational character of a triaxial nucleus was successful in each case. In addition, the geometrical analysis using the energy surface  $E'$  from Eq. (5.15) provides a clearer interpretation of the underlying motion, since the precession of  $\mathbf{I}$  is directly related to the trajectories attained by intersecting  $E'$  with the angular momentum sphere.

## 5.4 Concluding Remarks

In this chapter, a novel approach for the wobbling motion in odd-mass nuclei was presented, starting with the theoretical calculations and finally comparing the results with the experimental data. Indeed, the idea of Signature Partner Bands firstly employed by the team in **W<sub>1</sub>** was amended with the concept of Parity Partners, making a renormalization of the wobbling band structure and naming it **W<sub>2</sub>** (see subsection 5.1). It is shown that the Hamiltonian admits functions with both positive and negative parities, and thus  $^{163}\text{Lu}$  is considered as the testing nucleus. The renormalization of **W<sub>2</sub>** gives a new energy spectrum of the four TSD bands, which is expressed by Eq. (5.9). The same TDVE was applied to the states TSD1-2 and TSD4, except that herein, all four bands are obtained from the coupling of the same  $i_{13/2}$  odd proton with a core of even spin states (TSD1) and odd spin states (TSD2,4). The coupling schemes are sketched in Table 5.1. Compared to the **W<sub>1</sub>** method, here  $^{163}\text{Lu}$  is described by a single

fitting procedure, and it consisted of minimizing the  $\chi^2$ -function from Eq. (4.60) w.r.t. the free parameters defined in 4.59.

The numerical results were presented in Section 5.2, where one obtained a very good agreement with the experimental data for the excitation energies (recall Figs. 5.1 - 5.2), resulting in deviations of less than 100 keV across the spectrum. The numerical values of the fitting parameters provided in Table 5.2 were also interpreted, and a comparison with previous studies was made. The current model gives a realistic approximation of the triaxiality parameter and also the single-particle potential strength. In addition, the three moments of inertia given by the fit agree with the hydrodynamical model (i.e., the irrotational MOI) and Fig. 5.6 shows this feature. The last major step in the study was to examine the average of the total Hamiltonian on the trial function adopted in  $\mathbf{W}_2$ . One started with the expression of the classical energy function in the minimum point  $(0, I; 0, j)$  defined in Eq. (5.11). Then, two subsequent investigations were made, namely, i) finding the behavior of  $\mathcal{H}$  with respect to the polar coordinates  $(\theta, \varphi)$  that are used to generate the angular momentum components (Eq. (3.18)) and ii) extending the problem from 2D to 3D, by adopting the so-called energy surface. In the case i), by creating contour plots in the polar plane, three minima are observed; each surrounded by closed orbits that indicate a stable motion. Beyond a critical value  $\mathcal{H}_{\text{critical}}$ , the orbits become non-localized and they surround all three minimum points. In Fig. 5.14 the regions with stable and unstable characters are sketched, and a phase transition between them is highlighted. The case ii) aims at expressing  $\mathcal{H}$  in terms of the cartesian components of  $I$ , which is achieved via the energy surface emerging from Eq. (5.14). Its intersection with the angular momentum sphere will point out nuclear trajectories, i.e., manifolds in the angular momentum space that show the precessional motion of the spin states belonging to the wobbling bands of  $^{163}\text{Lu}$ .

The 3-dimensional technique presented in the last subsection concluded with the set of Figs. 5.15 - 5.18, which are very useful for getting a grasp on the inherent dynamics of the system. Certainly, through the clear dissimilarities between each nuclear phase (precession around  $x_1$ , criticality, and finally precession around  $x_3$ ), one is able to understand the geometry of the rotational motion for a triaxial nucleus. The exact energy for a given spin state  $I$  where unstable wobbling occurs (the middle inset from Figs. 5.15 - 5.18) was numerically determined for all four bands. Since the entire formalism is based on the dequantization of  $\hat{H}$  by virtue of

the variational principle and because the CEF is strictly described in terms of the canonical coordinates  $(r, \varphi; f, \psi)$ , the obtained trajectories can indeed be regarded as classical quantities.

*These key points conclude this chapter with a semi-classical description of the wobbling bands.*



# Chapter 6

## Study of the Wobbling Motion via a Boson Description

This last part will be focused on the wobbling phenomenon but with a different approach than Chapters 4 ( $\mathbf{W}_1$ ) and 5 ( $\mathbf{W}_2$ ), as this method does not share the same foundational concepts. All the theoretical calculations and results shown here correspond to a publication made by the team for the nucleus  $^{135}\text{Pr}$  in Ref. [135]. In the first section, a set of results for the description of the angular momentum via boson operators are briefly recalled from the  $\mathbf{W}_0$  formalism. In the second section, the Hamiltonian and its framework will be developed using the transformation laws from the previous section. Two different expansions for the total angular momentum are obtained through these boson calculations. Furthermore, the Jacobi elliptic functions are introduced and used to construct the potential energy for a triaxial rotor. By studying the first-order derivative for the elliptic potential, the critical points can be acquired. The points of local and global minima are of interest here, because a second-order expansion around them leads to analytical expressions for the total energy and wobbling frequency of the triaxial system. The third section invokes a semi-classical analysis, giving equations for the total energy in terms of the angular momentum components. Depending on the axis with the largest MOI of the triaxial rotor, three situations can occur, where each of the 1-, 2-, and 3-axis have the largest MOI. Phase diagrams that show the energy function in terms of a polar representation for the a.m. components are constructed. These provide useful information regarding the stability of the wobbling motion. The electromagnetic transitions and their expressions are treated in

the fourth section, while a comparison of the data concerning energies and transition probabilities between the model and the experimental measurements for  $^{135}\text{Pr}$  is given in the fifth section. Concluding remarks on this research are provided at the end of the chapter.

## 6.1 Angular Momentum - Boson Representation

Besides the odd-mass case study performed by the team in Ref. [39] for  $^{163}\text{Lu}$  using the  $\mathbf{W}_0$  formalism, the first part of that paper consisted in describing wobbling motion for even-even nuclei using a *boson expansion* of the angular momentum components. The problem considered a triaxial rigid rotor with moments of inertia  $\mathcal{I}_k$  described by the known rotor Hamiltonian (recall Section 2.3.2 and Eq. (2.55)):

$$\hat{H}_R = \frac{\hat{R}_1}{2\mathcal{I}_1} + \frac{\hat{R}_2}{2\mathcal{I}_2} + \frac{\hat{R}_3}{2\mathcal{I}_3} , \quad (6.1)$$

and angular momentum components  $\hat{R}_k$ . The calculations were applied successfully to  $^{158}\text{Er}$ , where the model described rotational energies and transition probabilities very well. Since a full review of  $\mathbf{W}_0$  would be out of scope, only the relevant aspects concerning the boson representation for the angular momentum will be succinctly outlined.

From that initial quantal problem, a variational principle (similar recipe as the one portrayed in Section 4.2.1, but only for one set of coordinates) brings the system into a classical view, where the eigenvalue problem becomes a system of classical equations in a phase space (see Section II.A and II.B from Ref. [39]). Summarizing the calculations, one obtained *i*) a pair of conjugate variables (i.e.,  $r$  and  $\varphi$ ) and *ii*) two equations of motion (recall discussion from Section 4.2.2 and Eq. (4.12)) as:

$$\frac{\partial \mathcal{H}}{\partial r} = \dot{\varphi} , \quad \frac{\partial \mathcal{H}}{\partial \varphi} = -\dot{r} , \quad (6.2)$$

with  $\mathcal{H}$  as the average of  $\hat{H}_R$  with the trial function. If the average values of the angular momentum components are expressed in terms of the phase space

coordinates  $(r, \varphi)$ , then the following equations emerge:

$$\begin{aligned} J_+^{\text{cls}} &\equiv \langle \hat{R}_+ \rangle = \sqrt{r(2I-r)} e^{i\varphi}, \\ J_-^{\text{cls}} &\equiv \langle \hat{R}_- \rangle = \sqrt{r(2I-r)} e^{-i\varphi}, \\ J_3^{\text{cls}} &\equiv \langle \hat{R}_3 \rangle = r - I. \end{aligned} \quad (6.3)$$

Their algebra is governed by the Poisson brackets, which define their inner product:

$$\{J_+^{\text{cls}}, J_-^{\text{cls}}\} = -2i J_3^{\text{cls}}, \quad \{J_{\pm}^{\text{cls}}, J_3^{\text{cls}}\} = \pm i J_{\pm}^{\text{cls}}. \quad (6.4)$$

The three functions  $J_+^{\text{cls}}$ ,  $J_-^{\text{cls}}$ ,  $J_3^{\text{cls}}$  together with the Poisson brackets from Eq. (6.4) generate a classical algebra  $\text{SU}(2)_{\text{cls}}$ . A pair of complex functions  $f$  and  $g$  defined in this classical phase space will have their associated Poisson bracket:

$$\{f, g\} = \frac{\partial f}{\partial \varphi} \frac{\partial g}{\partial r} - \frac{\partial f}{\partial r} \frac{\partial g}{\partial \varphi}. \quad (6.5)$$

The classical coordinates belonging to that phase space were re-quantized through the *Dyson boson expansion* [160], which signified a change of the picture from the classical  $\text{SU}(2)_{\text{cls}}$  back to a quantized view. Firstly, the quantization starts with two canonical complex variables written in terms of the conjugate coordinates  $(r, \varphi)$ :

$$\begin{aligned} \mathcal{C} &= \sqrt{2I} \sqrt{\frac{r}{(2I-r)}} e^{-i\varphi}, \\ \mathcal{B}^* &= \frac{1}{\sqrt{2I}} \sqrt{r(2I-r)} e^{i\varphi}, \end{aligned} \quad (6.6)$$

and the Poisson bracket is:  $\{\mathcal{B}^*, \mathcal{C}\} = i$ . The quantization process within the Dyson representation implies that a new set of quantal operators  $b$  and  $b^\dagger$  should replace the two complex coordinates, and the inner product defined by the Poisson bracket becomes the commutator operator:

$$(\mathcal{C}, \mathcal{B}^*, \{, \}) \implies (b, b^\dagger, -i [, ]) . \quad (6.7)$$

The transformation employed in Eq. (6.7) will introduce the following set of angular momentum components:

$$\begin{aligned}\hat{J}_+^D &= \sqrt{2I}b^\dagger , \\ \hat{J}_-^D &= \sqrt{2I} \left(1 - \frac{b^\dagger b}{2I}\right) b , \\ \hat{J}_3^D &= I - b^\dagger b .\end{aligned}\tag{6.8}$$

The set of angular momentum components  $\hat{J}^D$  provided in Eq. (6.8) marks the onset of the *Dyson boson representation*. A function that depends on the variables from Eq. (6.6) can be quantized by first writing its expression in terms of  $\mathcal{C}$  and  $\mathcal{B}^*$  and then replacing both variables by the boson operators  $b$  and  $b^\dagger$ . The transformation is boson-like because of the nature of  $b$  and  $b^\dagger$ . These operators obey the boson canonical commutation relations:

$$[b, b^\dagger] = 1 , [b, b] = [b^\dagger, b^\dagger] = 0 .\tag{6.9}$$

The classical energy function  $\mathcal{H}$  can be written in terms of the variables  $\mathcal{C}$  and  $\mathcal{B}$  and then replace them with the boson operators  $b$  and  $b^\dagger$ . Consequently, the Dyson representation of the rotor Hamiltonian  $\hat{H}_R$  is obtained, which was denoted by  $\hat{H}_D$ . The search for *real* eigenvalues for  $\hat{H}_D$  was made through the *Bargmann representation* [161–163]. This mapping assigns to the operators  $b, b^\dagger$  two differential operators, which leads to a differential equation for  $\hat{H}_D$ :

$$b^\dagger \rightarrow x , b \rightarrow \frac{d}{dx} .\tag{6.10}$$

Indeed, by applying the mapping from Eq. (6.10), the eigenvalue problem becomes equivalent to solving the second-order differential equation (recall Eq. 2.34 from Ref. [39]):

$$\left[p(x^4)\frac{d^2}{dx^2} + q(x^3)\frac{d}{dx} - r(x^2)\right] G = E'G .\tag{6.11}$$

Further calculations from that work gave the energy spectrum for  $^{158}\text{Er}$ , providing unique results for the even-even deformed nuclei. The *transitions* from a quantal space ( $\hat{H}_R$ ) to a classical space ( $\mathcal{H}$ ), and then a re-quantized ( $\hat{H}_D$ ) showed some

remarkable features of the approach. In all three cases, a great agreement with the experimental data was obtained for the yrast band and the first two excited bands. The finding that the semi-classical treatment gives similar results with quantal methods, which are inherently more complex, was a key result that emerged from  $\mathbf{W}_0$ .

## 6.2 Theoretical Framework

The boson representation of the angular momentum operator was introduced in Section 6.1 because the study from Ref. [135] is based on such representations. In this paper, the team proposed a novel formalism in which the angular momentum components are expanded in terms of boson operators. In contrast to  $\mathbf{W}_0$ , here the even-odd mass nuclei are considered. By using the *Bargmann mapping*, the eigenvalue equation associated with the model Hamiltonian is brought to a Schrödinger-like structure.

### 6.2.1 Potential Energy for the PRM Hamiltonian

Since the initial problem consists of an odd- $A$  nucleus, the particle-triaxial rotor Hamiltonian is adopted. A rigid-coupling approximation is considered, meaning that the angular momentum of the odd particle is aligned with the core. The Hamiltonian for the system will become (keeping the notations consistent with the work from Ref. [135]):

$$\hat{H}_{\text{rot}} = \sum_k A_k \left( \hat{I}_k - \hat{j}_k \right)^2, \quad (6.12)$$

where  $k = 1, 2, 3$ , and  $A_k$  is the inertia factor (used throughout the previous chapters). As per the *rigid coupling*, the single-particle a.m.  $\mathbf{j}$  will stay in the principal plane (1, 2), meaning that the vector is described by  $\mathbf{j} = (j \cos \theta, j \sin \theta, 0)$ . In addition, the largest MOI is considered the one along the 2-axis (i.e.,  $\mathcal{I}_2$ ). In a first-order approximation, the angular momentum component  $\hat{I}_2$  can be expanded as:

$$\hat{I}_2 = I \left( 1 - \frac{1}{2} \frac{\hat{I}_1^2 + \hat{I}_3^2}{I^2} \right), \quad (6.13)$$

and through this expansion, the Hamiltonian from Eq. (6.12) can be rewritten as:

$$\hat{H}_{\text{rot}} = A\hat{H}' + (A_1 I^2 - A_2 j_2 I) + \sum_{k=1,2} A_k \hat{j}_k^2 . \quad (6.14)$$

For the terms in Eq. (6.14) the following notations have been adopted [135]:

$$\begin{aligned} \hat{H}' &= \hat{I}_2^2 + u\hat{I}_3^2 + 2v_0\hat{I}_1 , \\ u &= \frac{A_3 - A_1}{A} , \\ v_0 &= -\frac{A_1 j_1}{A} , \\ A &= A_2 \left(1 - \frac{j_2}{I}\right) - A_1 , \\ A > 0 , \quad -1 < u < 1 . \end{aligned} \quad (6.15)$$

Taking a closer look at the Hamiltonian depicted in Eq. (6.14), it can be seen that  $\hat{H}'$  looks like the triaxial rotor Hamiltonian, but amended with a new term, which would act as a constraint on the system (*cranking-like term*), making it rotate around the one-axis. In this research, the cranking axis is set to be 1-axis. Following the same recipe as in the  $\mathbf{W}_0$  case, the a.m. components are expressed in terms of the raising and lowering operators:

$$\hat{I}_{\pm} = \hat{I}_2 \pm i\hat{I}_3 , \quad \hat{I}_0 \equiv \hat{I}_1 . \quad (6.16)$$

The a.m. components satisfy the commutation relations (in the rotating reference frame):

$$[\hat{I}_-, \hat{I}_+] = 2\hat{I}_0 , \quad [\hat{I}_{\pm}, \hat{I}_0] = \pm\hat{I}_{\pm} . \quad (6.17)$$

The transformation from Eq. (6.17) keeps the same commutation relations for the angular momentum components. Using these variables, the expression of  $\hat{H}'$  from Eq. (6.15) becomes:

$$\hat{H}' = \frac{1-u}{4} (\hat{I}_+^2 + \hat{I}_-^2) + \frac{1+u}{4} (\hat{I}_+\hat{I}_- + \hat{I}_-\hat{I}_+) + 2v_0\hat{I}_0 . \quad (6.18)$$

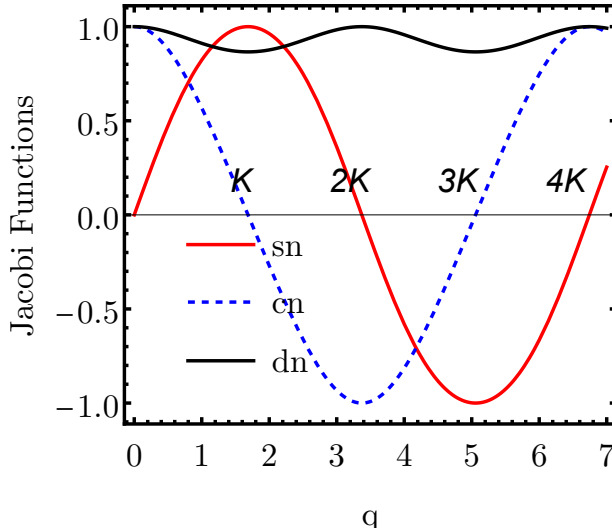


FIGURE 6.1: The elliptic functions  $\text{sn}$ ,  $\text{cn}$ , and  $\text{dn}$  from Eq. (6.20) are represented as functions of  $q$ . The value of the *elliptic modulus*  $k$  is set to  $1/2$ .

The Schrödinger equation associated with this Hamiltonian:

$$\hat{H}' |\Psi\rangle = E |\Psi\rangle , \quad (6.19)$$

is expressed in terms of two conjugate variables  $q$  and  $d/dq$  with the help of the Jacobi Elliptic functions  $\text{sn}$ ,  $\text{cn}$ , and  $\text{dn}$  [164, 165]. These functions are used quite often in physics, especially in non-linear problems [166], and they are defined as:

$$\begin{aligned} s &\equiv \text{sn}(q, k) , \quad c \equiv \text{cn}(q, k) , \quad d \equiv \text{dn}(q, k) , \\ k &= \sqrt{|u|} , \quad k' = \sqrt{1 - k^2} , \\ q &= \int_0^\varphi \frac{1}{\sqrt{1 - k^2 \sin^2(x)}} dx \equiv F(\varphi, k) . \end{aligned} \quad (6.20)$$

An alternative representation for the elliptic functions is in terms of the trigonometric functions [167]:

$$s = \sin \varphi , \quad c = \cos \varphi , \quad d = \sqrt{1 - k^2 s^2} , \quad (6.21)$$

where  $\varphi$  is also known as the *Jacobi Amplitude*:  $\varphi = \text{amu}(q, k)$  [168]. The behavior of  $s$ ,  $c$ , and  $d$  is graphically shown in Fig. 6.1. It can be observed that these functions are periodic, with the periods  $4K$ ,  $4K$ , and  $2K$ , respectively. The value of  $K$  is given by replacing  $\varphi = \pi/2$  in  $F(\varphi, k)$  from Eq. (6.20).

Referring back to the angular momentum components, these can be written in terms of the elliptic functions and the variables  $q$ ,  $d/dq$  as such [135]:

$$\begin{aligned}\hat{I}_{\pm} &= i \frac{c \mp d}{k's} \left( I \pm \hat{I}_0 \right) , \\ \hat{I}_0 &= Icd - s \frac{d}{dq} ,\end{aligned}\quad (6.22)$$

which would make the Hamiltonian  $\hat{H}'$  from Eq. (6.18) achieve the following shape:

$$\hat{H}' = -\frac{d^2}{dq^2} - 2v_0s \frac{d}{dq} + I(I+1)s^2k^2 + 2v_0cdI . \quad (6.23)$$

By changing the wave-function  $|\Psi\rangle$  to:

$$|\Psi\rangle = (d - kc)^{-\frac{v_0}{k}} |\Phi\rangle , \quad (6.24)$$

the Schrödinger equation will have two fully separated *kinetic* and *potential* terms:

$$\left[ -\frac{d^2}{dq^2} + V(q) \right] |\Phi\rangle = E |\Phi\rangle . \quad (6.25)$$

The potential term  $V(q)$  is defined as [135]:

$$V(q) = [I(I+1)k^2 + v_0^2] s^2 + (2I+1) v_0cd . \quad (6.26)$$

and it is graphically represented in Fig. 6.2. It can be seen that  $V(q)$  has a symmetry to the change of sign for the coordinate  $q$ . If the potential is calculated for the interval  $q \in [-4K, 4K]$ , it has three deep symmetric wells, with degenerate minima, and two local minima surrounding  $q = \pm 2K$ . The states near the local minima are meta-stable, meaning that through a tunneling effect, they can transition to adjacent minima. These characteristics are illustrated in Fig. 6.3.

By adopting the Bargmann representation for the angular momentum representation depicted in Eq. (6.22), a set of boson operators for the variable  $q$  and its first-derivative operator can be mapped:

$$q \rightarrow b^\dagger , \quad \frac{d}{dq} \rightarrow b , \quad (6.27)$$

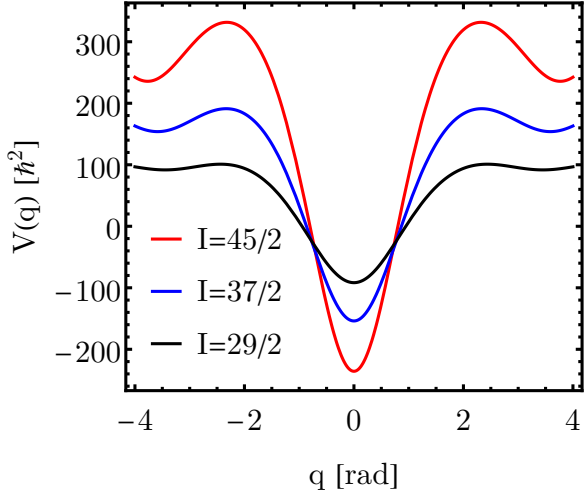


FIGURE 6.2: The potential energy as function of  $q$  for several values of the angular momentum  $I$ . For the calculation of  $V(q)$ , the MOI were set to  $\mathcal{I}_1 : \mathcal{I}_2 : \mathcal{I}_3 = 95 : 100 : 85 \text{ } \hbar\text{MeV}^{-2}$ ,  $j = 13/2$ , and  $\theta = -80^\circ$ .

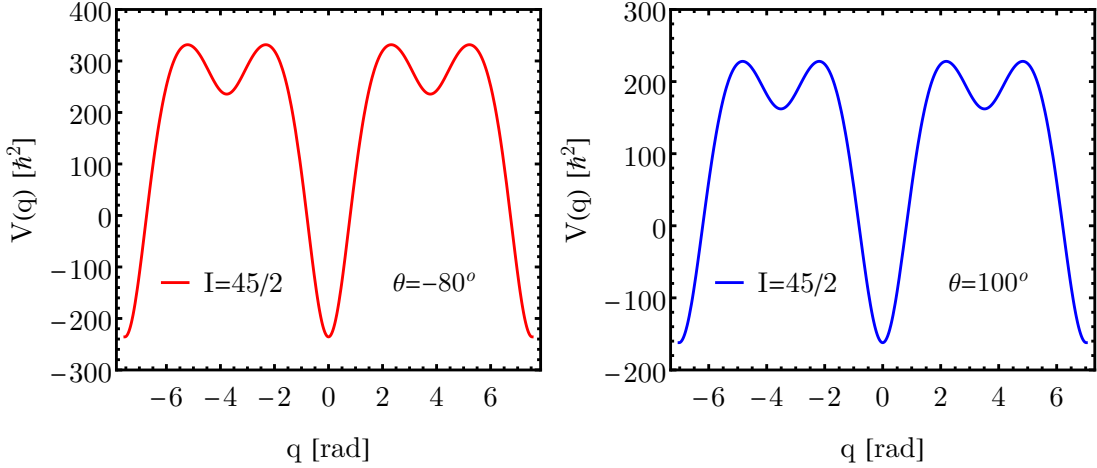


FIGURE 6.3: The potential energy  $V(q)$  for  $\theta = -80^\circ$  and  $\theta + \pi$ , but for an extended range of the variable  $q$ , such that the deep and local minima can be seen. The same moments of inertia are used as in Fig. 6.1.

and this results in the three components  $\hat{I}_{\mp}$  and  $\hat{I}_0$  becoming [135]:

$$\begin{aligned}\hat{I}_+ &= i \frac{cb^\dagger - db^\dagger}{k' sb^\dagger} (I + Icb^\dagger db^\dagger - sb^\dagger b) , \\ \hat{I}_- &= i \frac{cb^\dagger + db^\dagger}{k' sb^\dagger} (I - Icb^\dagger db^\dagger + sb^\dagger b) , \\ \hat{I}_0 &= Icb^\dagger db^\dagger - sb^\dagger b .\end{aligned}\quad (6.28)$$

*This is the first time in literature when such a transformation emerges.* The remarkable features of the work presented in Ref. [135] are the boson expansion

of angular momentum components obtained from elliptic functions  $s$ ,  $c$ , and  $d$ , and the application of the Bargmann mapping depicted in Eq. (6.27) to these components.

### 6.2.2 Another boson expansion for the angular momentum

Particular attention should be paid to the case where  $k = 0$ , as the elliptic functions will have the following values:

$$q = \varphi, \quad d = 1, \quad K = \frac{\pi}{2}, \quad k' = 1. \quad (6.29)$$

Using these values, the components from Eq. (6.28) can be re-written such that in the rotating frame they become:

$$\begin{aligned} \hat{I}_+ &= i[-I \sin b^\dagger + (1 - \cos b^\dagger) b^\dagger], \\ \hat{I}_- &= i[I \sin b^\dagger + (1 + \cos b^\dagger) b], \\ \hat{I}_0 &= I \cos b^\dagger - b \sin b^\dagger, \end{aligned} \quad (6.30)$$

which can be simplified even more if the trigonometric functions are expanded and only the leading terms are kept:

$$\begin{aligned} \hat{I}_+ &= i\left[-Ib^\dagger + \frac{1}{2}b(b^\dagger)^2\right], \\ \hat{I}_- &= 2ib, \\ \hat{I}_0 &= I - b^\dagger b. \end{aligned} \quad (6.31)$$

The components from Eq. (6.31) are similar to the ones from the Dyson boson expansion (recall Eq. (6.7)), making it clear now that the representations shown in Eq. (6.28) and Eq. (6.30) are generalizations of the Dyson representation.

### 6.2.3 Harmonic Approximation of the Energy

One can aim at solving numerically Eq. (6.25), but there could be a rather simpler and more *elegant* approach to this. Adopting the harmonic approximation (as described in the previous chapters) can provide valid results. The first step is to



FIGURE 6.4: The potential  $V(q)$  from Eq. (6.26), near the  $q = 2K$  minimum point. It can be observed that the minimum character appears only for  $I > 19/2$ .

analyze the stationary points of the elliptic potential  $V(q)$ . Its first-order derivative is given by [135]:

$$\frac{d}{dq}V(q) = s \left[ (I(I+1)k^2 + v_0^2) 2cd - (2I+1)v_0 k'^2 - (2I+1)v_0 2k^2 c^2 \right]. \quad (6.32)$$

There are five minima, located at  $q = 0, \pm 2K, \pm 4K$ . Remarkable that for  $q = \pm 2K$  the two minima emerge for angular momentum values that are larger than  $19/2$ . This is emphasized in Fig. 6.4, where it can be seen that the minima are flat at the beginning, but their depth increases with increasing values of  $I$ .

The angular momentum can be studied in terms of its orientation near the minimum points. This is achieved if the boson expansion is written as [135]:

$$\begin{aligned} \hat{I}_+ &= \frac{i}{k'} \left[ I(-d + ck^2)s - (c-d)\frac{d}{dq} \right], \\ \hat{I}_- &= \frac{i}{k'} \left[ I(d + ck^2)s + (c+d)\frac{d}{dq} \right], \\ \hat{I}_0 &= Icd - s\frac{d}{dq}, \end{aligned} \quad (6.33)$$

and for  $q = \pm 2K$  (that is  $\varphi = \pm\pi$ ) one has  $\hat{I}_0 = -I$ , while  $q = 0$  (i.e.,  $\varphi = 2$ ) will lead to  $\hat{I}_0 = I$ . Consequently, in the local minima, the total angular momentum will align anti-parallel with the 1-axis, and for the deep minimum  $q = 0$  the angular momentum is aligned along the (1)-axis. Expanding the elliptic potential  $V(q)$  up to second order in the coordinate, an equation that looks similar to the harmonic

oscillator is obtained for the Hamiltonian  $\hat{H}_{\text{rot}}$  (firstly introduced in Eq. (6.12)):

$$E_n = A_1 I^2 + \hbar\omega \left( n + \frac{1}{2} \right) + e_{\text{sp}} , \quad (6.34)$$

where the single-particle term is defined as:

$$e_{\text{sp}} = \sum_{i=1,2} A_i j_i^2 - (2I+1)A_1 j_1 - IA_2 j_2 . \quad (6.35)$$

The frequency  $\omega$  from Eq. (6.34) has the expression:

$$\begin{aligned} \omega^2 = & \left[ (2I+1) \left( A_2 - A_1 - \frac{A_2 j_2}{I} \right) + 2A_1 j_1 \right] \cdot \\ & \cdot [(2I+1)(A_3 - A_1) + 2A_1 j_1] - (A_3 - A_1) \left( A_2 - A_1 - \frac{A_2 j_2}{I} \right) . \end{aligned} \quad (6.36)$$

The Hamiltonian  $\hat{H}_{\text{rot}}$  is connected to  $\hat{H}'$  via Eq. (6.14), meaning that the final energy spectrum of  $\hat{H}'$  will be given by:

$$\begin{aligned} E'_n = & A_1 I^2 + \hbar\omega' \left( n + \frac{1}{2} \right) + e_{\text{sp}} , \\ e_{\text{sp}} = & \sum_{i=1,2} A_i j_i^2 - (2I+1)A_1 j_1 - IA_2 j_2 , \end{aligned} \quad (6.37)$$

with the wobbling frequency  $\omega'$  having the following definition:

$$\begin{aligned} \omega'^2 = & \left[ (2I+1) \left( A_2 - A_1 - \frac{A_2 j_2}{I} \right) - 2A_1 j_1 \right] [(2I+1)(A_3 - A_1) - 2A_1 j_1] - \\ & - (A_3 - A_1) \left( A_2 - A_1 - \frac{A_2 j_2}{I} \right) \end{aligned} \quad (6.38)$$

The two wobbling frequencies, i.e.,  $\omega$  and  $\omega'$  are both graphically represented in Fig. 6.5. As the angular momentum components  $j_1$  and  $j_2$  depend on the angle  $\theta$ , the evolution of both frequencies is plotted as a function of this coordinate. It can be seen from the two curves that both wobbling frequencies have a maximum value  $\approx 1$ , but  $\omega_{\text{max}}$  is located at  $\theta \approx -0.7$  rad, while  $\omega'_{\text{max}}$  is at  $\theta \approx -2.4$  rad. Moreover, the two frequencies intersect each other at the points  $\theta = -\pi/2$  and  $\theta = \pi/2$ .



FIGURE 6.5: The two wobbling frequencies  $\omega$  (Eq. (6.36)) and  $\omega'$  (Eq. (6.38)) as function of the coordinate  $\theta$  for a fixed set of MOI  $\mathcal{I}_1 : \mathcal{I}_2 : \mathcal{I}_3 = 91 : 9 : 51 \hbar^2 \text{MeV}^{-1}$  and single-particle angular momentum  $j = 13/2$ .

### 6.3 Classical Description of the Hamiltonian

Going further with the analysis performed in Ref. [135], the quantal operators associated with the angular momentum are dequantized, through the algebra:

$$[ , ] \longrightarrow -i\{ , \} , \quad (6.39)$$

where the Poisson brackets replace the commutator. The dequantization procedure consists of replacing the operators  $\hat{I}_k$  with the classical components of the angular momentum  $I_k$ . The conjugate coordinate of  $I_k$  are further denoted by  $\varphi_k$  and the three angular momentum components  $I_k$  are hereafter denoted by  $x_k$ . With this algebra, the quantal Hamiltonian from Eq. (6.15) will be equivalent to:

$$H' = x_2^2 + ux_3^2 + 2v_0 I_x . \quad (6.40)$$

Such an approach was also used when studying the Classical Energy Function (CEF) from Chapter 5 (recall Eq. (5.10)). The equations of motion for  $H'$  are

(time derivatives are specified by the dot symbol):

$$\begin{aligned}\dot{x}_1 &= 2(1-u)x_2x_3 , \\ \dot{x}_2 &= 2(x_1u - v_0)x_3 , \\ \dot{x}_3 &= -2(x_1 - v_0)x_2 .\end{aligned}\tag{6.41}$$

The two constants of motion for this classical problem are:

$$E = x_2^2 + ux_3^2 + 2v_0x_1 ,\tag{6.42}$$

and:

$$I^2 = x_1^2 + x_2^2 + x_3^2 ,\tag{6.43}$$

which is in complete agreement with the fact the total energy and the total angular momentum are conserved quantities. Now that the classical counterpart of  $\hat{H}'$  is analytically obtained, there can be several situations that can lead to the description of the harmonic-like motion of the even-odd system. Namely, by considering the three angular momentum components  $x_1$ ,  $x_2$ , and  $x_3$  in the *polar coordinate system* (defined by the coordinates  $\theta$  and  $\varphi$ ), one can have multiple considerations.

### Case A1

The maximal MOI corresponds to the 2-axis. The Cartesian coordinates are changed to the polar ones via:

$$x_2 = I \cos \theta_2 , \quad x_3 = I \sin \theta_2 \cos \varphi_2 , \quad x_1 = I \sin \theta_2 \sin \varphi_2 .\tag{6.44}$$

The energy function  $H'$  can be expressed in terms of the conjugate coordinates  $(x_2, \varphi_2)$ :

$$H' = x_2^2 \left( 1 - u \cos^2 \varphi_2 - \frac{v_0}{I} \sin \varphi_2 \right) + uI^2 \cos^2 \varphi_2 + 2v_0I \sin \varphi_2 .\tag{6.45}$$

This function has a minimum value of  $H'|_{\min} = -2v_0I$  at  $(x_2, \varphi_2) = (0, -\pi/2)$ , and the second derivatives for  $H'$  in that point are:

$$\begin{aligned}\frac{\partial^2 H'}{\partial x_2^2}\Big|_{\min} &= 2\left(2 + \frac{v_0}{I}\right), \\ \frac{\partial^2 H'}{\partial \varphi_2^2}\Big|_{\min} &= 2\left(u + \frac{v_0}{I}\right)I^2.\end{aligned}\quad (6.46)$$

If the classical energy function is expanded up to the second order around the minimum point, then  $H'$  will look like this:

$$H'^{(2)} = -2v_0I\left(1 + \frac{v_0}{I}\right)\bar{x}_2^2 + \left(u + \frac{v_0}{I}\right)I^2\bar{\varphi}_2^2,\quad (6.47)$$

where the deviation of the coordinates from the minimum point was denoted by  $(\bar{x}_2, \bar{\varphi}_2)$  and the superscript (2) suggests the second order expansion. This kind of function describes an oscillator with the frequency:

$$\omega^{(2)} = 2\sqrt{(I + v_0)(Iu + v_0)}.\quad (6.48)$$

In the minimum point, the angular momentum components are  $(x_1, x_2, x_3) = (-I, 0, 0)$  and  $E = -2v_0I$ . In Fig. 6.6 the energy function  $H'$  is graphically represented for  $x_2 = 0$  and  $\varphi_2 = -\pi/2$ , respectively, by keeping one coordinate fixed and varying the other. On both plots, the minimum value for  $H'$  is achieved at the value  $-2Iv_0$ .

## Case A2

Another minimum point for  $H'$  is  $(0, \pi/2)$ , in which the angular momentum is  $(x_1, x_2, x_3) = (I, 0, 0)$  and the energy is  $E = 2v_0I$ . Repeating the second order expansion for  $H'$ , the following formula is attained:

$$H'^{(2)} = 2v_0I + \left(1 - \frac{v_0}{I}\right)\bar{x}_2^2 + I^2\left(u - \frac{v_0}{I}\right)\bar{\varphi}_2^2,\quad (6.49)$$

which describes a harmonic oscillator with a frequency:

$$\omega^{(2)} = 2\sqrt{(I - v_0)(uI - v_0)}.\quad (6.50)$$



FIGURE 6.6: The classical energy  $H'$  from Eq. (6.45) evaluated for a fixed  $x_2 = 0$  (left) and fixed  $\varphi_2 = -\pi/2$  (right). The calculations were done for  $\mathcal{I}_1 : \mathcal{I}_2 : \mathcal{I}_3 = 10 : 40 : 20 \text{ } \hbar\text{MeV}^{-1}$ . The single-particle angular momentum  $j = 11/2$ .

### Case A3

A third set of conjugate variables for which  $H'$  is minimal is:

$$(x_2, \varphi_2) = (0, \arcsin\left(\frac{v_0}{Iu}\right)) .$$

With this set of coordinates the energy function will become after expansion:

$$H'^{(2)} = uI^2 + \frac{v_0^2}{u} + (1-u)\bar{x}_2^2 - u\left(I^2 - \frac{v_0^2}{u^2}\right)\bar{\varphi}_2^2 . \quad (6.51)$$

For a positive value of  $u$ , but confined inside  $u \in (0, 1)$  the coordinates consist of a *saddle point* with angular momentum components:

$$(x_1, x_2, x_3) = \left(\frac{v_0}{u}, 0, \sqrt{I^2 - \frac{v_0^2}{u^2}}\right) ,$$

and energy:

$$E = I^2u + \frac{v_0^2}{u} .$$

Summarizing the situations A1, A2, and A3, there are three stationary points for  $H'$  when the maximal MOI is along the 2-axis, (i.e., the quantization axis). The points are provided in Table 6.1, where values for  $x_2$  and  $\varphi_2$  are accompanied by

TABLE 6.1: The stationary points for the classical energy function depicted in Eq. (6.40), when the quantization axis is the 2-axis. Each point corresponds to the cases  $A1$ ,  $A2$ , and  $A3$ , respectively.

Point $p$	$x_2$	$\varphi_2$	A.m. components ( $x_1, x_2, x_3$ )	$E$	Character of the stationary point
$p_1^A(m)$	0	$-\frac{\pi}{2}$	$(-I, 0, 0)$	$E = -2v_0I$	minimum (m)
$p_2^A(m)$	0	$\frac{\pi}{2}$	$(I, 0, 0)$	$E = 2v_0I$	minimum (m)
$p_3^A(s)$	0	$\arcsin\left(\frac{v_0}{Iu}\right)$	$\left(\frac{v_0}{u}, 0, \sqrt{I^2 - \frac{v_0^2}{u^2}}\right)$	$E = \left(I^2u + \frac{v_0^2}{u}\right)$	saddle (s)

the angular momentum components and the value of the energy. Moreover, the character of each stationary point is also mentioned.

Considering that the polar coordinates used to define the three angular momentum components can be replaced in the expression of  $H'$  from Eq. (6.40), then an energy function that will depend explicitly on  $\theta_2$  and  $\varphi_2$ . This *polar representation of the classical energy function* can be represented for a given interval of  $\theta_2$  and  $\varphi_2$ , respectively. Fixing the total angular momentum  $I$ , the single-particle a.m.  $j$ , the three MOI, and the value of  $\theta$  (not to be confused with the polar  $\theta_2$ ), a contour plot such as the one shown in Fig. 6.7 can be obtained. Within the contour plot, there are several stationary points: one deep minimum, one local minimum, and two saddle points. Every point lies along the  $\theta_2 = \pi/2$  coordinate. To better perceive how the minima and saddle points are located, Fig. 6.8 shows the evolution of  $H'$  for  $\theta_2 = \pi/2$ . Keep in mind that both figures are evaluated for the same set of constants.

### Case B1

Going further with the analysis, a second approach would be to consider the 3-axis as the quantization axes, meaning that now the largest MOI is around this axis. The angular momentum components written in terms of the polar coordinates  $(\theta_3, \varphi_3)$  will be defined in the following way:

$$x_1 = I \sin \theta_3 \cos \varphi_3 , \quad x_2 = I \sin \theta_3 \sin \varphi_3 , \quad x_3 = I \cos \theta_3 , \quad (6.52)$$



FIGURE 6.7: Contour plot for the energy  $H'$  from Eq. (6.40), defined in terms of the polar coordinates. The calculations are done for the A1-A2-A3 cases (i.e., maximal MOI is  $\mathcal{I}_2$ ). The single-particle angular momentum is  $j = 11/2$ , the total angular momentum  $I = 19/2$ , the MOI are  $\mathcal{I}_1 : \mathcal{I}_2 : \mathcal{I}_3 = 10 : 40 : 20 \text{ } \hbar^2 \text{MeV}^{-1}$ , and  $\theta = 70^\circ$ . The four stationary points are illustrated, namely two minima - one local and one global - (denoted by "m") and two saddle points (denoted by "s").

In the same way as the  $A$ -cases. the total energy  $H'$  can be expressed in terms of the  $x_3$  coordinate and the polar  $\varphi_3$  one:

$$H'^{(2)} = x_3^2 \left( u - \sin^2 \varphi_3 - \frac{v_0}{I} \cos \varphi_3 \right) + I^2 \sin^2 \varphi_3 + 2v_0 I \cos \varphi_3 . \quad (6.53)$$

The first stationary point of Eq. (6.53) with a minimum character is  $(x_3, \varphi_3) = (0, \pi)$ . For this point, the angular momentum components are  $(x_1, x_2, x_3) = (-I, 0, 0)$ , hinting at the fact that the total a.m. is oriented along the one-axis. The value of the energy in this point is  $E = -2v_0 I$ . The harmonic Hamiltonian given in the second-order expansion around this point is:

$$H'^{(2)} = -2v_0 I + \left( u + \frac{v_0}{I} \right) \bar{x}_3^2 + I^2 \left( 1 + \frac{v_0}{I} \right) \bar{\varphi}_3^2 , \quad (6.54)$$

having a similar shape for the wobbling frequency as per the  $A1$  case. Similarly



FIGURE 6.8: The classical energy  $H'$  from Eq. (6.40), for a fixed  $\theta_2 = \pi/2$  and  $\varphi \in [0, 2\pi]$ . The single-particle angular momentum is  $j = 11/2$ , the total angular momentum  $I = 19/2$ , the MOI are  $\mathcal{I}_1 : \mathcal{I}_2 : \mathcal{I}_3 = 10 : 40 : 20 \hbar^2 \text{MeV}^{-1}$ , and  $\theta = 70^\circ$ . The critical points present in Fig. 6.7 are also illustrated here by the dashed vertical lines (two minima with red color and two saddle points with blue color).

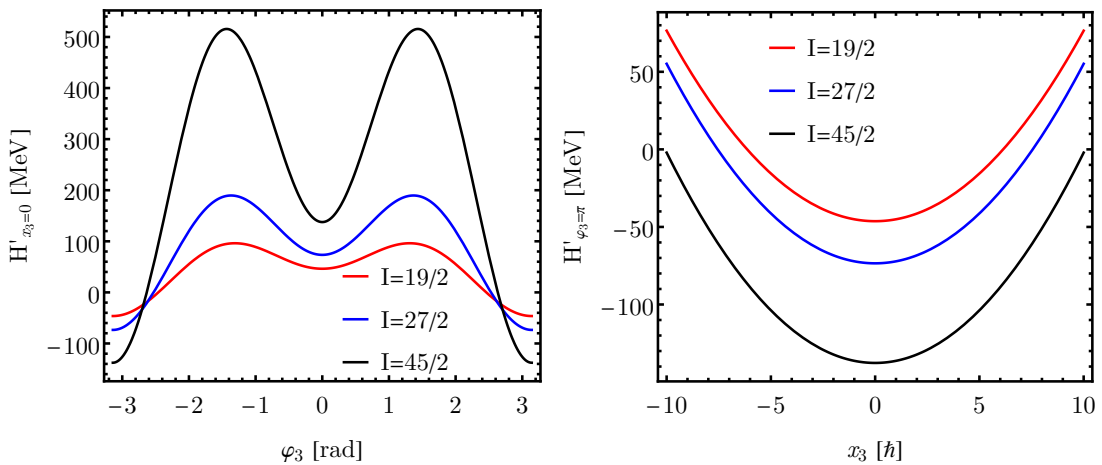


FIGURE 6.9: The classical energy  $H'$  from Eq. (6.53) evaluated for a fixed  $x_3 = 0$  (left) and fixed  $\varphi_3 = \pi$  (right). The calculations were done for  $\mathcal{I}_1 : \mathcal{I}_2 : \mathcal{I}_3 = 10 : 20 : 40 \hbar^2 \text{MeV}^{-1}$ . The single-particle angular momentum  $j = 11/2$ .

as for the  $A1$  case, the Hamiltonian  $H'$  is also represented in terms of only one coordinate at a time, where each of the coordinates is fixed to  $x_3 = 0$  and  $\varphi_3 = \pi$ , respectively. These plots are shown in Figs. 6.9.

## B2 case

Another stationary point for Eq. (6.53) is  $(x_3, \varphi) = (0, 0)$ , which is also a minimum. The second order expansion of  $H'$  gives:

$$H' = 2v_0I + \left(u - \frac{v_0}{I}\right)\bar{x}_3^2 + I^2\left(1 - \frac{v_0}{I}\right)\bar{\varphi}_3^2, \quad (6.55)$$

and moreover  $(x_1, x_2, x_3) = (I, 0, 0)$ , and  $E = 2v_0I$ . The wobbling frequency is:

$$\omega^{(2)} = 2\sqrt{\left(1 - \frac{v_0}{I}\right)\left(u - \frac{v_0}{I}\right)I^2}. \quad (6.56)$$

## B3 case

Lastly, the stationary point  $(x_3, \varphi_3) = (0, \arccos \frac{v_0}{I})$  is a maximum, giving a.m. components:

$$(x_1, x_2, x_3) = \left(v_0, \sqrt{I^2 - v_0^2}, 0\right), \quad (6.57)$$

and energy  $E = I^2 + v_0^2$ . For this maximum point, the energy function  $H'$  becomes:

$$H'^{(2)} = I^2 + v_0^2 + (u - 1)\bar{x}_3^2 + (v_0^2 - I^2)\bar{\varphi}_3^2. \quad (6.58)$$

The contour plot of the energy function  $H'$  can be obtained in the same manner as for A situations, i.e., taking the polar coordinates  $(\theta_3, \varphi_3)$  that are used in the expression of the angular momentum components from Eq. (6.52), and evaluate  $H'(\theta_3, \varphi_3)$  for fixed values of  $j$ ,  $I$ ,  $\mathcal{I}_1$ ,  $\mathcal{I}_2$ ,  $\mathcal{I}_3$ , and  $\theta$ . The contour plot together with the evolution of  $H'(\pi, \varphi_3)$  are drawn in Figs. 6.10 - 6.11.

Analyzing the Figs. 6.10 - 6.11, five stationary points can be observed: two maxima denoted by "M" (magenta color) and three minima denoted by "m" (red color). All the stationary points for the B cases are identified in Table 6.2, similarity as for the A situations.

## Case C1

Lastly, the situation when the largest MOI corresponds to the 1-axis should be analyzed. Choosing the 1-axis as the quantization axis, the a.m. components are

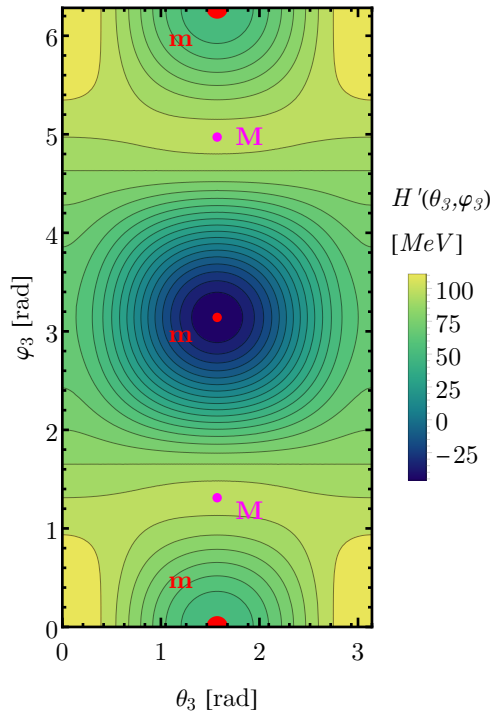


FIGURE 6.10: Contour plot for the energy  $H'$  from Eq. (6.40), defined in terms of the polar coordinates. The calculations are done for the B1-B2-B3 cases (i.e., maximal MOI is  $\mathcal{I}_3$ ). The single-particle angular momentum is  $j = 11/2$ , the total angular momentum  $I = 19/2$ , the MOI are  $\mathcal{I}_1 : \mathcal{I}_2 : \mathcal{I}_3 = 10 : 20 : 40 \text{ } \hbar^2 \text{MeV}^{-1}$ , and  $\theta = 70^\circ$ . The five stationary points are illustrated, namely two maxima (denoted by "M") and three minimum points (denoted by "m"; one global and two local).

TABLE 6.2: The stationary points for the classical energy function depicted in Eq. (6.40), when the quantization axis is the 3-axis. Each point corresponds to the cases  $B1$ ,  $B2$ , and  $B3$ , respectively.

Point $p$	$x_3$	$\varphi_3$	A.m. components ( $x_1, x_2, x_3$ )	$E$	Character of the stationary point
$p_1^B(m)$	0	$\pi$	$(-I, 0, 0)$	$E = -2v_0I$	minimum (m)
$p_2^B(m)$	0	0	$(I, 0, 0)$	$E = 2v_0I$	minimum (m)
$p_3^B(M)$	0	$\arccos(\frac{v_0}{I})$	$\left(v_0, \sqrt{I^2 - v_0^2}, 0\right)$	$E = I^2(1 + v^2)$	maximum (M)

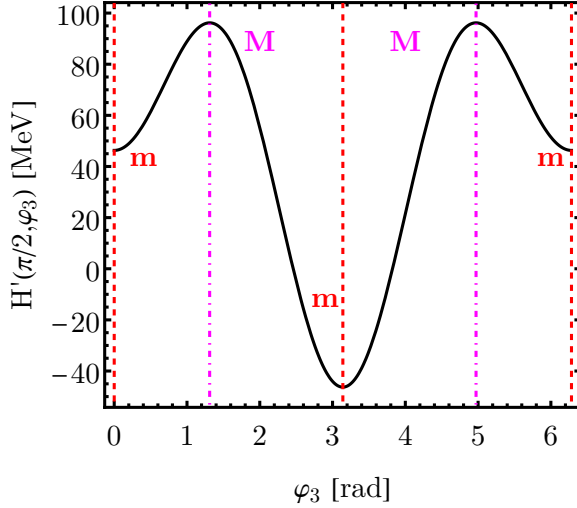


FIGURE 6.11: The classical energy  $H'$  from Eq. (6.40), for a fixed  $\theta_2 = \pi/2$  and  $\varphi \in [0, 2\pi]$ . The single-particle angular momentum is  $j = 11/2$ , the total angular momentum  $I = 19/2$ , the MOI are  $\mathcal{I}_1 : \mathcal{I}_2 : \mathcal{I}_3 = 10 : 20 : 40 \hbar^2 \text{MeV}^{-1}$ , and  $\theta = 70^\circ$ . The critical points present in Fig. 6.10 are illustrated by the dashed vertical lines (magenta for the maxima and red for the minima).

expressed in terms of the polar coordinates:

$$x_1 = I \cos \theta_1, \quad x_2 = I \sin \theta_1 \cos \varphi_1, \quad x_3 = I \sin \theta_1 \sin \varphi_1, \quad (6.59)$$

with the associated Hamiltonian:

$$H' = (I^2 - x_1^2) (\cos^2 \varphi_1 + u \sin^2 \varphi_1) + 2v_0 x_1. \quad (6.60)$$

The Hamiltonian from Eq. (6.60) has a stationary point at  $(x_1, \varphi_1) = (\frac{v_0}{u}, \frac{\pi}{2})$ . This is a *saddle* point when  $u \in (0, 1)$ . The second order expansion of  $H'$  is therefore:

$$H'^{(2)} = uI + \frac{v_0}{u} - u\bar{x}_1^2 + (1-u) \left( I^2 - \frac{v_0^2}{u^2} \right) \bar{\varphi}_1^2. \quad (6.61)$$

### Case C2

Another stationary point for  $H'$  is  $(v_0, 0)$ , which has a maximum character, giving angular momentum components  $(x_1, x_2, x_3) = (v_0, \sqrt{I^2 - v_0}, 0)$  and  $E = I^2 + v_0^2$ . The second order expansion of the energy function is:

$$H'^{(2)} = I^2 + v_0 - \bar{x}_1^2(u-1) \left( I^2 - v_0^2 \right) \bar{\varphi}_1^2. \quad (6.62)$$

TABLE 6.3: The stationary points for the classical energy function depicted in Eq. (6.40), when the quantization axis is the 1-axis. Each point corresponds to the cases  $C1$ , and  $C2$ , respectively.

Point $p$	$x_1$	$\varphi_1$	A.m. components ( $x_1, x_2, x_3$ )	$E$	Character of the stationary point
$p_1^C(s)$	0	$\pi$	$\left(\frac{v_0}{u}, 0, \sqrt{\left(I^2 - \frac{v_0^2}{u}\right)}\right)$	$E = I^2 u + \frac{v_0^2}{u}$	saddle (s)
$p_2^C(M)$	$v_0$	0	$\left(v_0, \sqrt{I^2 - v_0^2}, 0\right)$	$E = I^2 + v_0^2$	maximum (M)

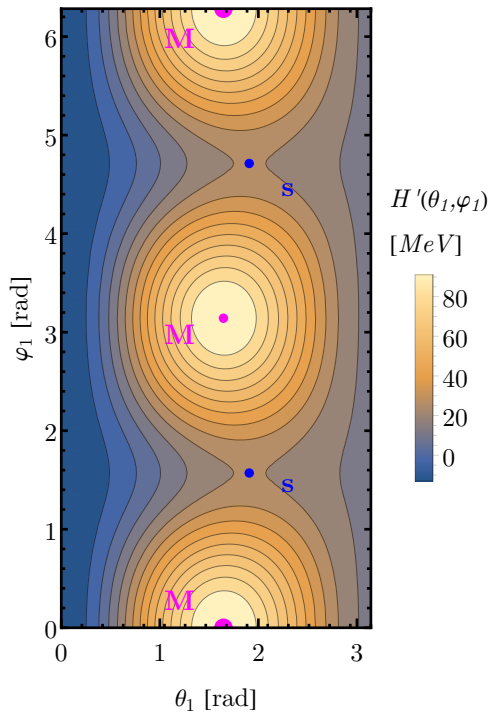


FIGURE 6.12: Contour plot for the energy  $H'$  from Eq. (6.40), defined in terms of the polar coordinates. The calculations are done for  $\mathcal{I}_1 : \mathcal{I}_2 : \mathcal{I}_3 = 80 : 10 : 50 \hbar^2 \text{MeV}^{-1}$  (i.e., the 1-axis is the quantization axis). The single-particle angular momentum is  $j = 11/2$ , the total angular momentum  $I = 19/2$ , and  $\theta = 70^\circ$ . The five stationary points are illustrated, namely three maxima (denoted by "M") and two saddle points (denoted by "s").

Similarly as in cases A-B, a contour plot showing the behavior of the energy function  $H'$  would be useful. This is shown in Fig. 6.12, where the calculation of  $H'(\theta_1, \varphi_1)$  used a different set of MOI, namely:  $\mathcal{I}_1 : \mathcal{I}_2 : \mathcal{I}_3 = 80 : 10 : 50 \hbar^2 \text{MeV}^{-1}$ . The maxima from Fig 6.12 would illustrate that a rotation around the 1-axis (the cranking axis for the initial system) is not possible. The critical points for the C cases are recorded in Table 6.3.

The three situations A-B-C that were analyzed can be summarized with the following aspects:

- there are six minima: A1, A2, B1, B2, and A3, C1 (when  $u \in (-1, 0)$ )
- two maxima appear for the cases B3 and C2
- when  $u \in (0, 1)$ , there are two saddle points: A3 and C1.

When the minimum points are considered, the total angular momentum is oriented along a principal axis (either the 1- or  $-1$ -axis). However, for the maxima and saddle points, the angular momentum lies in a principal plane instead of being aligned along a preferred axis. The A3 and C1 cases result in a total a.m. that is oriented in the  $(x_1, x_3)$  plane. The stationary points are of minimum, maximum, or saddle character depending on the signs of the diagonal matrix elements of Hessian associated to  $H'(\theta, \varphi)$ . More precisely:

1. *minimum*: all the diagonal m.e. are positive
2. *saddle*: one m.e. is positive and one m.e. is negative
3. *maximum*: all the diagonal m.e. are negative

If the Hessian is set to numerically vanish, then an equation is obtained for the parameters  $u$  and  $v \equiv v_0/I$  at which the critical points are degenerate:

$$(1 - u)(1 - v^2)(v^2 - u^2)(v^2 - u) = 0 . \quad (6.63)$$

Each factor from this equation will generate a curve within the  $(u, v)$  plane (called a *separatrix*). These separatrices are bordering manifolds that define unique nuclear phases. This phase diagram is sketched in Fig. 6.13. For the sake of completeness, the points corresponding to the values  $(u, v)$  from the bases A-B-C are all represented on the same diagram, but with  $v$  taken as an absolute value, to avoid negative ranges that are obtained when the 1-axis is the quantization axis. Keep in mind that the different values for these parameters emerge from the change in the ordering of the three moments of inertia (recall Eq. (6.15)).

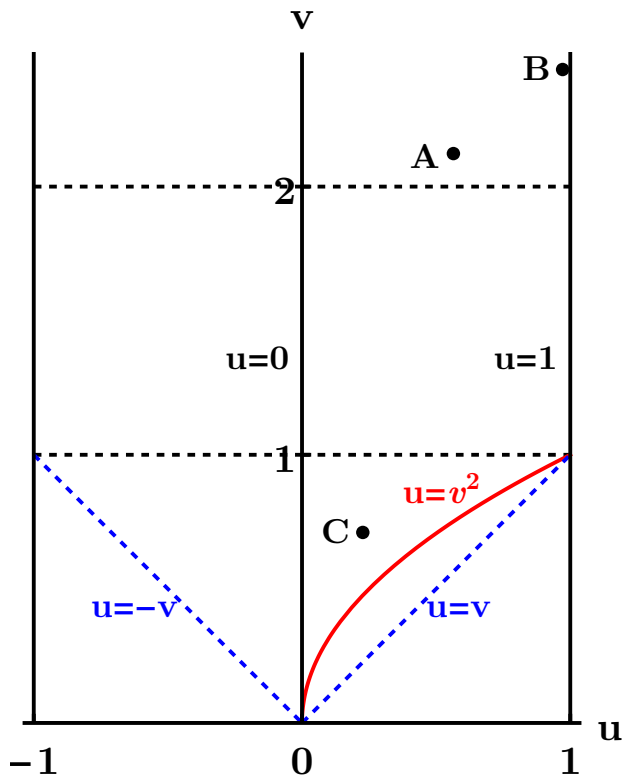


FIGURE 6.13: The phase diagram associated with the parametric formula given in Eq. (6.63). Each of the conditions that make the equation vanish is represented by a separatrix, such that different regions depict *different nuclear phases*. The numerical values of  $u$  and  $v$  obtained from cases A-B-C are also represented within the plot.

## 6.4 Electromagnetic Transitions

The next part of the team's work in Ref. [136] was to obtain an analytical description for the electromagnetic operators, such that the boson model can be compared with real experimental data. Starting with the electric transitions, the wave function must be introduced. The wave function for a spin state  $I$  must be *the solution* of the Schrödinger equation for the total angular momentum  $I$ . Because i) the system is cranked around the 1-axis and ii) the a.m. projection  $I_1$  is equal to  $-I$  in the minimum point, then the  $K$  quantum number (i.e., the projection of  $I$  on the 1-axis in the intrinsic frame of reference) should also be  $-I$ . Thus, a solution to the Schrödinger equation could be employed:

$$\Psi_{IM} = \Phi_{I,-I} |IM, -I\rangle , \quad (6.64)$$

where  $|IMK\rangle$  are the Wigner-D functions, which were introduced and used in the previous chapters (see Eq. (4.7)).

For the *quadrupole transition operator*, the following expression was used (slightly modified when compared to Eq. (4.65)):

$$\mathcal{M}(E_2; \mu) = \sqrt{\frac{5}{16\pi}} e(Q_{2-2}\mathcal{D}_{\mu-2}^2 + Q_{20}\mathcal{D}_{\mu 0}^2 + Q_{22}\mathcal{D}_{\mu 2}^2) , \quad (6.65)$$

with  $Q_{20}$  and  $Q_{2\pm 2}$  denoting the  $K = \{-2, 0, 2\}$  components of the quadrupole transition operator. From the expressions of the wave function given in Eq. (6.25), it is clear that it will depend on the conjugate variables  $q$  and  $d/dg$ . For this reason, the quadrupole components need to be expressed as functions of these variables. If the components are firstly written in terms of the angular momentum, one has:

$$Q_{20} = \left( -\frac{1}{4} \sqrt{\frac{2}{3}} (\hat{I}_+ \hat{I}_- + \hat{I}_- \hat{I}_+) + \sqrt{\frac{2}{3}} \hat{I}_1^2 \right) \bar{Q}_0 , \quad Q_{2\pm 2} = \frac{1}{2} \hat{I}_\pm^2 \bar{Q}_2 . \quad (6.66)$$

The factors  $\bar{Q}_0$  and  $\bar{Q}_2$  are the *intrinsic quadrupole components*. Then, by using the Bargmann representation of the a.m. components, around the minimum point  $Q_{20}$  and  $Q_{2\pm 2}$  become [135]:

$$\begin{aligned} Q_{20} &= \frac{1}{\sqrt{6}} \left[ 3\bar{q}^2 \frac{d^2}{d\bar{q}^2} - 3(2I-1)\bar{q} \frac{d}{d\bar{q}} + I(2I-1) - I(I-1)(1+k^2)\bar{q}^2 \right] \bar{Q}_0 , \\ Q_{2\pm 2} &= \frac{1}{k'^2} \left\{ [(1+k^2)\bar{q}^2 - 2] \frac{d^2}{d\bar{q}^2} - (2I-1)(1+k^2)\bar{q} \frac{d}{d\bar{q}} \right\} \bar{Q}_2 \times \\ &\quad \times \frac{1}{k'^2} \left\{ I [(I+1)(1+k^2) + k^2(k^2+3)] \bar{q}^2 - I(1+k^2) \right\} \bar{Q}_2 . \end{aligned} \quad (6.67)$$

To calculate the matrix elements of the transition operator, the overlap factors for the interband and intraband transitions need to be determined. As per the calculations of Ref. [135], it was shown that both  $\langle \Phi_{I,-I} | \Phi_{I-1,-I+1} \rangle$  and  $\langle \Phi_{I,-I} | \Phi_{I-2,-I+2} \rangle$  are very close to unity, such that they can be fixed to 1. The reduced transition probabilities can be evaluated using the following formula:

$$B(E2; I \rightarrow I') = |\langle \psi_I | \mathcal{M}(E2) | \Psi_{I'} \rangle|^2 . \quad (6.68)$$

The intrinsic quadrupole moments  $\bar{Q}_2$  and  $\bar{Q}_0$  are taken as *free parameters* within this approach, and the matrix elements for  $\langle \Psi_I | \mathcal{M}(E2) | \Psi_{I-2} \rangle$  (intraband) and

$\langle \Psi_I | |\mathcal{M}(E2)| |\Psi_{I-1} \rangle$  (interband) are given analytically in Eqs. (6.5) and (6.6) from Ref. [135].

The *magnetic dipole transition* operator is defined as [135]:

$$\mathcal{M}(M1; \mu) = \frac{3}{4\pi} \mu_N \sum_{\nu} \left( g_R \hat{R}_{\nu} + g_j \hat{j}_{\nu} \right) \mathcal{D}_{\mu\nu}^1 \equiv M_{1\mu}^{\text{coll}} + M_{1\mu}^{\text{sp}} , \quad (6.69)$$

where the terms  $R_{\nu}$  and  $j_{\nu}$  are the spherical components of the core and the odd single-particle. The gyromagnetic factors of the core and the particle are denoted by  $g_R$  and  $g_j$ , respectively. The matrix elements of the collective and single-particle transition operators  $M_{1\mu}^{\text{coll}}$  and  $M_{1\mu}^{\text{sp}}$  are provided in the set of Eqs. (6.10) - (6.12) from Ref. [135]. Therein, the values for the gyromagnetic factors are provided as well. These are used to get the analytical expression of the reduced transition probability for the magnetic dipole:

$$B(M1; I \rightarrow I') = |\langle \Psi_I | |\mathcal{M}(M1)| |\Psi_{I'} \rangle|^2 . \quad (6.70)$$

## 6.5 Numerical Results

The entire formalism developed through Ref. [135] was tested numerically for the odd- $A$  nucleus  $^{135}\text{Pr}$ . This odd-mass nucleus was chosen because experimental evidence point out its wobbling character [112] (and later erratum in Ref. [169]), although there are some ongoing debates about whether the experimental measurements are valid or not [131]. For this isotope, there are three confirmed wobbling bands, here denoted by B1 (band one), B2 (band two), and B3 (band three). Sensharma et. al. [113] consider in their study for this nucleus that B1 is the yrast, B2 is the one-phonon, and finally that B3 is the two-phonon wobbling band. By contrast, a previous work by Matta et. al. [112] only identified one such excited wobbling band.

The formalism assumes that the problem is described by a Hamiltonian such as the one from Eq. (6.12), which is associated with the even-even core surrounded by an odd nucleon: the odd  $h_{11/2}$  proton. The core is considered to have a set of moments of inertia  $\mathcal{I}_k$  ( $k = 1, 2, 3$ ) that are *free parameters*. Moreover, the proton is *rigidly coupled* to the core and placed in the (1, 2)-plane, with the tilting angle  $\theta$ . As a result, the model only considers four free parameters, i.e., three moments

of inertia and the single-particle tilt:

$$\mathcal{P}_{\text{fit}} = [\mathcal{I}_1, \mathcal{I}_2, \mathcal{I}_3, \theta]. \quad (6.71)$$

These values are determined via a fitting procedure for the three wobbling bands in  $^{135}\text{Pr}$ . The adopted fitting procedure is quite similar to the one that the team developed for  $\mathbf{W}_1$  and  $\mathbf{W}_2$ , but any key difference will be pointed out in the following sections.

### 6.5.1 Excitation Energies

The bands B1 and B2 are signature partner bands, having an opposite signature quantum number (+1/2 for the favored and -1/2 for the unfavored). Due to this reason, the wobbling phonon numbers are  $n_{B1} = n_{B2} = 0$  for the first two bands and  $n_{B3} = 1$  for the third, meaning that B3 is a one-phonon excitation (band B3 is a *one-phonon excitation* of B2). This is similar to the condition employed in the  $\mathbf{W}_1$  approach, where one studied the electromagnetic properties of several Lu isotopes. Since the *excitation energies* are obtained by subtracting the band-head  $E_{I_b}$  value ( $I_b$  signifies the spin of the true ground state of the yrast band B1), one must consider the analytical expressions [135]:

$$\begin{aligned} E_I^{\text{exc;B1}} &= A_1 I^2 + (2I + 1)A_1 j_1 - IA_2 j_2 + \frac{1}{2}\omega_I - E_{11/2}, \\ I &= R + j, R = 0, 2, 4, \dots \in \text{B1}, \\ E_I^{\text{exc;B2}} &= A_1 I^2 + (2I + 1)A_1 j_1 - IA_2 j_2 + \frac{1}{2}\omega_I - E_{11/2}, \\ I &= R + j, R = 1, 3, 5, \dots \in \text{B2}, \\ E_I^{\text{exc;B3}} &= A_1 I^2 + (2I + 1)A_1 j_1 - IA_2 j_2 + \frac{3}{2}\omega_I - E_{11/2}, \\ I &= R + j, R = 1, 3, 5, \dots \in \text{B3}, \end{aligned} \quad (6.72)$$

where it can be seen that the analytical formulas for the first two bands are identical, but the angular momenta will differ by one unit. The band B3 being a one-phonon excitation, a state  $I + 1$  is obtained by exciting with one-wobbling quanta the  $I$  state from B2. The *wobbling frequency*  $\omega_I$  is an angular-momentum

TABLE 6.4: The four free parameters obtained by fitting the experimental energies of  $^{135}\text{Pr}$  (taken from Ref. [112]) using the set of energies from Eq. (6.72). For the moments of inertia, the unit is  $\hbar^2\text{MeV}^{-1}$ .

$\mathcal{I}_1$	$\mathcal{I}_2$	$\mathcal{I}_3$	$\theta$ [degrees]	N.o. states	RMS [MeV]
91	9	51	-119	20	0.174

dependent function given as [135]:

$$\omega_I^2 = \left[ (2I+1) \left( A_2 - A_1 - \frac{A_2 j_2}{I} \right) + 2A_1 j_1 \right] [(2I+1)(A_3 - A_1) + 2A_1 j_1] - \\ - (A_3 - A_1) \left( A_2 - A_1 - \frac{A_2 j_2}{I} \right). \quad (6.73)$$

In order to understand Eq. (6.72), one might recall the diagram from Fig. 4.9, which shows how the excitation energies can be regarded. The parameters  $\mathcal{P}_{\text{fit}}$  obtained by fitting the experimental energies of  $^{135}\text{Pr}$  with Eq. (6.72) are provided in Table 6.4. It should be mentioned that several conditions were restricted when searching for  $\mathcal{P}_{\text{fit}}$  (i.e., some sort of *validity conditions*):

- The factor  $A$  must be greater than zero (recall Eq. (6.15))
- The factor  $u$  from the same equation must be  $u \in (0, 1)$
- The wobbling frequency  $\omega_I$  as well as the one obtained by expanding  $H'$  around the local minimum (that is  $\omega'_I$  from Eq. (6.38)) must be real functions of  $\theta$  and  $\theta + \pi$
- The elliptic potential from Eq. (6.26) must be a real function for  $\theta$  and  $\theta + \pi$ .

With these criteria in check, the fitting procedure was performed and calculations gave an RMS of about 0.170 MeV. Comparing this work with other models from the literature, such as Ref. [170] ( $\approx 0.160$  MeV) and Ref. [55] ( $\approx 0.150$  MeV) it can be concluded that a semi-classical analysis of the boson description for odd-mass wobbling nuclei is quite realistic. The excitation energies for all three bands are graphically represented as level schemes in Figs. 6.14 - 6.15. From these figures, a few points are worth mentioning. For example, it can be seen that for B1 the model gives slightly larger excitation energies across the spectrum, especially for the states close to the band-head and the most excited states. For B2, the slightly larger theoretical energies are obtained for the low-spin region, while the end of



FIGURE 6.14: The excitation energies  $E_I^{\text{exc};\text{B}1}$  in  $^{135}\text{Pr}$  (Eq. (6.72)), calculated with the parameter set  $\mathcal{P}_{\text{fit}}$ . The experimental data are taken from Ref. [113].

the spectrum is a bit underestimated. Interestingly, the one-phonon wobbling band seems to be described very accurately by the model, without any noticeable differences.

Taking a closer look at the numerical values from Table 6.4, it can be seen that the fit predicted the MOI order to be of the type  $\mathcal{I}_1 > \mathcal{I}_3 > \mathcal{I}_2$ . With these values, one can graphically represent the elliptic potentials for  $V(\theta)$  and  $V(\theta + \pi)$ , as provided by Eq. (6.26). The results are shown in Fig. 6.16 for three values of angular momentum  $I$  and the two angles.

Looking at the two potentials associated with  $^{135}\text{Pr}$  from Fig. 6.16, several features can be observed. Firstly, the deepest minimum for  $\theta$  is located at  $2K$ , while for

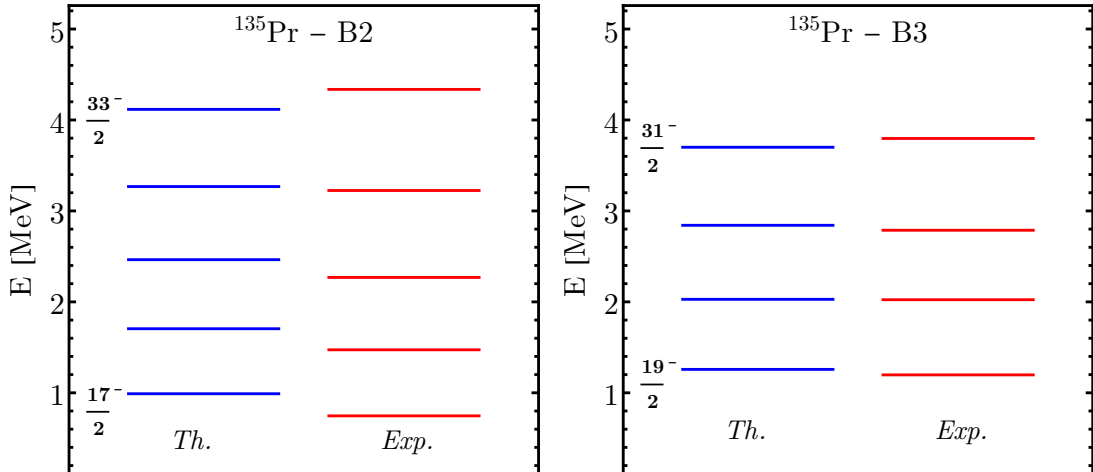


FIGURE 6.15: The excitation energies  $E_I^{\text{exc};\text{B}2}$  (left) and  $E_I^{\text{exc};\text{B}3}$  (right) in  $^{135}\text{Pr}$  (Eq. (6.72)), calculated with the parameter set  $\mathcal{P}_{\text{fit}}$ . The experimental data are taken from Ref. [113].

$\theta + \pi$  is at  $q = 0$  (recall that  $K$  is the period of the elliptic functions used to express  $V(q)$ ). This is remarkable since it contrasts the initial consideration of  $\mathcal{I}_2$  as being the maximal MOI, which should have the global minima located at  $q = 0$ . One reason might be the coupling between the even-even core and the odd nucleon, as their interaction can affect both the MOI's ordering and the position of the deepest minimum for the triaxial potential. It is a unique highlight of the boson description where such an effect is identified. Because the global minimum for  $\theta + \pi$  stays at  $q = 0$ , one can assert that by drastically switching the orientation angle between the odd-particle and the core, a *phase transition occurs*, affecting the MOI from  $\mathcal{I}_1 = \mathcal{I}_{\max}$  to  $\mathcal{I}_2 = \mathcal{I}_{\max}$ .

Aiming at the initial assumption of  $\mathcal{I}_2$  as the largest NOI, a second fitting procedure was also developed. The fit consisted of equating the excitation energies for the first two states in B1 and the second state from B2. A parameter set that suits the MOI order was obtained for  $\theta = 140^\circ$ :  $\mathcal{P}_{\text{fit}} = [13, 101, 53, 140^\circ]$ . However, this parameter set does not improve the quality of the initial fit, keeping the deviations from the experimental values along the same magnitude. For this set of parameters, the elliptic triaxial potential has the deepest minimum at  $q = 0$ , which is consistent with the  $\mathcal{I}_2 > \mathcal{I}_{1,3}$ . This solution is not valid because it violates the positivity condition for the factor  $A$  from Eq. (6.15).

Since the potential when  $\theta = -114^\circ$  has the global minimum in  $q = 2K$ , it is worth adjusting the fitting model and using the wobbling frequency  $\omega'$  from Eq. (6.38)

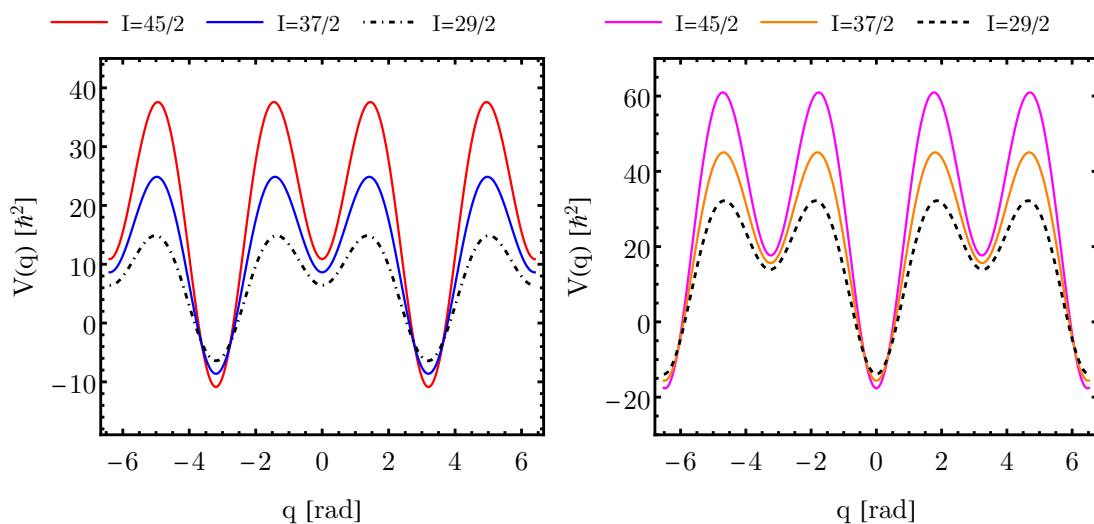


FIGURE 6.16: The elliptic potential from Eq. (6.26) as function of the coordinate  $q$ . The expression of  $V(q)$  is evaluated for the inertia factors from Table 6.4 with  $\theta = -119^\circ$  (left) and  $\theta = 61^\circ$  (right).



FIGURE 6.17: The triaxial potential from Eq. (6.26) associated to  $^{135}\text{Pr}$ , evaluated for the case of maximal MOI along 2-axis. The three MOI are  $\mathcal{I}_1 : \mathcal{I}_2 : \mathcal{I}_3 \approx 13 : 101 : 53 \hbar^2 \text{MeV}^{-1}$ ,  $\theta = 140^\circ$  (**left**), and  $\theta = 320^\circ$  (**right**).



FIGURE 6.18: The triaxial potential from Eq. (6.26) associated to  $^{135}\text{Pr}$ , evaluated using  $\omega'$  instead of  $\omega$  (see Eq. (6.38)). The MOI are:  $\mathcal{I}_1 : \mathcal{I}_2 : \mathcal{I}_3 \approx 89 : 12 : 48 \hbar^2 \text{MeV}^{-1}$ ,  $\theta = -71^\circ$  (**left**), and  $\theta = 109^\circ$  (**right**).

for the excitation energies. The expression of  $\omega'$  was obtained by expanding  $V(q)$  up to second order in the local minima  $q = \pm 2K$ , making it perfectly suitable for the calculus of the excitation energies from in Eq. (6.72). Indeed, repeating the fitting procedure the results are  $\mathcal{P}_{\text{fit}} = [89, 12, 48, -71^\circ]$ . This also provides an RMS that is similar to the initial one. It is somewhat expected that the change in the wobbling frequency  $\omega \rightarrow \omega'$  would lead to similar excitation energies, as they differ by a constant amount, independent of  $I$  [135]. For the sake of completeness, the elliptic potential  $V(q)$  is graphically represented for the set of MOI,  $\theta$ , and  $\theta + \pi$  given by the alternative fitting procedures in Figs. 6.17 - 6.18.

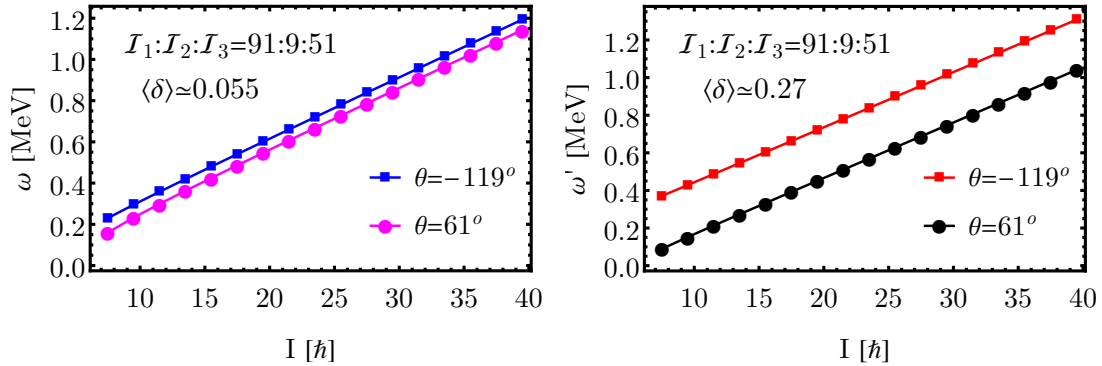


FIGURE 6.19: The wobbling frequency as function of angular momentum for  $^{135}\text{Pr}$ , according to Eq. (6.36) (left) and Eq. (6.38) (right). The calculations are done for the parameters provided in Table 6.4. The value  $\langle \delta \rangle$  represents the average spacing between the two frequencies (see text for more details).

Taking a look at all three sets of potentials from Figs. 6.16 - 6.18, it can be seen that except for the case of  $\mathcal{I}_2 = \mathcal{I}_{\max}$ , the  $V(q)$  ranges are quite close to each other. The very large values for  $V(q)$  from Fig. 6.17 show that the transverse wobbling for  $^{135}\text{Pr}$  is unstable. Notice the alternating character of the deepest minima for the angle  $\theta$  (i.e., between the plots for  $\theta$  and  $\theta + \pi$ ). The very sharp minimum points also indicate that the core + particle interaction stabilizes near  $q = 0, 2K, \dots$ .

The wobbling frequency for  $^{135}\text{Pr}$  can be easily determined by using the moments of inertia and the angle  $\theta$  in the analytical expressions from Eq. (6.36) for  $\omega$  and Eq. (6.38) for  $\omega'$ , respectively. A set of graphical representations are made in Figs. 6.19 - 6.21 where each plot is generated using the numerical values from Table 6.4 (for the first set of plots), the fit when  $\mathcal{I}_2 = \mathcal{I}_{\max}$  (second set of plots), and lastly, the fit when the excitation energies are evaluated with  $\omega'$  (third set of plots).

Note the linear behavior of the phonon energy w.r.t. angular momentum. Moreover, the energy for  $\omega$  lies higher in magnitude than its  $\theta + \pi$  partner, except for the case of 2-axis quantization (that is Fig. 6.20), where it can be seen that  $\omega'(\theta + \pi)$  is larger. In terms of the differences between the frequency evaluated for  $\theta$  and  $\theta + \pi$ , they are quite constant across the entire spin range for all figures, with the smallest difference achieved for  $\omega$  from Fig. 6.19. If the difference between  $\omega(\theta)$  and  $\omega(\theta + \pi)$  for a given angular momentum  $I$  is denoted by  $\delta(\omega_I)$ :

$$\delta(\omega_I) = \omega(\theta) - \omega(\theta + \pi) , \quad (6.74)$$



FIGURE 6.20: The wobbling frequency as function of angular momentum for  $^{135}\text{Pr}$ , according to Eq. (6.36) (**left**) and Eq. (6.38) (**right**). The calculations are done for the parameters obtained by fitting Eq. (6.72) such that  $I_2 = I_{\max}$ . The value  $\langle \delta \rangle$  represents the average spacing between the two frequencies (see text for more details).

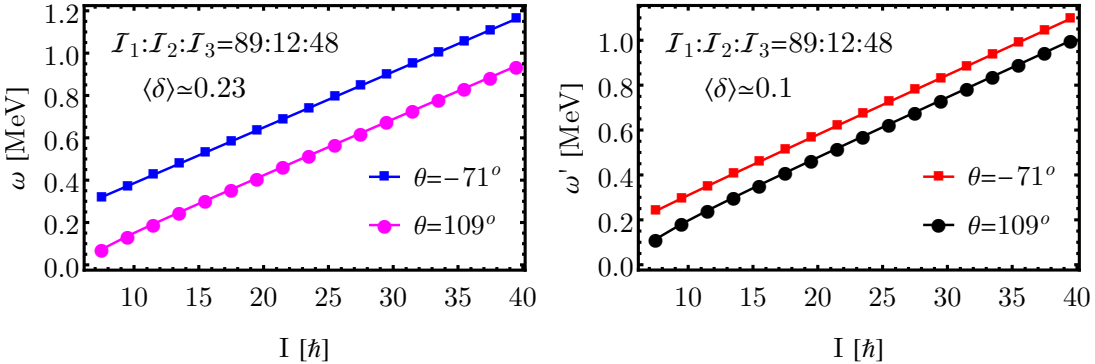


FIGURE 6.21: The wobbling frequency as function of angular momentum for  $^{135}\text{Pr}$ , according to Eq. (6.36) (**left**) and Eq. (6.38) (**right**). Results were achieved with the parameters given by a fit of Eq. (6.72) using  $\omega'$  in its analytical expression. The value  $\langle \delta \rangle$  represents the average spacing between the two frequencies (see text for more details).

then one can compute the average  $\langle \delta \rangle$  across each of the three sets of figures. The same can be done for  $\delta(\omega'_I)$ , and these numbers are shown on all six plots.

### 6.5.2 On the Chiral Character of the Wobbling Motion

As discussed in the chapter dedicated to the signatures of triaxial nuclei (recall Section 2.3.6), the *chirality* corresponds to a transformation that brings a right-handed system into a left-handed one. The change of the sign for the a.m. defines the chiral transformation itself. Thus, the invariance to a chiral transformation is given by the conservation of the rotational energy when the rotational axis is changed. Referring back to the initial Hamiltonian from Eq. (6.12), this consists

of a sum of two terms, one that is symmetric to a chiral transformation and one that is antisymmetric:

$$\hat{H}_{\text{rot}} = \hat{H}_{\text{symm}} + \hat{H}_{\text{asymm}} . \quad (6.75)$$

If  $|\Psi\rangle$  is an eigenstate for the symmetric Hamiltonian and  $\hat{C}$  defines a chiral transformation, then  $\hat{C}|\Psi\rangle$  is also an eigenstate for  $\hat{H}_{\text{symm}}$ , and it corresponds to the same eigenvalue. From the equality:

$$\hat{C}|\Psi\rangle = |\Psi\rangle , \quad (6.76)$$

it results that the state has a chirality equal to one. On the other hand, if  $|\Phi\rangle$  is an eigenstate for the asymmetric term with an eigenvalue  $E$ , then  $\hat{C}|\Phi\rangle$  is also an eigenstate for  $\hat{H}_{\text{asymm}}$ , but it will correspond to the energy  $-E$ . The eigenvalues of  $\hat{H}_{\text{asymm}}$  split into two groups; each being the mirror image of the other. Such a property is said to be *of chiral type*. The chirality for the eigenstates of  $\hat{H}_{\text{asymm}}$  is negative (i.e.,  $-1$ ), since  $\hat{C}|\Phi\rangle = -|\Phi\rangle$ .

Based on the description of the chirality for  $\hat{H}_{\text{symm}}$  and  $\hat{H}_{\text{asymm}}$ , the eigenstates for the total Hamiltonian  $\hat{H}_{\text{rot}}$  are mixtures of the two types of chirality: positive and negative. Within the calculations performed in this chapter for  $^{135}\text{Pr}$ , the change  $\mathbf{I} \rightarrow -\mathbf{I}$  is obtained by changing the orientation angle of the single-particle from  $\theta$  to  $\theta + \pi$ . All the calculations that were graphically represented for  $V(q)$  and  $\omega$  in the previous subsection were made for the orientation of the nucleon that emerged from the fitting procedure and the *chiral transformed* one. If the potential evaluated for  $\theta$  is  $V$ , then the chiral potential for  $\theta + \pi$  is indeed  $\hat{C}V\hat{C}^{-1}$ . From the potential energy represented throughout Figs. 6.16 - 6.18, one can extract the *symmetric* and *asymmetric* parts:

$$\begin{aligned} V_{\text{symm}} &= \frac{1}{2}(V_\theta + V_{\theta+\pi}) , \\ V_{\text{asymm}} &= \frac{1}{2}(V_\theta - V_{\theta+\pi}) . \end{aligned} \quad (6.77)$$

The symmetric and asymmetric potentials are represented as a function of the coordinate  $q$  in Fig. 6.22, for the moments of inertia and the single-particle orientation angle provided by fitting the excitation energies of Eq. (6.72). For keeping a



FIGURE 6.22: The symmetric **left** and asymmetric **right** potentials from Eq. (6.77) associated to  $^{135}\text{Pr}$ . The numerical evaluation is done with the fitting parameters from Table 6.4.

concise representation, only  $I = 45/2$  was considered. Note the oscillatory character of  $V_{\text{symm}}$  that is more pronounced, with very deep minima and maxima across the  $q$  range. The asymmetric potential is almost flat when  $q \approx 2K$ .

The elliptic triaxial potential  $V(q)$  expressed in Eq. (6.26) is a function that depends explicitly on the elliptic modulus  $k$ . Moreover, the modulus was defined in terms of the factor  $u = (A_3 - A_1)/A$  (recall Eq. (6.15)). From that formula, it is obvious that  $k$  will change when  $\theta$  changes, through the re-adjustment of the single-particle a.m. components  $j_1$  and  $j_2$ . As a result, the period  $K$  (which gives the location of critical points) will also depend on the orientation angle  $\theta$ . When comparing  $V_{\text{symm}}$  and  $V_{\text{asymm}}$  for a shared set of coordinates  $q$ , an offset  $\Delta K = |K_\theta - K_{\theta+\pi}|$  is required to compensate for the difference in their periods.

The excitation energies from Eq. (6.72) can also be *decomposed* into symmetric and asymmetric terms. For the yrast states (i.e., the band B1) the *chiral pair* of excitation energies are defined as [135]:

$$\begin{aligned} E_I^{\text{exc;B1}}(\text{symm}) &= A_1 I^2 + \frac{1}{2} [\omega_I(\theta) + \omega_I(\theta + \pi)] , \\ E_I^{\text{exc;B1}}(\text{asymm}) &= (2I + 1) A_1 j_1 - I A_2 j_2 + \frac{1}{2} [\omega_I(\theta) - \omega_I(\theta + \pi)] , \end{aligned} \quad (6.78)$$

where it can be seen that the wobbling frequency  $\omega(\theta)$  and its *chiral partner*  $\omega(\theta + \pi)$  appear. For the set of MOI provided in Table 6.4 and  $\theta = -119^\circ$ , the symmetric and asymmetric excitation energies for B1 are numerically evaluated and plotted against the total spin  $I$  in Figs. 6.23.

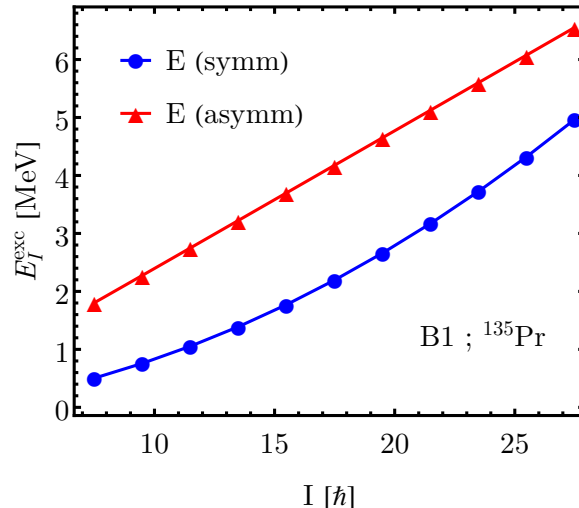


FIGURE 6.23: The symmetric and asymmetric excitation energies from Eq. (6.78) for  $^{135}\text{Pr}$ , evaluated for the parameters given in Table 6.4. The lines connecting the dots are just to guide the eye.

The two sets of excitation energies  $E(\text{symm})$  and  $E(\text{asymm})$  correspond to two bands of opposite chirality. Indeed, the symmetric values correspond to a symmetric Hamiltonian and chirality +1, while the asymmetric values have negative chirality -1 and belong to an asymmetric Hamiltonian. Looking at Fig. 6.23, it can be seen that both bands are relatively close to each other, and they almost have similar behavior for the total angular momentum. Nevertheless, the quadratic increase of  $E(\text{symm})$  is noticeable. The rather constant energy spacing between the two bands is a feature specific to chiral bands [135] (see the chiral bands from Figs. 2.32 - 2.33). The fact that the initial Hamiltonian contains a linear term is another feature of the chiral motion, which means that the wobbling and chiral properties seem to be somewhat connected for  $^{135}\text{Pr}$ . This is the first time both phenomena are studied on the same family of bands, and the only property that holds against a decisive unified character of wobbling and chiral bands in  $^{135}\text{Pr}$  would be the rotational axis (that is, for a chiral nucleus, the rotational axis lies outside any of the principal planes - recall Fig. 2.34). More experimental data on this isotope would help to conclude whether these two bands are of a chiral type or not.

TABLE 6.5: The obtained numerical values for the electromagnetic transitions are compared with the experimental data for  $^{135}\text{Pr}$ . Only the states for which experimental data are available were considered [112].

	$\frac{B(E2;I^-\rightarrow(I-1)^-)}{B(E2;I^-\rightarrow(I-2)^-)}$		$\frac{B(M1;I^-\rightarrow(I-1)^-)}{B(E2;I^-\rightarrow(I-2)^-)}$		$\mu_N^2(\text{eb})^{-2}$	$\delta_{I^-\rightarrow(I-1)^-}$	MeV · fm
$I^\pi$	Th.	Exp.	Th.	Exp.		Th.	Exp.
$21/2^-$	0.400	$0.843 \pm 0.032$	0.08	$0.164 \pm 0.014$	1.97	$-1.54 \pm 0.009$	
$25/2^-$	0.450	$0.500 \pm 0.025$	0.056	$0.035 \pm 0.009$	-2.82	$-2.384 \pm 0.037$	
$29/2^-$	0.497	$\geq 0.261 \pm 0.014$	0.041	$\leq 0.016 \pm 0.004$	-3.82	-	
$33/2^-$	0.543	-	0.031	-	-4.96	-	

### 6.5.3 Electromagnetic Transitions

The E2 and M1 reduced transition probabilities are calculated according to Eq. (6.68) and Eq. (6.70), respectively. The initial and final wave functions are determined from the calculus of energies, connecting in this way the electromagnetic transitions to the model Hamiltonian. As already mentioned, the numerical values for these quantities require two adjustable parameters:  $\bar{Q}_0$  and  $\bar{Q}_2$ . The parameters used in this work are [135]:

$$\bar{Q}_0 = -30.02 \text{ e} \cdot \text{fm}^2/\hbar^2, \quad \bar{Q}_2 = 136.39 \text{ e} \cdot \text{fm}^2/\hbar^2. \quad (6.79)$$

The results for the  $E2_{\text{out}}/E2_{\text{in}}$  branching ratios,  $M1/E2$  branching ratios, and the mixing ratios  $\delta$  for  $^{135}\text{Pr}$  are compared with the experimental data in Table. 6.5.

From the results shown in Table 6.5, it can be seen that a reasonable agreement with the experimental data is obtained for the few states. The increasing behavior for the mixing ratio w.r.t. angular momentum is well reproduced. On the other hand, the experimental data for the  $B(E2)_{\text{out}}/B(E2)_{\text{in}}$  values seem to decrease with spin, while an increase is observed for the theoretical data. The same situation is met for the  $B(M1)_{\text{out}}/B(E2)_{\text{in}}$  values. This is expected because within the current model, the solutions to  $\hat{H}_{\text{rot}}$  are increasing functions w.r.t. the total angular momentum. The calculations involved in this model reproduce the ones obtained through a diagonalization procedure [144], which enforces a previous statement made by the team in Refs. [39, 100]; i.e., the solutions obtained via a Bargmann representation are identical to the solutions of the Schrödinger equation. Keep in mind that the boson description uses a semi-classical Hamiltonian that does not include any additional terms such as parity or quadrupole-quadrupole.

Simply by assuming a particle-rotor system amended with a planar rotation of the single-particle, the wobbling properties of odd- $A$  nuclei are accurately described.

### 6.5.4 Concluding Remarks

Throughout Chapter 6 a unique approach to the study of triaxial nuclei was presented. It started with the Hamiltonian specific for an even-even core interacting with a single-particle [39, 100, 136]. The coupling term, which describes the motion of the odd nucleon in a deformed mean field generated by the core is *a priori ignored*, since the odd nucleon will be rigidly aligned with the core, requiring only a coupling angle for the odd nucleon. Such a property will not lead to any modifications of the energy spectrum and only a free parameter  $\theta$  playing the role of coupling angle is necessary for this model.

The initial Hamiltonian was expressed in terms of the angular momentum components as ladder operators in Eq. (6.18). By using the Bargmann mapping for the angular momentum components [161], the ladder operators become functions of boson creation and annihilation operators (see Eq. (6.28)). The Hamiltonian is further written in this boson space by doing an *elliptic expansion* on the angular momentum (recall Eq. (6.23)). This is done via the Jacobi elliptic functions provided in Eq. (6.20). Usually, these are used for describing complex but periodic systems, because they consist of generalized trigonometric functions. As a matter of fact, the rotation of the triaxial nucleus can be seen as a *periodic motion*, with the wobbling frequency directly emphasizing such character.

From the Hamiltonian's eigenvalue equation, a Schrödinger equation is reached, with a fully separated kinetic and potential term, which was given in Eq. (6.25). Through the adoption of the elliptic functions and the Bargmann representation, an expression for the triaxial potential is acquired (i.e., Eq. (6.26)). When represented as a function of the generalized coordinate  $q$ , the potential energy exhibits four symmetric minima: two for the positive values of  $q$  and two for the negative interval (Fig. 6.3). The presence of multiple *periodic* minima for the potential  $V(q)$  is a specific feature of the elliptic functions. This is one of the reasons why elliptic representation for the initial Hamiltonian was chosen, such that the existence of periodic minima would allow for the existence of stability regions where wobbling states are allowed.

Performing a Harmonic Approximation on the energy function for the triaxial rotor, an expression containing three specific terms emerges; one term quadratic in the total angular momentum  $I$ , the harmonic-like wobbling term, and the single-particle term  $e_{\text{sp}}$  (as per summation in Eq. (6.34)). An alternative description for the wobbling frequency  $\omega$  and total energy  $E_n$  can be obtained if the elliptic potential  $V(q)$  is expanded in local minima (instead of the deepest minima) and the results were given in Eqs. (6.37) - (6.38). The expression for this energy function was studied in Section 6.3, utilizing *polar representations* constructed from the fully-classical angular momentum representation of Eq. (6.44), Eq. (6.52), and Eq. (6.59). Through a set of contour plots for the classical energy function  $H'$  (Eq. (6.40)), regions of stable/unstable wobbling motion could be identified, and Figs. 6.10 - 6.12 illustrate the behavior.

Furthermore, the expression of  $E_n$  is used to evaluate the numerical values for the *excitation energies* of  $^{135}\text{Pr}$ . This isotope has three wobbling bands, and the fitting procedure adopted in the current model describes them very well, providing similar results with other existing models within the literature. Section 6.5 gives the results concerning excitation energies from Eq. (6.72), which are represented in Figs. 6.14 - 6.15, and also the electromagnetic transition probabilities are provided in Table 6.5. The triaxial potential is graphically represented for several spin states, with the parameter set  $\mathcal{P}_{\text{fit}}$  from Table 6.4. The symmetric behavior of  $V(q)$  relative to the sign of the coordinate is clearly visible, together with the local/global minima (check Figs. 6.16 - 6.18). Plots for the coupling angle  $\theta$  as well as the *chiral partner*  $\theta + \pi$  were depicted.

A very good agreement with the experimental data is obtained in this formalism. Although the model started with the hypothesis that the maximal MOI is  $\mathcal{I}_2$ , the fitting results show  $\mathcal{I}_1 = \mathcal{I}_{\max}$ . The two-fold reason for such a behavior might be: i) the *re-normalization* of the three MOI, due to the linear terms present in the angular momentum and ii) the Coriolis interaction, proportional to  $I_1$ , which is stimulated by the highly rotating triaxial system. Nevertheless, through this classical description it is shown that a transverse wobbling behavior would not be possible, a situation that is in favor of the comments made in Ref. [158].

Lastly, in Section 6.5.2, a special analysis is exploited for the initial Hamiltonian  $\hat{H}_{\text{rot}}$ . The two unique fingerprints for triaxiality in nuclei are discussed, namely the

wobbling and chiral motions. Based on the intrinsic structure of  $\hat{H}_{\text{rot}}$ , both a symmetric and an asymmetric part could be identified, where the symmetric/asymmetric character is reflected by the chiral transformation  $\theta = \pi \longrightarrow \theta_{\text{chiral}} = \theta + \pi$ . Thus, for the potential  $V(q)$ , a symmetric and an asymmetric term were composed (see Eq. (6.77)), and their graphical representations show remarkable behavior (see Fig. 6.22). The same analysis could be performed for the excitation energy of the yrast band, and two energy bands were analytically obtained according to Eq. (6.78). From the plot shown in Fig. 6.23 for  $^{135}\text{Pr}$ , the two collections of energies (that is  $E_I^{\text{exc};\text{B}1}(\text{symm})$  and  $E_I^{\text{exc};\text{B}1}(\text{asymm})$ , respectively) appear as two different bands, which could be interpreted as *a pair of chiral bands for this isotope*. It is conspicuous that only adopting a boson description for the triaxial nucleus could lead to the emergence of both wobbling- and chiral-like energies, marking a possible start of a new unified approach in the identification of wobbling/chiral structures for other isotopes.

*These key points conclude this chapter on a boson description for the wobbling motion.*



# Chapter 7

## General Conclusions

This thesis presents a comprehensive analysis of several publications on the subject of Nuclear Structure. The primary objective was to investigate nucleonic matter that exhibits a lack of axial symmetry. In recent years, nuclear triaxiality has gained prominence as a topic of significant interest due to the challenges associated with its experimental measurement. Furthermore, the theoretical description of triaxially deformed nuclei necessitates the use of specific methods or approximations that can be quite complex.

Starting with Section 2.1 from [Chapter 2](#), the nuclear surface is introduced in Eq. (2.1), which was parametrized in terms of the collective coordinates and spherical harmonics. The relevant excitation mode for triaxiality is given by the quadrupole deformation, having  $\lambda = 2$ . The quadrupole deformation introduces two parameters that give an insight with respect to the elongation and departure from axial symmetry of a nucleus, by means of the quadrupole deformation parameter  $\beta_2$  and triaxiality parameter  $\gamma$ . The two parameters, which are provided in Eq. (2.5), dictate the stretching of the nuclear axes, and this was shown in Fig. 2.2. From the representation of a general ellipsoid in terms of  $\beta_2$  and  $\gamma$ , all the possible shapes that posses axial symmetry appear at certain values of  $\gamma$ , while the unique triaxial region is found in the region  $\gamma \in (0, 60)$  (see Fig. 2.3).

The theoretical study of deformed nuclei is performed in [Chapter 2](#), where the Nilsson Model is employed (recall Section 2.2.2). The single-particle energies are obtained as a sum between the anisotropic harmonic oscillator, a spin-orbit term, and the centrifugal term. The last two terms are defined with the strength parameters  $\kappa$  and  $\mu$ , which are specific to this theory. The collective model is described

in the same chapter (see Section 2.2.4), and it emphasized the behavior of the nuclear shapes in terms of the moments of inertia, i.e., the irrotational and rigid MOI provided in Eq. (2.30). These quantities are crucial to the development of the model. Their behavior with respect to the asymmetry parameter  $\gamma$  was depicted in Fig. 2.11. In terms of nuclear rotations and vibrations, several experimental spectra are graphically shown in Fig. C.2 from Appendix C, Figs. 2.13 - 2.14, and Fig. 2.17. The spectra of nuclear rotations and vibrations are important for understanding wobbling nuclei with respect to the angular momentum (the nuclear vibrations and rotations are treated in Sections 2.2.6 and 2.2.7, respectively).

Important quantities for collective phenomena used in the numerical application, such as the moments of inertia (including the kinematic and dynamical MOI from Eqs. (2.46) - (2.47)) and the quadrupole moment (measure of deformation or departure of the nuclear shape away from spherical symmetry) were discussed in detail throughout Section 2.2.9. The Hamiltonian depicted in Eq. (2.70) marks the onset of the theoretical model adopted in this work, and from the Triaxial PRM Hamiltonian, the energy spectra and transition probabilities are obtained for odd-mass Lu isotopes.

*Chiral bands* and *wobbling motion* are unique fingerprints of triaxial deformation. Any experimental identification of these two effects is a decisive test that can pinpoint triaxial nuclei. For the chiral case, it was shown in Section 2.3.6 that the spectra emerge from the coupling of three angular momenta: a proton, a neutron, and the core, leading to a trihedral system lacking chiral symmetry. Some examples of spectra are shown in Fig. 2.32 - 2.33. In Fig. 2.34 the geometry of the mutual coupling between the angular momenta is shown. Also in Chapter 2, the Triaxial Particle + Rotor Model has been analytically treated (section 2.3.3), since that Hamiltonian was the foundation of this work. Firstly the Hamiltonian for the symmetric case is considered, starting with Eq. (2.55), then a single-particle term is added via Eq. (2.60). This term represents the motion of a valence nucleon within a quadrupole deformed mean-field generated by an even-even core. As a matter of fact, this single-particle term is given by the Nilsson's deformed shell model (Eq. (2.63)). The single-particle potential strength  $V$  is used to parametrize the interaction and it is incorporated into the numerical implementation of the energy spectrum. As a purely theoretical application, the matrix elements for the single-particle energies of protons and neutrons are calculated according to Eq.

(2.66). A set of graphical representations are made, showing their behavior with respect to the quadrupole deformation parameter  $\beta_2$  and triaxiality  $\gamma$ .

Triaxial nuclei rotate around any of the three principal axes, with the main rotation about the axis with largest MOI. The contribution from the other two axes has a vibrational character, and through a first approximation, this kind of motion can be described analytically by a harmonic-like Hamiltonian. In **Chapter 3** it is shown that the wobbling motion differs from the even- $A$  to odd- $A$  nuclei. Indeed, for systems with even number of nucleons, the energy spectrum is achieved in the so-called *Harmonic Approximation* by Eq. (3.14), where the wobbling phonon number represents a tilting strength of the total angular momentum away from the axis with largest MOI. The final energy spectrum is characterized by a rotational motion around this MOI and a frequency of oscillation of the nucleus. The behavior follows Eq. (3.11) and it is depicted in Fig. 3.3. The *Harmonic Approximation* is tested for  $^{130}\text{Ba}$  nucleus, which has two wobbling bands. The experimental data are well reproduced by a fitting procedure that has the three moments of inertia as free parameters. The actual workflow regarding the numerical algorithm for calculating wobbling energies and transition probabilities is provided in Section 3.1.2 (see results in Figs. 3.5 - 3.7). While the results can be compared to alternative methods found in literature such as Chen et al. [99], they are distinct and specific to this work.

For the wobbling motion in odd-mass nuclei, a *Frozen Approximation* is illustrated, showing that the spectrum contains a similar harmonic-like term, but with a different behavior for the wobbling frequency. This behavior is dictated by the alignment of the odd-particle with the even-even triaxial core. Two wobbling scenarios may arise depending on whether the particle's angular momentum aligns itself along (*longitudinal*) or perpendicular (*transverse*) to the axis of largest moment of inertia. The workflow diagrams 3.9 - 3.11 show how these two wobbling regimes can occur, based on an overlap between the density distributions of the core and the single-particle. These diagrams also illustrate the precessional + oscillatory behavior of the total a.m., which is the first geometrical representation of such a precessional cone in the literature. The wobbling frequency in odd nuclei was analyzed via Eq. (3.32), showing that it depends on the three MOI as in Fig. 3.13. In addition, the catalogue from Fig. 3.21 containing all known wobblers is another remarkable result of this research. Therein, the experimental wobbling

energy, the number of wobbling bands, and deformation parameters ( $\beta_2$  and  $\gamma$ ) are shown for each nucleus.

**Chapters 3, 4, and 5** do also have separate sets of conclusions and discussions, so one can refer to the individual sections 3.4, 4.5, 5.4, respectively. For this reason, only a brief revision of the emerging characteristics is mentioned here:

- an initial quantal Hamiltonian of Triaxial Particle-Rotor type is employed as the foundational tool for describing wobbling motion
- the Hamiltonian is brought to a classical form by means of the *variational principle* (according to Eq. (4.4))
- in the classical view, the dynamics are described by two sets of coordinates, i.e., one for the even-even core and one for the single-particle (Eqs. (4.11) - (4.12))
- the excitation energies can be analytically determined through the utilization of five free parameters, as indicated in Equation (4.59)
- **Chapter 4** employs a re-normalization of the wobbling bands (Eqs. (4.53) - (4.54)) by applying the variational principle to not only the ground-state, but also other bands. This is called **W<sub>1</sub>** formalism throughout the thesis. The TSD1 and TSD2 bands in <sup>161,163,165,167</sup>Lu are signature partners, meaning that the phonon numbers are  $(n_{w_1}, n_{w_2}) = (0, 0)$
- two fitting procedures are employed for <sup>163</sup>Lu, as the fourth triaxial band is obtained from the coupling of a different valence proton ( $h_{9/2}$ ). Results regarding energies and transition probabilities verify the experimental data very well
- *the novel approach* called **W<sub>2</sub>** is employed in **Chapter 5**, treating TSD2 and TSD4 in <sup>163</sup>Lu as *parity partners*: *a set of bands with opposite parity that emerge from the same single-particle alignment (the  $i_{13/2}$  proton) but different core*
- The formalism **W<sub>2</sub>** adopts a unified fitting procedure for the spectrum of <sup>163</sup>Lu, and the experimental data are very well reproduced (see Figs. 5.1 - 5.2)

- geometrical interpretations of the wobbling motion are realized in the space generated by the angular momentum components, showing the classical trajectories of the **I** (recall the set of Figs. 5.15 - 5.18)
- classical trajectories and the identification of *stable/unstable* wobbling motion (see Figs. 5.8 - 5.11) are unique concepts of this research and they provide a clear picture with the dynamics of a triaxial system
- for a given spin state belonging to the wobbling spectra, the nucleus can execute precessional motion up to a certain energy (critical point). Beyond this value a phase transition occurs, where the total angular momentum changes the axis it precesses about.

The last chapter is dedicated to a completely different description for the wobbling motion, but also studied in the framework of odd-mass nuclei. Through a unique method that requires a boson description of the angular momenta and also the help of the Jacobi Elliptic Functions [164], the wobbling motion in  $^{135}\text{Pr}$  nucleus is treated in a classical fashion, obtaining results that agree with the experimental measurements. More conclusions are available in Section 6.5.4 within the chapter.

*The semi-classical analysis of wobbling motion in triaxial nuclei, as portrayed in this work, has proven to be a remarkable and efficient tool. It yields realistic results that are comparable to those obtained through more complex and difficult alternative descriptions. A notable characteristic of the developed model is its close congruence with classical dynamics.*

To summarize the entire work encapsulated in this thesis, **six publications** are presented: **two** research papers that introduce the re-normalization in terms of Signature Partner Bands for the triaxial bands in  $^{161,163,165,167}\text{Lu}$  (i.e., Refs. [101, 136]), **two** more papers that extend this formalism with Parity Partner Bands in  $^{163}\text{Lu}$  (that is Refs. [103, 137]), **one** paper devoted to the geometry of the wobbling mode in odd-mass nuclei (i.e., Ref. [105]), and lastly, **one** paper that covers odd-mass nuclei and give a unified description of the wobbling + chiral phenomena (i.e., Ref. [135]).



# Appendix A

## Shell Model

### A.1 Shell model

The idea that an atomic nucleus can have a structure that behaves rather similarly as the atom itself has been enforced by the experimental observations that were done across time. The sharp and discrete discontinuities of nuclear properties, such as the nucleon separation energy, point out that nucleus can be explained through the existence of *shells*. Some examples of observations indicating this are:

- When adding a nucleon to a nucleus, there are certain places where the *binding energy* of the next nucleon becomes considerably smaller than the previous one.
- Separation energies for both the protons and neutrons suffer drastic changes, having strong deviations from the predictions of the semi-empirical mass formula [171], the discontinuities being represented by major shell closures (complete filling) [20].
- The neutron absorption cross-section has a substantial decrease in value at the neutron magic numbers
- Great abundance of nuclides where  $Z$  and  $N$  are magic numbers.

The sudden discontinuities occur at specific values of the proton  $Z$  and neutron  $N$  numbers: these are called *magic numbers*. Currently, these magic numbers correspond to  $Z$  or  $N = 2, 8, 20, 28, 50, 82, 126$ , and they represent the major shells.



FIGURE A.1: The first excited energy states  $2^+$  of nuclei with even  $Z$  and  $N$  are graphically represented with respect to the proton number. Each connecting line represents a set of isotopes. Figure taken from Ref. [76].

There are also two *weakly magic numbers*: 40 and 64. One can examine the values for the first excited states  $2^+$  that are shown in Figs. A.1, A.2. Indeed, these values show some peaks, each peak corresponding to a particular magic number. This results are part of the work of Raman et al. [172], where the transition probabilities from the ground state to the first-excited  $2^+$  state in even-even nuclei were evaluated.

The shell model starts from the basic assumption that the nucleus is a *mean-field potential*, where the motion of a single nucleon is caused by all the other nucleons. In other words, the nucleon is moving inside an average potential generated by all the other constituents of the nucleus. Of course that all the nucleons under the influence of this mean field occupy the energy levels which correspond to a series of sub-shells verifying the *Pauli exclusion principle*. Having a general expression for the potential that reproduces all the magic numbers and the observed nuclear properties is therefore crucial. Since the model starts from the concept of independent (non-interacting) particle motion within an average potential, finding each

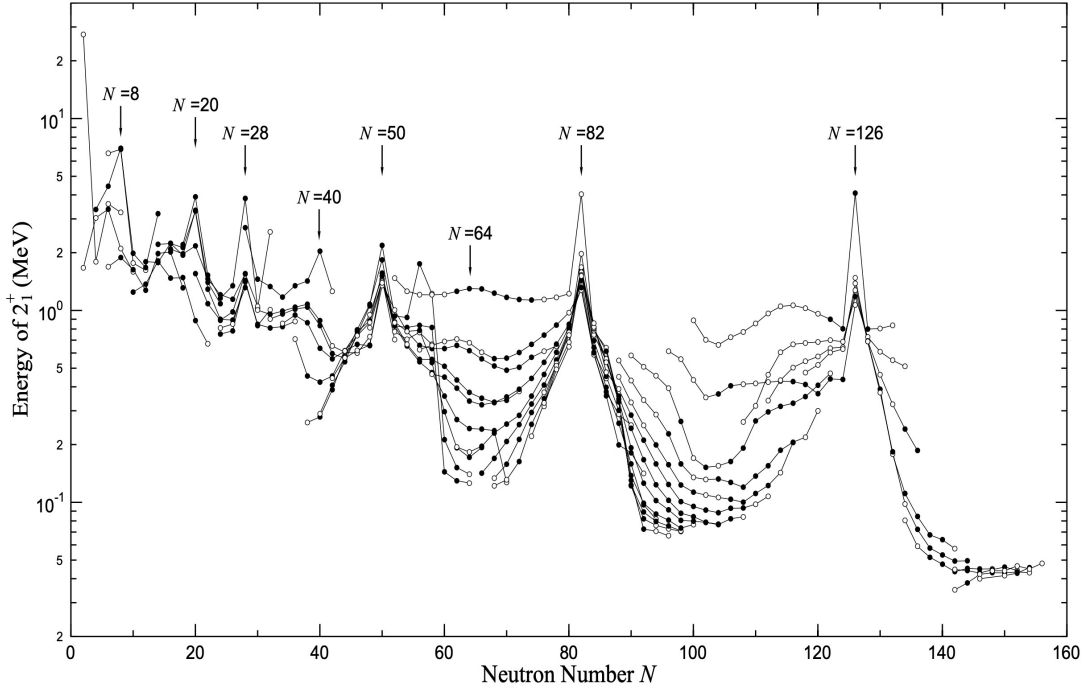


FIGURE A.2: The first excited energy states  $2^+$  of nuclei with even  $Z$  and  $N$  are graphically represented with respect to the neutron number. Each connecting line represents a set of isotopes. Figure taken from Ref. [76].

energy will be equivalent of solving the Schrödinger equation:

$$-\frac{\hbar^2}{2m} \nabla^2 \psi_i(r) + V(r) \psi_i(r) = e_i \psi_i(r) \quad (\text{A.1})$$

where  $e_i$  represents the energy (eigenvalue),  $\psi_i$  represents the wave-function (eigenstates), and  $V(r)$  is the nuclear potential whose expression must be evaluated. The choice of  $V(r)$  will be dictated by the reproduction of various experimental data (such as nuclear saturation, scattering, nuclear reactions, and so on). For the motion of an independent particle, an obvious first attempt would be the *simple harmonic oscillator* (SHO), which has the known expression:

$$V(r) = \frac{1}{2} m(\omega_i r)^2 , \quad (\text{A.2})$$

with  $\omega_i$  as the frequency of the basic harmonic-like motion of the particle in the nucleus. With Eq. (A.2), the motion of the nucleon has a straightforward expression:

$$\frac{\hbar^2}{2m} \nabla^2 \psi_i(r) + \frac{1}{2} m(\omega r)^2 \psi_i(r) = e_i \psi_i(r) . \quad (\text{A.3})$$

This Schrödinger equation has its energy eigenvalues under to form:

$$e_N = \left( N + \frac{3}{2} \right) \hbar\omega , \quad (\text{A.4})$$

where  $N$  is the number of oscillator quanta which describes each major shell (also called the *principal quantum number*). One should keep in mind that such an expression is typical for a three-dimensional and isotropic harmonic oscillator. The principal quantum number  $N$  is furthermore defined as:

$$N = 2(n - 1) + l , \quad (\text{A.5})$$

with  $n$  and  $l$  being the *radial* quantum number and *orbital angular momentum* quantum number, respectively, taking values  $n = 1, 2, 3, \dots$  and  $l = 0, 1, 2, \dots, n - 1$ . In this first approximation, all the levels with the same principal quantum number  $N$  are *degenerate*, with a maximal degeneracy given by  $2(2l+1)$ . However, by using only the SHO term as the expression of  $V(r)$ , only the first three magic numbers are reproduced, meaning that some additional term(s) might be needed in order to consistently obtain the series of magic numbers.

Furthermore, the steepness of the SHO can be corrected with an *attractive* term proportional to  $l$ -squared. This acts as a centrifugal term which provides an angular momentum barrier, lifting the degeneracy between the levels with the same principal quantum number  $N$  and different values for the orbital angular momentum  $l$ . This SHO+ $l^2$  adjustment is still not enough, such that a so-called *spin-orbit* coupling term of the form  $\vec{l} \cdot \vec{s}$  must be also added. This term comes from the consideration that the nucleon-nucleon interaction has a spin dependence, and the potential depends on the intrinsic spin  $s$  ( $\vec{s}$ ) and the orbital angular momentum  $l$  ( $\vec{l}$ ) of a nucleon. Since  $\vec{j} = \vec{l} + \vec{s}$ , two possible states emerge from a single value of  $l$  (depending on whether  $\vec{s}$  is parallel or anti-parallel to  $\vec{l}$ ). The final will consist of the *Modified Harmonic Oscillator* (MHO).

$$V(r) = \frac{1}{2}(\omega r)^2 + B \vec{l}^2 + A \vec{l} \cdot \vec{s} . \quad (\text{A.6})$$

For the sake of simplicity, the centrifugal term will be denoted within formulas without the vector symbol. Since the intrinsic spin of a nucleon is  $s = 1/2$ , for a given value of  $l$ , there can be two values for the *total angular momentum* (a.m.)  $j = l \pm 1/2$ : one for each spin orientation with respect to the direction of the

orbital a.m. Moreover, for every value of  $l = 0, 1, 2, 3, 4, \dots$ , there is a similar notation  $l = s, p, d, f, g, \dots$ , respectively. Regarding the spectroscopic notation, usually, the value of  $j$  is considered as a subscript;  $nl_j$  (for example  $1p_{1/2}$  and  $1p_{3/2}$ ). For high enough shells, there can be splittings between  $j + 1/2$  and  $j - 1/2$  that are large enough to lower the  $j + 1/2$  state from one oscillator shell  $n$  to one located below  $n - 1$ . These types of levels are called *intruder states*, and they have opposite parity  $\pi = (-1)^l$  with respect to the shell that these levels will occupy.

Going back to the expression of the  $\vec{l} \cdot \vec{s}$  term from Eq. (A.6) and denoting it with  $V_{ls}(r)$ , its contribution to the total potential can be regarded as a surface effect and it can be expressed as a function that depends on the radial coordinate as such [15]:

$$V_{ls}(r) = -a_{ls} \frac{\partial V(r)}{\partial r} \vec{l} \cdot \vec{s}, \quad (\text{A.7})$$

where  $V(r)$  is the expression for a central potential and  $a_{ls}$  is a strength constant.

The nuclear potential is now able to reproduce all the magic numbers. It is also possible to formulate the total energy of a single-particle within the average potential. Thus, the Hamiltonian of this simple system (i.e., the MHO) can be formulated as such:

$$\begin{aligned} H &= -\frac{\hbar^2}{2m} \nabla^2 + V_{\text{SHO}} + (l^2)_{\text{term}} + (\vec{l} \cdot \vec{s})_{\text{term}} = -\frac{\hbar^2}{2m} \nabla^2 + V_{\text{MHO}}, \\ H &= -\frac{\hbar^2}{2m} \nabla^2 + \frac{1}{2} m(\omega r)^2 + Bl^2 + A\vec{l} \cdot \vec{s}. \end{aligned} \quad (\text{A.8})$$

The evolution from a SHO, then SHO+ $l^2$ , and finally SHO+ $l^2 + \vec{l} \cdot \vec{s}$  or modified oscillator potential is illustrated in Fig. A.3, where it can be seen how each extra term removes a degeneracy, with the complete reproduction of the magic numbers in the third column. The *intruder* levels can also be observed, where states with  $j = l + 1/2$  from a particular  $n$  are so low, that they lie below an  $n - 1$  adjacent level.

Another, more realistic potential that can be used in order to reproduce the specific shell model calculation is the so-called Woods-Saxon potential. Because of the short-range character of the strong nuclear force, it is safe to assume that this potential should behave in the same manner as the density distribution of the

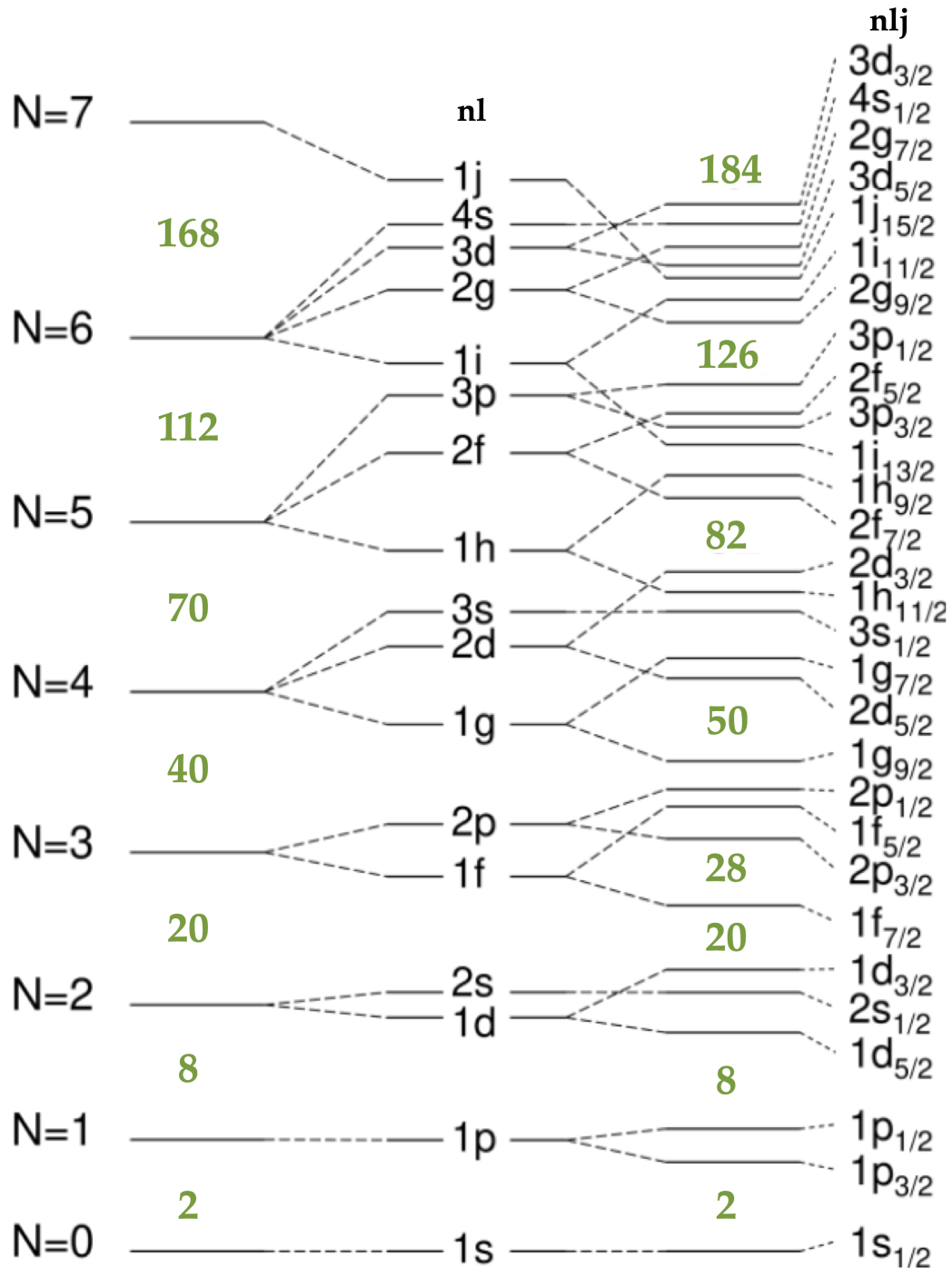


FIGURE A.3: The energy levels obtained via calculation of the shell model potential using the simple oscillator (SHO), the SHO amended with a centrifugal term  $l^2$ , and finally the modified oscillator (MHO) that contains a spin-orbit term. The ‘correct’ magic numbers are the ones in the right-most column.

Figure is adapted from Refs. [20, 76].

nucleons. Since for medium and heavy nuclei, the Fermi-like functions (distributions) are the ones that best fit the experimentally measured data, this potential should have the following form [173]:

$$V_{\text{ws}}(r) = -\frac{V_0}{1 + e^{\frac{r-R_0}{a}}} , \quad (\text{A.9})$$

where  $V_0$  represents the depth of the potential ( $\approx 50$  MeV, in order to reproduce the experimental separation energies for the nucleons),  $a$  is the surface thickness (or *diffuseness parameter*, giving information about how fast the potential drops to zero) with a value of approximately 0.5 fm, and  $R_0$  is the nuclear radius ( $R_0 = 1.2A^{1/3}$  fm). The nature of this potential is of *central type* and Eq. (A.9) is not enough to reproduce the higher magic numbers. As such, the addition of a spin-orbit term, similarly as in the case of MHO potential, is required [174]:

$$V_{\text{total}} = V_{\text{ws}}^{\text{central}} + V_{ls}(r)\vec{l} \cdot \vec{s} . \quad (\text{A.10})$$

The only good quantum numbers in the case of the WS potential are the total a.m.  $j$  and the parity  $\pi = (-1)^l$ . The expectation value of the spin-orbit term  $\vec{l} \cdot \vec{s}$  can be given as:

$$\langle ls \rangle = \hbar^2 \begin{cases} \frac{l}{2} & \text{for } j = l + \frac{1}{2} \\ -\frac{l+1}{2} & \text{for } j = l - \frac{1}{2} \end{cases} . \quad (\text{A.11})$$

and the spacing between two levels can be furthermore expressed as [174]:

$$\Delta E_{ls} = \frac{2l+1}{2}\hbar^2 \langle V_{ls} \rangle . \quad (\text{A.12})$$

The experimental evidence points to the fact that  $V_{ls}(r)$  is negative, meaning that states with  $j = l - 1/2$  are shifted higher than  $j = l + 1/2$ . Some characteristics of the WS potential are the following:

1. It increases with the increase of  $R$ , meaning that it has an *attractive nature*
2. It flattens out for large enough  $A$  in the center of the nucleus
3. It rapidly goes to zero as  $R$  increases (given by the diffuseness parameter), indicating its short-range nature



FIGURE A.4: The shape of the Woods-Saxon potential, defined by Eq. (A.9). The parameters are arbitrarily chosen as:  $V_0 = 50$  MeV,  $R = 5.57$  fm, and  $a = 0.5$  fm.

4. When  $R = R_0$  (that is for the nucleons near the surface), a large force towards the center of the nucleus is experienced by the these nucleons.

The Hamiltonian that describes the motion of the nucleon within the mean-field potential is given by:

$$H = -\frac{\hbar^2}{2m} \nabla^2 - \frac{V_0}{1 + e^{\frac{r-R_0}{a}}} + A \vec{l} \cdot \vec{s}, \quad (\text{A.13})$$

and the shape of a typical Woods-Saxon potential is shown in Fig. A.4. A comparison between the Woods-Saxon potential, a SHO, and the square-well-like potential is made in Fig A.5. The difference between the pure form of the Woods-Saxon potential and the total potential amended with the spin-orbit contribution can be seen in Fig. A.6.

So far, the general discussion concerning nuclear models was made for the case where each nucleon is treated as an *independent* particle moving in an average (mean-field) potential. However, such an assumption is not accurate enough (especially for the nuclei that lie far away from the closed shells), and this problem should be treated within a *many-body* approach: considering the mutual interaction between the nucleons. These interactions are also called *residual interactions* [15, 17]. With these residual interactions, an accurate depiction of the nucleus

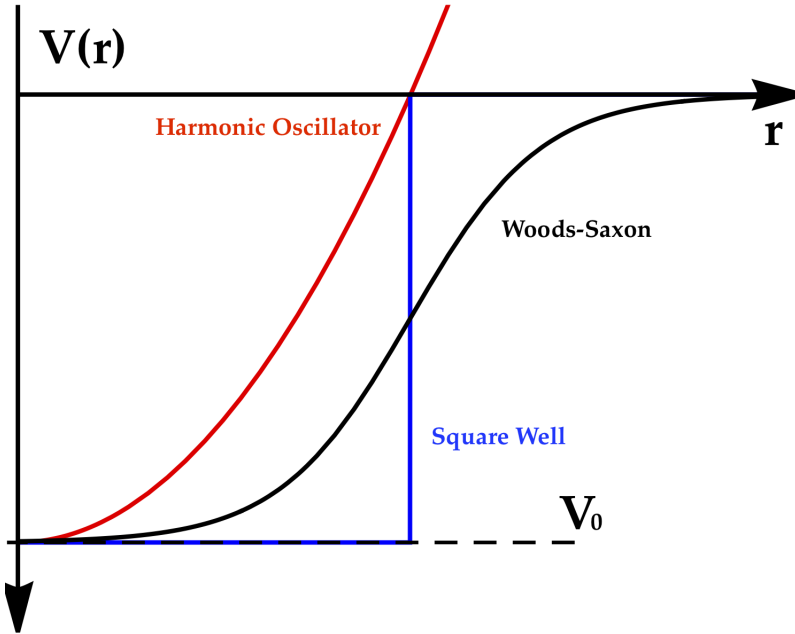


FIGURE A.5: A schematic representation with the three kind of potentials used to describe the shell model: harmonic oscillator, Woods-Saxon, and for completeness, the square-well.

might be achieved. The *Deformed Shell Model* will be employed in the following sections, reaching to the famous Nilsson model of describing the nucleus.

## A.2 Nilsson Orbitals

Recalling Fig. 2.7, the splitting of an orbital into  $j + 1/2$  magnetic sub-states can be viewed as a set of energies where the nucleon is *orbiting* around the bulk nucleus with an orbit that has a certain *tilt* angle  $\theta$  (see the orbits depicted in Figs. 2.5 - 2.6). The tilting angle is conceptually shown in Fig. A.7. For that particular orbit, the angle is given by the expression [15, 20]:

$$\begin{aligned} \sin \theta &= \frac{\Omega}{j} , \\ \theta &= \arcsin \left( \frac{\Omega}{j} \right) . \end{aligned} \quad (\text{A.14})$$

The change of  $\theta$  is rather slow for low  $\Omega$  projections, while rapid changes take place at high  $\Omega$  values. As a numerical example, the  $\theta$  variation is studied for the

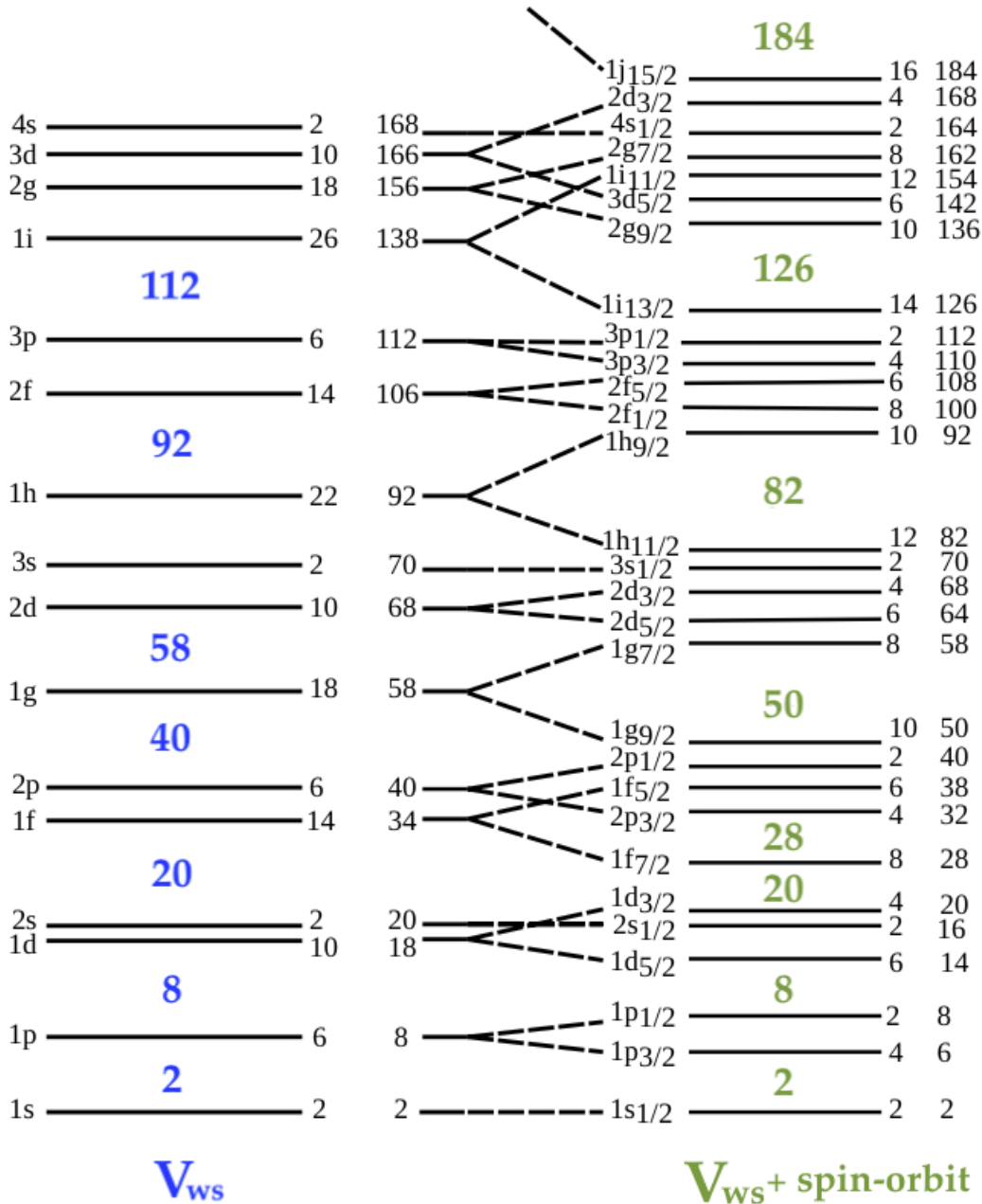


FIGURE A.6: The energy levels calculated for the Woods-Saxon potential given by Eq. (A.9) (left-side), and the single-particle energies with the spin-orbit correction added, as in Eq. (A.10) (right-side). Figure adapted from Ref. [77].

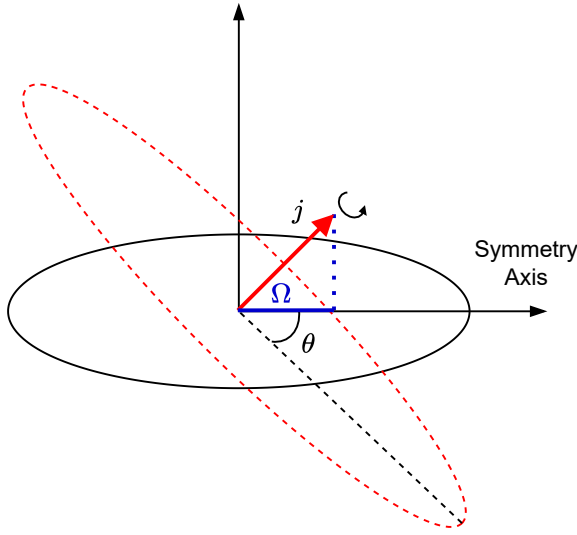


FIGURE A.7: The orbit of a single particle orbiting the deformed nucleus, defined by the projection of the particle's a.m.  $\Omega$  (on the symmetry axis) and the tilting angle  $\theta$ . Figure inspired from Ref. [15]

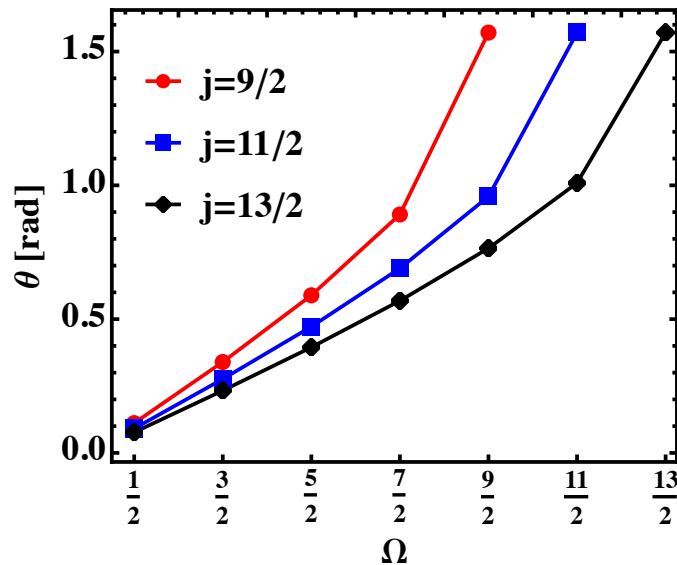


FIGURE A.8: The change in  $\theta$  angle defined in Eq. (A.14) with increasing values of  $\Omega$ , for a few orbitals  $j$ .

orbits  $j = \{9/2, 11/2, 13/2\}$ , with their corresponding projections. The evolution with  $\Omega$  for different orbits can be seen in Fig. A.8.

The splitting of an orbital  $j$  into multiple sub-states (see Fig. 2.7) emerges from the considerations regarding the change in tilting angle and also the fact that the difference in energy is rather smooth (high) depending on low (high)  $\Omega$  values. Based on this discussion, it is clear that a full Nilsson diagrams is constructed

with the configuration mixing of different  $j$  values. Remarkable, *no two lines in the Nilsson diagram with similar  $\Omega$  values can cross each other*. When two such orbits come close to each other, they must repel as shown in Fig. B.5. Explaining the behavior of the lines that appear in the Nilsson diagrams 2.8 - 2.9 is straightforward: each line represents a Nilsson state, starting out straight and then sloping downward or upward, depending on the angle of the orbit relative to the bulk nucleus. The *curving* of an orbit starts when it approaches another level with the same quantum number  $\Omega$  and parity  $\pi$ . Thus, the structure of any Nilsson diagram relies on three main features [15]:

- the  $\Omega$  splitting
- repulsion between two levels
- single-particle shell model energies

Taking a closer look at the Nilsson from Fig. 2.9, there are two orbits within the 82-126 neutron gap that can be analyzed in terms of *mixing*:  $f_{7/2}$  and  $h_{9/2}$ , respectively. Obviously, the lack of deformation implies a degeneracy of these orbits, but when deformation occurs, splitting kicks in. The angle of the orbital orientation  $\theta$  depends on the ratio  $\Omega/j$  (recall  $\theta = \arcsin(\Omega/j) \approx \Omega/j$  at low  $\Omega$ ). Small tilting angles will occur due to i) small values of  $\Omega$  or ii) high  $j$ . As a result, the energies for the orbits  $\Omega = 1/2, 3/2, 5/2$  belonging to the  $h_{9/2}$  shell are decreasing in energy faster with deformation than those from  $f_{7/2}$  orbit. Consequently, the different rates of decrease for the Nilsson energies will overcome any small spherical energy separation  $f_{7/2} - h_{9/2}$ , making the orbits with low  $\Omega$  to approach each other, leading to a more pronounced mixing. However, as discussed in B, two orbits defined by the same quantum numbers cannot cross, causing the apparition of an *inflection point*. The points can be seen when looking at the  $\Omega = 5/2$  and  $\Omega = 7/2$  orbits, which correspond to  $f_{7/2}$  and  $h_{9/2}$ .

The single-particle Hamiltonian can be written in the general form, starting from the expression Eq. (2.19):

$$H_{\text{Nil}} = -\frac{\hbar^2}{2m} + \frac{1}{2}m(\omega_0 r)^2 - \frac{4}{3}\sqrt{\frac{\pi}{5}}m(\omega_0 r)^2\epsilon Y_2^0(\theta, \varphi) - 2\kappa\hbar\omega_0(\vec{l} \cdot \vec{s}) - 2\kappa\hbar\omega_0\mu(l^2 - \langle l^2 \rangle_N) . \quad (\text{A.15})$$

The expressions for the oscillator frequencies were already defined as functions of the deformation parameter  $\epsilon$  and they keep the same form as Eqs. (2.22) - (2.23). It is worth mentioning that both forms of  $H_{\text{Nil}}$  from Eq. (2.19) and Eq. (A.15) are equivalent. Moreover, they describe the structure of the deformed nuclei in the limits of large deformations (via Eq. (2.19)) and small deformations (via Eq. (A.15)). Within literature, the two parameters are taken to be  $\kappa \approx 0.06$  and  $\mu$  varies between  $\mu = 0 \sim 0.7$ .

When the deformations are small,  $j$  is a good quantum number, and the Eq. (A.15) represents a Hamiltonian for the AHO plus a *perturbation* that is proportional to  $\epsilon r^2 Y_2^0$ . Therefore, one can consider the eigenstates of the Hamiltonian as states labelled by the quantum numbers  $N, l, j$ , and  $m$ . It is possible to obtain a shift in energies relative to  $\epsilon = 0$  if the angular part  $Y_2^0$  is treated as a perturbation [15]:

$$\Delta E_{Nljm} = -\frac{4}{3}\sqrt{\frac{\pi}{5}}m\omega_2^0\epsilon \langle Nljm | r^2 Y_2^0 | Nljm \rangle . \quad (\text{A.16})$$

Furthermore, one can perform a separation of the radial and the angular parts while using the known relation for a harmonic oscillator potential:

$$\frac{1}{2}m\omega_0^2 \langle Nljm | r^2 | Nljm \rangle = \frac{1}{2}\hbar\omega_0 \left( N + \frac{3}{2} \right) , \quad (\text{A.17})$$

and together with the evaluation of the matrix elements for spherical harmonics, the final expression for the energy shift at small deformations is:

$$\Delta E_{Nljm} = -\frac{2}{3}\hbar\omega_0 \left( N + \frac{2}{3} \right) \epsilon \frac{[3K^2 - j(j+1)] \left[ \frac{3}{4} - j(j+1) \right]}{(2j-1)j(j+1)(2j+1)} , \quad (\text{A.18})$$

where the projection  $m$  was replaced with the total angular momentum projection onto  $z$ -axis  $K$ . Based on Eq. (A.18), the following properties for a Nilsson diagram emerge:

- There is a  $K^2$  dependence for the energy shifts
- The quadrupole deformation parameter ( $\epsilon$  or  $\beta$ ) shows a clear linear dependence for  $\Delta E_{Nljm}$
- Another linear dependence for the shifts is induced by the principal (oscillator) quantum number  $N$



FIGURE A.9: The energy shift  $\Delta E$  for two orbits:  $h_{9/2}$  and  $i_{13/2}$  for a given deformation  $\epsilon = 0.22$ . The dashed vertical lines (colored) represent the value for  $K$  where the ‘change’ from downward sloping curves to upward sloping curves takes place (that is  $K \approx 0.65j$ ). This is just an illustrative example inspired from the discussion regarding single-particle orbits in Ref. [15]

- When the deformation parameter is positive, there are more downward sloping orbits than upward ones (example discussed below)

For a value  $j > 1/2$ , the terms  $[3K^2 - j(j+1)]$  and  $3/4 - j(j+1)$  are negative, resulting in the following types of orbits: [20]:

$$\text{downward sloping: } K < \sqrt{\frac{j(j+1)}{3}} \approx \frac{j}{1.8} = 0.57j , \quad (\text{A.19})$$

$$\text{upward sloping: } K > 0.57j . \quad (\text{A.20})$$

It was already shown that the angular orientation (i.e., the tilting angle  $\theta$ ) of an orbit is given by  $\theta = \arcsin(K/j)$ . For a ratio  $K/j = 0.65$ , the tilting angle is  $\theta = 40^\circ$ . The physical implication is that any larger *tilt* of an orbit within a prolate quadrupole deformation is energetically unfavorable. In Fig. A.9 two different  $j$  orbits, namely  $h_{9/2}$  and  $i_{13/2}$  are studied in terms of their energy shifts according to Eq. (A.18). It can be seen that there are more downward sloping orbitals, since the quadrupole deformation parameter has been set to a positive value  $\epsilon = 0.22$ .

Based on the principal quantum number  $N$ , there is another important physical consequence. The dependence on  $N$  will imply that the slopes of any Nilsson energy level will be *steeper* for larger values of  $N$ . Thus, heavier nuclei will tend to deform much easier than lighter ones. The explanation was done in Refs.

[1, 15, 20]. Shortly, a nucleon belonging to a high oscillator shell will have a large average radius (the expectation value of  $r^2$  was provided in Eq. (A.18) via the expression  $\langle r^2 \rangle = (N + 3/2)$  [17]). As the nucleus deforms, the density distribution of the nuclear matter will approach that orbit. The effect on the orbiting nucleon to decrease its energy rapidly as the nuclear matter comes closer to the orbit is due to the *attractive* nature of the nuclear force. Clearly, this effect is less obvious for a particle in a lower oscillator shell that is already very close to the rest of the nuclear matter.

The centrifugal  $\vec{l}^2$  and spin-orbit  $\vec{l} \cdot \vec{s}$  terms from Eq. (A.15) will become negligible in the limit of *large deformation*, such that the Nilsson Hamiltonian will become just like an AHO. In this special case, the motion will separate into *independent* oscillations in the direction of the symmetry axis and the perpendicular plane (i.e., in the direction of  $z$ -axis and  $xy$  plane). Consequently, the good quantum numbers for this kind of situation are the  $n_z$  and  $(n_x + n_y)$  oscillator quantum numbers. Since the eigenvalues for a one-dimensional (and, implicitly for the three-dimensional) harmonic oscillator are established, the energy spectrum for single-particle orbits in the regime of large  $\epsilon$  will be given by [15]:

$$E_{n_x, n_y, n_z} = \hbar\omega_x(N - n_z + 1) + \hbar\omega_z \left( n_z + \frac{1}{2} \right) . \quad (\text{A.21})$$

The remarkable feature of the Hamiltonian is its invariance to rotations about the  $z$  axis. The projections for the particle's orbital and spin a.m. are constants of motion. As it was discussed, the sum of the two projections  $\Lambda$  and  $\Sigma$  is indeed  $\Omega$  or, equivalently,  $K$  in the case of  $\vec{R}$  being perpendicular to the  $z$ -axis. Concluding, the importance of the Nilsson Deformed Model was made clear enough in this section. Its importance within the rest of the present work will be justified later on, where based on a Particle-Rotor-Model [1, 4], it will play a crucial role in determining the Hamiltonians specific to the nuclei of interest.



# Appendix B

## Two-State Mixing

In the work of Casten [15], an analytical approach is given for the mixing of two different states (energy levels). It starts from the basic idea of two initial levels, each with its corresponding energy  $E_1$  and  $E_2$ , and their associated wave-functions (denoted here by  $\psi_1$  and  $\psi_2$ ). Any interaction between them is reflected into the mixing matrix element  $\langle \psi_1 | V_{\text{int}} | \psi_2 \rangle$ , where  $V_{\text{int}}$  is the arbitrary interaction between the states. This is sketched in Fig. B.1.

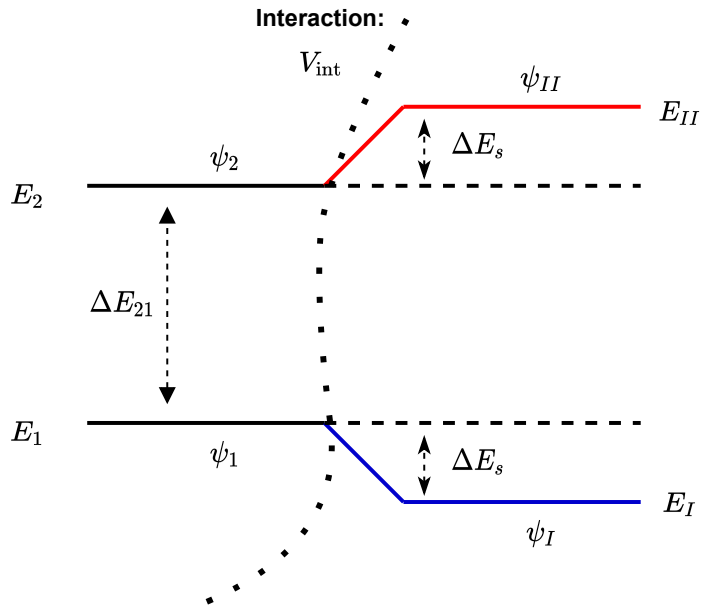


FIGURE B.1: Defining the mixing between two different states, with two corresponding energies and wave-functions. Interaction is illustrated via the curved line and  $V_{\text{int}}$  term.

The problem consists of finding the final energies and wave-functions, this being done via the diagonalization procedure of a  $2 \times 2$  matrix. The main diagonal of this matrix contains the two energies and the off-diagonal terms represent the interaction itself. The final states will be denoted with  $(E_I, E_{II})$  for the energies and  $(\psi_I, \psi_{II})$  for the wave-functions. As a general rule, the mixing depends on the initial separation  $\Delta E_{21} = (E_2 - E_1)$  and the matrix element  $\langle \psi_1 | V_{\text{int}} | \psi_2 \rangle$ . For a large spacing the effect of a given matrix element will be quenched. Moreover, even a small matrix element can introduce a large mixing if the energy separation between the states is negligible (that is, the unperturbed states lie close to each other).

A reduction from these two parameters can be performed, obtaining a general mixing expression that is valid for any arbitrary interaction and any initial spacing. As a first step, one should define the ratio between the spacing of the unperturbed states ( $\Delta E_{21}$ ) and the strength of the matrix element:

$$R = \frac{\Delta E_{21}}{V_{\text{int}}} . \quad (\text{B.1})$$

With this quantity, the newly perturbed energies  $E_I$  and  $E_{II}$  become [15]:

$$E_I = \frac{1}{2}(E_1 + E_2) + \frac{\Delta E_{21}}{2} \sqrt{1 + \frac{4V_{\text{int}}^2}{\Delta E_{21}^2}} , \quad (\text{B.2})$$

$$E_{II} = \frac{1}{2}(E_1 + E_2) - \frac{\Delta E_{21}}{2} \sqrt{1 + \frac{4V_{\text{int}}^2}{\Delta E_{21}^2}} . \quad (\text{B.3})$$

Additionally, the amount by which each energy is shifted after the interaction is denoted in Fig. B.1 by  $\Delta E_S$ , and its expression depends on  $\Delta E_{12}$  as:

$$|\Delta E_S| = |E_{II} - E_2| = |E_I - E_1| = \frac{\Delta E_{21}}{2} \left[ \sqrt{1 + \frac{4}{R^2}} - 1 \right] . \quad (\text{B.4})$$

The two perturbed wave functions are as follows:

$$\begin{aligned} \psi_I &= \alpha\psi_1 + \beta\psi_2 , \\ \psi_{II} &= -\beta\psi_1 + \alpha\psi_2 , \end{aligned} \quad (\text{B.5})$$



FIGURE B.2: **Left:** The dependence of  $R$  on the mixing amplitude  $\beta$ . **Right:** The dependence of  $R$  on the energy shift of the perturbed states ( $\Delta E_S$ ).

where the two amplitudes  $\alpha$  and  $\beta$  must verify the condition  $\alpha^2 + \beta^2 = 1$  and:

$$\beta = \frac{1}{\left\{ 1 + \left[ \frac{R}{2} + \sqrt{\frac{R^2}{4} + 1} \right]^2 \right\}^{1/2}} \quad (\text{B.6})$$

It is noteworthy that the amplitude  $\beta$  is in fact a function that only depends on  $R$  (i.e., the ratio between the unperturbed energy splitting and the interaction strength). Similarly, by dividing the shift in energy  $\Delta E_S$  to the initial splitting  $\Delta E_{21}$ , one will obtain an expression that is independent of the initial level spacing:

$$\frac{|\Delta E_S|}{\Delta E_{21}} = \frac{|E_{II} - E_2|}{\Delta E_{21}} = \frac{|E_I - E_1|}{\Delta E_{21}} = \frac{1}{2} \left[ \sqrt{1 + \frac{4}{R^2}} - 1 \right] \quad (\text{B.7})$$

The importance of these formula will be now emphasized through a numerical example. Firstly, the evolution of the ratio of the unperturbed shift and the interaction can be graphically represented as functions of the small mixing amplitude  $\beta$  though Eq. (B.6). The obtained result is shown in Fig. B.2. Following this analysis, the shape of  $R$  as a function of the energy shift of the perturbed states can be visualized in Fig. B.2.

For an arbitrary case where two initial states are separated by, say  $\Delta_{21} = 0.07$  MeV, and they become *perturbed* via the interaction with a strength  $V_{\text{int}} = 0.03$  MeV, this gives a value of  $R = 3.5$  and a mixing amplitude of  $\beta = 0.256$ . The

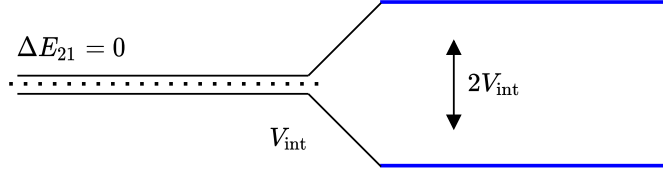


FIGURE B.3: The *strong mixing* limit for two energy levels that are interacting via a perturbation. The initial two levels are degenerate, such that their splitting is null.

two states be both shifted by  $\Delta E_S = 5.31$  keV (accounting for about 7.6% of the initial separation). Indeed, for this particular example, the perturbation results in an energy shift that is rather small compared to the initial state spacing.

Besides the numerical example discussed above, there are also two other important limiting situations when the states interact via a perturbation. The first one is the so-called *strong mixing limit*, when the initial states are degenerate (i.e., there is practically no spacing between them and  $\Delta_{21} = 0$ ). In this situation, the analytical expressions from Eq. (B.4) fail to provide a quantitative analysis, but from Eq. (B.3) a small adjustment can be made:

$$E_{I,II} = \frac{1}{2} [(E_1 + E_2) \pm 2V_{\text{int}}] = E_0 \pm V_{\text{int}} , \quad (\text{B.8})$$

where the initial (common) energy of the degenerate states is denoted by  $E_0$ . The above equation indicates that the energy shift is only given by the *mixing matrix element*. This means that the final separation energy for a two-state isolated system can never be closer than twice the interaction strength ( $2V_{\text{int}}$ ). In the degeneracy case, the values for  $\beta$  and  $\alpha$  are readily obtained: ( $\beta = \alpha = 1/\sqrt{2} = 0.707$ ), such that the states are completely mixed. Consequently, the mixed wavefunctions of two (initially) degenerate states do not depend on the strength  $V_{\text{int}}$ . The limiting case of *strong mixing* is sketched in Fig. B.3.

The second limiting case is called *weak mixing limit*, corresponding to a very large value of  $R$  (meaning that the initial separation of the states is very large compared to the magnitude of the interaction itself). The shift in energy of the perturbed states in this case is given by:

$$\frac{|\Delta E_S|}{\Delta E_{21}} = \frac{1}{R^2} , \quad (\text{B.9})$$

and a graphical representation for weak mixing is shown in Fig. B.4.



FIGURE B.4: The *weak mixing* limit for two energy levels that are interacting via a perturbation. The interaction strength is much smaller than the initial spacing between states, resulting in a very small energy splitting  $\Delta E_S$ .

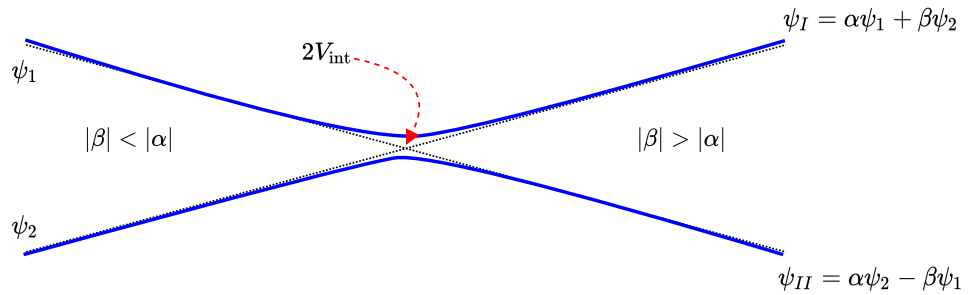


FIGURE B.5: The *non-crossing* between two states. The arrow marks the closest point at which the two states can interact with each other (i.e., the inflection point).

As a final step in the analysis of two-state mixing, it is worth mentioning a corner-case that will help to get a better grasp of the Nilsson orbitals from Chapter 2 (recall Section 2.2.2). Consider two states (say  $\psi_1$  and  $\psi_2$ ) whose energies are parametrized in terms of some argument  $c_{\text{nuc}}$  relevant for the nuclear structure of that system (e.g.,  $c_{\text{nuc}}$  could be the quadrupole deformation and the two initial states are in fact Nilsson orbits). If there indeed exists mixing between the two states, *they can never cross each other*. The two mixed states will always repel and they can never be closer than twice the mixing matrix element  $V_{\text{int}}$  after mixing occurs. In Fig. B.5 the behavior of non-crossing for the mixed states is sketched. The point at which the two states are the closest to each other represents the case when the wave-functions contain similar admixtures of each of the initial states (unperturbed). The *inflection point* can be seen in Fig. B.5.



# Appendix C

## Rotational Bands in Nuclei

Based on the behavior of  $\mathbf{j}$  and its coupling with the collective angular momentum, two rotational rotational modes can occur. The two scenarios are *Deformation aligned bands* and *Rotation aligned bands* [42], and the two modes will be described herein. A graphical representation with both rotational schemes can be seen in Fig. C.1.

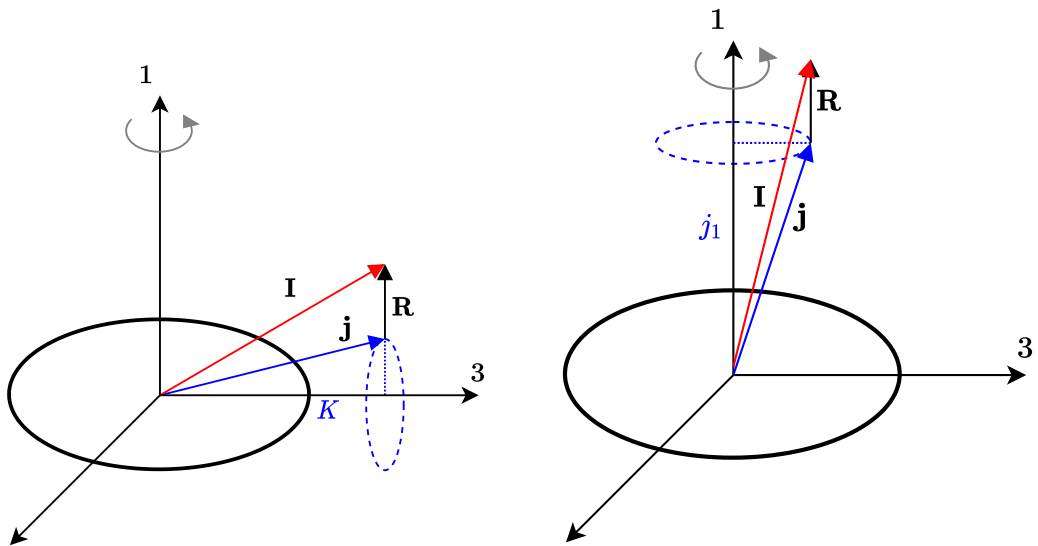


FIGURE C.1: The geometrical interpretation with the two ways a nucleus can exhibit rotational bands: Deformed Aligned Bands (**left**) and Rotation Aligned Bands (**right**). The projection of the single-particle's total a.m. on the deformation and rotation axes is denoted by  $K$  and  $j_1$ , respectively.

## C.1 Deformation Aligned Bands

This case is also known as *strong-coupling limit* [25], since the particle's a.m. is tightly coupled to the deformation axis (i.e., the symmetry axis). The general Hamiltonian will be:

$$H_{\text{rot}} = H_0 + H_{\text{coupl}} , \quad (\text{C.1})$$

where  $H_0$  is the operator containing the squared components  $I_k$  of  $\mathbf{I}$  and the extra *coupling term* represents the Coriolis force [17]. The Coriolis effect is reflected by the coupling of the collective motion of the nucleus to the odd nucleon's motion. Despite that, it can be neglected at small rotations. The projection of the particle's a.m. on the symmetry axis is a good quantum number and if  $\mathbf{R}$  is pointing in a direction perpendicular to the deformation axis, then  $\Omega = K$ . Accordingly, the energy spectrum will be given by:

$$E_{\text{rot}}(I) = \frac{\hbar^2}{2\mathcal{I}_{\perp}} [I(I+1) - K(K+1)] , \quad (\text{C.2})$$

or more formally:

$$E_{\text{rot}}(I) = \frac{\hbar^2}{2\mathcal{I}_{\perp}} [I(I+1) - K^2] + E_0(K) . \quad (\text{C.3})$$

The rotational band will be constructed on the ground-state  $E_0(K)$ , where the total spin  $I$  will consist of a sequence  $I = K, K+1, K+2, \dots$  having  $K \neq 1/2$ . Consequently, rotational bands will have consecutive states differing by only one unit of angular momentum. It should be pointed out that odd- $A$  nuclei can have multiple rotational bands built on different values of  $K$ . For  $K = 1/2$ , the band structure will follow:

$$E_{\text{rot}}(I) = \frac{\hbar^2}{2\mathcal{I}_{\perp}} \left[ I(I+1) + a(-)^{I+\frac{1}{2}} \left( I + \frac{1}{2} \right) \right] . \quad (\text{C.4})$$

The nature of  $(-1)^{I+1/2}$  will be explained in the next section, which depicts the *Rotation Aligned Bands*. Moreover, the term  $a$  is called the *decoupling parameter* [17], and it can be determined from the first two experimental energy levels. Experimental data exhibiting rotational bands with  $K = 1/2$  and  $K \neq 1/2$  are shown for two odd- $A$  nuclei in Fig. C.2.



FIGURE C.2: Rotational bands in odd- $A$  nuclei with the  $K$  quantum number equal to  $K = 1/2$  (**left**) and  $K \neq 1/2$  (**right**).

## C.2 Rotation Aligned Bands

This situation is also called the *decoupling limit* [1] and it leads to the apparition of *decoupled bands*. Here the total angular momentum is more aligned with the axis of rotation, and its maximum projection is along this axis. This usually happens at high-spins, making the odd-particle's a.m. to tilt away from the symmetry axis and gradually align with the direction of rotation (via the Coriolis effect). As such, the coupling term  $H_{\text{coupl}}$  from  $H_{\text{rot}}$  is not neglected here:

$$H_{\text{rot}} = \frac{\hbar^2}{2I_{\perp}} (\mathbf{I}^2 + \mathbf{j}^2 - 2\mathbf{I} \cdot \mathbf{j}) . \quad (\text{C.5})$$

It is usually preferred to work with the raising and lowering operators:  $\mathbf{I}_{\pm} = \mathbf{I}_1 \pm i\mathbf{I}_2$  (and similarly for  $\mathbf{j}$ ), bringing  $H_{\text{rot}}$  to the following expression:

$$H_{\text{rot}} = \frac{\hbar^2}{2I_{\perp}} \hat{I}^2 + \frac{\hbar^2}{2I_{\perp}} \hat{j}^2 - \frac{\hbar^2}{I_{\perp}} K^2 + H_{\text{Coriolis}} , \quad (\text{C.6})$$

$$H_{\text{Coriolis}} = -\frac{\hbar^2}{2I_{\perp}} (\mathbf{I}_+ \mathbf{j}_- + \mathbf{I}_- \mathbf{j}_+) . \quad (\text{C.7})$$

The Coriolis term mixes bands differing in the  $K$  by one unit, effect that is negligible at high deformations and low spins, since the single-particle motion is tightly bound to the bulk nucleus. On the other hand, at very high rotations it becomes

significant. Consequently, the Coriolis effect most probably occurs in prolate nuclei for an ‘almost empty’  $j$ -shell and oblate nuclei for an ‘almost full’  $j$ -shell. When the single-particle angular momentum is oriented with the direction of rotation, the projection of  $\mathbf{j}$  can be denoted by  $j_1$  (keeping a consistency with Fig. 2.16). The spectrum of the decoupled bands will be:

$$E_{\text{rot}}(I) = \text{const.} + \frac{\hbar^2}{2\mathcal{I}_{\perp}}(I - j_1)(I - j_1 + 1) , \quad (\text{C.8})$$

where the coupling terms have been encapsulated in  $\text{const.}$ . This leads to a spin sequence  $I = j_1, j_1 + 2, j_1 + 4 \dots$ , which differs from the previous case via the constant  $2\hbar$  angular momentum difference of two consecutive levels.

In order to understand the terms  $(-1)^{I+1/2}$  from Eq. (C.4), it is required to describe the wave-function of the particle-core system. Indeed, using the specific quantum numbers  $I, K, M$  with their meaning explained in Fig. 2.16, the wave-function will be written as a combination of rotational (the Wigner- $\mathcal{D}_{MK}^I$  functions) and single-particle components [4, 175]:

$$\Psi_{MK}^I = |IMK\rangle = N [\phi_K \mathcal{D}_{MK}^I + (-)^{I+K} \phi_{-K} \mathcal{D}_{M-K}^I] , \quad (\text{C.9})$$

where  $N$  is the normalization constant  $N = \sqrt{\frac{2I+1}{16\pi^2}}$ . This linear combination of states with  $K$  and  $-K$  induces a degeneracy due to the invariance with respect to rotations by  $\pi$  around the rotational axis [1, 79]. The factor  $(-)^{I+K} \equiv \alpha$  is called the *signature* and it reflects whether a system is invariant or not to such an rotation. More precisely, the *signature quantum number* for a state  $I$  in an odd- $A$  nucleus is given as [176]:

$$\alpha_I = \frac{1}{2}(-)^{I-\frac{1}{2}} , \quad (\text{C.10})$$

which results in the favored states having  $\alpha_{\text{favored}} = \frac{1}{2}$  and the unfavored states having  $\alpha_{\text{unfavored}} = -\frac{1}{2}$ .

Depending on the signature, the nuclear states are split in two sets: one that follows  $I = K, K+2, K+4, \dots$  and  $I = K+1, K+3, K+5, \dots$ . This is the reason why for the decoupled bands, one can regard them as an ‘initial’ rotational band  $I, I+1, \dots$  that is ‘broken’ apart in two sequences: one that is favored and one that is unfavored (opposite signatures). An example is the odd- $A$  nucleus where the favored bands have spins  $I_{\text{favored}} = \frac{1}{2}, \frac{5}{2}, \frac{9}{2}, \dots$  and their unfavored *partner* bands

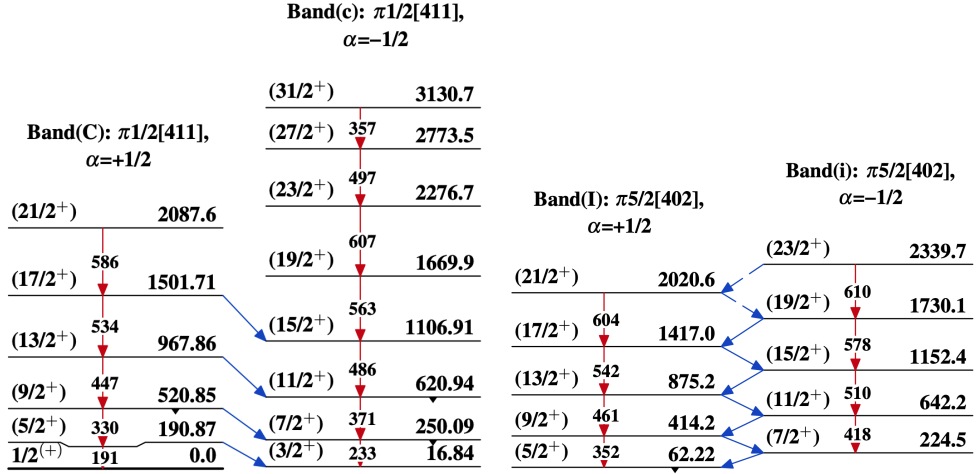


FIGURE C.3: Experimental level schemes for  $^{163}\text{Lu}$  showing pairs of signature partner bands. **Left pair:** the two bands are built on a proton with  $j = 1/2$  and positive parity. **Right pair:** sequences built on a proton with  $j = 5/2$  with the same parity. The Nilsson quantum numbers are defined for each band (recall Eq. (2.25)). Note the lower energies for the favored states. Interband transitions are marked with the blue arrows. The level schemes were taken from Ref. [92].

have spins  $I_{\text{unfavored}} = \frac{3}{2}, \frac{7}{2}, \frac{11}{2}, \dots$ , which are also known as *signature partners*. In fact, taking a closer look at the rotational bands shown in Fig. C.2, each consecutive level is a state with different signature, meaning that each ‘group’ of colors classifies into a set of favored (blue) and unfavored (magenta) states. The concept of signature partners will be crucial for a developed formalism that aims at describing rotational motion of highly deformed nuclei. This is treated throughout Chapters 4 and 5.

This divided set of partner bands has some characteristics that can be observed throughout experimental measurements. Firstly, the splitting of the two branches implies that the favored states will generally have lower excitation energy than their unfavored partners. This is also proved by the expression of the rotor energy given in Eq. (C.4), where the decoupling parameter will cause an upward (downward) shift in energy for states with  $I = 1/2, 5/2, 9/2, \dots$  ( $I = 3/2, 7/2, 11/2, \dots$ ) if  $a$  is positive (negative). The experimental data from Fig. C.3 shows how the favored partner lies lower with respect to its unfavored partner bands, each having the corresponding spin sequence  $\Delta I = 2$  for intraband states and  $\Delta I = 1$  for interband states. Such spectra are often met in the decay schemes for odd-mass nuclei where the rotational motion is governed by the core + particle coupling scheme.



# Appendix D

## Personal Contributions

Several papers were published in academic journals throughout the course of the doctoral studies, spanning from 2018 to 2022. Some of them are directly connected to the main topic of the thesis and others were published *in parallel*, while working on other projects outside the topic of triaxial nuclei. As mentioned in the general conclusions presented in Chapter 7, six scholarly articles are presented in this work and all of them were published in ISI indexed academic journals. Presentations and posters were also developed and shared at various conferences nation-wide or internationally.

### D.1 Published Papers

Nomenclature:

- **in-scope:** papers presented within this thesis, which were published between 2018-2022. Their results consists of original contribution on the field of Nuclear Structure.
- **out-of-scope:** papers that were not presented in this thesis, which were published between 2018-2022.

**D.1.1 ISI Indexed Papers Published In-Scope****D.1.2 ISI Indexed Papers Published Out-of-Scope****D.1.3 Non-ISI Papers Published Out-of-Scope****D.2 Conferences****D.2.1 International****D.2.2 National**

# List of Figures

2.1	Graphical representation of the first few modes of excitations of the nuclear surface. The figure is taken from Ref. [10]. . . . .	9
2.2	Graphical representation with the stretching of the nuclear axes $\delta R_k$ , $k = 1, 2, 3$ , corresponding to the increase in axis lengths along the $x$ , $y$ , and $z$ directions. The representation used an arbitrary value $\beta_2 = 0.3$ . Figure was reproduced according to the calculations done in Ref. [10]. . . . .	13
2.3	Beta-gamma plane divided into six regions. The part delimited from $\gamma = 0^\circ$ to $\gamma = 60^\circ$ can be considered as the representative one, while others can be reproduced from this interval. . . . .	14
2.4	Geometrical interpretation of the Nilsson's asymptotic quantum numbers. This figure is inspired from Ref. [19] . . . . .	20
2.5	A simple sketch showing the single-particle orbits for the $j = 7/2$ nucleonic state, along the symmetry axis for a <i>prolate</i> deformation. The actual projections are $\Omega_1 = \frac{1}{2}$ , $\Omega_2 = \frac{3}{2}$ , $\Omega_3 = \frac{5}{2}$ , and $\Omega_4 = \frac{7}{2}$ . The figure was inspired from Ref. [20]. . . . .	21
2.6	A simple sketch showing the single-particle orbits for the $j = 7/2$ nucleonic state, along the symmetry axis for an <i>oblate</i> deformation. The actual projections are $\Omega_1 = \frac{1}{2}$ , $\Omega_2 = \frac{3}{2}$ , $\Omega_3 = \frac{5}{2}$ , and $\Omega_4 = \frac{7}{2}$ . The figure was inspired from Ref. [20]. . . . .	22
2.7	The effect of deformation for the particle state $f_{7/2}$ . It can be seen that $\Omega_1$ component lies lowest in energy for the oblate deformation and $\Omega_4$ component lies the lowest in energy for an oblate deformation. . . . .	23
2.8	A Nilsson diagram for protons or neutrons, with $Z$ or $N \leq 50$ . Picture taken from Ref. [22]. . . . .	24
2.9	A Nilsson diagram for neutrons, with $82 \leq N \leq 126$ . Picture taken from Ref. [22]. . . . .	25
2.10	The vibration of a nucleus whose equilibrium shape is a spheroid, with nuclear radius $R_0$ ( <i>average nuclear radius</i> ) and the nuclear radius $R$ at a different moment in time. The equilibrium shape is represented by the red color, while the surface vibration is represented by the blue color. The oscillations are depicted through the double arrows. . . . .	27
2.11	Comparison between the rigid-like and irrotational-like MOI defined in Eq. (2.30), which are typical for a rigid rotator or an irrotational motion of a fluid. The deformation parameter $\beta$ is fixed $\beta = 0.3$ . . . . .	29

- 2.12 Illustration of vibrational bands built as excitations of multiple phonons on a ground state. The left side reflects an ideal harmonic vibrator, with the degenerate spin states indicated for each level. Right side shows non-degenerate vibrational levels that exist in nuclei. Keep in mind that each phonon level is built as multiple excitations of a *quadrupole phonon*. . . . . 30
- 2.13 Vibrational bands in even- $A$  nuclei. **Left:** The experimental energy levels for  $^{120}\text{Te}$ . The triplet states that correspond to  $\lambda = 2$  can be seen, together with the quintuplet formed by adding three phonons to the  $0^+$  ground state. Experimental data are taken from [32]. **Middle:** The experimental data for  $^{60}\text{Ni}$ . For simplicity, only the first two phonon states are represented. Experimental data were taken from Ref. [33]. **Right:** The experimental data for a vibrational-like structure in  $^{44}\text{Ca}$  [34]. Note the highest energy level coming from the vibrational motion corresponding to an *octupole* mode ( $\lambda = 3$ ). . . . . 31
- 2.14 The experimental data of the vibrational states in  $^{63}\text{Cu}$  [35]. The  $2^+$  phonon state in  $^{62}\text{Ni}$  is also shown. The experimental data for  $^{62}\text{Ni}$  are taken from Ref. [36]. The blue rectangle tries to emphasize that the quadruplet in  $^{63}\text{Cu}$  is formed by the coupling of the odd proton to the  $2^+$  vibrational state from the neighboring nucleus. . . . . 32
- 2.15 The  $\beta$  and  $\gamma$  vibrations occurring in nuclei. The initial nucleus in this example is of prolate type. Each mode of vibration is visualized from the side-view and top-view, respectively. This figure was inspired from Ref. [31]. . . . . 33
- 2.16 The coupling of the collective angular momentum with the angular momentum of a single-particle for an axially deformed nucleus that is rotating about an axis perpendicular to the deformation axis. . . . . 34
- 2.17 Experimental data showing the rotational bands in even-even nuclei. Note the spacing between the states that increases with  $I$  via the rule from Eq. (2.33). Experimental data are taken from Refs. [40, 41]. . . . . 35
- 2.18 The energy spectrum specific to the Collective Model with *Rotations + Vibration*. Each quantum number is also shown at the bottom of the bands. This figure is taken from Ref. [31]. . . . . 37
- 2.19 The experimental ratio  $R_{4+/2+}$  in even- $Z$  and even- $N$  nuclei. Each line is connecting sequences of isotopes. Note the two important values for  $R_{4+/2+}$ , namely 2 and 3.33 given for a perfect vibrator and a pure rotator, respectively. Text with magenta color marks the magic numbers for  $Z$  or  $N$ . This plot was inspired from Ref. [15]. . . . . 38
- 2.20 The moment of inertia as function of rotational frequencies for three even-even nuclei. **Left:** The MOI for  $^{162,164}\text{Hf}$  nuclei, with their corresponding rotational ground-state bands. **Right:** The MOI for the first two rotational bands in  $^{166}\text{Hf}$ . Experimental data for these two nuclei are taken from Ahmad et al. [47]. . . . . 41

2.21 <b>Left:</b> The MOI for $^{158}\text{Er}$ nucleus, with the ground-state band $K^\pi = 0^+$ and the $\beta$ -vibrational band with the same quantum numbers. Experimental data are taken from [40]. <b>Right:</b> The MOI for $^{160}\text{Yb}$ compared with $^{162}\text{Er}$ . Experimental data are taken from [49] ( $A = 158$ ) and [50] ( $A = 162$ ). . . . . .	41
2.22 The quadrupole deformation parameter $\beta_2$ as a function of the mass number $A$ for a few isotopes in the rare-earth region. These values were determined from the experimental transition probabilities $0^+ \rightarrow 2^+$ . The figure is reproduced from Ref. [15]. . . . .	43
2.23 The average flattened (oblate) density distribution generated by the rotation of a prolate nucleus. As the ‘initial’ prolate nucleus with its nuclear density (represented by the gray ellipse with dashed borders) being distributed along the deformed axis exhibits rotation, the rotated shape will generate an averaged oblate disk along the rotational axis (represented by the blue). This is why the observed quadrupole moment $Q$ will have a negative sign if $Q_0 > 0$ . . . . .	44
2.24 The measured quadrupole moments $Q$ as per Eq. (2.54), given in units of $ZR^2$ , as function of the odd proton ( $Z$ ) and neutron ( $N$ ) numbers, respectively (arrows signify the magic numbers). Experimental data are taken from Ref. [17]. . . . .	46
2.25 The measured quadrupole moment for the first excited $2^+$ states in even-even nuclei. The expression of $Q$ was defined in Eq. (2.51). The lines between data-points connect the isotope sequences. The figure was reproduced with the experimental data taken from [20]. . . . .	46
2.26 The quadrupole potential $\hat{H}_{\text{int}}^{\text{quad}}$ as defined in Eq. (2.62), represented as a function of the angular coordinates $\theta$ and $\varphi$ . Calculations were done with fixed parameters $\beta_2$ , $\gamma$ , and for $A = 163$ . . . . .	51
2.27 The quadrupole potential $\hat{H}_{\text{int}}^{\text{quad}}$ as defined in Eq. (2.62). Calculations were done with fixed parameters $\beta_2$ , $\gamma$ , and $A = 163$ . . . . .	52
2.28 The evolution of the diagonal matrix elements $h_{jk}$ defined in Eqs. (2.68) - (2.69) w.r.t. the quadrupole parameter $\beta_2$ , for one proton on a deformed $j$ -shell and a fixed triaxiality parameter $\gamma$ . See text for details. . . . .	53
2.29 The evolution of the diagonal matrix elements $h_{jk}$ defined in Eqs. (2.68) - (2.69) w.r.t. the triaxiality parameter $\gamma$ for one proton on a deformed $j$ -shell and a fixed deformation parameter $\beta_2$ . See text for details. . . . .	53

- 2.30 **Left:** Potential energy surface for  $^{174}\text{Hf}$ , evaluated at a constant rotational frequency. Positive parity and signature  $\alpha = 0$  were considered in the evaluation. Four minima that could be attributed to known configurations are identified which are marked with red colored dots (normal deformation) and blue dots (strong deformation). This figure was adapted from Ref. [63]. **Right:** PES for some even-even nuclei. Note the rather shallow triaxial minima for all nuclei, and the  $\gamma$ -soft nature of all the nuclei except for  $^{106}\text{Pd}$ , whose minimum is achieved at a null triaxiality parameter. This figure was taken from Ref. [64]. . . . . 55
- 2.31 **Left:** PES for  $^{135}\text{Pr}$ . The figure is taken from the work of Frauendorf et al. [9]. **Right:** PES for the odd- $A$  isotope  $^{163}\text{Lu}$  evaluated at a fixed spin  $I = 53/2$  with positive parity and positive signature. The red dot corresponds to a global minimum for normal deformed structure, while the blue diamonds represent two additional minima which correspond to strong deformation. This figure is adapted from Ref. [65]. . . . . 56
- 2.32 The energy spectra for the odd-odd  $^{136}\text{Pm}$  isotope, in which the chiral doublet built on the configuration  $\pi h_{11/2} \otimes \nu h_{11/2}$  appears. Experimental data is from Ref. [91] and the level scheme is adapted from Ref. [92]. . . . . 59
- 2.33 The energy spectra for the odd-odd  $^{132}\text{La}$  isotope, in which the chiral doublet built on the configuration  $\pi h_{11/2} \otimes \nu h_{11/2}$  appears. Experimental data is taken from Refs. [93, 94]. . . . . 60
- 2.34 Left- and right-handed chiral systems for a triaxial odd-odd nucleus, indicating the mutually perpendicular angular momentum vectors. The two valence nucleons are colored with blue (proton) and magenta (neutron). These figures were inspired from [80]. Considering the discussion regarding alignments, the proton a.m.  $\mathbf{j}_\pi$  is aligned with the  $s$ -axis, the neutron a.m.  $\mathbf{j}_\nu$  with the  $l$ -axis, and the even-even core a.m.  $\mathbf{R}$  with the  $m$ -axis of the ellipsoid. The alignments for the core and the particles are described in text. . . . . 61
- 3.1 **Left:** A typical wobbling structure for even-even nuclei. The yrast band contains even angular momenta since the band has signature  $\alpha = 0$ , while the first excited band has odd spins and  $\alpha = 1$ . **Right:** The increase of tilting angle between the rotational axis (the 3-axis in this case) and the total angular momentum  $\mathbf{I}$ . With each wobbling phonon number, the total angular momentum generates a ‘stronger’ precessional motion (illustrated by the colored ellipses). . . . . 67
- 3.2 The kinetic and potential terms from Eq. (3.15) are graphically represented as function of  $I_1$  and  $I_2$ , respectively. The a.m. components vary from 0 to  $10\hbar$ . The MOI for each curve are as follows:  $\mathcal{I}_1 : \mathcal{I}_2 : \mathcal{I}_3 = 10 : 25 : 20$  (red),  $\mathcal{I}_1 : \mathcal{I}_2 : \mathcal{I}_3 = 10 : 25 : 40$  (blue),  $\mathcal{I}_1 : \mathcal{I}_2 : \mathcal{I}_3 = 10 : 25 : 60$  (black),  $\mathcal{I}_1 : \mathcal{I}_2 : \mathcal{I}_3 = 30 : 25 : 10$  (magenta). The unit for MOI is  $\hbar^2\text{MeV}^{-1}$ . . . . . 67

3.3	<b>Left:</b> The energy spectrum for an even-even triaxial nucleus, with the main rotation around the 3-axis, according to Eq. (3.14). <b>Right:</b> The wobbling frequency (as per Eq. (3.11)) plotted together with the linear terms $t_1$ and $t_2$ (Eq. (3.7)), which are used to express $\hbar\omega_w$ . The unit for $\mathcal{I}_k$ , $k = 1, 2, 3$ is $\hbar^2 \text{ MeV}^{-1}$ .	68
3.4	The geometrical representation of the first and second component of the total angular momentum $\mathbf{I}$ as functions of the polar angles, according to Eq. (3.18).	69
3.5	Comparison between the experimental and theoretical excitation energies (Eq. (3.25)) for the two wobbling bands of $^{130}\text{Ba}$ (B1 and B2). Experimental data are taken from Ref. [98]. The theoretical data was obtained by fitting Eq. (3.14) as described in text, with the parameters defined in Table 3.1. Note that the band-head $I^\pi = 10^+$ state from B1 is missing from the spectrum, since it was subtracted from each level.	72
3.6	<b>Left:</b> The wobbling energies for $^{130}\text{Ba}$ calculated with Eq. (3.24) (see text for explanation on the green region). For the first state of B2, the energy was determined as $E_{\text{wob}}(11^+) = E_{\text{B2}}(11^+) - \frac{1}{2}E_{\text{B1}}(12^+)$ since the band-head state of B1 is zero (as per the definition of excitation energy given in Eq. (3.25)). <b>Right:</b> The rotational frequencies for the two wobbling bands of $^{130}\text{Ba}$ , calculated using Eq. (2.44).	73
3.7	The interband quadrupole transition probabilities (Eq. (3.21)) from the first excited wobbling band (B2) to the yrast band (B1) for $^{130}\text{Ba}$ .	75
3.8	A schematic representation of a <i>simple wobbler</i> , where the total angular momentum is doing a precessional motion about the axis with the largest MOI. In this particular sketch, the axis with the largest MOI is denoted by $m$ for intermediate/medium. The long and short axes are labelled $l$ and $s$ , respectively. The small-amplitude oscillations of $\mathbf{R}_{\mathcal{C}}$ are depicted with the (black) encircled sine wave. Notation of the angular momentum is consistent with Table 3.4. This figure was adapted from Ref. [103] and inspired from Ref. [104].	77
3.9	The workflow of a quasi-particle with particle character $\mathcal{Q}_p$ in its coupling with a triaxial rotor $\mathcal{C}$ . Each of the five ‘steps’ represents a characteristic involved in the wobbling motion, as described in text. Namely, for $\mathcal{Q}_p$ coming from the bottom of a $j$ -shell and coupling with the $s$ -axis of the even-even core $\mathcal{C}$ (1) will maximize the density overlap (2), which will minimize their interaction (3), minimizing the total energy (4), and finally stabilizing the triaxial structure (5) to a TW. The long $l$ -axis has been ignored within the drawings. In the bottom-most picture, the precessional cone of the total a.m. is shown, oscillating along the $s$ -axis.	80

- 3.10 The workflow of a quasi-particle with hole character  $\mathcal{Q}_h$  in its coupling with a triaxial rotor  $\mathcal{C}$ . Each of the five ‘steps’ represents a characteristic involved in the wobbling motion, as described in text. Namely, for  $\mathcal{Q}_h$  coming from the top of a  $j$ -shell and coupling with the  $l$ -axis of the even-even core  $\mathcal{C}$  (1) will minimize the density overlap (2), which will minimize their interaction (3), minimizing the total energy (4), and finally stabilizing the triaxial structure (5) to a TW. The short  $s$ -axis has been ignored within the drawings. In the bottom-most picture, the precessional cone of the total a.m. is shown, oscillating along the  $l$ -axis. . . . . 81
- 3.11 The workflow of a particle  $\mathcal{Q}_p$  in its coupling with a triaxial rotor  $\mathcal{C}$  within LW mode. Each of the five ‘steps’ represents a characteristic involved in the wobbling motion, as described in text. Namely, for  $\mathcal{Q}_p$  coming from the middle of a  $j$ -shell and coupling with the  $m$ -axis of the even-even core  $\mathcal{C}$  (1) will maximize the density overlap (2), which will minimize their interaction (3), minimizing the total energy (4), and finally stabilizing the triaxial structure (5). In the bottom-most picture, the precessional cone of the total a.m. is shown, oscillating along the  $m$ -axis. . . . . 82
- 3.12 The reduced inertia parameter defined in Eq. (3.29) as a function of spin. **Left:** The angular momentum of the quasi-particle is fixed (i.e.,  $j = 13/2$ ) and different values for  $A_3$  are attributed. The vertical grid-line corresponds to the spin value at which  $\mathcal{A}_3$  becomes positive. The horizontal dashed lines correspond to the numerical values of  $A_3$  indicated in the legend. **Right:** The value of  $A_3$  is fixed and different values for  $j$  are considered. . . . . 83
- 3.13 The wobbling frequency for an odd- $A$  nucleus with  $j = 13/2$ . **Left:** The *longitudinal wobbler* case with two sets of MOI, where only  $\mathcal{I}_2$  changes. **Right:** The *transverse wobbler* case with two sets of MOI, where only  $\mathcal{I}_2$  is different. Note the vertical grid-lines in the right inset that signify the critical angular momentum where the wobbling frequency reaches zero. The maximum value reached in the TW regime is given by Eq. (3.36). The unit for MOI is  $\hbar^2 \text{MeV}^{-1}$ . 85
- 3.14 Geometrical representation with the alignment scheme for a longitudinal wobbler and a transverse wobbler. The a.m. vectors for the quasi-particle, the core, and the total system are represented by  $\mathbf{j}_{\mathcal{Q}}$ ,  $\mathbf{R}_{\mathcal{C}}$ , and  $\mathbf{I}$ , respectively. Note that the precessional motion with oscillator-like behavior of  $\mathbf{I}$  is illustrated with the encircled sine wave (black color). The resulting motion of the total a.m. will consist in a precessional cone that is properly depicted in Figs. 3.9-3.11. . . . . 86
- 3.15 The experimental wobbling energy, defined through the Eq. (3.24), for nuclei within the  $A \approx 100$  mass region. . . . . 87

3.16 The experimental wobbling energy, defined through the Eq. (3.24), for nuclei within the $A \approx 130$ mass region. For $^{134}\text{Ce}$ , the two abbreviations denote the bands with lower deformation (L.D.) and higher deformation (H.D.), respectively. For $^{136}\text{Nd}$ , the two configurations are represented by $2-Q_h$ for the neutron holes and $2-Q_p$ for the protons that couple with the core. See text for more details. . . . .	90
3.17 The experimental wobbling energy, defined through the Eq. (3.24), for nuclei within the $A \approx 160$ mass region. . . . .	91
3.18 The experimental wobbling energy, defined through the Eq. (3.24), for nuclei within the $A \approx 180$ mass region. Data are taken from references cited in text for each isotope. Note that for $^{183}\text{Au}$ , there are two configurations which cause wobbling motion, namely, the protons $\pi i_{13/2}$ (positive parity) and $\pi h_{9/2}$ (negative parity). Nandi et al. [128] suspect that the behavior of the former band is justified by a transverse-like wobbling frequency which increases up to a certain spin before it starts to decrease. This is illustrated via the small inset inside the first figure, where the wobbling frequencies for a TW nucleus are sketched (according to Eq. (3.32) and Fig. 3.13). . . . .	93
3.19 The angular momentum evolution with respect to the (experimental) rotational frequency $\omega_{\text{rot}}$ for $^{133}\text{La}$ ( <b>left</b> ) and $^{135}\text{Pr}$ ( <b>right</b> ). The backbending region for the latter nucleus is illustrated within the colored sector. Since the MOI of the $s$ -axis is smaller, more and more collective a.m. will be added to this axis, causing a decrease in the wobbling frequency (TW). The dotted magenta line represents the angular momentum value for the odd proton. . . . .	95
3.20 Example of a wobbling nucleus that appears in the chart shown in Fig. 3.21. This particular case is for $^{187}\text{Au}$ . Experimental $E_{\text{wob}}$ are calculated according to Eq. (3.24). . . . .	96
3.21 Unified chart showing all the currently known wobblers. See Fig. 3.20 for legend. <i>Strong deformation</i> is marked with red color for $\beta_2$ . . . . .	97
4.1 The mechanism of action for the phonon operator introduced in Ref. [39]. The operator is creating excited states with a given angular momentum from the ground state bands. The angular momentum of the core is defined as $\mathbf{R}_{\mathcal{Q}}$ , while the quasi-particle a.m. is denoted by $\mathbf{j}_{\mathcal{Q}}$ . The ground-state band emerges from the coupling of these two, giving rise to a series of spins $I_i = R_i + j$ (where $R = \{\dots, R_i - 2, R_i, R_i + 2 \dots\}$ ). Acting with $\Gamma_1^\dagger$ $n$ -times on any of these states, an excited level in the $n_w = n$ wobbling band is obtained. In this example a rotational core having even spin states has been chosen, however the same principle applies if the spin states are odd. . . . .	101
4.2 The evolution of $\mathcal{A}_\varphi$ with respect to the generalized coordinate $\varphi$ , at different MOI orderings. The values 1, 3, 7 were chosen and they are interchanged between the three inertia factors. This figure is equivalent for $\mathcal{A}_\psi$ . . . . .	108

- 4.3 The mixed canonical factor  $\mathcal{A}_{\varphi\psi}$  from Eq. (4.16), as function of the coordinates  $\varphi$  and  $\psi$ . Both coordinates vary within the interval  $[0, \pi]$ . All insets share common labelling for the OX and OY axes. . . . . 109
- 4.4 The canonical factor  $\mathcal{A}_\gamma$  from Eq. (4.16), as a function of the coordinates  $(f, \psi)$  corresponding to the single-particle  $\mathcal{Q}$ . The  $j$ -shell has been fixed to  $j = 13/2$ . In terms of the two variables,  $f$  varies within  $[0, 2j]$  while  $\psi$  is inside the interval  $[0, \pi]$ . All insets share a common labelling for the OX and OY axes. . . . . 110
- 4.5 **Left:** Contour lines showing the values of  $\mathcal{I}_0$  and  $V$  at which both lhs from Eq. (4.26) vanish (denoted here by  $f_1$  and  $f_2$ , respectively). **Right:** The contour  $F = 0$  (lhs of Eq. (4.28)) as function of the parameters  $\mathcal{I}_0$  and  $V$ . **Both:** Darker (lighter) color corresponds to negative (positive) values. The calculations were done for fixed values of  $I, j, \gamma, A_1, A_2, A_3$ . Units are  $\hbar^2 \text{MeV}^{-1}$  for  $\mathcal{I}_0$  and MeV for  $V$ . . . . . 114
- 4.6 **Left:** The oscillator frequencies  $\omega_1$  and  $\omega_2$  from Eq. 4.35. For this particular example,  $j = 13/2$  and the ordering  $A_3 > A_2 > A_1$  is chosen, according to the conditions of existence for  $\omega_1$  and  $\omega_2$ . The intersection point between  $\omega_1$  and  $\omega_2$  is marked by the red vertical line around  $I \approx 24\hbar$ . See text for details on the two colored regions split by the black vertical line. **Right:** The oscillator frequency  $\omega_2$  from Eq. (4.35) within the  $(\gamma, V)$  plane. The value of  $\gamma = 25^\circ$  is marked with the dashed vertical line just to guide the eye. Each contour line represents an energy difference of about 0.20 MeV. . . . . 122
- 4.7 The canonicity factors from Eq. (4.42) are graphically represented as function of spin  $I$  for arbitrary MOI,  $V$  and  $\gamma$ . The single-particle angular momentum is set to  $j = 13/2$ . For the calculations, the two  $A_k$  orderings kept the same numerical values and only  $A_2$  and  $A_3$  were interchanged. The regions where  $I \leq j$  (hatched area) and  $I \geq j$  (green area) that are split by the vertical dashed line are pointed out as well. . . . . 123
- 4.8 The canonicity factor  $k_2$  from Eq. (4.42) in the  $(\gamma, V)$  plane, evaluated at fixed inertia factors and angular momenta. The value of  $\gamma = 25^\circ$  is marked by the vertical dashed line just to guide the eye. 123
- 4.9 The overall workflow for solving the minimization of the  $\chi^2$ -function (Eq. (4.60)). Initially, the absolute energy of the band-head  $I_b$  (Eq. (4.61) - red color) is subtracted from every state  $I$  (Eq. (4.30) - black color) in order to obtain the excitation energy (Eq. (4.62) - blue color). This is applied to the entire spectrum. Next, the inputs from Tables 4.2 - 4.6 are used in the minimization of  $\chi^2$ . The fitting function returns the set of parameters  $\mathcal{P}_{\text{fit}}$  (Eq. (4.59)), finalizing thus the numerical procedure. . . . . 133
- 4.10 The fitted MOI (see Table 4.7) plotted as a function of the mass number  $A$ . The unfilled symbols represent the band TSD4 from  $^{163}\text{Lu}$ . This figure was taken as is from Ref. [136]. . . . . 134

4.11 Fitted values for the single particle potential strength $V$ as function of the mass number $A$ . The separate procedure for TSD4 in $^{163}\text{Lu}$ is marked by the blue dot. For an illustrative purpose, the average value across the entire mass region is also represented by the dashed horizontal line. The actual numerical values of $V$ are specified in Table 4.7. . . . .	136
4.12 The experimental and theoretical excitation energies provided by Eq. (4.62) for the two wobbling bands in $^{161}\text{Lu}$ . Experimental data are taken from Ref [123]. The figures are taken from Ref. [136]. . . . .	136
4.13 The experimental and theoretical excitation energies provided by Eq. (4.62) for the two wobbling bands in $^{163}\text{Lu}$ . Experimental data are taken from Ref [145]. The figures are taken from Ref. [136]. . . . .	137
4.14 The experimental and theoretical excitation energies provided by Eq. (4.62) for the three wobbling bands in $^{165}\text{Lu}$ . Experimental data are taken from Ref [124]. The figures are taken from Ref. [136].	137
4.15 The experimental and theoretical excitation energies provided by Eq. (4.62) for the three wobbling bands in $^{167}\text{Lu}$ . Experimental data are taken from Ref [125]. The figures are taken from Ref. [136].	138
4.16 The theoretical wobbling energies as per Eq. (3.24) compared with the experimental ones for $^{163}\text{Lu}$ ( <b>left</b> ) and $^{165}\text{Lu}$ ( <b>right</b> ). Note that the $n = 1$ and $n = 0$ bands are TSD3 and TSD2 within the current description. The figures are taken from Ref. [136]. . . . .	139
4.17 The theoretical and experimental alignments for $^{163}\text{Lu}$ , according to Eq. (4.63), as function of the rotational frequency (Eqs. (2.42) - (2.44)). The figures are taken from Ref. [136]. . . . .	140
4.18 The theoretical and experimental alignments for $^{165}\text{Lu}$ , according to Eq. (4.63), as function of the rotational frequency (Eqs. (2.42) - (2.44)). The figures are taken from Ref. [136]. . . . .	140
4.19 The theoretical and experimental alignments for $^{161}\text{Lu}$ ( <b>left</b> ) and $^{167}\text{Lu}$ ( <b>right</b> ), according to Eq. (4.63), as function of the rotational frequency (Eqs. (2.42) - (2.44)). The figures are taken from Ref. [136]. . . . .	141
4.20 The excitation energy relative to a rotor reference $E_{\text{ref}} = 0.0075I(I+1)$ as function of the total angular momentum, for $^{161}\text{Lu}$ . The figures are taken from Ref. [136]. . . . .	142
4.21 Comparison between theoretical and experimental excitation energy relative to a rotor reference $E_{\text{ref}} = 0.0075I(I+1)$ for $^{165}\text{Lu}$ , as function of the total angular momentum. The zero- and one-wobbling-phonon bands TSD2-3 are plotted on the same figure. The figures are taken from Ref. [136]. . . . .	142
4.22 Comparison between theoretical and experimental excitation energy relative to a rotor reference $E_{\text{ref}} = 0.0075I(I+1)$ for $^{167}\text{Lu}$ , as function of the total angular momentum. The figures are taken from Ref. [136]. . . . .	142

- 4.23 The excitation energy relative to a rotor reference  $E_{\text{ref}} = 0.0075I(I+1)$  as function of the total angular momentum, for  $^{163}\text{Lu}$ . The figures are taken from Ref. [136]. . . . . 143
- 4.24 The theoretical dynamic moment of inertia defined in Eq. (2.47) for the isotopes  $^{161}\text{Lu}$  (**left**) and  $^{167}\text{Lu}$  (**right**) is compared with the experimental data. The rotational frequency is defined as  $\hbar\omega_I = dE/dI = E_\gamma(I \rightarrow I-2)/2$ . The figures are taken from Ref. [136]. . . . . 144
- 4.25 The dynamic moment of inertia defined in Eq. (2.47) for  $^{163}\text{Lu}$ . The rotational frequency is defined as  $\hbar\omega_I = dE/dI = E_\gamma(I \rightarrow I-2)/2$ . The figures are taken from Ref. [136]. . . . . 145
- 4.26 The dynamic moment of inertia defined in Eq. (2.47) for  $^{165}\text{Lu}$  showing the band TSD1 (**left**) and the bands TSD2-3 (**right**). The rotational frequency is defined as  $\hbar\omega_I = dE/dI = E_\gamma(I \rightarrow I-2)/2$ . The figures are taken from Ref. [136]. . . . . 145
- 4.27 Schematic representation with the electric quadrupole and magnetic dipole transitions occurring in wobbling spectra of nuclei. The *intraband* values ( $E_{2\text{in}}$ ; blue) represent the transitions between an initial state  $I_i$  and a final state  $I_f$  belonging to the same band, which are characterized by  $\Delta I = I_i - I_f = 2\hbar$ . On the other hand, the *interband* values ( $E_{2\text{out}}$ ; red) take place between states belonging to two contiguous bands, and they are characterized by  $\Delta I = 1\hbar$ . Lastly, the magnetic transitions are marked by the green  $M1$  arrow. . . . . 147
- 4.28 The calculated quadrupole moments  $Q_0$  and  $Q_2$  from 4.65. The unit for  $Q$  is  $e \cdot b$ . See text for details on their numerical determination. Figure is taken as is from Ref. [136]. . . . . 151
- 4.29 The static quadrupole moment from Eq. (4.76) graphically represented as a function of total spin  $I$  for the first band in  $^{163}\text{Lu}$ . **Left:** Calculations are done with  $K = 1/2$ . **Right:** Calculations are done with  $K = I$ . The magenta lines represent the limits  $-\langle Q_I \rangle/2$  (left inset) and  $\langle Q_I \rangle$  (right inset). . . . . 154
- 4.30 The static quadrupole moment from Eq. (4.76) graphically represented as a function of total spin  $I$  for the band TSD2 in  $^{163}\text{Lu}$ . **Left:** Calculations are done with  $K = 1/2$ . **Right:** Calculations are done with  $K = I$ . The magenta lines represent the limits  $-\langle Q_I \rangle/2$  (left inset) and  $\langle Q_I \rangle$  (right inset). . . . . 156
- 4.31 The branching ratio for E2 transitions in  $^{163}\text{Lu}$  (**left**) and  $^{165}\text{Lu}$  (**right**). The spin states belong to TSD2 in both isotopes. Experimental data are taken from Refs. [58, 156, 157] ( $A = 163$ ) and Ref. [124] ( $A = 165$ ). . . . . 158
- 4.32 **Left:** The calculated branching ratio for E2 transitions in  $^{163}\text{Lu}$  are compared with the experimental data of Ref. [125]. **Right:** The ratio  $B(M1)/B(E2)_{\text{in}}$  measured in units of  $\mu_N^2/(e^2 b^2)$  for a few states connecting TSD2 and TSD1 from  $^{163}\text{Lu}$ . Experimental data are taken from Ref. [145]. . . . . 159

4.33	The static magnetic moment $\mu_I$ for $^{163}\text{Lu}$ , calculated according to Eq. (4.82). The value of $K$ was fixed to $K = I - 1$ for every $I$ state belonging to TSD2 decaying to $I - 1 \in \text{TSD1}$ . . . . .	160
5.1	The excitation energies (Eq. (4.62)) of $^{163}\text{Lu}$ for the bands TSD1 and TSD2, obtained in the $\mathbf{W}_2$ formalism using Eq. (5.9). Calculations were done with the parameters presented in Table 5.2. . . . .	173
5.2	The excitation energies (Eq. (4.62)) of $^{163}\text{Lu}$ for the bands TSD3 and TSD4, obtained in the $\mathbf{W}_2$ formalism using Eq. (5.9). Calculations were done with the parameters presented in Table 5.2. . . . .	174
5.3	Wobbling energy for $^{163}\text{Lu}$ obtained in the $\mathbf{W}_2$ formalism and compared with the experimental results. The theoretical values were calculated with Eq. (3.24). . . . .	175
5.4	The wobbling frequencies, i.e., the two solutions of Eq. (3.13) as a function of the total spin. Calculations are made with the parameter set provided in Table 5.2. . . . .	175
5.5	Comparison between the MOI obtained in the approach $\mathbf{W}_2$ (current chapter) and $\mathbf{W}_1$ (as per Chapter 4). Note that there was a separate minimization of the $\chi^2$ -function for TSD4 within the previous formalism. The numerical values for $\mathcal{I}_{1,2,3}$ are taken from Tables 4.7 and 5.2. . . . .	177
5.6	The rigid ( <b>left</b> ) and hydrodynamical ( <b>right</b> ) MOI as function of $\gamma$ . The scaling factors for both types of MOI are determined by fixing $\mathcal{I}_1^{\text{rig}}$ and $\mathcal{I}_1^{\text{irr}}$ to the fitted $\mathcal{I}_1$ with the deformation parameters $(\beta, \gamma) = (0.38, 22^\circ)$ . The black, red, and blue points represented the numerical values of $\mathcal{I}_1$ , $\mathcal{I}_2$ , and $\mathcal{I}_3$ from Table 5.2, respectively. The value $\gamma = 22^\circ$ from the fit is marked with the dashed magenta line just to guide the eye. . . . .	177
5.7	<b>Right:</b> The term $T_{\text{core}}$ from Eq. (5.12) as function of the angular momentum $I$ at different orderings for $A_k$ (the arbitrary values 0.05, 0.025, 0.011 $\hbar^{-2}\text{MeV}$ were interchanged between each factor). The magenta line is for the inertia factors provided by the fit. <b>Left:</b> The term $T_{\text{sp}}$ from Eq. (5.12), evaluated for three different single-particle angular momenta using the potential strength and the three MOI from Table 5.2. . . . .	180
5.8	The classical energy function (Eq. (5.11)) as a function of the polar coordinates for two states from TSD1 (i.e., $I = 25/2^+$ and $53/2^+$ ), evaluated using the fit parameters from Table 5.2. The minimum points of $\mathcal{H}$ are marked by the red dots. See the text for an explanation of the dashed contour styling. . . . .	181
5.9	The classical energy function (Eq. (5.11)) as a function of the polar coordinates for two states from TSD2 (i.e., $I = 31/2^+$ and $91/2^+$ ), evaluated using the fit parameters from Table 5.2. The minimum points of $\mathcal{H}$ are marked by the red dots. See the text for an explanation of the dashed contour styling. . . . .	181

- 5.10 The classical energy function (Eq. (5.11)) as a function of the polar coordinates for two states from TSD3 (i.e.,  $I = 33/2^+$  and  $57/2^+$ ), evaluated using the fit parameters from Table 5.2. The minimum points of  $\mathcal{H}$  are marked by the red dots. See the text for an explanation of the dashed contour styling. . . . . 182
- 5.11 The classical energy function (Eq. (5.11)) as a function of the polar coordinates for two states from TSD4 (i.e.,  $I = 47/2^-$  and  $83/2^-$ ), evaluated using the fit parameters from Table 5.2. The minimum points of  $\mathcal{H}$  are marked by the red dots. See the text for an explanation of the dashed contour styling. . . . . 182
- 5.12 The CEF from Eq. (5.11) is evaluated in one of its minimum points ( $m_1 = (\pi/2, 0)$  given in Table 5.3) and plotted with respect to the angular momentum. The calculations are done using the fitting parameters from Table 5.2. . . . . 183
- 5.13 The evolution of  $\mathcal{H}$  for different values of  $I$ , obtained by keeping one polar coordinate fixed and letting the other one vary in its normal interval. **Left:** The coordinate  $\theta$  is fixed to  $\theta = \pi/2$  and  $\varphi = [0, 2\pi]$ . **Right:** The coordinate  $\varphi$  is fixed to  $\varphi = 0$  and  $\theta = [0, \pi]$ . . . . . 184
- 5.14 A schematic illustration showing the three regions that can be identified for a triaxial nucleus within the  $\mathbf{W}_2$  formalism. The stable motion is characterized by the closed orbits around the minimal points  $m_{1,2,3}$  suggesting the precession of  $\mathbf{I}$  around the 1-axis. Furthermore, for a fixed angular momentum, a critical value of  $\mathcal{H}$  is marked by the thick orange lines. Beyond this region, the rotational motion becomes unstable, marking a phase transition. . . . . 185
- 5.15 The nuclear trajectories for the state  $I = 25/2^+$  from TSD1 in  $^{163}\text{Lu}$ . The left inset shows the trajectory of the system corresponding to the real energy of the spin (i.e., the red ellipses that surround  $x_1$ ). The rotational axis is marked by the red color, signifying that the nucleus wobbles around it. . . . . 187
- 5.16 The nuclear trajectories for the state  $I = 27/2^+$  from TSD2 in  $^{163}\text{Lu}$ . The left inset shows the trajectory of the system corresponding to the real energy of the spin (i.e., the red ellipses that surround  $x_1$ ). The rotational axis is marked by the red color, signifying that the nucleus wobbles around it. . . . . 188
- 5.17 The nuclear trajectories for the state  $I = 33/2^+$  from TSD3 in  $^{163}\text{Lu}$ . The left inset shows the trajectory of the system corresponding to the real energy of the spin (i.e., the red ellipses that surround  $x_1$ ). The rotational axis is marked by the red color, signifying that the nucleus wobbles around it. . . . . 188
- 5.18 The nuclear trajectories for the state  $I = 47/2^+$  from TSD4 in  $^{163}\text{Lu}$ . The left inset shows the trajectory of the system corresponding to the real energy of the spin (i.e., the red ellipses that surround  $x_1$ ). The rotational axis is marked by the red color, signifying that the nucleus wobbles around it. . . . . 188

6.1	The elliptic functions sn, cd, and dn from Eq. (6.20) are represented as functions of $q$ . The value of the <i>elliptic modulus</i> $k$ is set to $1/2$ .	199
6.2	The potential energy as function of $q$ for several values of the angular momentum $I$ . For the calculation of $V(q)$ , the MOI were set to $\mathcal{I}_1 : \mathcal{I}_2 : \mathcal{I}_3 = 95 : 100 : 85 \text{ } \hbar\text{MeV}^{-2}$ , $j = 13/2$ , and $\theta = -80^\circ$ .	201
6.3	The potential energy $V(q)$ for $\theta = -80^\circ$ and $\theta + \pi$ , but for an extended range of the variable $q$ , such that the deep and local minima can be seen. The same moments of inertia are used as in Fig. 6.1.	201
6.4	The potential $V(q)$ from Eq. (6.26), near the $q = 2K$ minimum point. It can be observed that the minimum character appears only for $I > 19/2$ .	203
6.5	The two wobbling frequencies $\omega$ (Eq. (6.36)) and $\omega'$ (Eq. (6.38)) as function of the coordinate $\theta$ for a fixed set of MOI $\mathcal{I}_1 : \mathcal{I}_2 : \mathcal{I}_3 = 91 : 9 : 51 \text{ } \hbar^2\text{MeV}^{-1}$ and single-particle angular momentum $j = 13/2$ .	205
6.6	The classical energy $H'$ from Eq. (6.45) evaluated for a fixed $x_2 = 0$ (left) and fixed $\varphi_2 = -\pi/2$ (right). The calculations were done for $\mathcal{I}_1 : \mathcal{I}_2 : \mathcal{I}_3 = 10 : 40 : 20 \text{ } \hbar\text{MeV}^{-1}$ . The single-particle angular momentum $j = 11/2$ .	208
6.7	Contour plot for the energy $H'$ from Eq. (6.40), defined in terms of the polar coordinates. The calculations are done for the A1-A2-A3 cases (i.e., maximal MOI is $\mathcal{I}_2$ ). The single-particle angular momentum is $j = 11/2$ , the total angular momentum $I = 19/2$ , the MOI are $\mathcal{I}_1 : \mathcal{I}_2 : \mathcal{I}_3 = 10 : 40 : 20 \text{ } \hbar^2\text{MeV}^{-1}$ , and $\theta = 70^\circ$ . The four stationary points are illustrated, namely two minima - one local and one global - (denoted by "m") and two saddle points (denoted by "s").	210
6.8	The classical energy $H'$ from Eq. (6.40), for a fixed $\theta_2 = \pi/2$ and $\varphi \in [0, 2\pi]$ . The single-particle angular momentum is $j = 11/2$ , the total angular momentum $I = 19/2$ , the MOI are $\mathcal{I}_1 : \mathcal{I}_2 : \mathcal{I}_3 = 10 : 40 : 20 \text{ } \hbar^2\text{MeV}^{-1}$ , and $\theta = 70^\circ$ . The critical points present in Fig. 6.7 are also illustrated here by the dashed vertical lines (two minima with red color and two saddle points with blue color).	211
6.9	The classical energy $H'$ from Eq. (6.53) evaluated for a fixed $x_3 = 0$ (left) and fixed $\varphi_3 = \pi$ (right). The calculations were done for $\mathcal{I}_1 : \mathcal{I}_2 : \mathcal{I}_3 = 10 : 20 : 40 \text{ } \hbar^2\text{MeV}^{-1}$ . The single-particle angular momentum $j = 11/2$ .	211
6.10	Contour plot for the energy $H'$ from Eq. (6.40), defined in terms of the polar coordinates. The calculations are done for the B1-B2-B3 cases (i.e., maximal MOI is $\mathcal{I}_3$ ). The single-particle angular momentum is $j = 11/2$ , the total angular momentum $I = 19/2$ , the MOI are $\mathcal{I}_1 : \mathcal{I}_2 : \mathcal{I}_3 = 10 : 20 : 40 \text{ } \hbar^2\text{MeV}^{-1}$ , and $\theta = 70^\circ$ . The five stationary points are illustrated, namely two maxima (denoted by "M") and three minimum points (denoted by "m"; one global and two local).	213

- 6.11 The classical energy  $H'$  from Eq. (6.40), for a fixed  $\theta_2 = \pi/2$  and  $\varphi \in [0, 2\pi]$ . The single-particle angular momentum is  $j = 11/2$ , the total angular momentum  $I = 19/2$ , the MOI are  $\mathcal{I}_1 : \mathcal{I}_2 : \mathcal{I}_3 = 10 : 20 : 40 \text{ } \hbar^2 \text{MeV}^{-1}$ , and  $\theta = 70^\circ$ . The critical points present in Fig. 6.10 are illustrated by the dashed vertical lines (magenta for the maxima and red for the minima). . . . . 214
- 6.12 Contour plot for the energy  $H'$  from Eq. (6.40), defined in terms of the polar coordinates. The calculations are done for  $\mathcal{I}_1 : \mathcal{I}_2 : \mathcal{I}_3 = 80 : 10 : 50 \text{ } \hbar^2 \text{MeV}^{-1}$  (i.e., the 1-axis is the quantization axis). The single-particle angular momentum is  $j = 11/2$ , the total angular momentum  $I = 19/2$ , and  $\theta = 70^\circ$ . The five stationary points are illustrated, namely three maxima (denoted by "M") and two saddle points (denoted by "s"). . . . . 215
- 6.13 The phase diagram associated with the parametric formula given in Eq. (6.63). Each of the conditions that make the equation vanish is represented by a separatrix, such that different regions depict *different nuclear phases*. The numerical values of  $u$  and  $v$  obtained from cases A-B-C are also represented within the plot. . . . . 217
- 6.14 The excitation energies  $E_I^{\text{exc};\text{B}1}$  in  $^{135}\text{Pr}$  (Eq. (6.72)), calculated with the parameter set  $\mathcal{P}_{\text{fit}}$ . The experimental data are taken from Ref. [113]. . . . . 222
- 6.15 The excitation energies  $E_I^{\text{exc};\text{B}2}$  (**left**) and  $E_I^{\text{exc};\text{B}3}$  (**right**) in  $^{135}\text{Pr}$  (Eq. (6.72)), calculated with the parameter set  $\mathcal{P}_{\text{fit}}$ . The experimental data are taken from Ref. [113]. . . . . 222
- 6.16 The elliptic potential from Eq. (6.26) as function of the coordinate  $q$ . The expression of  $V(q)$  is evaluated for the inertia factors from Table 6.4 with  $\theta = -119^\circ$  (**left**) and  $\theta = 61^\circ$  (**right**). . . . . 223
- 6.17 The triaxial potential from Eq. (6.26) associated to  $^{135}\text{Pr}$ , evaluated for the case of maximal MOI along 2-axis. The three MOI are  $\mathcal{I}_1 : \mathcal{I}_2 : \mathcal{I}_3 \approx 13 : 101 : 53 \text{ } \hbar^2 \text{MeV}^{-1}$ ,  $\theta = 140^\circ$  (**left**), and  $\theta = 320^\circ$  (**right**). . . . . 224
- 6.18 The triaxial potential from Eq. (6.26) associated to  $^{135}\text{Pr}$ , evaluated using  $\omega'$  instead of  $\omega$  (see Eq. (6.38)). The MOI are:  $\mathcal{I}_1 : \mathcal{I}_2 : \mathcal{I}_3 \approx 89 : 12 : 48 \text{ } \hbar^2 \text{MeV}^{-1}$ ,  $\theta = -71^\circ$  (**left**), and  $\theta = 109^\circ$  (**right**). . . . . 224
- 6.19 The wobbling frequency as function of angular momentum for  $^{135}\text{Pr}$ , according to Eq. (6.36) (**left**) and Eq. (6.38) (**right**). The calculations are done for the parameters provided in Table 6.4. The value  $\langle \delta \rangle$  represents the average spacing between the two frequencies (see text for more details). . . . . 225
- 6.20 The wobbling frequency as function of angular momentum for  $^{135}\text{Pr}$ , according to Eq. (6.36) (**left**) and Eq. (6.38) (**right**). The calculations are done for the parameters obtained by fitting Eq. (6.72) such that  $\mathcal{I}_2 = \mathcal{I}_{\text{max}}$ . The value  $\langle \delta \rangle$  represents the average spacing between the two frequencies (see text for more details). . . . . 226

6.21	The wobbling frequency as function of angular momentum for $^{135}\text{Pr}$ , according to Eq. (6.36) ( <b>left</b> ) and Eq. (6.38) ( <b>right</b> ). Results were achieved with the parameters given by a fit of Eq. (6.72) using $\omega'$ in its analytical expression. The value $\langle \delta \rangle$ represents the average spacing between the two frequencies (see text for more details). . . . .	226
6.22	The symmetric <b>left</b> and asymmetric <b>right</b> potentials from Eq. (6.77) associated to $^{135}\text{Pr}$ . The numerical evaluation is done with the fitting parameters from Table 6.4. . . . .	228
6.23	The symmetric and asymmetric excitation energies from Eq. (6.78) for $^{135}\text{Pr}$ , evaluated for the parameters given in Table 6.4. The lines connecting the dots are just to guide the eye. . . . .	229
A.1	The first excited energy states $2^+$ of nuclei with even $Z$ and $N$ are graphically represented with respect to the proton number. Each connecting line represents a set of isotopes. Figure taken from Ref. [76]. . . . .	242
A.2	The first excited energy states $2^+$ of nuclei with even $Z$ and $N$ are graphically represented with respect to the neutron number. Each connecting line represents a set of isotopes. Figure taken from Ref. [76]. . . . .	243
A.3	The energy levels obtained via calculation of the shell model potential using the simple oscillator (SHO), the SHO amended with a centrifugal term $l^2$ , and finally the modified oscillator (MHO) that contains a spin-orbit term. The ‘correct’ magic numbers are the ones in the right-most column. Figure is adapted from Refs. [20, 76].	246
A.4	The shape of the Woods-Saxon potential, defined by Eq. (A.9). The parameters are arbitrarily chosen as: $V_0 = 50$ MeV, $R = 5.57$ fm, and $a = 0.5$ fm. . . . .	248
A.5	A schematic representation with the three kind of potentials used to describe the shell model: harmonic oscillator, Woods-Saxon, and for completeness, the square-well. . . . .	249
A.6	The energy levels calculated for the Woods-Saxon potential given by Eq. (A.9) (left-side), and the single-particle energies with the spin-orbit correction added, as in Eq. (A.10) (right-side). Figure adapted from Ref. [77]. . . . .	250
A.7	The orbit of a single particle orbiting the deformed nucleus, defined by the projection of the particle’s a.m. $\Omega$ (on the symmetry axis) and the tilting angle $\theta$ . Figure inspired from Ref. [15] . . . . .	251
A.8	The change in $\theta$ angle defined in Eq. (A.14) with increasing values of $\Omega$ , for a few orbitals $j$ . . . . .	251
A.9	The energy shift $\Delta E$ for two orbits: $h_{9/2}$ and $i_{13/2}$ for a given deformation $\epsilon = 0.22$ . The dashed vertical lines (colored) represent the value for $K$ where the ‘change’ from downward sloping curves to upward sloping curves takes place (that is $K \approx 0.65j$ ). This is just an illustrative example inspired from the discussion regarding single-particle orbits in Ref. [15] . . . . .	254

---

B.1	Defining the mixing between two different states, with two corresponding energies and wave-functions. Interaction is illustrated via the curved line and $V_{\text{int}}$ term. . . . .	257
B.2	<b>Left:</b> The dependence of $R$ on the mixing amplitude $\beta$ . <b>Right:</b> The dependence of $R$ on the energy shift of the perturbed states ( $\Delta E_S$ ). . . . .	259
B.3	The <i>strong mixing</i> limit for two energy levels that are interacting via a perturbation. The initial two levels are degenerate, such that their splitting is null. . . . .	260
B.4	The <i>weak mixing</i> limit for two energy levels that are interacting via a perturbation. The interaction strength is much smaller than the initial spacing between states, resulting in a very small energy splitting $\Delta E_S$ . . . . .	261
B.5	The <i>non-crossing</i> between two states. The arrow marks the closest point at which the two states can interact with each other (i.e., the inflection point). . . . .	261
C.1	The geometrical interpretation with the two ways a nucleus can exhibit rotational bands: Deformed Aligned Bands ( <b>left</b> ) and Rotation Aligned Bands ( <b>right</b> ). The projection of the single-particle's total a.m. on the deformation and rotation axes is denoted by $K$ and $j_1$ , respectively. . . . .	263
C.2	Rotational bands in odd- $A$ nuclei with the $K$ quantum number equal to $K = 1/2$ ( <b>left</b> ) and $K \neq 1/2$ ( <b>right</b> ). . . . .	265
C.3	Experimental level schemes for $^{163}\text{Lu}$ showing pairs of signature partner bands. <b>Left pair:</b> the two bands are built on a proton with $j = 1/2$ and positive parity. <b>Right pair:</b> sequences built on a proton with $j = 5/2$ with the same parity. The Nilsson quantum numbers are defined for each band (recall Eq. (2.25)). Note the lower energies for the favored states. Interband transitions are marked with the blue arrows. The level schemes were taken from Ref. [92]. . . . .	267

# List of Tables

3.1	The parameter set $\mathcal{P}_{\text{fit}}$ obtained from the fitting procedure of the excitation energies of the two wobbling bands (B1 and B2) for $^{130}\text{Ba}$ . The model function corresponds to the energy of a simple wobbler (see Eq. (3.14)). . . . .	72
3.2	The numerical values for the quantities which are required to determine the quadrupole transition probabilities $B(E2)$ defined in Eqs. (3.20) - (3.22). The parameter set $\mathcal{P}_{\text{fit}}$ was obtained through the fitting procedure and the values are shown in Table 3.1. The intraband transition probabilities $B(E2)$ are evaluated for states $(n, I) \rightarrow (n, I - 2)$ . . . . .	74
3.3	The ratios $B(E2)_{\text{out}}/B(E2)_{\text{in}}$ for $^{130}\text{Ba}$ . The interband transitions signify the change from a state $I$ in band B2 to a state $I - 1$ in band B1. The experimental data (where available) are taken from Ref. [98, 99]. . . . .	75
3.4	The adopted notations for describing odd- $A$ nuclei by means of particles and angular momenta. These symbols will be used throughout the rest of the work. . . . .	78
4.1	The positivity conditions for the two solutions $\Omega_{1,2}$ given in Eq. (4.22). The trivial solution $B = C = 0$ has been dismissed. . . . .	114
4.2	The spin, parity, and signature assignments for $^{163}\text{Lu}$ taken from experimental measurements [145]. Concerning the notation $\pi(l_j)$ , it signifies an odd proton in the $l$ -orbital with angular momentum $j$ . The last two columns represent the key difference between the formalisms $\mathbf{W}_0$ and $\mathbf{W}_1$ . . . . .	125
4.3	The wobbling phonon numbers $(n_{w_1}, n_{w_2})$ and the phonon term $\mathcal{F}_{n_{w_1} n_{w_2}}^I$ are provided in the first three columns for $^{163}\text{Lu}$ . The first ( $I_0$ ) and terminus ( $I_t$ ) states of each band are given in the next two columns. Last column contains the quasi-particles involved in the particle + rotor coupling, which are denoted according to Eqs. (4.53) - (4.54). . . . .	127
4.4	Spin and parity assignments for $^{161}\text{Lu}$ , which are required for the excitation energy calculations (first column). The single-particle and the core states are shown in the third and fourth column. The wobbling phonon numbers from Eq. (4.31) are shown in the penultimate column. The band-head $I_b$ of this isotope is also given in the last column. . . . .	132

4.5 Spin and parity assignments for $^{165}\text{Lu}$ , which are required for the excitation energy calculations (first column). The single-particle and the core states are shown in the third and fourth column. The wobbling phonon numbers from Eq. (4.31) are shown in the penultimate column. The band-head $I_b$ of this isotope is also given in the last column. . . . .	132
4.6 Spin and parity assignments for $^{167}\text{Lu}$ , which are required for the excitation energy calculations (first column). The single-particle and the core states are shown in the third and fourth column. The wobbling phonon numbers from Eq. (4.31) are shown in the penultimate column. The band-head $I_b$ of this isotope is also given in the last column. . . . .	132
4.7 The fitting parameters $\mathcal{P}_{\text{fit}}$ , i.e., the moments of inertia, the single-particle potential strength, and the triaxiality $\gamma$ for each Lu isotope. The number of wobbling states (n.o.s.) and the root-mean-square error are also given in the last two columns. . . . .	134
4.8 The reduced intraband transition probabilities for $^{161,163,165,167}\text{Lu}$ obtained through Eq. (4.72) are compared with the experimental data (where available) taken from Ref. [145]. . . . .	153
4.9 The reduced interband transition probabilities for connecting states $I \in \text{TSD2} \rightarrow I - 1 \in \text{TSD1}$ . Experimental data are taken from Ref. [145]. . . . .	154
4.10 The quadrupole transition moment $Q_I$ (Eq. (4.75)) and the static quadrupole moment $Q_{\text{SQM}}$ (Eq. (4.76)). For the calculation of $Q_{\text{SQM}}$ , $K$ was fixed to $K = 1/2$ . The experimental data are taken from Refs. [65, 145, 152]. The unit of measure is consistent with the one employed by Görgen et al. [152]. . . . .	155
4.11 The numerical results for the reduced $M1$ transitions between states $I \in \text{TSD2} \rightarrow I - 1 \in \text{TSD1}$ . The calculated mixing ratio $\delta(E2/M1)$ (Eq. (4.81)) are also shown in comparison with the experimental data, which are taken from Refs. [65, 145, 152]. . . . .	158
5.1 Details for the normalization employed in $\mathbf{W}_2$ . From the second left-most column one has: the number of energy states $n_s$ within each wobbling band of $^{163}\text{Lu}$ , the valence nucleon $j^\pi = 13/2^+$ , the a.m. for the core $\mathbf{R}_c$ , the total a.m. $\mathbf{I}$ , and the corresponding coupling scheme as per Section 5.1. . . . .	172
5.2 The parameter set $\mathcal{P}$ of Eq. (4.59) obtained by minimizing the $\chi^2$ -function for $^{163}\text{Lu}$ in the renormalization of $\mathbf{W}_2$ . A unique fitting was applied for all four TSD bands of the isotope. . . . .	172
5.3 The minimum points of $\mathcal{H}$ for a fixed ordering of the inertia factors. The orderings are chosen in agreement with the fit parameters from Table 5.2. . . . .	180
6.1 The stationary points for the classical energy function depicted in Eq. (6.40), when the quantization axis is the 2-axis. Each point corresponds to the cases $A1$ , $A2$ , and $A3$ , respectively. . . . .	209

6.2	The stationary points for the classical energy function depicted in Eq. (6.40), when the quantization axis is the 3-axis. Each point corresponds to the cases $B1$ , $B2$ , and $B3$ , respectively. . . . .	213
6.3	The stationary points for the classical energy function depicted in Eq. (6.40), when the quantization axis is the 1-axis. Each point corresponds to the cases $C1$ , and $C2$ , respectively. . . . .	215
6.4	The four free parameters obtained by fitting the experimental energies of $^{135}\text{Pr}$ (taken from Ref. [112]) using the set of energies from Eq. (6.72). For the moments of inertia, the unit is $\hbar^2\text{MeV}^{-1}$ . . . . .	221
6.5	The obtained numerical values for the electromagnetic transitions are compared with the experimental data for $^{135}\text{Pr}$ . Only the states for which experimental data are available were considered [112]. . . . .	230



# Bibliography

- [1] Aage Niels Bohr and Ben R Mottelson. *Nuclear Structure (In 2 Volumes)*. World Scientific Publishing Company, 1998.
- [2] H Morinaga and PC Gugelot. Gamma rays following ( $\alpha$ , xn) reactions. *Nuclear Physics*, 46:210–224, 1963.
- [3] CM Raduta, AA Raduta, R Poenaru, and Al H Raduta. Simultaneous description of wobbling and chiral properties in even–odd triaxial nuclei. *Journal of Physics G: Nuclear and Particle Physics*, 49(2):025105, 2022.
- [4] AS Davydov and GF Filippov. Rotational states in even atomic nuclei. *Nuclear Physics*, 8:237–249, 1958.
- [5] Ikuko Hamamoto. Wobbling excitations in odd-a nuclei with high-j aligned particles. *Physical Review C*, 65(4):044305, 2002.
- [6] Yoshifumi R Shimizu and Masayuki Matsuzaki. Nuclear wobbling motion and electromagnetic transitions. *Nuclear Physics A*, 588(3):559–596, 1995.
- [7] Makito Oi, Ahmad Ansari, Takatoshi Horibata, and Naoki Onishi. Wobbling motion in the multi-bands crossing region. *Physics Letters B*, 480(1-2):53–60, 2000.
- [8] QB Chen, SQ Zhang, PW Zhao, and J Meng. Collective hamiltonian for wobbling modes. *Physical Review C*, 90(4):044306, 2014.
- [9] S Frauendorf and F Dönau. Transverse wobbling: A collective mode in odd-a triaxial nuclei. *Physical Review C*, 89(1):014322, 2014.
- [10] Walter Greiner and Joachim A Maruhn. *Nuclear models*. Springer, 1996.
- [11] Peter Ring and Peter Schuck. *The nuclear many-body problem*. Springer Science & Business Media, 2004.

- [12] Aage Bohr. *Rotational states of atomic nuclei*. Munksgaard, 1954.
- [13] Samuel SM Wong. *Introductory nuclear physics*. John Wiley & Sons, 2008.
- [14] G Andersson, SE Larsson, G Leander, P Möller, Sven Gösta Nilsson, Ingemar Ragnarsson, Sven Åberg, R Bengtsson, J Dudek, B Nerlo-Pomorska, et al. Nuclear shell structure at very high angular momentum. *Nuclear Physics A*, 268(2):205–256, 1976.
- [15] R Casten and Richard F Casten. *Nuclear structure from a simple perspective*, volume 23. Oxford University Press on Demand, 2000.
- [16] Sven Gösta Nilsson. Binding states of individual nucleons in strongly deformed nuclei. *Dan. Mat. Fys. Medd.*, 29(CERN-55-30):1–69, 1955.
- [17] Carlos A Bertulani. *Nuclear physics in a nutshell*. Princeton University Press, 2007.
- [18] C Gustafson, IL Lamm, B Nilsson, and SG Nilsson. Nuclear deformabilities in the rare-earth and actinide regions with excursions off the stability line and into the super-heavy region. Technical report, Lund Inst. of Tech., Sweden, 1967.
- [19] Adam Benjamin Garnsworthy. *Neutron-proton interactions in heavy self-conjugate nuclei*. University of Surrey (United Kingdom), 2007.
- [20] Kenneth S Krane. *Introductory nuclear physics*. John Wiley & Sons, 1991.
- [21] Biswarup Das. *Nuclear Structure Studies At High Angular Momentum In Mass 100 Region*. PhD thesis, HOMI BHABHA NATIONAL INSTITUTE, 2018.
- [22] Ingemar Ragnarsson and Sven Gvsta Nilsson. Shapes and shells in nuclear structure. *Shapes and Shells in Nuclear Structure*, 2005.
- [23] Charles H Townes, HM Foley, and W Low. Nuclear quadrupole moments and nuclear shell structure. *Physical Review*, 76(9):1415, 1949.
- [24] M Goldhaber and AW Sunyar. Classification of nuclear isomers. *Physical Review*, 83(5):906, 1951.

- [25] Aage Niels Bohr and Benjamin Roy Mottelson. Collective and individual-particle aspects of nuclear structure. *Dan. Mat. Fys. Medd.*, 27(CERN-57-38):1–174, 1953.
- [26] Lise Meitner and Otto Robert Frisch. Disintegration of uranium by neutrons: a new type of nuclear reaction. *Nature*, 143(3615):239–240, 1939.
- [27] Niels Bohr and John Archibald Wheeler. The mechanism of nuclear fission. *Physical Review*, 56(5):426, 1939.
- [28] WD Myers and WJ Swiatecki. The nuclear droplet model for arbitrary shapes. *Annals of Physics*, 84(1-2):186–210, 1974.
- [29] James Rainwater. Nuclear energy level argument for a spheroidal nuclear model. *Physical Review*, 79(3):432, 1950.
- [30] Albert Messiah. *Quantum mechanics*. Courier Corporation, 2014.
- [31] ZP Li and D Vretenar. Model for collective motion. *arXiv preprint arXiv:2203.07608*, 2022.
- [32] K Kitao, Y Tendow, and A Hashizume. Nuclear data sheets for  $a = 120$ . *Nuclear Data Sheets*, 96(2):241–390, 2002.
- [33] E Browne and JK Tuli. Nuclear data sheets for  $a = 60$ . *Nuclear Data Sheets*, 114(12):1849–2022, 2013.
- [34] Jun Chen, Balraj Singh, and John A Cameron. Nuclear data sheets for  $a = 44$ . *Nuclear Data Sheets*, 112(9):2357–2495, 2011.
- [35] Bai Erjun and Huo Junde. Nuclear data sheets for  $a = 63$ . *Nuclear Data Sheets*, 92(1):147–252, 2001.
- [36] Alan L Nichols, Balraj Singh, and Jagdish K Tuli. Nuclear data sheets for  $a = 62$ . *Nuclear Data Sheets*, 113(4):973–1114, 2012.
- [37] TM Corrigan, FJ Margenau, and SA Williams. Exact solution of the quadrupole surface vibration hamiltonian in body-fixed coordinates. *Physical Review C*, 14(6):2279, 1976.
- [38] Ikuko Hamamoto. Interplay between one-particle and collective degrees of freedom in nuclei. *Physica Scripta*, 91(2):023004, 2016.

- [39] AA Raduta, R Poenaru, and L Gr Ixaru. Semiclassical unified description of wobbling motion in even-even and even-odd nuclei. *Physical Review C*, 96(5):054320, 2017.
- [40] N Nica. Nuclear data sheets for  $a=158$ . *Nuclear Data Sheets*, 141:1–326, 2017.
- [41] Elizabeth A McCutchan. Nuclear data sheets for  $a=180$ . *Nuclear Data Sheets*, 126:151–372, 2015.
- [42] Pierre Celestin Uwitonze. *Assignment of Spin and Parity to States in the Nucleus 196T1*. PhD thesis, Rhodes University, 2015.
- [43] R Bengtsson and S Frauendorf. Quasiparticle spectra near the yrast line. *Nuclear Physics A*, 327(1):139–171, 1979.
- [44] Samuel M Harris. Higher order corrections to the cranking model. *Physical Review*, 138(3B):B509, 1965.
- [45] R Bengtsson, H Frisk, FR May, and JA Pinston. Signature inversion—a fingerprint of triaxiality. *Nuclear Physics A*, 415(2):189–214, 1984.
- [46] J Kvasil and RG Nazmitdinov. Backbending and  $\gamma$  vibrations. *Physical Review C*, 69(3):031304, 2004.
- [47] Saddon T Ahmad, M Kotb, Idris H Salih, and Hewa Y Abdullah. Backbending phenomena in even-even [formula omitted] hf isotopes. *Physics of Atomic Nuclei*, 84(1):18–29, 2021.
- [48] CS Wu, L Cheng, CZ Lin, and JY Zeng. Relation between the kinematic and dynamic moments of inertia in superdeformed nuclei. *Physical Review C*, 45(5):2507, 1992.
- [49] N Nica. Nuclear data sheets for  $a=160$ . *Nuclear Data Sheets*, 176:1–428, 2021.
- [50] CW Reich. Nuclear data sheets for  $a=162$ . *Nuclear Data Sheets*, 108(9):1807–2034, 2007.
- [51] AS Davydov and AA Chaban. Rotation-vibration interaction in non-axial even nuclei. *Nuclear Physics*, 20:499–508, 1960.

- [52] Ben R Mottelson and JG Valatin. Effect of nuclear rotation on the pairing correlation. *Physical Review Letters*, 5(11):511, 1960.
- [53] J Krumlinde and Z Szymański. On the effect of quadrupole pairing interaction on the backbending behaviour in rotating nuclei. *Physics Letters B*, 53(4):322–324, 1974.
- [54] Kris LG Heyde. The nuclear shell model. In *The Nuclear Shell Model*, pages 58–154. Springer, 1994.
- [55] R Budaca. Tilted-axis wobbling in odd-mass nuclei. *Physical Review C*, 97(2):024302, 2018.
- [56] Peter Möller, Ragnar Bengtsson, B Gillis Carlsson, Peter Olivius, and Takatoshi Ichikawa. Global calculations of ground-state axial shape asymmetry of nuclei. *Physical review letters*, 97(16):162502, 2006.
- [57] SW Ødegård, GB Hagemann, and DR Jensen. Evidence for the wobbling mode in nuclei. *Physical review letters*, 86(26):5866, 2001.
- [58] DR Jensen, GB Hagemann, and I Hamamoto. Evidence for second-phonon nuclear wobbling. *Physical review letters*, 89(14):142503, 2002.
- [59] Shi Wen-Xian and Chen Qi-Bo. Wobbling geometry in a simple triaxial rotor. *Chinese Physics C*, 39(5):054105, 2015.
- [60] J Peng, J Meng, and SQ Zhang. Description of chiral doublets in a 130 nuclei and the possible chiral doublets in a 100 nuclei. *Physical Review C*, 68(4):044324, 2003.
- [61] Tord Bengtsson. A method to remove virtual interactions with applications to nuclear spectroscopy. *Nuclear Physics A*, 496(1):56–92, 1989.
- [62] Tord Bengtsson. The high-spin structure of 158er: A theoretical study. *Nuclear Physics A*, 512(1):124–148, 1990.
- [63] MK Djongolov, DJ Hartley, LL Riedinger, Filip G Kondev, RVF Janssens, K Abu Saleem, I Ahmad, DL Balabanski, MP Carpenter, P Chowdhury, et al. Extending the region of triaxial superdeformation: candidate tsd bands in 174hf. *Physics Letters B*, 560(1-2):24–30, 2003.

- [64] K Nomura and CM Petrache. Examining the wobbling interpretation of low-lying bands in gamma-soft nuclei within the interacting boson-fermion model. *arXiv e-prints*, pages arXiv–2106, 2021.
- [65] D Jensen, GB Hagemann, and I Hamamoto. Wobbling phonon excitations, coexisting with normal deformed structures in  $^{163}\text{Lu}$ . *Nuclear Physics A*, 703(1-2):3–44, 2002.
- [66] Yingqiong Gu. *Theoretical investigation of triaxial strong deformation and tidal waves in nuclei*. University of Notre Dame, 2007.
- [67] Chong Qi, Roberto Liotta, and Ramon Wyss. Recent developments in radioactive charged-particle emissions and related phenomena. *Progress in Particle and Nuclear Physics*, 105:214–251, 2019.
- [68] R Budaca and AI Budaca. Deformation dependence of the screened decay law for proton emission. *Nuclear Physics A*, 1017:122355, 2022.
- [69] Peter Möller, Arnold J Sierk, Takatoshi Ichikawa, Akira Iwamoto, Ragnar Bengtsson, Henrik Uhrenholt, and Sven Åberg. Heavy-element fission barriers. *Physical Review C*, 79(6):064304, 2009.
- [70] Bing-Nan Lu, En-Guang Zhao, Shan-Gui Zhou, et al. Potential energy surfaces of actinide nuclei from a multidimensional constrained covariant density functional theory: Barrier heights and saddle point shapes. *Physical Review C*, 85(1):011301, 2012.
- [71] F Palumbo and A Richter. Splitting of the magnetic dipole giant resonance and triaxial deformation. *Physics Letters B*, 158(2):101–102, 1985.
- [72] Gregoire Henning. *Stability of trans fermium elements at high spin: measuring the fission barrier of  $^{254}\text{No}$* . PhD thesis, Paris 11, 2012.
- [73] J Simpson. The euroball spectrometer. *Zeitschrift für Physik A Hadrons and Nuclei*, 358(2):139–143, 1997.
- [74] I-Yang Lee. The gammasphere. *Nuclear Physics A*, 520:c641–c655, 1990.
- [75] Akaa Daniel Ayangeakaa. *Exotic Modes of Collective Excitations: Nuclear Tidal Waves and Chirality*. PhD thesis, University of Notre Dame, 2013.
- [76] James Till Matta. *Exotic Nuclear Excitations: The Transverse Wobbling Mode in  $^{135}\text{Pr}$* . Springer, 2017.

- [77] Michael Christopher Lewis. *Lifetime Measurements of Excited States in  $^{163}\text{W}$  and the Properties of Multiparticle Configurations in  $^{156}\text{Lu}$* . The University of Liverpool (United Kingdom), 2019.
- [78] Nirupama Sensharma. *Wobbling Motion in Nuclei: Transverse, Longitudinal and Chiral*. University of Notre Dame, 2021.
- [79] Stefan Frauendorf and Jie Meng. Tilted rotation of triaxial nuclei. *Nuclear Physics A*, 617(2):131–147, 1997.
- [80] K Starosta, T Koike, CJ Chiara, DB Fossan, DR LaFosse, AA Hecht, CW Beausang, MA Caprio, JR Cooper, R Krücken, et al. Chiral doublet structures in odd-odd  $n=75$  isotones: Chiral vibrations. *Physical review letters*, 86(6):971, 2001.
- [81] SQ Zhang, Bin Qi, SY Wang, and J Meng. Chiral bands for a quasi-proton and quasi-neutron coupled with a triaxial rotor. *Physical Review C*, 75(4):044307, 2007.
- [82] J Meng, B Qi, SQ Zhang, and SY Wang. Chiral symmetry in atomic nuclei. *Modern Physics Letters A*, 23(27n30):2560–2567, 2008.
- [83] R Budaca. Semiclassical description of chiral geometry in triaxial nuclei. *Physical Review C*, 98(1):014303, 2018.
- [84] R Budaca. From chiral vibration to tilted-axis wobbling within broken chiral symmetry. *Physics Letters B*, 817:136308, 2021.
- [85] AA Raduta, CM Raduta, and Amand Faessler. A new picture for the chiral symmetry properties within a particle–core framework. *Journal of Physics G: Nuclear and Particle Physics*, 41(3):035105, 2014.
- [86] AA Raduta and CM Raduta. Description of the chiral bands in  $^{188,190}\text{Os}$ . *arXiv preprint arXiv:1407.5059*, 2014.
- [87] AA Raduta and CM Raduta. Semi-phenomenological description of the chiral bands in  $^{188,190}\text{Os}$ . *Journal of Physics G: Nuclear and Particle Physics*, 42(6):065105, 2015.
- [88] AA Raduta, Al H Raduta, and CM Petrache. Possible chiral symmetry in  $^{138}\text{Nd}$ . *arXiv preprint arXiv:1512.08656*, 2015.

- [89] AA Raduta. Specific features and symmetries for magnetic and chiral bands in nuclei. *Progress in Particle and Nuclear Physics*, 90:241–298, 2016.
- [90] AA Raduta, CM Raduta, and Al H Raduta. Alternative description of chiral properties in  $^{138}\text{Nd}$ . *Journal of Physics G: Nuclear and Particle Physics*, 44(4):045102, 2017.
- [91] EA Mccutchan. Nuclear data sheets for  $a = 136$ . *Nuclear Data Sheets*, 152:331–667, 2018.
- [92] MR Bhat. Evaluated nuclear structure data file (ensdf). In *Nuclear data for science and technology*, pages 817–821. Springer, 1992.
- [93] E Grodner, J Srebrny, Ch Droste, T Morek, A Pasternak, and J Kownacki. Ds<sub>am</sub> lifetime measurements in the yrast band of  $^{131}\text{La}$  and the chiral bands in  $^{132}\text{La}$ . *International Journal of Modern Physics E*, 13(01):243–246, 2004.
- [94] E Grodner, I Zalewska, T Morek, J Srebrny, Ch Droste, M Kowalczyk, J Mierzejewski, M Sałata, AA Pasternak, J Kownacki, et al. Lifetime measurements in  $^{128}\text{Cs}$  and  $^{132}\text{La}$  as a test of chirality. *International Journal of Modern Physics E*, 14(03):347–352, 2005.
- [95] Stefan Frauendorf. Spontaneous symmetry breaking in rotating nuclei. *Reviews of Modern Physics*, 73(2):463, 2001.
- [96] Makito Oi. Semi-classical and anharmonic quantum models of nuclear wobbling motion. *Physics Letters B*, 634(1):30–34, 2006.
- [97] Takuya Shoji and Yoshifumi R Shimizu. Microscopic description of nuclear wobbling motion rotation of triaxially deformed nuclei. *International Journal of Modern Physics E*, 15(07):1407–1416, 2006.
- [98] CM Petrache, PM Walker, S Guo, QB Chen, S Frauendorf, YX Liu, RA Wyss, D Mengoni, YH Qiang, A Astier, et al. Diversity of shapes and rotations in the  $\gamma$ -soft  $^{130}\text{Ba}$  nucleus: First observation of a t-band in the  $a = 130$  mass region. *Physics Letters B*, 795:241–247, 2019.
- [99] QB Chen, S Frauendorf, and CM Petrache. Transverse wobbling in an even-even nucleus. *Physical Review C*, 100(6):061301, 2019.

- [100] AA Raduta, R Poenaru, and Al H Raduta. Wobbling motion in lu within a semi-classical framework. *Journal of Physics G: Nuclear and Particle Physics*, 45(10):105104, 2018.
- [101] AA Raduta, R Poenaru, and CM Raduta. Towards a new semi-classical interpretation of the wobbling motion in 163lu. *Journal of Physics G: Nuclear and Particle Physics*, 47(2):025101, 2020.
- [102] YK Wang, FQ Chen, and PW Zhao. Two quasiparticle wobbling in the even-even nucleus 130ba. *Physics Letters B*, 802:135246, 2020.
- [103] R Poenaru and AA Raduta. Extensive study of the positive and negative parity wobbling states for an odd-mass triaxial nucleus i: Energy spectrum. *Romanian Journal of Physics*, 66(7-8), 2021.
- [104] N Sensharma, U Garg, QB Chen, S Frauendorf, DP Burdette, JL Cozzi, KB Howard, S Zhu, MP Carpenter, P Copp, et al. Longitudinal wobbling motion in au 187. *Physical review letters*, 124(5):052501, 2020.
- [105] R Poenaru and AA Raduta. Extensive study of the positive and negative parity wobbling states for an odd-mass triaxial nucleus ii: Classical trajectories. *Romanian Journal of Physics*, 66(9-10), 2021.
- [106] J Timár, QB Chen, B Kruzsicz, D Sohler, I Kuti, SQ Zhang, J Meng, P Joshi, R Wadsworth, K Starosta, et al. Experimental evidence for transverse wobbling in pd 105. *Physical review letters*, 122(6):062501, 2019.
- [107] JH Hamilton, SJ Zhu, YX Luo, AV Ramayya, S Frauendorf, JO Rasmussen, JK Hwang, SH Liu, GM Ter-Akopian, AV Daniel, et al. Super deformation to maximum triaxiality in a= 100–112; superdeformation, chiral bands and wobbling motion. *Nuclear Physics A*, 834(1-4):28c–31c, 2010.
- [108] YX Luo, JH Hamilton, AV Ramaya, JK Hwang, SH Liu, JO Rasmussen, S Frauendorf, GM Ter-Akopian, AV Daniel, Yu Ts Oganessian, et al. Triaxial and triaxial softness in neutron rich ru and pd nuclei. In *Exotic Nuclei: EXON-2012*, pages 215–224. World Scientific, 2013.
- [109] BF Lv, CM Petrache, R Budaca, A Astier, KK Zheng, P Greenlees, H Badran, T Calverley, DM Cox, T Grahn, et al. Experimental evidence for transverse wobbling bands in nd 136. *Physical Review C*, 105(3):034302, 2022.

- [110] S Chakraborty, HP Sharma, SS Tiwary, C Majumder, AK Gupta, P Banerjee, S Ganguly, S Rai, S Kumar, A Kumar, et al. Multiphonon longitudinal wobbling in  $^{127}\text{xe}$ . *Physics Letters B*, 811:135854, 2020.
- [111] S Biswas, R Palit, S Frauendorf, U Garg, W Li, GH Bhat, JA Sheikh, J Sethi, S Saha, Purnima Singh, et al. Longitudinal wobbling in  $^{133}\text{la}$ . *The European Physical Journal A*, 55(9):1–7, 2019.
- [112] James Till Matta. Transverse wobbling in  $^{135}\text{pr}$ . In *Exotic Nuclear Excitations: The Transverse Wobbling Mode in  $^{135}\text{Pr}$* , pages 77–93. Springer, 2017.
- [113] N Sensharma, U Garg, S Zhu, AD Ayangeakaa, S Frauendorf, W Li, GH Bhat, JA Sheikh, MP Carpenter, QB Chen, et al. Two-phonon wobbling in  $^{135}\text{pr}$ . *Physics Letters B*, 792:170–174, 2019.
- [114] R Ma, Y Liang, ES Paul, N Xu, DB Fossan, L Hildingsson, and RA Wyss. Competing proton and neutron rotational alignments: Band structures in  $\text{ba}~^{131}$ . *Physical Review C*, 41(2):717, 1990.
- [115] Navneet Kaur, A Kumar, G Mukherjee, Amandeep Singh, S Kumar, Rajbir Kaur, Varinderjit Singh, BR Behera, KP Singh, G Singh, et al. High spin structure in  $^{130,131}\text{ba}$ . *The European Physical Journal A*, 50(1):1–7, 2014.
- [116] C M Petrache. Search for transverse wobbling and chiral bands in  $^{131}\text{ba}$ . *LNL Annual Report*, 2018.
- [117] K Rojeeta Devi, Suresh Kumar, Naveen Kumar, FS Babra, Md SR Laskar, S Biswas, S Saha, P Singh, S Samanta, S Das, et al. Observation of multi-phonon transverse wobbling in  $^{133}\text{ba}$ . *Physics Letters B*, 823:136756, 2021.
- [118] CM Petrache and S Guo. Transverse wobbling motion in  $^{134}\text{ce}$  and  $^{136}\text{nd}$ . *arXiv preprint arXiv:1603.08247*, 2016.
- [119] CM Petrache, S Frauendorf, M Matsuzaki, R Leguillon, T Zerrouki, S Lunardi, D Bazzacco, CA Ur, E Farnea, C Rossi Alvarez, et al. Tilted axis rotation, candidates for chiral bands, and wobbling motion in  $^{138}\text{nd}$ . *Physical Review C*, 86(4):044321, 2012.
- [120] B. F. Lv, C. M. Petrache, A. Astier, E. Dupont, A. Lopez-Martens, P. T. Greenlees, H. Badran, T. Calverley, D. M. Cox, T. Grahn, J. Hilton, R. Julin,

- S. Juutinen, J. Konki, M. Leino, J. Pakarinen, P. Papadakis, J. Partanen, P. Rahkila, M. Sandzelius, J. Saren, C. Scholey, J. Sorri, S. Stolze, J. Uusitalo, A. Herzán, B. Cederwall, A. Ertoprak, H. Liu, S. Guo, M. L. Liu, Y. H. Qiang, J. G. Wang, X. H. Zhou, I. Kuti, J. Timár, A. Tucholski, J. Srebrny, and C. Andreoiu. Evolution from gamma-soft to stable triaxiality in  $^{136}\text{Nd}$  as a prerequisite of chirality. *Phys. Rev. C*, 98:044304, Oct 2018.
- [121] Fang-Qi Chen and CM Petrache. Microscopic investigation on the existence of transverse wobbling under the effect of rotational alignment: The  $\text{nd}$   $^{136}$  case. *Physical Review C*, 103(6):064319, 2021.
- [122] DR Jensen, GB Hagemann, I Hamamoto, B Herskind, G Sletten, JN Wilson, SW Ødegård, K Spohr, H Hübel, P Bringel, et al. Coexisting wobbling and quasiparticle excitations in the triaxial potential well of  $^{163}\text{Lu}$ . *The European Physical Journal A-Hadrons and Nuclei*, 19(2):173–185, 2004.
- [123] P Bringel, GB Hagemann, H Hübel, A Al-Khatib, P Bednarczyk, A Bürger, D Curien, G Gangopadhyay, B Herskind, DR Jensen, et al. Evidence for wobbling excitation in  $^{161}\text{Lu}$ . *The European Physical Journal A-Hadrons and Nuclei*, 24(2):167–172, 2005.
- [124] G Schönwaßer, H Hübel, GB Hagemann, P Bednarczyk, G Benzoni, A Bracco, P Bringel, R Chapman, D Curien, J Domscheit, et al. One- and two-phonon wobbling excitations in triaxial  $^{165}\text{Lu}$ . *Physics Letters B*, 552(1-2):9–16, 2003.
- [125] H Amro, WC Ma, GB Hagemann, RM Diamond, J Domscheit, P Fallon, A Görzen, B Herskind, H Hübel, DR Jensen, et al. The wobbling mode in  $^{167}\text{Lu}$ . *Physics Letters B*, 553(3-4):197–203, 2003.
- [126] DJ Hartley, RVF Janssens, LL Riedinger, MA Riley, A Aguilar, MP Carpenter, CJ Chiara, P Chowdhury, IG Darby, U Garg, et al. Wobbling mode in  $\text{ta } 167$ . *Physical Review C*, 80(4):041304, 2009.
- [127] Kosai Tanabe and Kazuko Sugawara-Tanabe. Algebraic description of tri- axially deformed rotational bands in odd mass nuclei. *Physical Review C*, 73(3):034305, 2006.
- [128] S Nandi, G Mukherjee, QB Chen, S Frauendorf, R Banik, Soumik Bhattacharya, Shabir Dar, S Bhattacharyya, C Bhattacharya, S Chatterjee, et al.

- First observation of multiple transverse wobbling bands of different kinds in au 183. *Physical Review Letters*, 125(13):132501, 2020.
- [129] KS Krane and RM Steffen. Determination of the e 2 m 1 multipole mixing ratios of the gamma transitions in cd 110. *Physical Review C*, 2(2):724, 1970.
- [130] W Hua, Siyuan Guo, and C. Petrache. Comment on "longitudinal wobbling in 133la" by s. biswas et al. *Preprint*, 2020.
- [131] S. Guo. Comment on "transverse wobbling in  $^{135}\text{pr}$  [phys. rev. lett. 114, 082501 (2015)]", 2020.
- [132] BF Lv, CM Petrache, EA Lawrie, S Guo, A Astier, KK Zheng, HJ Ong, JG Wang, XH Zhou, ZY Sun, et al. Evidence against the wobbling nature of low-spin bands in 135pr. *Physics Letters B*, 824:136840, 2022.
- [133] EA Lawrie, O Shirinda, and CM Petrache. Tilted precession and wobbling in triaxial nuclei. *Physical Review C*, 101(3):034306, 2020.
- [134] BF Lv, CM Petrache, EA Lawrie, A Astier, E Dupont, KK Zheng, P Greenlees, H Badran, T Calverley, DM Cox, et al. Tilted precession bands in nd 135. *Physical Review C*, 103(4):044308, 2021.
- [135] AA Raduta, CM Raduta, and R Poenaru. A new boson approach for the wobbling motion in even-odd nuclei. *Journal of Physics G: Nuclear and Particle Physics*, 48(1):015106, 2020.
- [136] AA Raduta, R Poenaru, and CM Raduta. New approach for the wobbling motion in the even-odd isotopes lu 161, 163, 165, 167. *Physical Review C*, 101(1):014302, 2020.
- [137] R Poenaru and AA Raduta. Parity partner bands in 163lu: A novel approach for describing the negative parity states from a triaxial super-deformed band. *International Journal of Modern Physics E*, 30(05):2150033, 2021.
- [138] Kosai Tanabe and Kazuko Sugawara-Tanabe. Selection rules for electromagnetic transitions in triaxially deformed odd-a nuclei. *Physical Review C*, 77(6):064318, 2008.
- [139] AA Raduta, R Budaca, and CM Raduta. Semiclassical description of a triaxial rigid rotor. *Physical Review C*, 76(6):064309, 2007.

- [140] QB Chen, SQ Zhang, PW Zhao, RV Jolos, J Meng, et al. Two-dimensional collective hamiltonian for chiral and wobbling modes. *Physical Review C*, 94(4):044301, 2016.
- [141] Roy J Glauber. Coherent and incoherent states of the radiation field. *Physical Review*, 131(6):2766, 1963.
- [142] Karl T Hecht and George Raymond Satchler. Asymmetric rotator model of odd-mass nuclei. *Nuclear Physics*, 32:286–318, 1962.
- [143] Wang Shou-Yu, Qi Bin, and Zhang Shuang-Quan. Coupling parameter in the single-j shell model. *Chinese Physics Letters*, 26(5):052102, 2009.
- [144] Kosai Tanabe and Kazuko Sugawara-Tanabe. Stability of the wobbling motion in an odd-mass nucleus and the analysis of pr 135. *Physical Review C*, 95(6):064315, 2017.
- [145] CW Reich and Balraj Singh. Nuclear data sheets for a= 163. *Nuclear Data Sheets*, 111(5):1211–1469, 2010.
- [146] John F Kenney. *Mathematics of statistics*. D. Van Nostrand, 1939.
- [147] Masayuki Matsuzaki, Yoshifumi R Shimizu, and Kenichi Matsuyanagi. Wobbling motion in atomic nuclei with positive- $\gamma$  shapes. *Physical Review C*, 65(4):041303, 2002.
- [148] H Toki and Amand Faessler. Asymmetric rotor model for decoupled bands in transitional odd-mass nuclei. *Nuclear Physics A*, 253(1):231–252, 1975.
- [149] GB Hagemann, JD Garrett, B Herskind, J Kownacki, BM Nyako, PL Nolan, JF Sharpey-Schafer, and PO Tjøm. Signature-dependent ml and e2 transition probabilities in 155ho and 157ho. *Nuclear Physics A*, 424(2):365–382, 1984.
- [150] QB Chen, S Frauendorf, N Kaiser, Ulf-G Meißner, and J Meng. g-factor and static quadrupole moment for the wobbling mode in 133la. *Physics Letters B*, 807:135596, 2020.
- [151] QB Chen, N Kaiser, Ulf-G Meißner, and J Meng. Static quadrupole moments of nuclear chiral doublet bands. *Physics Letters B*, 807:135568, 2020.

- [152] A Görgen, RM Clark, M Cromaz, P Fallon, GB Hagemann, H Hübel, IY Lee, AO Macchiavelli, G Sletten, D Ward, et al. Quadrupole moments of wobbling excitations in lu 163. *Physical Review C*, 69(3):031301, 2004.
- [153] Eite Tiesinga, Peter J Mohr, David B Newell, and Barry N Taylor. Codata recommended values of the fundamental physical constants: 2018. *Journal of Physical and Chemical Reference Data*, 50(3):033105, 2021.
- [154] Dmitrii Aleksandrovich Varshalovich, Anatolij Nikolaevic Moskalev, and Valerii Kelmanovich Khersonskii. *Quantum theory of angular momentum*. World Scientific, 1988.
- [155] Bingfeng Lv. *Chirality in the 136Nd and 135Nd nuclei*. PhD Thesis, 2019.
- [156] GB Hagemann. Wobbling phonon excitations in strongly deformed triaxial nuclei. *The European Physical Journal A-Hadrons and Nuclei*, 20(1):183–188, 2003.
- [157] I Hamamoto. Nuclear wobbling-phonon excitations with alignments. *Nuclear Physics A*, 722:C389–C394, 2003.
- [158] S Frauendorf. Comment on “stability of the wobbling motion in an odd-mass nucleus and the analysis of pr 135”. *Physical Review C*, 97(6):069801, 2018.
- [159] Kosai Tanabe and Kazuko Sugawara-Tanabe. Reply to “comment on ‘stability of the wobbling motion in an odd-mass nucleus and the analysis of pr 135’”. *Physical Review C*, 97(6):069802, 2018.
- [160] Freeman J Dyson. General theory of spin-wave interactions. *Physical review*, 102(5):1217, 1956.
- [161] V Bargmann. On the representations of the rotation group. *Reviews of Modern Physics*, 34(4):829, 1962.
- [162] B Jancovici and DH Schiff. The collective vibrations of a many-fermion system. *Nuclear Physics*, 58:678–686, 1964.
- [163] D Janssen, F Dönau, S Frauendorf, and RV Jolos. Boson description of collective states:(i). derivation of the boson transformation for even fermion systems. *Nuclear Physics A*, 172(1):145–165, 1971.
- [164] Carl Gustav Jacob Jacobi. *Fundamenta nova theoriae functionum ellipticarum*. Borntrager, 1829.

- [165] Naum Ilich Akhiezer. *Elements of the theory of elliptic functions*, volume 79. American Mathematical Soc., 1990.
- [166] Ivana Kovacic, Livija Cveticanin, Miodrag Zukovic, and Zvonko Rakaric. Jacobi elliptic functions: a review of nonlinear oscillatory application problems. *Journal of Sound and Vibration*, 380:1–36, 2016.
- [167] Eric W Weisstein. Jacobi elliptic functions. <https://mathworld.wolfram.com/>, 2002.
- [168] Eric W Weisstein. Jacobi amplitude. <https://mathworld.wolfram.com/>, 2002.
- [169] J. T. Matta, U. Garg, S. Zhu, R. Palit, S. S. Ghugre, A. D. Ayangeakaa, R. V. F. Janssens, and M. P. Carpenter. Erratum: Transverse wobbling in 135pr [phys. rev. lett. 114, 082501 (2015)]. *Phys. Rev. Lett.*, 127:139902, Sep 2021.
- [170] QB Chen, SQ Zhang, J Meng, et al. Wobbling motion in pr 135 within a collective hamiltonian. *Physical Review C*, 94(5):054308, 2016.
- [171] CF von Weizsacker. Zur theorie der kernmassen. *Zeitschrift fur Physik*, 96(7):431–458, 1935.
- [172] Subramanyan Raman, CW Nestor Jr, and P Tikkanen. Transition probability from the ground to the first-excited 2+ state of even–even nuclides. *Atomic Data and Nuclear Data Tables*, 78(1):1–128, 2001.
- [173] Roger D Woods and David S Saxon. Diffuse surface optical model for nucleon-nuclei scattering. *Physical Review*, 95(2):577, 1954.
- [174] Brian R Martin and Graham Shaw. *Particle physics*. John Wiley & Sons, 2017.
- [175] Xiaofeng Wang. *Exotic collective excitations at high spin: triaxial rotation and octupole condensation*. University of Notre Dame, 2007.
- [176] Yang Sun, Shuxian Wen, et al. Varied signature splitting phenomena in odd proton nuclei. *Physical Review C*, 50(5):2351, 1994.